Reducing the mysteries of sulfur metabolism in *Mycobacterium tuberculosis*

by

Devayani P. Bhave

A dissertation submitted in partial fulfillment
of the requirements for the degree of
Doctor of Philosophy
(Chemical Biology)
in the University of Michigan
2011

Doctoral Committee:

Associate Professor Kate S. Carroll, co-Chair
Associate Professor Bruce A. Palfey, co-Chair
Professor E. Neil G. Marsh
Associate Professor Zhaohui Xu

Devayani P. Bhave

2011

To my parents, grandparents and brother

Acknowledgements

I would like to express my sincere gratitude to my advisor, Professor Kate S. Carroll. She has truly been an inspirational mentor and facilitated in making my graduate school experience a productive and stimulating one. I have immensely benefitted from her guidance and her rigorous approach to research. I am also thankful to her for setting up challenging goals and for encouraging me to achieve them.

I am grateful to my dissertation committee members, Professors Neil Marsh, Zhaohui Xu, Vincent Pecoraro and Bruce Palfey for providing valuable feedback and many helpful suggestions to improve my research. I especially thank Professor Palfey for his flexibility and openness in serving on my committee.

I owe appreciation to all our collaborators for many discussions and detailed feedback, which contributed to this project: Professor Carsten Krebs (Pennsylvania State University), Professor Louis Noodleman and Dr. Wenge Han (The Scripps Research Institute), Professor James E. Penner-Hahn and Dr. Samuel Pazicni (University of Michigan). I am also grateful to Professor Stephen Ragsdale, Dr. Ryan Kunz, and all the members of the Ragsdale lab.

I would like to acknowledge all the past and present members of the Carroll lab. I was fortunate to work alongside such fun, intelligent and hard-working scientists. In particular, I thank Jiyoung Hong, Stephen Leonard and Candice Paulsen for their camaraderie, encouragement and for

Preface

This thesis is the compilation of published and unpublished work towards reducing the mysteries of sulfur metabolism in *Mycobacterium tuberculosis*. In particular, we elucidate mechanistic details of sulfonucleotide reductases (SRs) that catalyze the first committed step of reductive sulfur assimilation *en route* to the biosynthesis of all sulfur-containing metabolites in plants and bacteria. SRs have no human homolog and represent promising targets for therapeutic intervention.

In Chapter 1, we discuss sulfur metabolism enzymes that facilitate mycobacterial survival and introduce adenosine-5'-phosphosulfate reductase (APR) as an iron-sulfur cluster protein essential for the survival of persistent *M. tuberculosis*. Functions of iron-sulfur clusters in different proteins are summarized with a view to understanding the role of the cluster in APR. A portion of this discussion is published as a review for which the citation is Bhave, D. P., Muse, W.B., and Carroll, K.S., "Drug Targets in Mycobacterial Sulfur Metabolism," (2007) *Infect. Disord. Drug Targets* 7; 140-158.

Chapter 2 details the molecular determinants that underlie binding and specificity in APR and provides an active site model as a pharmacological roadmap for the rational design of potential inhibitors of APR. This study was published as Hong, J.A., Bhave, D.P., and Carroll, K.S., "Identification of Critical Ligand Binding Determinants in *Mycobacterium tuberculosis* Adenosine-5'-phosphosulfate Reductase," (2009) *J. Med. Chem.* 52; 5485-95.

Chapter 3 focuses on the spectroscopic characterization of the [4Fe-4S] cluster in APR from *M. tuberculosis*. A paramagnetic state of the cluster has been generated for the first time permitting the application of electron paramagnetic resonance and other forms of spectroscopies. Further, an essential role has been identified for active site residue Lys144, whose side chain serves as a link between with the [4Fe-4S] cluster and the substrate. Based on these findings, a role for the cluster in the catalytic mechanism of APR has been discussed. The citation for this article is Bhave, D.P., Hong, J.A., Lee, M., Jiang, W., Krebs, C., and Carroll, K.S., "Spectroscopic Studies on the [4Fe-4S] Cluster in Adenosine 5'-Phosphosulfate Reductase from *Mycobacterium tuberculosis*," (2010) *J. Biol. Chem.* 286; 1216-1226.

In Chapter 4, we present density functional theory calculations and extended x-ray fine structure spectroscopic analyses that reveals insights into the coordination, geometry and electrostatics of the [4Fe-4S] cluster in APR. Additionally, a comparison between models with and without the tandem cysteine pair coordination of the cluster suggests a role for the unique coordination in facilitating a compact geometric structure and modulating the electrostatics of the cluster. These findings are published as Bhave, D.P., Han, W.-G., Pazicni, S., Penner-Hahn, J. E., Carroll, K.S., and Noodleman, L., "Geometric and Electrostatic Study of the [4Fe-4S] Cluster of Adenosine-5'-Phosphosulfate Reductase from Broken Symmetry Density Functional Calculations and Extended X-ray Absorption Fine Structure Spectroscopy," (2011) *Inorg. Chem.* 50; 6610-6625.

Chapter 5 examines substrate specificity in the family of SRs and reports that contrary to prevailing view the phosphate-binding loop in SRs has a modest effect on substrate discrimination. Instead, by means of metalloprotein engineering, spectroscopic and kinetic

analyses, we demonstrate that the iron-sulfur cluster plays a pivotal role in substrate specificity and catalysis. The findings offer new insights into the evolution of this enzyme family, and have broader implications regarding the function of protein-bound iron-sulfur clusters. This work is under review as Bhave, D.P., Hong, J.A., Keller, R.L., M., Krebs, C., and Carroll, K.S., "Iron-Sulfur Cluster Engineering Provides Insight into the Evolution of Substrate Specificity among the Family of Sulfonucleotide Reductases," (2011), *manuscript under review in ACS Chem. Bio*.

Finally, Chapter 6 summarizes the key findings of this thesis and provides a discussion of future directions for understanding mechanistic details of APR and the involvement of the iron-sulfur cluster toward the rational development of inhibitors for APR.

Table of Contents

List of Figures

List of Schemes

List of Tables

List of Abbreviations

APS   adensoine-5′-phosphosulfate

AMP   adenosine 5′-phosphate

PAPS   3′-phosphoadenosine 5′-phosphosulfate

PAP   adenosine 3′,5′-diphosphate

ATP   adenosine 5′-triphosulfate

ADP   adenosine 5′-diphosphate

ADPβF   β-fluoro-5'-ADP

[4Fe-4S]   four iron, four sulfur

[2Fe-2S]   two iron, two sulfur

E   enzyme

Cys-Sγ–SO$_3^-$ S-sulfocysteine

P-loop   phosphate-binding loop

APR   adenosine 5′-phosphosulfate reductase

PAPR   3′-phosphoadenosine 5′-phosphosulfate reductase

MtAPR   *Mycobacterium tuberculosis* APR

PaAPR   *Pseudomonas aeruginosa* APR

EcPAPR   *Escherichia coli* PAPR

PpAPR-B   *Physcomitrella patens* APR

Bs(P)APR   *Bacillus subtilis* sulfonucleotide reductase

Trx   thioredoxin

NAD	nicotinaminde adenine dinucleotide
NADP	nicotinaminde adenine dinucleotide phosphate
HPLC	high-performance liquid chromatography
TFA	trifluoroacetic acid
Da	daltons
EPR	electron paramagnetic resonance
FAD	flavin adenine dinucleotide
DTT	dithiothreitol
IPTG	isopropyl-β-D-thio-galactoside
PMSF	phenylmethanesulfonylfluoride
ESI-FT-ICR MS	electrospray ionization Fourier transform ion cyclotron mass spectrometry
ESEEM	electron spin echo envelope modulation
ENDOR	electron nuclear double resonance
NMR	nuclear magnetic resonance
DFT	density functional theory
XAS	x-ray absorption spectroscopy
EXAFS	extended x-ray fine structure
XANES	x-ray absorption near-edge structure
FT	Fourier transform
PDB	protein data bank
COSMO	conductor-like screening solvation model
ESP	electrostatic potential
NSP	net spin population
ICP	inductively coupled plasma

UV-vis   ultraviolet-visible

k_{cat}/K_m second-order rate constant, catalytic efficiency

k_{max} single-turnover rate constant

$K_{1/2}$ protein concentration at which half the substrate in bound

K_d dissociation constant

K_i inhibition constant

K_{obs} observed rate constant

Tris   tris(hydroxymethyl)aminomethane

Bis-tris   1,3-bis(tris(hydroxymethyl)methylamino)

DTT   dithiothreitol

ABSTRACT

Reducing the mysteries of sulfur metabolism in *Mycobacterium tuberculosis*

by

Devayani Bhave

Co-Chairs: Kate S. Carroll and Bruce A. Palfey

Sulfur metabolic pathways are fundamental for survival and the expression of virulence in many pathogenic bacteria, including *Mycobacterium tuberculosis*. In addition, microbial sulfur metabolic pathways are largely absent in humans and therefore, represent unique targets for therapeutic intervention. However, many aspects of mycobacterial sulfur metabolism, such as mechanistic details of sulfonucleotide reductases (SRs) involved in assimilatory sulfate reduction, remain poorly understood and represent exciting areas of new or continued investigation. SRs catalyze the first committed step of reductive sulfur assimilation *en route* to the biosynthesis of all sulfur-containing metabolites. In this study, we elucidate the molecular binding determinants that underlie ligand binding and specificity of SRs and provide a pharmacological roadmap for the rational design of potential inhibitors of SRs. Next, we present a spectroscopic characterization of the iron-sulfur cofactor essential to one class of SRs and reveal mid-range electrostatic interactions between the iron-sulfur cluster and the substrate in the active site. Based on these data, we propose a role for the cluster in pre-organizing active

site residues and in substrate activation. Computational modeling and theoretical calculations corroborate these findings and in addition, suggest a role for the unique coordination of the iron-sulfur cluster in facilitating a compact geometric structure and modulating its electrostatic nature. Furthermore, metalloprotein engineering, kinetic and spectroscopic analyses demonstrate that the iron-sulfur cluster plays a pivotal role in substrate specificity and catalysis, and yield important structural information that can be used for the design of cluster-targeted SR inhibitors. The findings also provide new perspectives into the evolution of the SR family, and have broader implications regarding the function of protein-bound iron-sulfur clusters. Collectively, the work presented in this thesis contributes towards a better understanding of the catalytic mechanism of this unique class of enzymes and offers insights into strategies for therapeutic intervention.

Chapter 1

Identification of Drug Targets in Mycobacterial Sulfur Metabolism with a Focus on Adenosine-5'-phosphosulfate Reductase

1.1 Abstract

The identification of new antibacterial targets is urgently needed to address multidrug resistant and latent tuberculosis infection. Sulfur metabolic pathways are essential for survival and the expression of virulence in many pathogenic bacteria, including *Mycobacterium tuberculosis*. In addition, microbial sulfur metabolic pathways are largely absent in humans and therefore, represent unique targets for therapeutic intervention. In this review, we summarize our current understanding of the enzymes associated with the production of sulfated and reduced sulfur-containing metabolites in Mycobacteria. In particular, we focus on adenosine-5'-phosphosulfate reductase, which catalyzes the first committed step of reductive sulfur assimilation and is absent in humans. Adenosine-5'-phosphosulfate reductase harbors an iron-sulfur cluster that is essential for its catalytic activity; however, the precise role of the cluster is unknown. Investigation of the role of the cluster in the catalytic mechanism of this enzyme will lead to new

fundamental insights into iron-sulfur biochemistry and bacterial sulfur metabolism. In addition, the study would pave the way for the development of drugs for tuberculosis based on inhibitors that inactivate the enzyme by disrupting the biological function of the iron-sulfur cluster.

1.1.1 *Mycobacterium Tuberculosis*

Mycobacterium tuberculosis, the causative agent of tuberculosis (TB), is one of the most lethal infectious agents affecting humans [1-3]. The disease infects almost two billion people or one-third of the world's population, and accounts for an estimated 2 million deaths per year. The majority of people afflicted with TB live in developing countries, where lethal synergy with HIV infection also fuels the TB pandemic.

M. tuberculosis infection is difficult to treat, requiring 6-9 months of chemotherapy with a cocktail of four antibiotics – isoniazid, rifampin, pyrazinamide and ethambutol [4,5]. In large part, the lengthy drug therapy is necessary because mycobacteria exist as a metabolically diverse population within the human host [5]. Some bacteria will be actively dividing, rendering them susceptible to antibiotic treatment. However, less active subpopulations also exist in stationary phase or as dormant bacteria [6,7]. Since TB drugs target biological processes required for bacterial growth (e.g., cell wall biosynthesis), they are far less effective at killing the persistent population [5,8,9].

In addition to toxic side effects, the lengthy treatment regime results in poor patient compliance and drug resistant strains are beginning to emerge [10]. The World Health Organization estimates that up to 50 million persons worldwide are infected with multidrug resistant strains of *M. tuberculosis* (MDR-TB) [11]. This number continues to grow as 300,000 new MDR-TB cases

2

are diagnosed each year with 79 percent of individuals showing resistance to three or more frontline drugs [11]. Taken together, the growing problem of MDR-TB and the lack of drugs that effectively target persistent bacteria, stress the urgent need for identification of new antimicrobial targets [12,13].

Many fundamental aspects of mycobacterial metabolism and pathogenesis are poorly understood, in part because of the technical difficulties inherent to studying *M. tuberculosis*. The organism must be manipulated in a biosafety level 3 laboratory, and the slow growth rate (3 weeks for colonies, up to 1 year for completion of animal models) imposes limitations on apparent research productivity. However, the availability of complete mycobacterial genome sequences [14-17] and the maturation of methods for disrupting mycobacterial genes [18-20] have provided tools that can accelerate the discovery of potential drug targets and elucidate metabolic pathways that are essential for mycobacterial survival.

1.1.2 Overview Of TB Infection

M. tuberculosis infection is a complex process that initiates with aerosol inhalation to the host lung [6,21,22]. Therein, the mycobacteria are phagocytosed by alveolar macrophages. Upon entry into a macrophage, the TB bacilli interfere with normal phagosomal maturation, preventing fusion with lysosomes [23]. The ability of *M. tuberculosis* to side-step lysosomal degradation allows the bacilli to take up residence in an endosomal environment and multiply within the host cell. In response to the infection, macrophages produce pro-inflammatory signals – cytokines and chemokines – that recruit T-cells and neutrophils to the infected tissue [22,24-27]. These cells encircle the infected macrophage, walling it off from the surrounding tissue in a structure called a granuloma [28-31]. Within the context of the granuloma, T-cells

can proliferate in response to specific mycobacterial antigens and some may leave the granuloma to reenter the circulation; thus, the granuloma is a dynamic structure [32]. Activation of the immune response and induction of lung inflammation is part of the *M. tuberculosis* lifecycle [6,21,22]. The lung tissue damage caused by activated immune cells induces coughing and provides an exit strategy for the bacteria to spread to another host.

Less than 10% of infected individuals will develop active TB infection. In the rest, mycobacteria residing within granulomas enter into a persistent or "latent" state characterized by a lack of cell division and a change in basic metabolism [6,7,33,34]. These latent mycobacteria are difficult to eradicate since they are not reliant on machinery targeted by conventional antibiotics [5]. By unknown mechanisms, the infection can be reactivated after many years or decades to produce active, infectious TB. This event is often associated with compromised immune function due to coinfection with HIV, drug use, or aging. Hence, effective treatment of TB will require efficacy against persistent *M. tuberculosis*, or at the least a better understanding of the mechanisms underlying immune cell activation, bacterial adaptation and survival within the granuloma [5,13,31].

1.1.3 Sulfur and Mycobacterial Survival

To complete its lifecycle, *M. tuberculosis* must survive within the hostile, nutrient-poor and oxidizing environment of the host macrophage [7,30,35]. At the same time, *M. tuberculosis* must activate sufficient immune effector functions to induce granuloma formation in the lung [21,22]. This complex interplay between mycobacteria and the host immune system likely requires several host-pathogen interaction mechanisms and, once the granuloma has been formed, induction of metabolic pathways that allow the organism to persist. At present time,

the metabolic requirements of mycobacteria in the context of the granuloma are not fully understood. However, genes involved in the metabolism of sulfur have consistently been identified as up-regulated in response to oxidative stress, nutrient starvation and dormancy adaptation (culture conditions that model aspects of mycobacterial life in the granuloma) and during macrophage infection [36-45].

Sulfur is an essential element for life and plays a central role in numerous microbial metabolic processes [46]. In its reduced form, sulfur is used in the biosynthesis of the amino acids cysteine and methionine. Cysteine is incorporated into biomolecules such as proteins, coenzymes, and mycothiol (the mycobacterial equivalent of glutathione) (Figure 1.1). Found in all
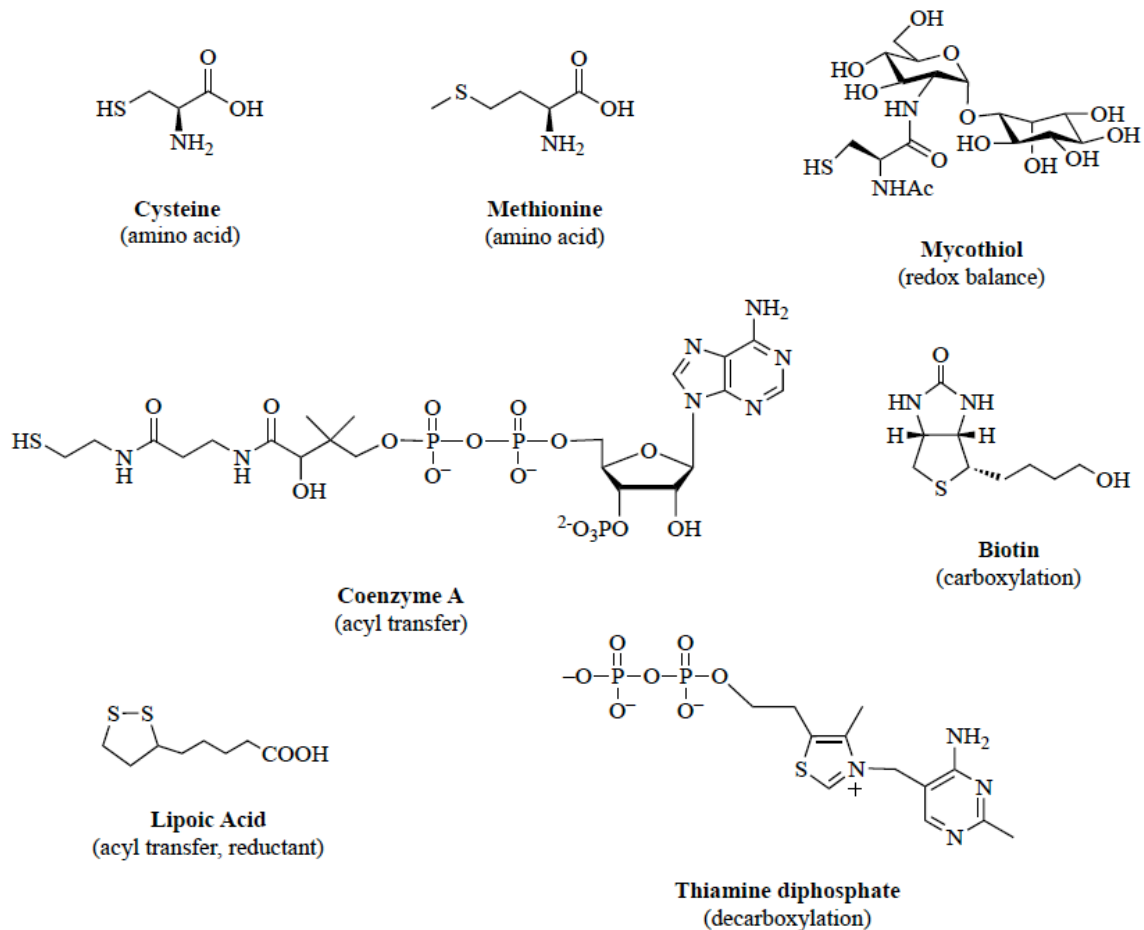
Figure 1.1 Reduced sulfur-containing metabolites in mycobacteria

actinomycetes, mycothiol regulates cellular redox status and is essential for *M. tuberculosis* survival [47]. Another reduced sulfur-containing metabolite, coenzyme A (CoA), is heavily utilized for lipid metabolism (a process that is central to mycobacterial cell wall maintenance and remodeling) [48].

In its oxidized form, sulfur is present as a sulfuryl moiety ($-SO_3^-$) that can modify hydroxyls and amines in proteins, polysaccharides and lipids (Figure 1.2) [49,50]. Extracellular presentation of sulfated metabolites plays important regulatory roles in cell-cell and host-pathogen communication [50]. Hence, acquisition and metabolism of sulfur is essential for mycobacterial virulence and survival.

Sulfolipid-1

Trehalose-2-sulfate

2-Sulfo-6-deoxytalose

Glycopeptidolipid IV
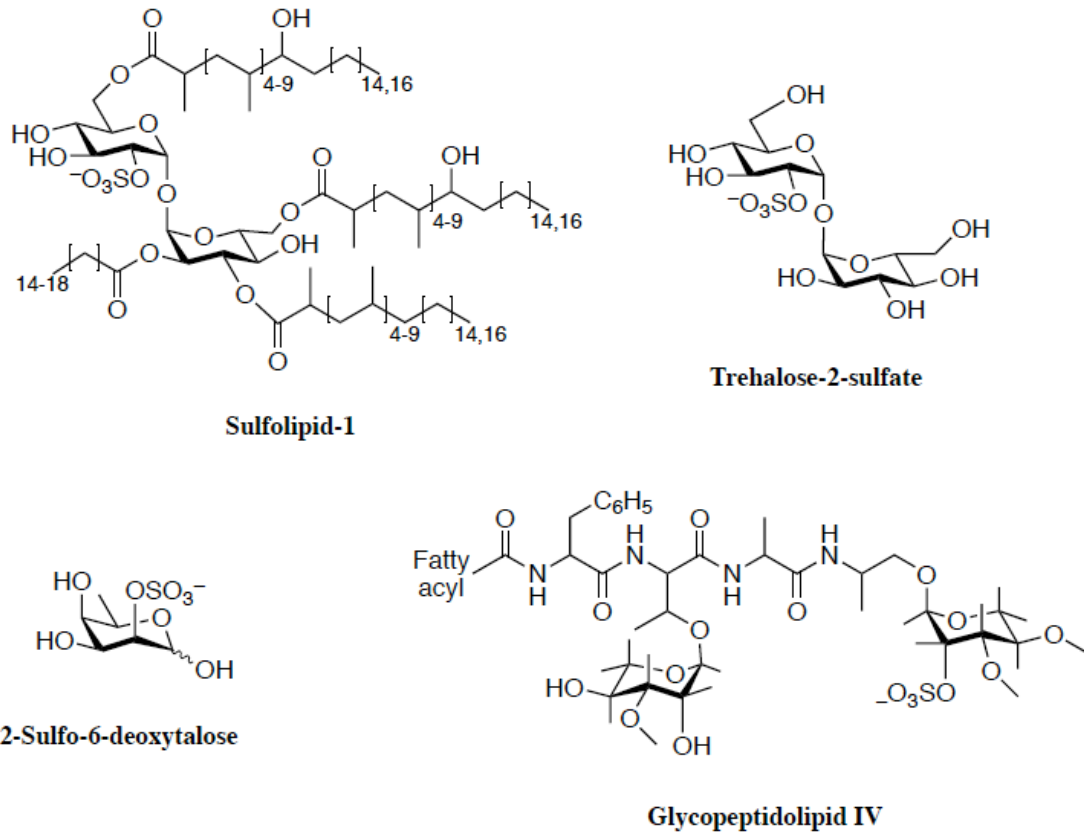
Figure 1.2 Sulfated metabolites in mycobacteria

The identification of new antibacterial targets is essential to address MDR- and latent-TB infection [13,51]. Toward this end, mycobacterial sulfur metabolism represents a promising new area for anti-TB therapy [50,52,53]. Numerous studies have validated amino acid biosynthetic pathways and downstream metabolites as antimicrobial targets [54-57] and sulfur metabolic pathways are required for the expression of virulence in many pathogenic bacteria [58-62]. In particular, mutants in mycobacterial sulfur metabolism genes are severely impaired in their ability to persist and cause disease [41,43,61,63-66]. Furthermore, most microbial sulfur metabolic pathways are absent in humans and therefore, represent unique targets for therapeutic intervention.

1.2. Sulfate Assimilation in Mycobacteria: An Overview

Sulfate assimilation begins with the active transport of inorganic sulfate (SO_4^{2-}) across the mycobacterial cell membrane by the CysTWA SubI ABC transporter complex (Figure 1.3) [67,68]. Once sulfate is imported, it is activated by ATP sulfurylase (encoded by cysND) via adenylation to produce adenosine-5'-phosphosulfate (APS) [39,53,69]. In mycobacteria, APS lies at a metabolic branch point [53]. For sulfation of biomolecules such as proteins, lipids and polysaccharides, APS is phosphorylated at the 3'-hydroxyl by APS kinase (encoded by cysC) to form 3'-phosphoadenosine-5'-phosphosulfate (PAPS), the universal sulfate donor for sulfotransferases (STs) [53,69,70]. Transfer of $-SO_3^-$ to hydroxyl or amino functionalities of biomolecules plays important roles in regulation of cell-cell communication and metabolism [50]. Alternatively, for production of reduced sulfur-containing metabolites, the sulfate moiety in APS is reduced to sulfite (SO_3^{2-}) by APS reductase (APR), the gene product of cysH [53,61,71,72]. Sulfite is further reduced to sulfide (S^{2-}) by sulfite reductase (encoded by nirA) [73] and is the form of sulfur that is used for the biosynthesis of sulfur-containing metabolites including cysteine, methionine,

coenzymes, and mycothiol [46,47,49]. Each branch of sulfate assimilation is discussed in terms of the available genetic and biochemical data below.
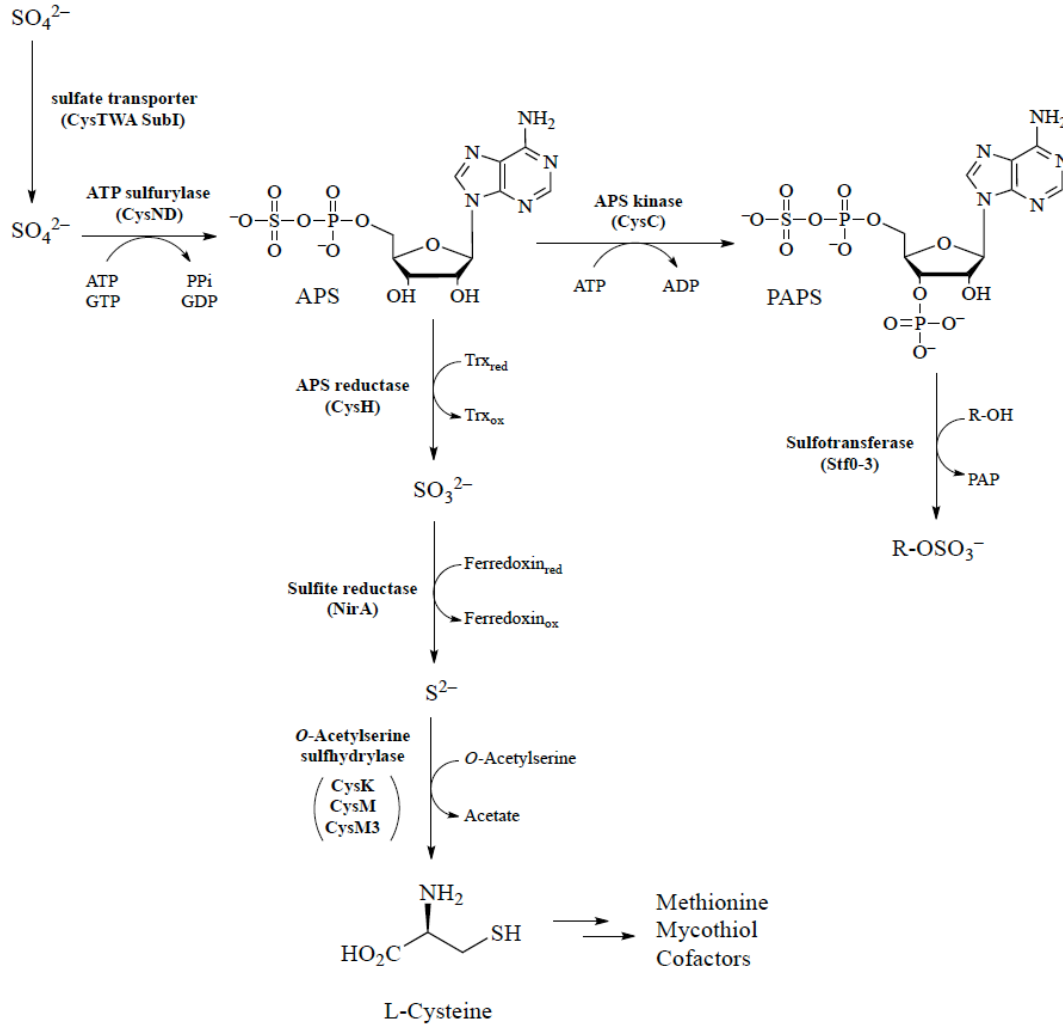
Figure 1.3 The sulfate assimilation pathway in mycobacteria

1.2.1 Sulfate Import and Activation

Present at 300-500 µM, inorganic sulfate is the fourth most abundant anion in human plasma [74]. Sulfate transporters have been identified in all major human tissues investigated to date, and of particular relevance to the intracellular lifestyle of *M. tuberculosis*, the existence of endosomal-associated transporters has also been demonstrated [74]. The genes encoding the

CysTWA SubI ABC transporter complex in mycobacteria have been identified by homology to *Escherichia coli* and *Salmonella typhimurium* [68], are essential [41], robustly up-regulated during oxidative stress [37], dormancy adaptation [36], and expressed in macrophages [44]. Consistent with this annotation, cysA or subI mutants (Δ*cysA* or Δ*subI*, respectively) in *M. bovis* bacillus Calmette-Guérin (BCG) – an attenuated, vaccine strain of *M. bovis* – are compromised in their ability to transport sulfate [68,75]. When grown in media supplemented with casamino acids, the rate of sulfate transport in Δ*cysA* is ~1.1% relative to wild-type *M. bovis* BCG [68]. The minor amount of transport is not enough to meet bacterial sulfur requirements and hence, these sulfate transport mutants are auxotrophic for reduced sulfur.

Interestingly, no significant difference in the number of viable bacilli was observed in the organs of mice infected with Δ*cysA* and wild-type *M. bovis* BCG up to 63 days post-infection [68]. These data indicate that *M. bovis* BCG may scavenge sufficient amounts of reduced sulfur from the host for survival. However, an important question raised from the findings of this study is whether the sulfur requirements for an attenuated *M. bovis* strain reflect those of *M. tuberculosis* known to elicit a more potent host immune response [21,22,32]. It is also possible that the mycobacterial genome encodes for an additional sulfate transporter which is not expressed under culture conditions, but is specifically up-regulated during infection [52]. In support of this hypothesis, mRNA array analysis shows significant up-regulation of hypothetical protein 1739c (annotated as a putative high affinity sulfate transporter) during *M. tuberculosis* infection of macrophages in response to nitric oxide [38] or hypoxia [45]. Additional studies will be required to confirm the function of the putative sulfate transporter and its relevance to sulfate acquisition *in vivo*.

Once sulfate is transported to the cytosol, ATP sulfurylase (encoded by *cysD*) catalyzes the first committed step in sulfate assimilation (Figure 1.3) [39,69]. In this reaction, the adenylyl moiety of adenosine 5'-triphosphate (ATP) is coupled to sulfate. The product that results, APS, contains a unique high-energy phosphoric-sulfuric acid anhydride bond – the biologically activated form of sulfate [49]. Formation of APS is energetically unfavorable (K_{eq} of 10^{-7} – 10^{-8} near physiological conditions) [49] and in prokaryotes, the hydrolysis of guanosine-5'-triphosphate (GTP) is coupled to sulfurylation of ATP to surmount this energetic hurdle [76]. The GTPase (encoded by *cysN*) forms a heterodimer with ATP sulfurylase (CysD) and synthesis of APS is driven 1.1×10^{6}-fold further during GTP hydrolysis [69]. Notably, eukaryotic ATP sulfurylases do not bear any sequence or structural similarity to their prokaryotic counterparts, nor do they employ a GTPase for PAPS biosynthesis [77]. These mechanistic and structural differences, in particular the unique G protein subunit, could be exploited to develop small molecule inhibitors of bacterial sulfate activation [52].

The final step in PAPS biosynthesis is catalyzed by APS kinase (encoded by *cysC*) [53,70]. In this reaction, ATP is utilized to phosphorylate the 3'-hydroxyl of APS. Depending on the organism, APS kinase can be encoded as a separate protein or as a fusion with ATP sulfurylase, without significant variation in catalytic mechanism [53,78]. Most eukaryotes (including humans) encode for ATP sulfurylase (CysD) and APS kinase (CysC) on a single polypeptide. In *M. tuberculosis*, however, APS kinase (Cys C) is genetically fused to the GTPase subunit (CysN) of ATP sulfurylase [53]. The APS kinase domain of *M. tuberculosis* CysNC was identified through sequence homology and confirmed by genetic complementation [53]. In a subsequent report, a mutant strain of *M. tuberculosis* that removes the APS kinase domain of the bifunctional *cysNC* gene was constructed [70]. As expected, the *cysC* knockout (Δ*cysC*) was able to grow on sulfate

as a sole sulfur source (indicating a functional ATP sulfurylase), but was unable to synthesize PAPS [70].

Fusion of APS kinase to the GTPase domain of ATP sulfurylase raised the interesting possibility of substrate channeling between subunits [52,78]. In this scenario, the final product PAPS, and not the APS intermediate, would be released into solution. Leyh and colleagues have recently tested this hypothesis for *M. tuberculosis* ATP sulfurylase [78]. Although PAPS synthesis is 5,800 times more efficient than APS synthesis [69], these studies demonstrate that APS is not channeled from the *M. tuberculosis* adenylyltransferase to the APS kinase domain [78], consistent with the domain arrangement proposed from a recent crystal structure of the CysNC complex [77].

Collectively, CysNC and D proteins form a multifunctional enzyme complex ~300 KDa (consistent with a trimer of CysNC•D heterodimers), referred to as the sulfate-activating complex (SAC) [39,69]. In *M. tuberculosis*, expression of the SAC operon is induced by conditions likely to be encountered by pathogenic mycobacteria within the macrophage, including sulfur limitation, oxidative stress, and is repressed by cysteine [37,39]. The SAC operon is also up-regulated during stationary phase growth, an *in vitro* model of persistent *M. tuberculosis* infection [36]. *M. tuberculosis* SAC gene expression is also augmented within the intracellular environment of the macrophage [44,79]. Taken together, these data are consistent with increased activity of sulfate-activating enzymes and flux through the sulfate assimilation pathway during mycobacterial infection.

1.2.2 Sulfotransferases and Sulfation

Sulfotransferases (STs), the enzymes that install sulfate esters, transfer sulfate from PAPS (produced by the SAC) to a hydroxyl or, less frequently, to an amide moiety on glycoproteins, glycolipids and metabolites (Figure 1.3) [50]. Sulfated metabolites are abundant in higher eukaryotes, particularly mammals, where they function primarily in cell-cell communication. For example, sulfated glycoproteins mediate interactions of leukocytes with endothelial cells at sites of chronic inflammation, sulfated peptides such as hirudin and cholecystokinin act as hormones, and sulfated glycolipids are involved in neuronal development [80,81]. In contrast, reports of sulfated metabolites in prokaryotes have been rare. In 1992, Long and colleagues reported the first functionally characterized sulfated metabolite from the prokaryotic world – the nodulation factor NodRm-1 from *Sinorhizobium meliloti* [82]. This sulfated glycolipid is secreted from the bacterium and acts on host plant cell receptors thereby initiating symbiotic infection [83].

Among pathogenic bacteria, only one family has been reported to produce sulfated metabolites – the *Mycobacteria*. More than 40 years ago, Goren and coworkers isolated an abundant sulfated glycolipid from the *M. tuberculosis* cell wall and characterized the structure shown in (Figure 1.2) [84-86]. Termed sulfolipid-1 or SL-1, this compound has only been observed in the tuberculosis complex; it is absent from non-pathogenic mycobacteria such as *M. smegmatis*. Comprising a trehalose-2-sulfate (T2S) core modified with four fatty acyl groups, SL-1 accounts for almost 1% of the dry weight of *M. tuberculosis*. Early studies found a correlation between the abundance of SL-1 and the virulence of different clinical *M. tuberculosis* isolates [87,88] and its location in the outer envelope has prompted speculation that it may be involved in host-pathogen interactions [89]. The exact function of SL-1, however, remains elusive (see [52] and references therein). Nonetheless, the biosynthetic pathway for SL-1 has recently been

elucidated [52,90-92] and a comprehensive study of mutants in SL-1 biosynthesis should help clarify the role of this sulfated glycolipid in the mycobacterial lifecycle.

In addition to SL-1, other novel sulfated metabolites have been identified in *M. tuberculosis* using an innovative metabolomic approach that combines genetic engineering, metabolic labeling with a stable sulfur isotope ($^{34}SO_4^{2-}$) together with mass spectrometry analysis [70] (Figure 1.2). Structurally distinct sulfated metabolites have also been identified in several other mycobacterial species, including *M. smegmatis*, *M. fortuitum*, and the HIV-associated opportunistic pathogen *M. avium* (Figure 1.2) [70,93-95]. Interestingly, in *M. avium* a sulfated cell wall glycopeptidolipid was recently found to be up-regulated in HIV patients with acquired drug resistance [93]. Significant work remains to fully characterize and elucidate the biological significance of sulfated metabolites found in mycobacteria. A major step toward this objective is to define the biosynthetic pathways of mycobacterial sulfated metabolites, including the STs responsible for installing the sulfuryl moiety.

In 2002, an analysis of mycobacterial genomes reported by Mougous and colleagues revealed a large family of open reading frames with homology to human carbohydrate sulfotransferases [50]. The predicted proteins shared regions of sequence homology associated with binding to their common substrate, PAPS. Presently, four such genes have been identified in *M. tuberculosis* (annotated as *stf0-3*) and the *M. avium* genome encodes nine putative STs (*stf*0, 1, 4-10) [52]. To date, of the 11 predicted STs found in mycobacterial genomes, genetic and biochemical studies have only been reported for Stf0 and Stf3.

Stf0 is present in a number of other pathogenic bacteria and initiates the biosynthesis of SL-1 by sulfating the disaccharide, trehalose, to form T2S (Figure 1.2) [92]. A knockout mutant of *stf0* has been reported in *M. tuberculosis* [96]. This study demonstrates that Stf0 is not required for survival in liquid culture, hinting toward a specific role in host infection. The structure of stf0 in complex with trehalose has recently been reported and has revealed several interesting features [92]. In the presence of trehalose, Stf0 forms a dimer both in solution and in the crystal structure. Moreover, Stf0-bound trehalose participates in the dimer interface, with hydroxyl groups from a glucose residue bound in one monomer forming interactions with the other monomer. Residues involved in substrate binding and dimerization have been identified, along with a possible general base (*i.e.*, Glu36) that may facilitate nucleophilic attack of the 2'-hydroxyl group on PAPS. A panel of synthetic glucose and trehalose analogs has also been tested for binding and found that any modification to the parent disaccharide compromises substrate sulfation [92]. Finally, a kinetic study of the enzyme using MS has also been reported [97]. The results address the order of substrates binding and are consistent with a random sequential mechanism involving a ternary complex with both PAPS [or 3'-phosphoadenosine-5'-phosphate, (PAP)] and trehalose (or T2S) bound in the active site.

Stf3 may play a regulatory role in *M. tuberculosis* virulence [98]. In a mouse model of TB infection, a mutant strain in which Stf3 was disrupted (Δ*stf3*) was unable to produce a sulfated molecule termed, "S881". Interestingly, when compared to wild-type *M. tuberculosis*, Δ*stf3* exhibited a hypervirulent phenotype. No relatives of the remaining *stf* family members are found in any other prokaryotic genomes, suggesting that they are unique to mycobacteria. Substrates for the majority of mycobacterial STs remain to be elucidated.

1.3 Oxidative Macrophage Antimicrobial Activity

In order to replicate and persist in its human host, *M. tuberculosis* must survive within the hostile environment of the macrophage, where bactericidal oxidants – superoxide ($O_2 \cdot^-$) and nitric oxide ($NO\cdot$) – are generated in response to infection [35]. Two enzymes, nicotinamide adenine dinucleotide phosphate-oxidase (NADPH oxidase) and inducible nitric oxide synthase (NOS2), are largely responsible for production of these reactive oxygen and nitrogen intermediates (termed ROI and RNI, respectively) [99,100].

NADPH oxidase is a membrane protein that generates $O_2 \cdot^-$ by transferring electrons from NADPH inside the cell across the phagosomal membrane; the electrons are coupled to molecular oxygen to produce $O_2 \cdot^-$ [101]. Subsequently, $O_2 \cdot^-$ can accept an electron spontaneously or be reduced by superoxide dismutase (SOD) to form hydrogen peroxide (H_2O_2) [102]. In turn, H_2O_2 can oxidize cellular targets or be converted into the highly damaging hydroxyl radical ($OH\cdot$) through the iron-catalyzed Fenton-Haber-Weiss reaction [103]. In the NOS2 reaction, the guanidino nitrogen of arginine undergoes a five-electron oxidation via a N-ω-hydroxy-L-arginine (NOHLA) intermediate to yield $\cdot NO$ [104]. The combination of the two oxidant-generating systems can also exert a synergistic effect in bacterial killing as macrophages can generate $O_2 \cdot^-$ simultaneously with $\cdot NO$, yielding the more reactive peroxynitrite ($ONOO^-$) [105]. A consequence of NADPH and NOS2 enzymatic activities and the resulting "oxidative burst" is that phagocytosed bacteria are killed by oxidative damage to a range of protein and DNA targets [35,104,106].

In mice, activation of macrophages induces production of NOS2 and phagosomal NADPH oxidase, via ligation of toll-like receptors (TLRs), or via stimulation by the cytokines IFN-γ or TNF-

α [107,108]. In mouse models of TB, numerous studies have demonstrated that NOS2 plays an essential role in controlling persistent infection. Macrophages can inhibit mycobacterial growth via NOS2-generated RNI, inhibition of NOS2 during persistent infection leads to reactivation of disease, and NOS2 gene-disrupted mice are extremely susceptible to TB infection [107,108]. More recently, a proteomics study has identified proteins in *M. tuberculosis* that are targeted by RNI stress [109]. Notably, many essential metabolic and antioxidant defense enzymes are among those proteins found modified for RNI.

While good evidence exists for ROI-mediated bacterial killing of other bacterial, fungal and parasitic pathogens, their bactericidal effect on mycobacteria has been less clear. Studies demonstrate that *M. tuberculosis* resists killing by ROI in vitro and that mice with defects in p47 or gp91 subunits of phagocyte NADPH oxidase (Phox) are also relatively resistant to TB infection [107,110]. However, NADPH oxidase is highly active during the persistent phase of *M. tuberculosis* infection in mice [111]. This observation suggests that *M. tuberculosis* must possess extremely effective detoxification pathways to counter ROI stress. Consistent with this hypothesis, mice deficient in the KatG catalase-peroxidase survived better in *pg91phox*-deficient mice [111]. More recently, it was shown that macrophages deficient in early stages of Phox assembly exhibited reduced bacterial killing, correlating with decreased production of ROI [112]. Taken together, these observations indicate that survival of *M. tuberculosis* within macrophages depends upon the ability of the bacterial to counter oxidative assault.

Mycobacteria produce enzymes such as SOD, peroxidases, catalase, and nitrosothiol reductase to help counteract the effect of ROI/RNI and promote intracellular survival and persistence in the host [35,113-115]. In addition to enzymatic detoxification of ROI and RNI, reduced sulfur-

containing metabolites are an essential component of bacterial antioxidant defense systems [116-120]. Specifically in mycobacteria, low molecular-weight thiols such as mycothiol (Figure 1.1), play a central role in maintaining a reducing cellular environment [47,116]. Proper redox homeostasis is essential for normal cellular function and to mitigate the effects of oxidative stress. Hence, the metabolic route used for the production of reduced sulfur-containing metabolites (Figure 1.3) is predicted to be important for mycobacterial survival [52,53,61]. Consistent with this hypothesis, expression of mycobacterial genes involved in reductive sulfate assimilation are induced by oxidative stress and within the environment of the macrophage [36-45].

1.4 Sulfate Reduction

APS reductase (APR, encoded by *cysH*) catalyzes the first committed step in the biosynthesis of reduced sulfur compounds (Figure 1.3). In this reaction, APS is reduced to SO_3^{2-} and adenosine-5'-phosphate (AMP) [121]. Thioredoxin (Trx), a 12.7 kDa protein with a redox-active disulfide bond, supplies the reducing potential necessary for this two-electron reduction [122]. The SO_3^{2-} product of this reaction is reduced further to S^{2-}, which is used for the biosynthesis of reduced sulfur-containing metabolites, such as cysteine, methionine, CoA, iron-sulfur clusters and mycothiol [46,67] (Figure 1.1). Consistent with its important metabolic role, APR was identified in a screen for essential genes in *M. bovis* BCG [41] and *cysH* is actively expressed during the dormant phase of *M. tuberculosis* and in the environment of the macrophage [36,44].

Humans do not reduce sulfate for *de novo* cysteine biosynthesis and therefore, do not have a CysH equivalent. Thus, APR would be an attractive drug target if the enzyme is required for bacterial survival or virulence *in vivo* [52,53,61,72]. To test this hypothesis, Senaratne and

coworkers generated an *M. tuberculosis* mutant strain lacking CysH (Δ*cysH*) [61]. As predicted, the mutant strain was auxotrophic for cysteine and could only be grown in media supplemented with this amino acid, methionine or glutathione (from which cysteine can be generated catabolically). The *cysH* mutant exhibited attenuated virulence in BALB/c and C57BL/6 immunocompetent mice. Growth kinetics in the lungs, spleen and liver of mice infected with Δ*cysH* or wild-type *M. tuberculosis* were also quantified. Strikingly, the number of colony-forming units recovered from the Δ*cysH* mutant mirrored those of wild-type *M. tuberculosis* during the acute stage of infection [up to 16 days post-infection (pi)]. However, the number of viable bacteria in the mutant became significantly less (*i.e.*, by 3 orders of magnitude) coincident with the emergence of adaptive TH1-mediated immunity and the induction of persistence in the mouse (between 16 and 42 days pi) [123]. In addition, Δ*cysH* was most compromised in the liver, where the host's oxidative antimicrobial response is thought to play an especially important role in antimicrobial defense. Since the replication of Δ*cysH* in mouse tissues during the first 16 days pi was identical to that of wild-type, these data suggest that mouse tissues can provide *M. tuberculosis* with sufficient reduced sulfur-containing amino acids (*e.g.*, cysteine and methionine), for initial growth (see discussion below) [52,61,68,124]. Hence, APR activity appears to be dispensable during the acute phase of infection, but indispensable in the later, persistence phase where access to or supply of reduced sulfur-containing nutrients becomes limiting [61].

As discussed above, NOS2 plays a vital role in controlling persistent *M. tuberculosis* infection in mice [6,125,126]. In order to test the role of APR in protecting the bacteria against the effects of NOS2, NOS2^{-/-} mice were infected with wild-type and Δ*cysH M. tuberculosis* [61]. In contrast to the observation made in wild-type mice, Δ*cysH* did not lose viability after the first 21 days pi

18

in NOS$^{-/-}$ mice; all mice succumbed to infection within 26 to 31 days. Thus, ΔcysH is significantly more virulent when NOS2 is absent. Taken together, these studies indicate that APR plays a central role in protecting *M. tuberculosis* against the effects of reactive nitrogen species produced by NOS2 and is critical for bacterial survival in the persistence phase of infection in mice [61]. Furthermore, a follow-up study demonstrates that immunization of mice with ΔcysH generates protection equivalent to that of the BCG vaccine in mice infected with *M. tuberculosis* [127].

The final step in sulfate reduction, the six electron reduction of SO_3^{2-} to S^{2-}, is catalyzed by sulfite reductase (encoded by *nirA*) (Figure 1.3) [73]. Like *cysH*, *nirA* is an essential gene [41] and is active during the dormant phase of *M. tuberculosis* [36,44]. The sulfite reductase in *M. tuberculosis* belongs to the family of ferredoxin-dependent sulfite/nitrite reductases [73]. These enzymes contain a [4Fe-4S] center and a siroheme. In this reaction, the external electron donor (likely ferredoxin) binds transiently to sulfite reductase and transfers electrons to the [4Fe-4S] center, one at a time. Subsequently, sulfite reduction is accomplished by transferring electrons from the cluster to the siroheme, which coordinates the sulfite substrate. In 2005, Schnell and coworkers reported the structure of *M. tuberculosis* NirA [73]. Interestingly, the structure depicts a covalent bond between the side chains of residues Tyr69 and Cys161 adjacent to the siroheme in the active site of sulfite reductase. Site-directed mutagenesis of either residue impairs catalytic activity, though their involvement in the mechanism of sulfite reduction is presently unknown [73].

1.5 Adenosine-5'-Phosphosulfate Reductase

Attenuation of Δ*cysH* in a mouse model of *M. tuberculosis* infection and the importance of APR in mycobacterial persistence further motivated investigation of the molecular details of the reaction catalyzed by APR [61]. Biochemical, spectroscopic, mass spectrometry and structural investigation of APR support a two-step mechanism, in which APS undergoes nucleophilic attack by an absolutely conserved cysteine to form an enzyme *S*-sulfocysteine intermediate, E-Cys-Sγ–SO_3^- [61,71,72,128,129]. In a subsequent step, SO_3^{2-} is released in a Trx-dependent reaction. During the catalytic cycle, nucleophilic attack at Sγ atom of the *S*-sulfocysteine intermediate results in the transient formation of a mixed disulfide between Trx and APR, with concomitant release of sulfite. The structure of this complex has recently been reported and reveals a unique protein-protein interface as a potential candidate for disruption by small molecule or peptide inhibitors [130].

In addition to the conserved catalytic cysteine, the primary sequence of APR is also distinguished by the presence of a conserved iron-sulfur cluster motif, -CysCys-X$_{\sim80}$-CysXXCys- [53,71]. Biochemical studies demonstrate that the four cysteines in this motif coordinate a [4Fe-4S] cluster, and that this cofactor is essential for catalysis [71,72]. However, the specific role of the cluster in APS reduction has remained elusive. In general, iron-sulfur clusters are protein cofactors that play critical roles in electron transfer, mediating cellular response through transcriptional or translational regulation, disulfide reduction or substrate binding and activation, among others [131-136]. The nature of these metal centers is briefly discussed in relation to their function in other iron-sulfur proteins.

1.5.1 Iron-sulfur Proteins

It has been estimated that nearly one-third of all known proteins require metal ions for their biological structure or function [137]. Metalloproteins associate with metal ions such as Mg^{2+}, Zn^{2+}, Fe^{2+}, Cu^{2+} etc. directly, through cofactors such as porphyrin or cobalamins, or by coordinating to metal-clusters via ligands such as O, N, S or C [138,139]. Iron is the most abundant transition metal in biology, commonly used for diverse redox-related functions as it can form a range of oxidation states. As such, the family of proteins containing iron is ubiquitous in living organisms where these proteins have been shown to incorporate from one to eight iron atoms in a single metal-binding site [140]. The simplest iron centers consist of a single iron atom coordinated to the protein by four cysteine residues as found in rubredoxin. On the other hand, ferredoxins have the more commonly found clusters with two, three or four iron centers bridged by either two or four inorganic sulfides [141,142]. These iron centers are typically coordinated to the protein scaffold by cysteine or histidine residues or less commonly by ligands such as aspartate, arginine and serine [139]. Both the nature of the ligands and solvent exposure has a strong influence on the redox potentials of these iron-centers [143].

Iron-sulfur clusters are versatile cofactors that mediate the biological function of numerous proteins (Figure 1.4). The most common role of iron-sulfur clusters is in electron transfer, based on the propensity of Fe to access multiple oxidation states by donating and accepting electrons in biological reactions [140]. Under physiological conditions, iron-sulfur clusters cover a wide range of reduction potentials, with midpoint reduction potentials varying from −700 mV to +500 mV [144,145]. Examples are found in bacterial and mitochondrial respiratory complexes I-III, photosystem I, ferredoxins and hydrogenases [139]. Amongst the non-electron transfer functions, iron-sulfur clusters can serve as active sites within enzymes. The classic example is

mitochondrial aconitase in which one of the irons within a [4Fe-4S] cluster serves as a Lewis acid catalyzing the abstraction of water from the substrate, citrate, which is converted to isocitrate [144].
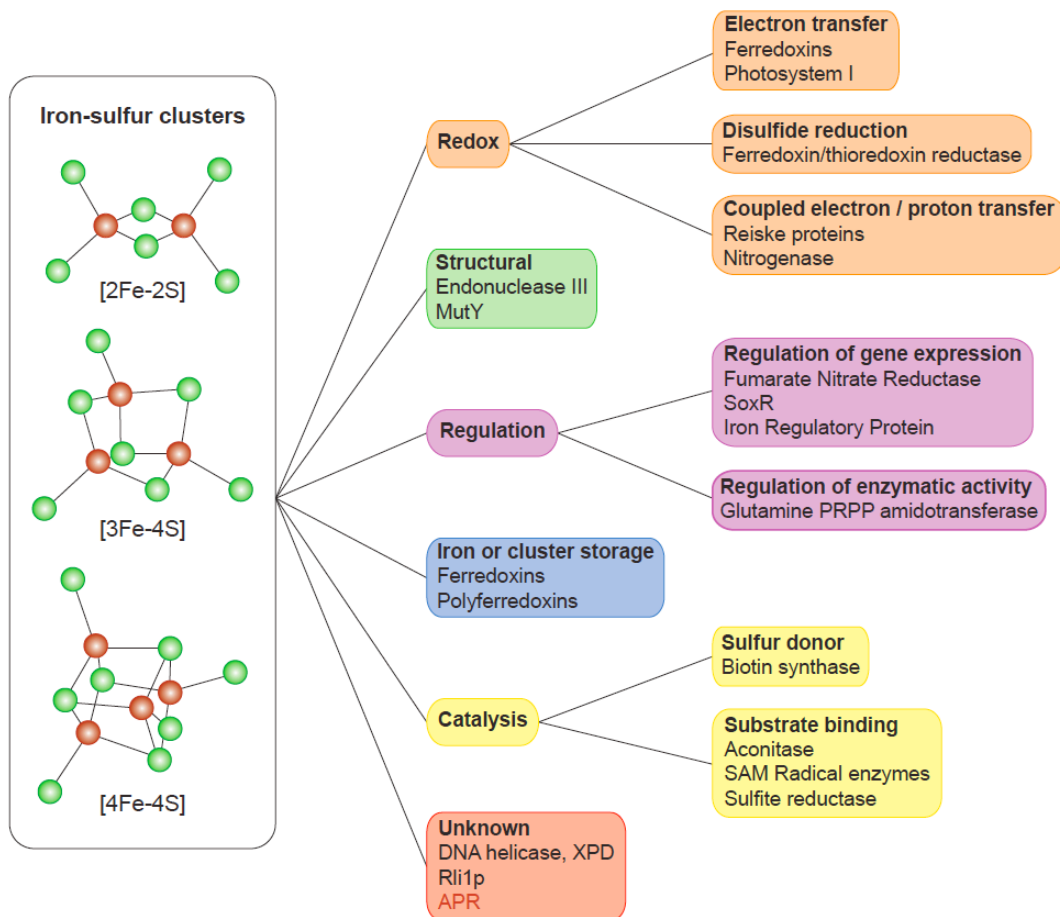
Figure 1.4 Diverse biological functions mediated by iron-sulfur clusters. Abbreviation used are APR, adenosine-5'-phosphosulfate reductase; SAM, S-adenosylmethionine; PRPP, phosphoribosylpyrophosphate. The clusters are represented by ball-and-stick models and are color-coded by atom type, with iron in red and sulfur in green.

Another function of iron-sulfur clusters was discovered in the family of *S*-adenosylmethionine (SAM) enzymes wherein [4Fe-4S] clusters are involved in the initiation of radical chemistry [146,147]. Iron-sulfur clusters have also been exploited in nature to play a role in regulatory and sensing mechanisms. For instance, transcriptional regulators like FNR (fumarate nitrate

reductase) proteins incorporate two $[4Fe-4S]^{2+}$ clusters per dimer which favor the binding of the protein to DNA and expression of proteins required for anaerobic metabolism. Upon exposure to oxygen, the $[4Fe-4S]^{2+}$ clusters are converted to $[2Fe-2S]^{2+}$ clusters and the resulting apoprotein is rendered transcriptionally inactive [148]. Iron-sulfur clusters have been attributed with several other catalytic functions in bacterial and eukaryotic enzymes involved in metabolism [142,145].

Additionally, iron-sulfur clusters have been shown to serve a structural role contributing to the stability of the protein. This role has been accomplished in Endonuclease III, the DNA repair enzyme in *E. coli*, where the iron-sulfur cluster straddles structural elements and stabilizes functionally important features of the enzyme [149,150]. Alternatively, the presence of an iron-sulfur center has been shown to protect an enzyme such as the amidotransferase of *Bacillus subtilis* from degradation by intracellular proteases [151]. Thus iron-sulfur clusters have been employed by myriad of proteins to serve a wide range of functions.

However, there are numerous proteins in which the iron-sulfur cluster is essential for biological activity but its precise role is still to be discovered. Recently the ATP-dependent DNA helicase, XPD (Rad3 in *Saccharomyces cerevisiae*) involved in nucleotide excision repair enzyme was shown to
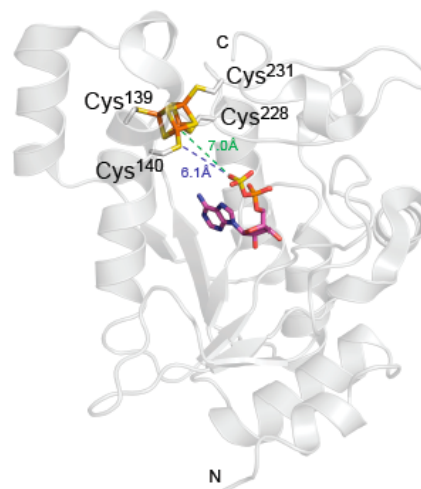
Figure 1.5. Structure of PaAPR bound to substrate APS. The [4Fe-4S] cluster is ligated by four cysteine residues at positions 139, 140, 228 and 231 (PDB code 2GOY). The shortest distances between the terminal sulfate moiety of APS and Fe and Sγ of Cys140 are 6.09 Å (blue dashes) and 7.03 Å (green dashes). C and N indicate the carboxyl- and amino- termini of the protein, respectively.

harbor essential iron sulfur clusters that may function in a way similar to glycosylases like endonuclease III [152,153]. Another example is the mammalian ferrochelatase, which catalyzes the insertion of ferrous iron into protoprophyrin during heme biosynthesis. The enzyme is strongly inhibited by nitric oxide, which destroys its [2Fe-2S] cluster, suggesting a possible regulatory role for the cluster as a NO sensor [154]. Similarly, the exact role of the iron-sulfur clusters in the eukaryotic ATP-binding cassette protein Rli1p involved in ribosome biogenesis and function is unknown, despite the availability of the crystal structure of the holoprotein [155,156]. The focus of our study is the sulfonucleotide reductase, APR, which poses a similar challenge.

The first structure of an assimilatory APR was recently reported, with its [4Fe-4S] cluster intact and APS bound in the active site [128] (Figure 1.5). While the iron-sulfur cluster in APR is required for catalytic activity it does not appear to function as a structural anchor or as an electron transfer conduit [128,157]. Studies reported by Carroll et al. in 2005 provided evidence that the cluster may play a role in substrate binding and activation [71]. In this work, it was shown that substrate binding, with concomitant formation of the thiosulfate-enzyme intermediate, protected the cluster against oxidation. Consistent with the biochemical observations, the x-ray crystal structure of APR revealed that APS binds in close proximity to the iron-sulfur center. Collectively, these observations highlight the unusual nature of this iron-sulfur cluster and set the stage for detailed investigation into the structure and function of this essential cofactor in APR. Specifically, our goal is to determine whether the iron-sulfur cluster in APR comes into direct contact or communicates with the substrate during the catalytic cycle. Results from these investigations would provide insights into the function of this cofactor and facilitate the rational design of inhibitors that target the metal site and inactivate APR. From a

fundamental perspective, these studies would advance our understanding of the catalytic mechanism of APR, which represents a promising target for antitubercular therapy.

1.6 Outlook

The emergence of antibiotic resistance and the problem of mycobacterial persistence in *M. tuberculosis* urgently stress the need for new target identification. Toward this end, mycobacterial sulfur metabolic pathways represent a promising new area for anti-TB therapy. In the last several years' excellent progress has been made, leading to the identification and validation of several potential drug targets in sulfate assimilation and MSH metabolism. At the same time, many aspects of mycobacterial sulfur metabolism remain poorly understood and represent exciting areas of new or continued investigation. One such challenge is presented by APR, which catalyzes the first committed step of sulfate reduction and has been validated as a drug target against latent phase tuberculosis. Elucidation of the function of the iron-sulfur cofactor of APR, a central unsolved question in this unique class of enzymes, is extremely relevant to the catalytic mechanism of the enzyme. Additionally, this investigation would yield important structural information that can be used for the design of cluster-targeted APR inhibitors. In a broader sense, the knowledge gained from this study would have important implications for the structural and electronic features of protein-associated iron-sulfur clusters.

1.7 References

1. Corbett EL, Watt CJ, Walker N, Maher D, Williams BG, Raviglione MC, Dye C: **The growing burden of tuberculosis: global trends and interactions with the HIV epidemic**. *Arch Intern Med* 2003, **163**:1009-1021.
2. Dye C, Scheele S, Dolin P, Pathania V, Raviglione MC: **Consensus statement. Global burden of tuberculosis: estimated incidence, prevalence, and mortality by country. WHO Global Surveillance and Monitoring Project**. *Jama* 1999, **282**:677-686.
3. Kochi A: **The global tuberculosis situation and the new control strategy of the World Health Organization. 1991**. *Bull World Health Organ* 2001, **79**:71-75.
4. Blumberg HM, Burman WJ, Chaisson RE, Daley CL, Etkind SC, Friedman LN, Fujiwara P, Grzemska M, Hopewell PC, Iseman MD, et al.: **American Thoracic Society/Centers for Disease Control and Prevention/Infectious Diseases Society of America: treatment of tuberculosis**. *Am J Respir Crit Care Med* 2003, **167**:603-662.
5. Zhang Y: **The magic bullets and tuberculosis drug targets**. *Annu Rev Pharmacol Toxicol* 2005, **45**:529-564.
6. Flynn JL, Chan J: **Tuberculosis: latency and reactivation**. *Infect Immun* 2001, **69**:4195-4201.
7. Zhang Y: **Persistent and dormant tubercle bacilli and latent tuberculosis**. *Frontiers in Bioscience* 2004, **9**:1111-1156.
8. Mitchison DA: **Basic mechanisms of chemotherapy**. *Chest* 1979, **76**:771-781.
9. Zhang Y: **Mechanisms of Drug Resistence in Mycobacterium tuberculosis**. *Frontiers in Bioscience* 2004, **9**:975-994.
10. Espinal MA: **The global situation of MDR-TB**. *Tuberculosis (Edinb)* 2003, **83**:44-51.
11. Organization WH: **The World Health Organization Global Tuberculosis Program**. 2003.
12. Duncan K: **Progress in TB drug development and what is still needed**. *Tuberculosis (Edinb)* 2003, **83**:201-207.
13. Zhang YP-M, K.; Denkins, S.: **New drug candidates and therapeutic targets for tuberculosis therapy**. *Drug Discovery Today* 2006, **11**:21-27.
14. Cole ST, Brosch R, Parkhill J, Garnier T, Churcher C, Harris D, Gordon SV, Eiglmeier K, Gas S, Barry CE, 3rd, et al.: **Deciphering the biology of Mycobacterium tuberculosis from the complete genome sequence**. *Nature* 1998, **393**:537-544.
15. Cole ST, Eiglmeier K, Parkhill J, James KD, Thomson NR, Wheeler PR, Honore N, Garnier T, Churcher C, Harris D, et al.: **Massive gene decay in the leprosy bacillus**. *Nature* 2001, **409**:1007-1011.
16. Garnier T, Eiglmeier K, Camus JC, Medina N, Mansoor H, Pryor M, Duthoy S, Grondin S, Lacroix C, Monsempe C, et al.: **The complete genome sequence of Mycobacterium bovis**. *Proc Natl Acad Sci U S A* 2003, **100**:7877-7882.
17. Li L, Bannantine JP, Zhang Q, Amonsin A, May BJ, Alt D, Banerji N, Kanjilal S, Kapur V: **The complete genome sequence of Mycobacterium avium subspecies paratuberculosis**. *Proc Natl Acad Sci U S A* 2005, **102**:12344-12349.
18. Glickman MS, Cahill SM, Jacobs WR, Jr.: **The Mycobacterium tuberculosis cmaA2 gene encodes a mycolic acid trans-cyclopropane synthetase**. *J Biol Chem* 2001, **276**:2228-2233.
19. Parish T, Stoker NG: **Use of a flexible cassette method to generate a double unmarked Mycobacterium tuberculosis tlyA plcABC mutant by gene replacement**. *Microbiology* 2000, **146 (Pt 8)**:1969-1975.
20. van Kessel JC, Hatfull GF: **Recombineering in Mycobacterium tuberculosis**. *Nat Methods* 2007, **4**:147-152.

21. Flynn JL, Chan J: **Immunology of tuberculosis**. *Annu Rev Immunol* 2001, **19**:93-129.
22. Houben EN, Nguyen L, Pieters J: **Interaction of pathogenic mycobacteria with the host immune system**. *Curr Opin Microbiol* 2006, **9**:76-85.
23. Vergne I, Chua J, Lee HH, Lucas M, Belisle J, Deretic V: **Mechanism of phagolysosome biogenesis block by viable Mycobacterium tuberculosis**. *Proc Natl Acad Sci U S A* 2005, **102**:4033-4038.
24. Giacomini E, Iona E, Ferroni L, Miettinen M, Fattorini L, Orefici G, Julkunen I, Coccia EM: **Infection of human macrophages and dendritic cells with Mycobacterium tuberculosis induces a differential cytokine gene expression that modulates T cell response**. *J Immunol* 2001, **166**:7033-7041.
25. Henderson RA, Watkins SC, Flynn JL: **Activation of human dendritic cells following infection with Mycobacterium tuberculosis**. *J Immunol* 1997, **159**:635-643.
26. Salgame P: **Host innate and Th1 responses and the bacterial factors that control Mycobacterium tuberculosis infection**. *Curr Opin Immunol* 2005, **17**:374-380.
27. Uehira K, Amakawa R, Ito T, Tajima K, Naitoh S, Ozaki Y, Shimizu T, Yamaguchi K, Uemura Y, Kitajima H, et al.: **Dendritic cells are decreased in blood and accumulated in granuloma in tuberculosis**. *Clin Immunol* 2002, **105**:296-303.
28. Cosma CL, Humbert O, Ramakrishnan L: **Superinfecting mycobacteria home to established tuberculous granulomas**. *Nat Immunol* 2004, **5**:828-835.
29. Russell DG: **Who puts the tubercle in tuberculosis?** *Nat Rev Microbiol* 2007, **5**:39-47.
30. Saunders BM, Cooper AM: **Restraining mycobacteria: role of granulomas in mycobacterial infections**. *Immunol Cell Biol* 2000, **78**:334-341.
31. Ulrichs T, Kaufmann SH: **New insights into the function of granulomas in human tuberculosis**. *J Pathol* 2006, **208**:261-269.
32. Lazarevic V, Nolt D, Flynn JL: **Long-term control of Mycobacterium tuberculosis infection is mediated by dynamic immune responses**. *J Immunol* 2005, **175**:1107-1117.
33. Boshoff HI, Barry CE, 3rd: **Tuberculosis - metabolism and respiration in the absence of growth**. *Nat Rev Microbiol* 2005, **3**:70-80.
34. Tufariello JM, Chan J, Flynn JL: **Latent tuberculosis: mechanisms of host and bacillus that contribute to persistent infection**. *Lancet Infect Dis* 2003, **3**:578-590.
35. Nathan C, Shiloh MU: **Reactive oxygen and nitrogen intermediates in the relationship between mammalian hosts and microbial pathogens**. *Proc Natl Acad Sci U S A* 2000, **97**:8841-8848.
36. Hampshire T, Soneji S, Bacon J, James BW, Hinds J, Laing K, Stabler RA, Marsh PD, Butcher PD: **Stationary phase gene expression of Mycobacterium tuberculosis following a progressive nutrient depletion: a model for persistent organisms?** *Tuberculosis (Edinb)* 2004, **84**:228-238.
37. Manganelli R, Voskuil MI, Schoolnik GK, Dubnau E, Gomez M, Smith I: **Role of the extracytoplasmic-function sigma factor sigma(H) in Mycobacterium tuberculosis global gene expression**. *Mol Microbiol* 2002, **45**:365-374.
38. Ohno H, Zhu G, Mohan VP, Chu D, Kohno S, Jacobs WR, Jr., Chan J: **The effects of reactive nitrogen intermediates on gene expression in Mycobacterium tuberculosis**. *Cell Microbiol* 2003, **5**:637-648.
39. Pinto R, Tang QX, Britton WJ, Leyh TS, Triccas JA: **The Mycobacterium tuberculosis cysD and cysNC genes form a stress-induced operon that encodes a tri-functional sulfate-activating complex**. *Microbiology* 2004, **150**:1681-1686.

40. Rengarajan J, Bloom BR, Rubin EJ: **Genome-wide requirements for Mycobacterium tuberculosis adaptation and survival in macrophages**. *Proc Natl Acad Sci U S A* 2005, **102**:8327-8332.

41. Sassetti CM, Boyd DH, Rubin EJ: **Comprehensive identification of conditionally essential genes in mycobacteria**. *Proc Natl Acad Sci U S A* 2001, **98**:12712-12717.

42. Sassetti CM, Boyd DH, Rubin EJ: **Genes required for mycobacterial growth defined by high density mutagenesis**. *Mol Microbiol* 2003, **48**:77-84.

43. Sassetti CM, Rubin EJ: **Genetic requirements for mycobacterial survival during infection**. *Proc Natl Acad Sci U S A* 2003, **100**:12989-12994.

44. Schnappinger D, Ehrt S, Voskuil MI, Liu Y, Mangan JA, Monahan IM, Dolganov G, Efron B, Butcher PD, Nathan C, et al.: **Transcriptional Adaptation of Mycobacterium tuberculosis within Macrophages: Insights into the Phagosomal Environment**. *J Exp Med* 2003, **198**:693-704.

45. Sherman DR, Voskuil M, Schnappinger D, Liao R, Harrell MI, Schoolnik GK: **Regulation of the Mycobacterium tuberculosis hypoxic response gene encoding alpha -crystallin**. *Proc Natl Acad Sci U S A* 2001, **98**:7534-7539.

46. Kredich NM: In *Escherichia coli and Salmonella: Cellular and Molecular Biology*, edn 2nd. Edited by Niedhardt FC: ASM Press; 1996:514-527. vol 1.]

47. Newton GL, Fahey RC: **Mycothiol biochemistry**. *Arch Microbiol* 2002, **178**:388-394.

48. Takayama K, Wang C, Besra GS: **Pathway to synthesis and processing of mycolic acids in Mycobacterium tuberculosis**. *Clin Microbiol Rev* 2005, **18**:81-101.

49. Leyh TS: **The physical biochemistry and molecular genetics of sulfate activation**. *Crit Rev Biochem Mol Biol* 1993, **28**:515-542.

50. Mougous JD, Green RE, Williams SJ, Brenner SE, Bertozzi CR: **Sulfotransferases and sulfatases in mycobacteria**. *Chem Biol* 2002, **9**:767-776.

51. Nathan C: **Antibiotics at the crossroads**. *Nature* 2004, **431**:899-902.

52. Schelle MW, Bertozzi CR: **Sulfate metabolism in mycobacteria**. *Chembiochem* 2006, **7**:1516-1524.

53. Williams SJ, Senaratne RH, Mougous JD, Riley LW, Bertozzi CR: **5'-adenosinephosphosulfate lies at a metabolic branch point in mycobacteria**. *J Biol Chem* 2002, **277**:32606-32615.

54. Aoki Y, Kondoh M, Nakamura M, Fujii T, Yamazaki T, Shimada H, Arisawa M: **A new methionine antagonist that has antifungal activity: mode of action**. *J Antibiot (Tokyo)* 1994, **47**:909-916.

55. Ejim LJ, Blanchard JE, Koteva KP, Sumerfield R, Elowe NH, Chechetto JD, Brown ED, Junop MS, Wright GD: **Inhibitors of bacterial cystathionine beta-lyase: leads for new antimicrobial agents and probes of enzyme structure and function**. *J Med Chem* 2007, **50**:755-764.

56. Jacques SL, Mirza IA, Ejim L, Koteva K, Hughes DW, Green K, Kinach R, Honek JF, Lai HK, Berghuis AM, et al.: **Enzyme-assisted suicide: molecular basis for the antifungal activity of 5-hydroxy-4-oxonorvaline by potent inhibition of homoserine dehydrogenase**. *Chem Biol* 2003, **10**:989-995.

57. Kugler M, Loeffler W, Rapp C, Kern A, Jung G: **Rhizocticin A, an antifungal phosphono-oligopeptide of Bacillus subtilis ATCC 6633: biological properties**. *Arch Microbiol* 1990, **153**:276-281.

58. Bogdan JA, Nazario-Larrieu J, Sarwar J, Alexander P, Blake MS: **Bordetella pertussis autoregulates pertussis toxin production through the metabolism of cysteine**. *Infect Immun* 2001, **69**:6823-6830.

59. Ejim LJ, D'Costa VM, Elowe NH, Loredo-Osti JC, Malo D, Wright GD: **Cystathionine beta-lyase is important for virulence of Salmonella enterica serovar Typhimurium**. *Infect Immun* 2004, **72**:3310-3314.

60. Lestrate P, Delrue RM, Danese I, Didembourg C, Taminiau B, Mertens P, De Bolle X, Tibor A, Tang CM, Letesson JJ: **Identification and characterization of in vivo attenuated mutants of Brucella melitensis**. *Mol Microbiol* 2000, **38**:543-551.

61. Senaratne RH, De Silva AD, Williams SJ, Mougous JD, Reader JR, Zhang T, Chan S, Sidders B, Lee DH, Chan J, et al.: **5'-Adenosinephosphosulphate reductase (CysH) protects Mycobacterium tuberculosis against free radicals during chronic infection phase in mice**. *Mol Microbiol* 2006, **59**:1744-1753.

62. Yang Z, Pascon RC, Alspaugh A, Cox GM, McCusker JH: **Molecular and genetic analysis of the Cryptococcus neoformans MET3 gene and a met3 mutant**. *Microbiology* 2002, **148**:2617-2625.

63. Sareen D, Newton GL, Fahey RC, Buchmeier NA: **Mycothiol is essential for growth of Mycobacterium tuberculosis Erdman**. *J Bacteriol* 2003, **185**:6736-6740.

64. Huet G, Daffe M, Saves I: **Identification of the Mycobacterium tuberculosis SUF machinery as the exclusive mycobacterial system of [Fe-S] cluster assembly: evidence for its implication in the pathogen's survival**. *J Bacteriol* 2005, **187**:6137-6146.

65. Huet G, Castaing JP, Fournier D, Daffe M, Saves I: **Protein splicing of SufB is crucial for the functionality of the Mycobacterium tuberculosis SUF machinery**. *J Bacteriol* 2006, **188**:3412-3414.

66. Buchmeier N, Fahey RC: **The mshA gene encoding the glycosyltransferase of mycothiol biosynthesis is essential in Mycobacterium tuberculosis Erdman**. *FEMS Microbiol Lett* 2006, **264**:74-79.

67. Wheeler PRB, J. S.: **General Metabolism and Biochemical Pathways of Tubercle Bacilli**. In *Tuberculosis and the Tubercle Bacillus*. Edited by Cole ST: ASM Press; 2005:309-339.

68. Wooff E, Michell SL, Gordon SV, Chambers MA, Bardarov S, Jacobs WR, Jr., Hewinson RG, Wheeler PR: **Functional genomics reveals the sole sulphate transporter of the Mycobacterium tuberculosis complex and its relevance to the acquisition of sulphur in vivo**. *Mol Microbiol* 2002, **43**:653-663.

69. Sun M, Andreassi JL, 2nd, Liu S, Pinto R, Triccas JA, Leyh TS: **The trifunctional sulfate-activating complex (SAC) of Mycobacterium tuberculosis**. *J Biol Chem* 2005, **280**:7861-7866.

70. Mougous JD, Leavell MD, Senaratne RH, Leigh CD, Williams SJ, Riley LW, Leary JA, Bertozzi CR: **Discovery of sulfated metabolites in mycobacteria with a genetic and mass spectrometric approach**. *Proc Natl Acad Sci U S A* 2002, **99**:17037-17042.

71. Carroll KS, Gao H, Chen H, Leary JA, Bertozzi CR: **Investigation of the iron-sulfur cluster in Mycobacterium tuberculosis APS reductase: implications for substrate binding and catalysis**. *Biochemistry* 2005, **44**:14647-14657.

72. Carroll KS, Gao H, Chen H, Stout CD, Leary JA, Bertozzi CR: **A conserved mechanism for sulfonucleotide reduction**. *PLoS Biol* 2005, **3**:e250.

73. Schnell R, Sandalova T, Hellman U, Lindqvist Y, Schneider G: **Siroheme- and [Fe4-S4]-dependent NirA from Mycobacterium tuberculosis is a sulfite reductase with a covalent Cys-Tyr bond in the active site**. *J Biol Chem* 2005, **280**:27319-27328.

74. Markovich D: **Physiological roles and regulation of mammalian sulfate transporters**. *Physioloigcal Reviews* 2001, **81**:1499-1533.

75. McAdam RA, Weisbrod TR, Martin J, Scuderi JD, Brown AM, Cirillo JD, Bloom BR, Jacobs WR, Jr.: **In vivo growth characteristics of leucine and methionine auxotrophic mutants of**

    Mycobacterium bovis BCG generated by transposon mutagenesis. *Infect Immun* 1995, **63**:1004-1012.

76. Liu C, Suo Y, Leyh TS: **The energetic linkage of GTP hydrolysis and the synthesis of activated sulfate**. *Biochemistry* 1994, **33**:7309-7314.

77. Mougous JD, Lee DH, Hubbard SC, Schelle MW, Vocadlo DJ, Berger JM, Bertozzi CR: **Molecular basis for G protein control of the prokaryotic ATP sulfurylase**. *Mol Cell* 2006, **21**:109-122.

78. Sun M, Leyh TS: **Channeling in sulfate activating complexes**. *Biochemistry* 2006, **45**:11304-11311.

79. Triccas JA, Berthet FX, Pelicic V, Gicquel B: **Use of fluorescence induction and sucrose counterselection to identify Mycobacterium tuberculosis genes expressed within host cells**. *Microbiology* 1999, **145 (Pt 10)**:2923-2930.

80. Armstrong JAB, C. R.: **Sulfotransferases as targets for therapeutic interventions**. *Current Opinion in Drug Discovery* 2000, **3**:502-515.

81. Fukuda M, Hiraoka N, Akama TO, Fukuda MN: **Carbohydrate-modifying sulfotransferases: structure, function, and pathophysiology**. *J Biol Chem* 2001, **276**:47747-47750.

82. Schwedock JS, Long SR: **Rhizobium meliloti genes involved in sulfate activation: the two copies of nodPQ and a new locus, saa**. *Genetics* 1992, **132**:899-909.

83. Roche P, Debelle F, Maillet F, Lerouge P, Faucher C, Truchet G, Denarie J, Prome JC: **Molecular basis of symbiotic host specificity in Rhizobium meliloti: nodH and nodPQ genes encode the sulfation of lipo-oligosaccharide signals**. *Cell* 1991, **67**:1131-1143.

84. Goren MB: **Sulfolipid I of Mycobacterium tuberculosis, strain H37Rv. II. Structural studies**. *Biochim Biophys Acta* 1970, **210**:127-138.

85. Goren MB: **Sulfolipid I of Mycobacterium tuberculosis, strain H37Rv. I. Purification and properties**. *Biochim Biophys Acta* 1970, **210**:116-126.

86. Goren MB, Brokl O, Das BC, Lederer E: **Sulfolipid I of Mycobacterium tuberculosis, strain H37RV. Nature of the acyl substituents**. *Biochemistry* 1971, **10**:72-81.

87. Gangadharam PR, Cohn ML, Middlebrook G: **Infectivity, Pathogenicity And Sulpholipid Fraction Of Some Indian And British Strains Of Tubercle Bacilli**. *Tubercle* 1963, **44**:452-455.

88. Goren MB, Brokl O, Schaefer WB: **Lipids of putative relevance to virulence in Mycobacterium tuberculosis: correlation of virulence with elaboration of sulfatides and strongly acidic lipids**. *Infect Immun* 1974, **9**:142-149.

89. Daffe M, Draper P: **The envelope layers of mycobacteria with reference to their pathogenicity**. *Adv Microb Physiol* 1998, **39**:131-203.

90. Bhatt K, Gurcha SS, Bhatt A, Besra GS, Jacobs WR, Jr.: **Two polyketide-synthase-associated acyltransferases are required for sulfolipid biosynthesis in Mycobacterium tuberculosis**. *Microbiology* 2007, **153**:513-520.

91. Converse SE, Mougous JD, Leavell MD, Leary JA, Bertozzi CR, Cox JS: **MmpL8 is required for sulfolipid-1 biosynthesis and Mycobacterium tuberculosis virulence**. *Proc Natl Acad Sci U S A* 2003, **100**:6121-6126.

92. Mougous JD, Petzold CJ, Senaratne RH, Lee DH, Akey DL, Lin FL, Munchel SE, Pratt MR, Riley LW, Leary JA, et al.: **Identification, function and structure of the mycobacterial sulfotransferase that initiates sulfolipid-1 biosynthesis**. *Nat Struct Mol Biol* 2004, **11**:721-729.

93. Khoo KH, Jarboe E, Barker A, Torrelles J, Kuo CW, Chatterjee D: **Altered expression profile of the surface glycopeptidolipids in drug-resistant clinical isolates of Mycobacterium avium complex**. *J Biol Chem* 1999, **274**:9778-9785.

94. Lopez JA, Ludwig EH, McCarthy BJ: **Polymorphism of human glycoprotein Ib alpha results from a variable number of tandem repeats of a 13-amino acid sequence in the mucin-like macroglycopeptide region. Structure/function implications**. *J Biol Chem* 1992, **267**:10055-10061.

95. McCarthy C: **Synthesis and release of sulfolipid by Mycobacterium avium during growth andcell division**. *Infect Immun* 1976, **14**:1241-1252.

96. Desmarais D, Jablonski PE, Fedarko NS, Roberts MF: **2-Sulfotrehalose, a novel osmolyte in haloalkaliphilic archaea**. *J Bacteriol* 1997, **179**:3146-3153.

97. Pi N, Hoang MB, Gao H, Mougous JD, Bertozzi CR, Leary JA: **Kinetic measurements and mechanism determination of Stf0 sulfotransferase using mass spectrometry**. *Anal Biochem* 2005, **341**:94-104.

98. Mougous JD, Senaratne RH, Petzold CJ, Jain M, Lee DH, Schelle MW, Leavell MD, Cox JS, Leary JA, Riley LW, et al.: **A sulfated metabolite produced by stf3 negatively regulates the virulence of Mycobacterium tuberculosis**. *Proc Natl Acad Sci U S A* 2006, **103**:4258-4263.

99. Huang PL, Dawson TM, Bredt DS, Snyder SH, Fishman MC: **Targeted disruption of the neuronal nitric oxide synthase gene**. *Cell* 1993, **75**:1273-1286.

100. Pollock JD, Williams DA, Gifford MA, Li LL, Du X, Fisherman J, Orkin SH, Doerschuk CM, Dinauer MC: **Mouse model of X-linked chronic granulomatous disease, an inherited defect in phagocyte superoxide production**. *Nat Genet* 1995, **9**:202-209.

101. Ushio-Fukai M: **Localizing NADPH oxidase-derived ROS**. *Sci STKE* 2006, **2006**:re8.

102. McCord JM, Fridovich I: **Superoxide dismutase. An enzymic function for erythrocuprein (hemocuprein)**. *J Biol Chem* 1969, **244**:6049-6055.

103. Hampton MB, Kettle AJ, Winterbourn CC: **Inside the neutrophil phagosome: oxidants, myeloperoxidase, and bacterial killing**. *Blood* 1998, **92**:3007-3017.

104. Chan JF, J. L.: **Nitric oxide in *Mycobacterium tuberculosis* infection.** In *Nitric Oxide and Infection*. Edited by Fang FC: Kluwer Academic and Plenum Publishers; 1999:281-310.

105. Padmaja S, Huie RE: **The reaction of nitric oxide with organic peroxyl radicals**. *Biochem Biophys Res Commun* 1993, **195**:539-544.

106. Schlosser-Silverman E, Elgrably-Weiss M, Rosenshine I, Kohen R, Altuvia S: **Characterization of Escherichia coli DNA lesions generated within J774 macrophages**. *J Bacteriol* 2000, **182**:5225-5230.

107. Chan J, Xing Y, Magliozzo RS, Bloom BR: **Killing of virulent Mycobacterium tuberculosis by reactive nitrogen intermediates produced by activated murine macrophages**. *J Exp Med* 1992, **175**:1111-1122.

108. Thoma-Uszynski S, Stenger S, Takeuchi O, Ochoa MT, Engele M, Sieling PA, Barnes PF, Rollinghoff M, Bolcskei PL, Wagner M, et al.: **Induction of direct antimicrobial activity through mammalian toll-like receptors**. *Science* 2001, **291**:1544-1547.

109. Rhee KY, Erdjument-Bromage H, Tempst P, Nathan CF: **S-nitroso proteome of Mycobacterium tuberculosis: Enzymes of intermediary metabolism and antioxidant defense**. *Proc Natl Acad Sci U S A* 2005, **102**:467-472.

110. Cooper AM, Segal BH, Frank AA, Holland SM, Orme IM: **Transient loss of resistance to pulmonary tuberculosis in p47(phox-/-) mice**. *Infect Immun* 2000, **68**:1231-1234.

111. Ng VH, Cox JS, Sousa AO, MacMicking JD, McKinney JD: **Role of KatG catalase-peroxidase in mycobacterial pathogenesis: countering the phagocyte oxidative burst**. *Mol Microbiol* 2004, **52**:1291-1302.

112. Daniel DS, Dai G, Singh CR, Lindsey DR, Smith AK, Dhandayuthapani S, Hunter RL, Jr., Jagannath C: **The reduced bactericidal function of complement C5-deficient murine**

macrophages is associated with defects in the synthesis and delivery of reactive oxygen radicals to mycobacterial phagosomes**. *J Immunol* 2006, **177**:4688-4698.

113. Dosanjh NS, Rawat M, Chung JH, Av-Gay Y: **Thiol specific oxidative stress response in Mycobacteria**. *FEMS Microbiol Lett* 2005, **249**:87-94.

114. Jaeger T, Budde H, Flohe L, Menge U, Singh M, Trujillo M, Radi R: **Multiple thioredoxin-mediated routes to detoxify hydroperoxides in Mycobacterium tuberculosis**. *Arch Biochem Biophys* 2004, **423**:182-191.

115. Jaeger T, Flohe L: **The thiol-based redox networks of pathogens: unexploited targets in the search for new drugs**. *Biofactors* 2006, **27**:109-120.

116. Buchmeier NA, Newton GL, Koledin T, Fahey RC: **Association of mycothiol with protection of Mycobacterium tuberculosis from toxic oxidants and antibiotics**. *Mol Microbiol* 2003, **47**:1723-1732.

117. Haramaki N, Han D, Handelman GJ, Tritschler HJ, Packer L: **Cytosolic and mitochondrial systems for NADH- and NADPH-dependent reduction of alpha-lipoic acid**. *Free Radic Biol Med* 1997, **22**:535-542.

118. Kwon YW, Masutani H, Nakamura H, Ishii Y, Yodoi J: **Redox regulation of cell growth and cell death**. *Biol Chem* 2003, **384**:991-996.

119. Muller S: **Redox and antioxidant systems of the malaria parasite Plasmodium falciparum**. *Mol Microbiol* 2004, **53**:1291-1305.

120. Rawat M, Newton GL, Ko M, Martinez GJ, Fahey RC, Av-Gay Y: **Mycothiol-deficient Mycobacterium smegmatis mutants are hypersensitive to alkylating agents, free radicals, and antibiotics**. *Antimicrob Agents Chemother* 2002, **46**:3348-3355.

121. Lampreia JP, A. S.; Moura, J. J. G.: **Adenylylsulfate reductases from sulfate-reducing bacteria**. *Methods in Enzymology* 1994, **243**:241-260.

122. Gonzalez Porque P, Baldesten A, Reichard P: **The involvement of the thioredoxin system in the reduction of methionine sulfoxide and sulfate**. *J Biol Chem* 1970, **245**:2371-2374.

123. Shi L, Jung YJ, Tyagi S, Gennaro ML, North RJ: **Expression of Th1-mediated immunity in mouse lungs induces a Mycobacterium tuberculosis transcription pattern characteristic of nonreplicating persistence**. *Proc Natl Acad Sci U S A* 2003, **100**:241-246.

124. Wheeler PR, Coldham NG, Keating L, Gordon SV, Wooff EE, Parish T, Hewinson RG: **Functional demonstration of reverse transsulfuration in the Mycobacterium tuberculosis complex reveals that methionine is the preferred sulfur source for pathogenic Mycobacteria**. *J Biol Chem* 2005, **280**:8069-8078.

125. MacMicking J, Xie QW, Nathan C: **Nitric oxide and macrophage function**. *Annu Rev Immunol* 1997, **15**:323-350.

126. MacMicking JD, North RJ, LaCourse R, Mudgett JS, Shah SK, Nathan CF: **Identification of nitric oxide synthase as a protective locus against tuberculosis**. *Proc Natl Acad Sci U S A* 1997, **94**:5243-5248.

127. Senaratne RH, Mougous JD, Reader JR, Williams SJ, Zhang T, Bertozzi CR, Riley LW: **Vaccine efficacy of an attenuated but persistent Mycobacterium tuberculosis cysH mutant**. *J Med Microbiol* 2007, **56**:454-458.

128. Chartron J, Carroll KS, Shiau C, Gao H, Leary JA, Bertozzi CR, Stout CD: **Substrate recognition, protein dynamics, and iron-sulfur cluster in Pseudomonas aeruginosa adenosine 5'-phosphosulfate reductase**. *J Mol Biol* 2006, **364**:152-169.

129. Gao H, Leary J, Carroll KS, Bertozzi CR, Chen H: **Noncovalent complexes of APS reductase from M. tuberculosis: delineating a mechanistic model using ESI-FTICR MS**. *J Am Soc Mass Spectrom* 2007, **18**:167-178.

130. Chartron J, Shiau C, Stout CD, Carroll KS: **3'-Phosphoadenosine-5'-phosphosulfate Reductase in Complex with Thioredoxin: A Structural Snapshot in the Catalytic Cycle(,)**. *Biochemistry* 2007.

131. Fukuyama K: **Structure and function of plant-type ferredoxins**. *Photosynth Res* 2004, **81**:289-301.

132. Kiley PJ, Beinert H: **Oxygen sensing by the global regulator, FNR: the role of the iron-sulfur cluster**. *FEMS Microbiol Rev* 1998, **22**:341-352.

133. Walters EM, Garcia-Serres R, Jameson GN, Glauser DA, Bourquin F, Manieri W, Schurmann P, Johnson MK, Huynh BH: **Spectroscopic characterization of site-specific [Fe(4)S(4)] cluster chemistry in ferredoxin:thioredoxin reductase: implications for the catalytic mechanism**. *J Am Chem Soc* 2005, **127**:9612-9624.

134. Beinert H, Kennedy MC, Stout CD: **Aconitase as Ironminus signSulfur Protein, Enzyme, and Iron-Regulatory Protein**. *Chem Rev* 1996, **96**:2335-2374.

135. Jarrett JT: **The generation of 5'-deoxyadenosyl radicals by adenosylmethionine-dependent radical enzymes**. *Curr Opin Chem Biol* 2003, **7**:174-182.

136. Johnson DC, Dean DR, Smith AD, Johnson MK: **Structure, function, and formation of biological iron-sulfur clusters**. *Annu Rev Biochem* 2005, **74**:247-281.

137. Ibers JA, Holm RH: **Modeling coordination sites in metallobiomolecules**. *Science* 1980, **209**:223-235.

138. Theil EC, Raymond KN: **Transition-Metal Storage, Transport, and Biomineralization**. In *Bioinorganic Chemistry*. Edited by Bertini I, Gray H, Lippard S, Valentine J: University Science Books; 1994:1-37.

139. Lill R: **Function and biogenesis of iron-sulphur proteins**. *Nature* 2009, **460**:831-838.

140. Beinert H, Holm RH, Munck E: **Iron-sulfur clusters: nature's modular, multipurpose structures**. *Science* 1997, **277**:653-659.

141. Holm RH, Kennepohl P, Solomon EI: **Structural and Functional Aspects of Metal Sites in Biology**. *Chem Rev* 1996, **96**:2239-2314.

142. Imlay JA: **Iron-sulphur clusters and the problem with oxygen**. *Mol Microbiol* 2006, **59**:1073-1082.

143. Johnson MK: **Iron-sulfur proteins: new roles for old clusters**. *Curr Opin Chem Biol* 1998, **2**:173-181.

144. Beinert H: **Iron-sulfur proteins: ancient structures, still full of surprises**. *J Biol Inorg Chem* 2000, **5**:2-15.

145. Outten FW, Theil EC: **Iron-based redox switches in biology**. *Antioxid Redox Signal* 2009, **11**:1029-1046.

146. Walsby CJ, Ortillo D, Yang J, Nnyepi MR, Broderick WE, Hoffman BM, Broderick JB: **Spectroscopic approaches to elucidating novel iron-sulfur chemistry in the "radical-Sam" protein superfamily**. *Inorg Chem* 2005, **44**:727-741.

147. Wang SC, Frey PA: **S-adenosylmethionine as an oxidant: the radical SAM superfamily**. *Trends Biochem Sci* 2007, **32**:101-110.

148. Khoroshilova N, Popescu C, Munck E, Beinert H, Kiley PJ: **Iron-sulfur cluster disassembly in the FNR protein of Escherichia coli by O2: [4Fe-4S] to [2Fe-2S] conversion with loss of biological activity**. *Proc Natl Acad Sci U S A* 1997, **94**:6087-6092.

149. Lukianova OA, David SS: **A role for iron-sulfur clusters in DNA repair**. *Curr Opin Chem Biol* 2005, **9**:145-151.

150. Fu W, O'Handley S, Cunningham RP, Johnson MK: **The role of the iron-sulfur cluster in Escherichia coli endonuclease III. A resonance Raman study**. *J Biol Chem* 1992, **267**:16135-16137.

151. Grandoni JA, Switzer RL, Makaroff CA, Zalkin H: **Evidence that the iron-sulfur cluster of Bacillus subtilis glutamine phosphoribosylpyrophosphate amidotransferase determines stability of the enzyme to degradation in vivo**. *J Biol Chem* 1989, **264**:6058-6064.

152. Rudolf J, Makrantoni V, Ingledew WJ, Stark MJ, White MF: **The DNA repair helicases XPD and FancJ have essential iron-sulfur domains**. *Mol Cell* 2006, **23**:801-808.

153. White MF: **Structure, function and evolution of the XPD family of iron-sulfur-containing 5'-->3' DNA helicases**. *Biochem Soc Trans* 2009, **37**:547-551.

154. Sellers VM, Johnson MK, Dailey HA: **Function of the [2FE-2S] cluster in mammalian ferrochelatase: a possible role as a nitric oxide sensor**. *Biochemistry* 1996, **35**:2699-2704.

155. Kispal G, Sipos K, Lange H, Fekete Z, Bedekovics T, Janaky T, Bassler J, Aguilar Netz DJ, Balk J, Rotte C, et al.: **Biogenesis of cytosolic ribosomes requires the essential iron-sulphur protein Rli1p and mitochondria**. *EMBO J* 2005, **24**:589-598.

156. Karcher A, Schele A, Hopfner KP: **X-ray structure of the complete ABC enzyme ABCE1 from Pyrococcus abyssi**. *J Biol Chem* 2008, **283**:7962-7971.

157. Kim SK, Rahman A, Bick JA, Conover RC, Johnson MK, Mason JT, Hirasawa M, Leustek T, Knaff DB: **Properties of the cysteine residues and iron-sulfur cluster of the assimilatory 5'-adenylyl sulfate reductase from Pseudomonas aeruginosa**. *Biochemistry* 2004, **43**:13478-13486.

Chapter 2

Identification of Critical Ligand Binding Determinants in *Mycobacterium*

tuberculosis Adenosine-5'-phosphosulfate Reductase

This work has been partially published as "Identification of Critical Ligand Binding Determinants in *Mycobacterium tuberculosis* Adenosine-5'-phosphosulfate Reductase" **2009** Journal of Medicinal Chemistry *52*; 5485-5495. My contributions to this work include optimization of the protocol for recombinant expression and purification of MtAPR, resulting in improved yield and stability of the protein, synthesis of two key ligands, and calculations for electrostatic surface potential of ligands.

2.1 Abstract

Mycobacterium tuberculosis adenosine 5′-phosphosulfate (APS) reductase is an iron-sulfur protein and a validated target to develop new anti-tubercular agents, particularly for the treatment of latent infection. To facilitate the development of potent and specific inhibitors of APS reductase (APR), we have probed the molecular determinants that underlie binding and specificity through a series of substrate and product analogs. Our study highlights the importance of specific substituent groups for substrate binding and provides functional evidence for ligand-specific conformational states. An active site model has been developed for *M. tuberculosis* APR that is in accord with the results presented here as well as prior structural data

35

reported for *Pseudomonas aeruginosa* APR and related enzymes. This model illustrates the functional features required for the interaction of APR with a ligand and provides a pharmacological road map for the rational design of small-molecules as potential inhibitors of APR present in human pathogens, including *M. tuberculosis*.

2.2 Introduction

Reduced sulfur appears in organic compounds essential to all organisms as constituents of proteins, coenzymes, and cellular metabolites [1-3]. In the amino acid cysteine, the thiol functional group plays important biological roles in redox chemistry, metal binding, protein structure and catalysis [4]. In many human pathogens such as *Mycobacterium tuberculosis* and *Pseudomonas aeruginosa*, activation of inorganic sulfur for the biosynthesis of cysteine proceeds via adenosine 5'-phosphosulfate (APS) [5,6]. This high-energy intermediate is produced by the action of ATP sulfurylase, which condenses sulfate and adenosine 5'-triphosphate (ATP) to form APS [1]. The iron-sulfur protein, APR catalyzes the first committed step in sulfate reduction and is a validated target to develop new anti-tubercular agents, particularly for the treatment of latent
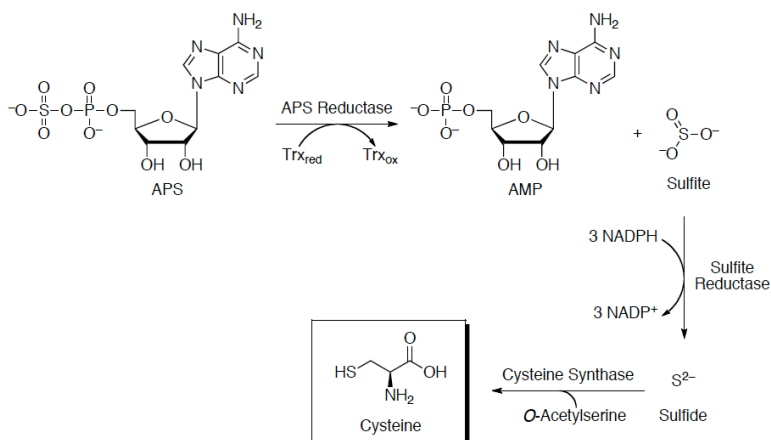
Figure 2.1 Sulfate assimilation pathway in *M. tuberculosis*. The majority of sulfate reducing bacteria use APS as their source of sulfite. In this reaction, APS is reduced to sulfite and adenosine-5'-monophosphate (AMP) by APR. Sulfite, in turn, is reduced by later enzymes in this metabolic pathway, forming first sulfide before incorporation into cysteine and, ultimately, to methionine and other essential reduced sulfur-containing biomolecules.

infection [7-9].

APR catalyzes the reduction of APS to sulfite (HSO_3^-) and adenosine 5'-monophosphate (AMP) using reduction potential supplied by the protein cofactor, thioredoxin as shown in Figure 2.1. Functional and structural studies have been used to investigate the mechanism of APR from sulfate-assimilating bacteria [10-12]. The proposed mechanism in Figure 2.2 involves nucleophilic attack by cysteine 256[1] on the sulfur atom in APS to form an enzyme S-sulfocysteine intermediate, E-Cys-Sγ–SO_3^-, which is then reduced through intermolecular thiol-disulfide exchange with thioredoxin. The iron-sulfur cluster in APR is essential for activity; however, it

Figure 2.2 Mechanism of sulfonucleotide reduction

is not involved in redox chemistry and its exact role remains unknown [6,11].

Crystal structure determination at 2.7 Å of *P. aeruginosa* APR in complex with APS provided the first insight into the molecular basis for substrate recognition (Figure 2.3) [12]. *M. tuberculosis* and *P. aeruginosa* APRs are related by high sequence homology (27.2% of sequence identity and 41.4% of sequence similarity), particularly in the residues that line the active site. The protein monomer folds as a single domain with a central six-stranded β sheet, interleaved with seven α-helices (Figure 2.3). Opposite the nucleotide at one end of the active site is the [4Fe-4S] cluster.

---

[1] Residue numbers throughout manuscript correspond to the APS reductase sequence from *P. aeruginosa* (Appendix 2.5.3).

Three additional elements define the active site: the P-loop (residues 60-66), the LDTG motif (residues 85-88) and the Arg-loop (residues 162-173). APS fits into the active site cavity with the phosphosulfate moiety extending toward the protein surface and ten residues interact directly, via hydrogen bonding or hydrophobic interactions with the substrate. The C-terminal segment of residues 250-267, which carries the catalytically essential Cys256, is disordered in this structure, but would be positioned above the active site cleft.
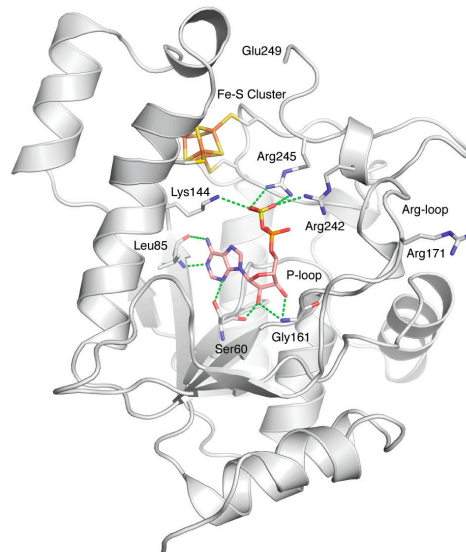
Figure 2.3 The structure of *P. aeruginosa* APS reductase in complex with substrate, APS (PDB 2GOY). The C-terminal segment of residues starting at Glu249 carries the catalytically essential Cys256 and is disordered.

Not all organisms that assimilate sulfate reduce APS as the source of sulfite. Through divergent evolution, some organisms, such as Escherichia coli and *Saccharomyces cerevisiae* reduce the related metabolite 3'-phosphoadenosine-5'-phosphosulfate (PAPS) [10], which is produced by APS kinase from ATP and APS [13]. PAPS reductases lack the iron-sulfur cofactor, but utilize the same two-step mechanism shown in Figure 2.2 [10,11]. *S. cerevisiae* PAPS reductase, crystallized in the presence of the product, 3'-phosphoadenosine 5'-phosphate (PAP) [14] has a fold similar to APR (1.6-Å rms deviation over 117 residues). In the structure of yeast PAPS reductase, the Arg-loop and C-terminal segment are folded over the active site and this conformation reveals additional enzyme-ligand contacts, which may also form between APR and its substrate, APS.

Even though *M. tuberculosis* has plagued humans for millennia, the antibiotic regime is complex and effective drugs that specifically target latent TB infection are yet to be developed [15]. Novel targets [16,17] and treatment strategies [18,19] are emerging, but new avenues for therapeutic intervention must continue to be explored in order to combat multidrug-resistant strains of TB, which pose a significant threat to global human health [20]. To this end, APR represents an attractive target for therapeutic intervention because it is essential for mycobacterial survival in the latent phase of TB infection [9] and humans do not possess an analogs metabolic pathway. Recently, we have discovered small-molecule inhibitors of APR through virtual ligand screening [21]. However, the development of more specific and potent inhibitors will be greatly aided through knowledge of the functional importance of interactions between the substrate and enzyme at the active site, which have not yet been experimentally addressed.
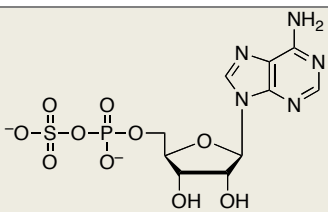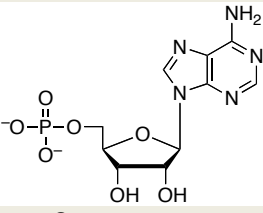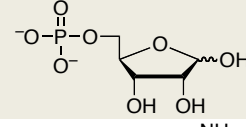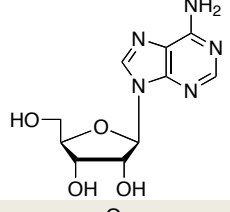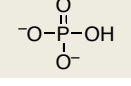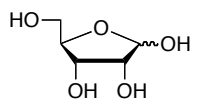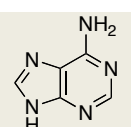
Herein, we probe binding determinants of the *M. tuberculosis* APR active site using synthetic ligand analogs. These studies define chemical groups that are essential for molecular recognition and reveal a network of electrostatic interactions, which play an important role in substrate discrimination. An active site model has been developed for *M. tuberculosis* APR that is in accord with the results presented here as well as prior structural data reported for *P. aeruginosa* APR and related enzymes. This model illustrates the functional features required for the interaction of APR with a ligand and provides a pharmacological road map for the rational design of small-molecules as potential inhibitors of APR present in human pathogens, including *M. tuberculosis*.

2.3 Results and Discussion

The substrate and fragments studied and results obtained in these experiments are summarized

in Tables 2.1-2.3 and Figures 2.4-2.9.

2.3.1 Substrate Affinity. As a starting point to explore the molecular recognition properties of

APR, we determined the K_d value of substrate APS for *M. tuberculosis* APR from the dependence

of the observed rate constant for S-sulfocysteine formation (Appendix 2.5.4), as described in

Experimental procedures. The substrate APS binds to APR with a K_d value of 0.2 µM (Table 2.1),

which is ~3-fold lower than the value of the reported substrate K_m [22].

Table 2.1 Ligand dissociation constants for substrate-fragments with APR.

Ligand	Structure	K_d [μM][c]	ΔΔG [kcal/mol][d]	pKa
APS[a]		0.20	N/A	~2 (O)[e]
AMP		5.4	2.0	6.8 (O) [23]
5'-Phosphoribose		93	5.1	~6.8 (O)[f]
Adenosine		3000	5.8	3.6 (N1), 12.4 (O) [24]
Phosphate		66000	7.7	1.97 (O), 6.82 (O), 12.5 (O) [25]
Ribose		680000	9.1	12.22 (O) [26]
Adenine[b]		≥ 90000	≥ 7.3	4.15 (N1), 9.80 (N9) [26]
Sulfate[b]		≥ 310000	≥ 8.6	-3 (O), 1.89 (O) [27]

[a] The K_d of APS was measured under single turnover conditions, in the absence of thioredoxin, as described in the methods section. [b] Due to the limits of solubility or solution ideality the reported values are lower limits. [c] For substrate-fragments in this table values of K_i were determined under single turnover conditions from the dependence of the observed rate constant at a given inhibitor concentration under conditions of subsaturating APS, such that K_i is equal to the K_d. Each value reflects the average of at least two independent experiments, and the standard deviation was less than 15% of the value of the mean. Kinetic data were nonlinear-least squares fit to a model of competitive inhibition. [d] Energetic difference in affinity of APS relative to inhibitor, $ΔΔG = -RT\ln(K_d^{APS}/K_d^{Fragment})$. [e] pKa estimated from value measured for 2'-deoxy-5'-phosphoribose (Hirota, 1984). [f] pKa estimated from value measured for 3'-phospho-5'-adenosinephosphosulfate (Falany, 1997).

2.3.2 Affinity of Substrate Fragments. To gain further insight into substrate recognition of *M. tuberculosis* APR, we analyzed the energetic contribution of individual portions of APS to the enzyme-binding interaction. The results obtained in these experiments are summarized in Table 2.1. The product AMP differs chemically from the natural substrate, APS, by the absence of the
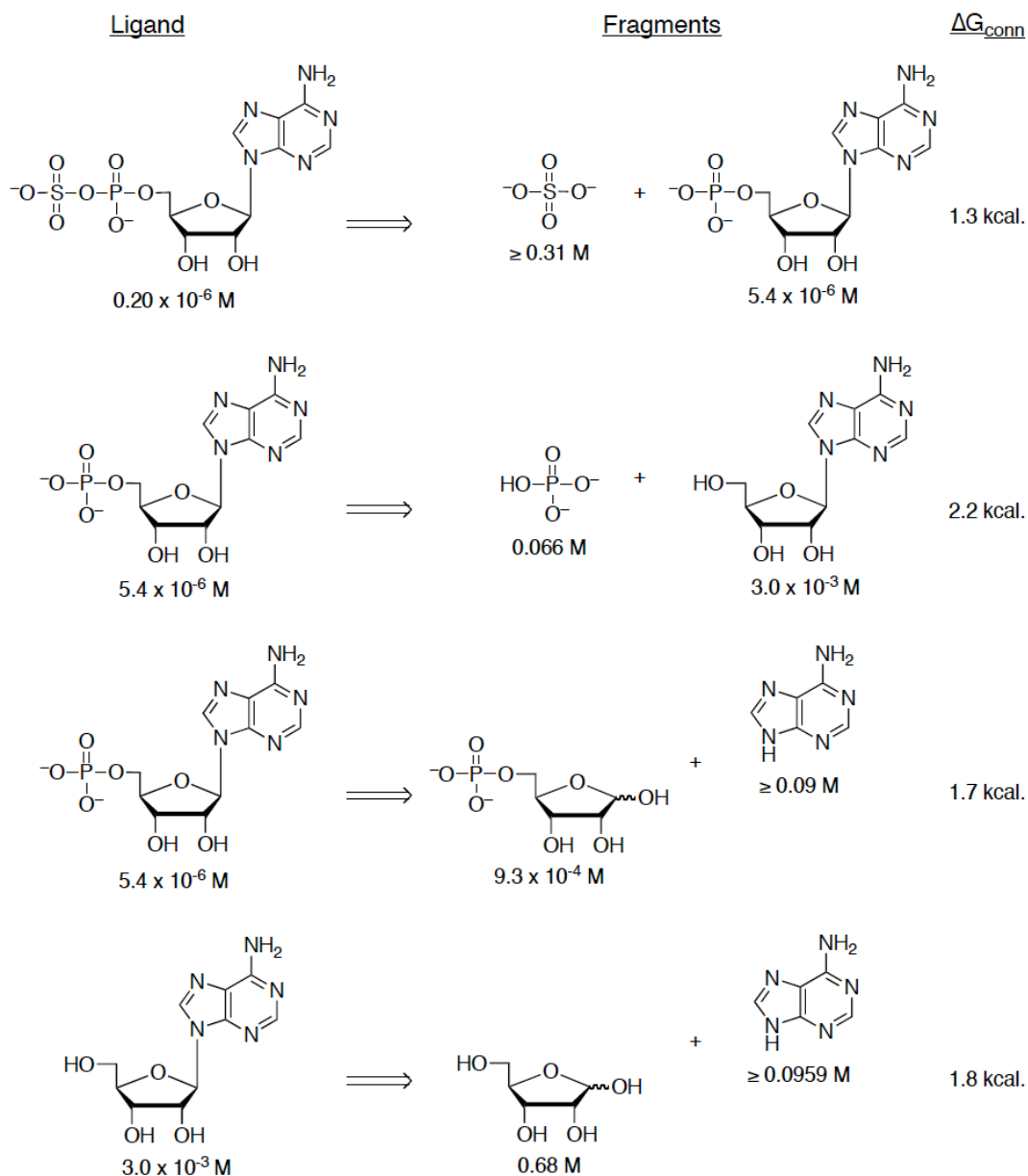
Figure 2.4 Effects of cutting the substrate, APS and the product, AMP into fragments on ligand K_d values. The energetic effect that results from connectivity was calculated based on the affinity of the parent ligand 'XY', compared with the affinities of its pieces, 'X' and 'Y': $\Delta G_{conn} = -RT\ln(K_{XY}/K_X K_Y)$, as previously reported (Dzingeleski, 1993).

sulfate moiety. The loss of sulfate from APS reduced binding to APR about 30-fold (2 kcal/mol), demonstrating that the AMP moiety makes a substantial contribution (7.3 kcal/mol) to the overall binding affinity (9.3 kcal/mol) of APS. Deletion of the adenine or phosphate group from AMP decreased binding to APR by ~170-fold (3.1 kcal/mol) and ~550-fold (3.8 kcal/mol), respectively. Fragments of adenosine – D-ribose and adenine – exhibited weak binding activity toward APR (0.2 and ≤1.5 kcal/mol). The respective free energy of binding to sulfate and phosphate dianions was ≤0.7 and 1.6 kcal/mol. Figure 2.4 summarizes the binding properties of the substrate, APS and product, AMP for *M. tuberculosis* APR as compared with those of the fragments obtained by cutting these ligands at several positions, including the glycosidic bond, and at α- or β-positions within the diester moiety. In all cases, the K_d value of APS or AMP was lower than those of its pieces. However, the free energies (ΔG_{conn}) associated with these connectivity effects for APR are modest (≤2.2 kcal/mol), as compared to values that have been determined for adenosine [28] and cytidine deaminases [29] (~10 kcal/mol).

2.3.3 Affinity of Substrate Analogs

2.3.3.1 β-Nucleotide Substitution. The results above suggest that the β-sulfate group plays a modest role (≤2.0 kcal/mol) in molecular recognition of APS. To probe this observation in further detail, we investigated binding affinities for a panel of nucleotide analogs containing systematic modifications at the β-position (Table 2.2 and Figure 2.5). A phosphate oxyanion has nearly the same size and shape as a sulfate oxyanion, four atoms arranged tetrahedrally around a sulfur instead of a phosphorous [30,31]. However, the overall charge of these analogs differs since the β-sulfate is monoanionic, whereas the β-phosphate is dianionic. Replacement of the β-sulfate moiety with β-phosphate, as in adenosine 5'-diphosphate (ADP), diminished binding to APR about 20-fold (1.8 kcal/mol). To determine whether this decrease in binding affinity is due

to additional negative charge at the β-position of ADP, relative to APS, we examined sulfur (ADPβS), fluorine (ADPβF), or amine (AMPPN) substitution of the β-phosphate nonbridging oxygen atom in ADP (Table 2.2 and Figure 2.5). Sulfur substitution is considered to be a good
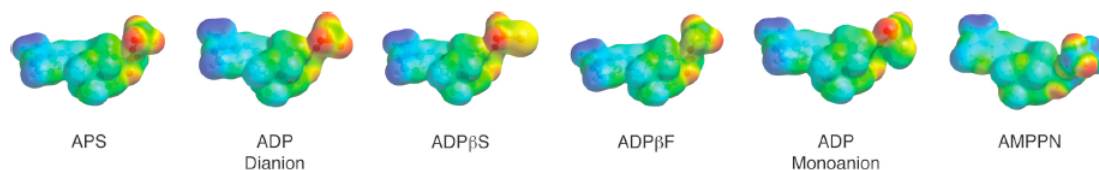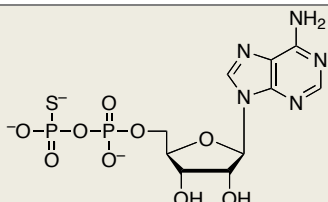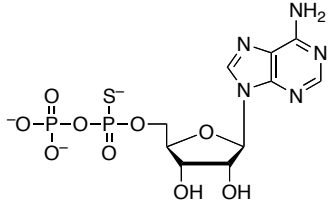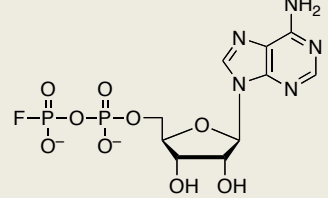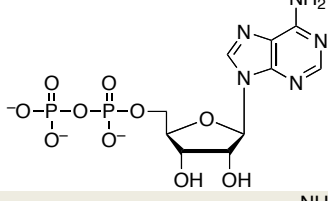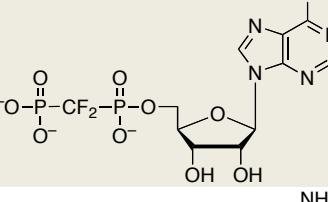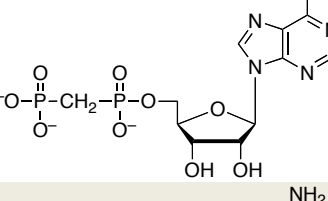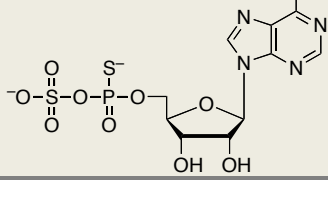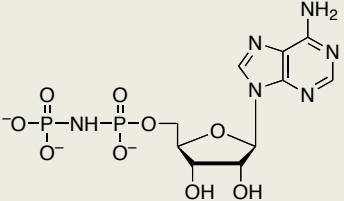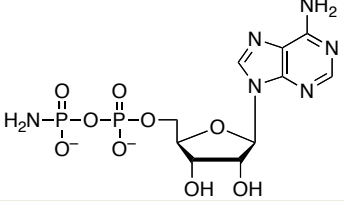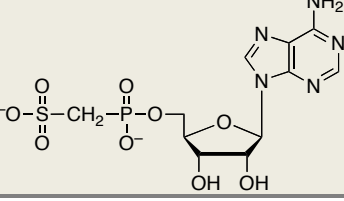
Figure 2.5 Electrostatic potential surfaces of substrate, APS and related nucleotide analogs. Color gradient: red corresponds to most negative and blue corresponds to most positive.

mimic of the phosphate moiety since it is isosteric, pseudoisoelectronic, and has a similar charge distribution and similar net charge at physiological pH [32,33]. Fluorine substitution replaces an ionizable hydroxyl group, thereby mimicking the protonated nucleotide species in net charge at all pH values [34] and, at neutral pH, amine substitution neutralizes the -1 charge at the β-position. Compared to ADP, substitution by sulfur increased binding affinity by 2.0 kcal/mol, fluorine increased binding by less than two-fold (0.3 kcal/mol), and introduction of the amine group decreased the free energy of binding for APR by 2.8 kcal/mol.

Taken together, the above data suggest that a net charge of -2 correlates with potent enzyme-ligand interactions. The negative charge can be localized entirely to the α-position, as in AMP, or it can be distributed across the diester, as in ADPβF. The similarity of Kd values for AMP and ADP could reflect different modes of nucleotide binding. For example, the α-phosphate of AMP could occupy the same position as the β-phosphate in ADP, thereby establishing key electrostatic interactions with Lys144, Arg242, and Arg245 (Figure 2.3). However, an upward shift in the position of AMP would likely weaken important enzyme-binding contacts with the adenine ring and ribose sugar of AMP (Figure 2.3).

Table 2.2 Ligand dissociation constants for substrate analogs with APR.

Ligand	Structure	K_d [μM][a]	ΔΔG [kcal/mol][b]	pKa
ADPβS		0.15	-0.17	5.2 (O)[32]
ADPαS[c]		0.80	0.83	6.8 (O)[35]
ADPβF		2.5	1.5	N/A
ADP		4.3	1.8	6.4 (O)[35]
AMPCF$_2$P		13	2.5	~5.7 (O)[d]
AMPCP		27	2.9	8.1 (O)[36]
APSαS[c]		43	3.2	~1.6 (O)[e]

Ligand	Structure	K_d [μM][a]	ΔΔG [kcal/mol][b]	pKa
AMPNP		260	4.3	7.7 (O), 8.25 (N)[37]
AMPPN		410	4.6	3.0 (O), 8.15 (N)[f]
APSβM		700	4.9	~3.7 (O)[g]
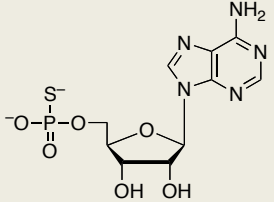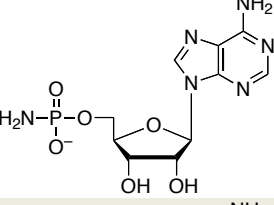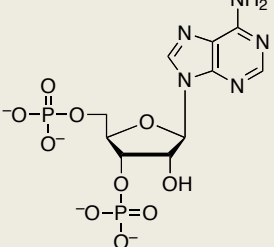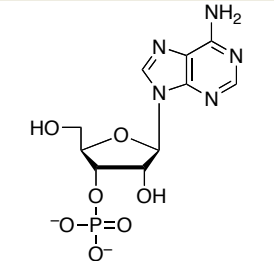
[a] For substrate analogs in this table values of K_i were determined under single turnover conditions from the dependence of the observed rate constant at a given inhibitor concentration under conditions of subsaturating APS, such that K_i is equal to the K_d. Each value reflects the average of at least two independent experiments, and the standard deviation was less than 15% of the value of the mean. Kinetic data were nonlinear-least squares fit to a model of competitive inhibition. [b] Energetic difference in affinity of APS relative to inhibitor, ΔΔG = -RTln(K_d^{APS}/K_d^{Analog}). [c] K_d value for the diastereoisomeric mixture of R_p and S_p isomers. [d] pKa estimated from value for mono- and difluoro-substituted benzylphosphonic acid (Rye, 2005) . [e] pKa estimated from effect of thio-substitution on ADPαS (Cullis 1992). [f] pKa estimated from value measured for phosphoramidic acid (Chanley, 1963). [g] pKa estimated from effect of β-methylene-substitution on AMPCP (Vogel, 1982).

An alternative possibility is that the C-terminus and Arg-loop of APR could adopt different conformations, depending on whether ADP or AMP is bound at the active site. In other words, binding energy gained through additional charge-charge interactions between the β-phosphate moiety of ADP, Lys144, Arg242 and Arg245 could be cancelled by a decrease in favorable interactions with residues in the C-terminus and the Arg-loop. Evidence in support for the latter proposal is provided in Section 2.5 below.

Interestingly, substitution of fluorine by an oxyanion had a marginal effect on binding affinity, whereas thiolate substitution increased binding potency by almost 30-fold. The larger size and polarizability of the sulfur atom could enhance binding affinity by: i) shortening the distance to residues that directly contact the ligand, and/or ii) enabling additional electrostatic or stacking interactions with APR [38]. Finally, we note that neutralizing the -1 charge of the β-phosphate, as in AMPPN, is clearly unfavorable. This significant energetic penalty likely results from repulsive electrostatic interactions between the amine group, which is protonated at physiological pH (Figure 2.5), and adjacent positively charged residues (Figure 2.3). In line with this hypothesis, the binding affinity of AMPPN for APR increased at elevated pH (Appendix 2.5.1).

2.3.3.2 α-β Bridging Oxygen Substitution. Interactions between the 5'-phosphate and two highly conserved residues – Arg171 and His259 – are observed in the structure of *S. cerevisiae* PAPS reductase bound to PAP [14]. However, owing to the mobility of the Arg-loop and C-terminal residues, no direct contacts to the α-phosphate are observed in the structure of APR [12] (Figure 2.3). To gain insight into the functional importance of these contacts for *M. tuberculosis* APR we examined the contribution of the α-β bridging oxygen to binding affinity (Table 2.2). Replacing the Pα-O-Sβ bridging oxygen in APS with a methylene group (Pα-CH$_2$-Sβ) significantly decreased binding affinity by ~3,500-fold (4.9 kcal/mol). Comparison of ADP with AMPNP (Pα-NH–Pβ), AMPCF$_2$P (Pα-CF$_2$-Pβ), and AMPCP (Pα-CH$_2$-Pβ) shows that imino, difluoromethylene, or methylene substitutions reduced binding potency by approximately 60-fold (2.5 kcal/mol), 3-fold (0.7 kcal/mol), and 6-fold (1.1 kcal/mol), respectively.

Table 2.3 Ligand dissociation constants for product AMP analogs with APR.

Ligand	Structure	K_d [μM][a]	ΔΔG [kcal/mol][b]	pKa
5'-AMPS		3.3	-0.30	5.3 (O) [32]
5'-AMPN		100	1.8	~3.0 (N), ~8.15 (O)[c]
3',5'-ADP		770	3.0	2.49 (O), 8.61(O) [39]
3'-AMP		3200	3.8	5.92 (O) [23]

[a] For analogs in this table values of K_i were determined under single turnover conditions from the dependence of the observed rate constant at a given inhibitor concentration under conditions of subsaturating APS, such that K_i is equal to the K_d. Each value reflects the average of at least two independent experiments, and the standard deviation was less than 15% of the value of the mean. Kinetic data were nonlinear-least squares fit to a model of competitive inhibition. [b] Energetic difference in affinity of AMP relative to inhibitor, ΔΔG = -RTln(K_d^{AMP}/K_d^{Analog}). [c] pKa estimate from value measured for phosphoramidic acid (Chanley, 1963).

The above findings demonstrate that the α-β bridging oxygen does contribute to ligand recognition. Nonetheless, these data pose several questions: Why is the methylene substitution more detrimental for APS binding, relative to the energetic penalty paid for analogs modification

of ADP? And, why does AMPNP bind more weakly to APR compared to AMPCF$_2$P? Replacing the bridging oxygen with a methylene group decreases the S/P–X–P bond angle, increases S/P–X bond length, increases the negative charge density on nonbridging oxygens, but makes the phosphate and sulfate groups less acidic [40,41]. It is possible that methylene substitution of ADP is less detrimental to binding because i) the phosphonate moiety has more torsional freedom, allowing the nucleotide to adopt an alternative favorable binding mode, and/or ii) conformational differences in the C-terminal and Arg-loop segments minimize unfavorable contacts to the α-β bridging position of AMPCP. NMR studies show that AMPPNP and PNP exist in solution primarily as the imido tautomers [37]. Thus, the observed decrease in binding affinity could be due to restricted rotation about the Pα-NH–Pβ bonds.

2.3.3.3 α-Nucleotide Substitution. Next, we examined the effect of sulfur substitution at the α-nonbridging oxygen atom using the analogs, APSαS[2] and ADPαS (Table 2.2). Comparison of APS and APSαS shows that sulfur substitution for oxygen decreased binding by more than 200-fold (3.2 kcal/mol). However, compared to ADP, the binding potency of ADPαS increased by approximately 5-fold (1 kcal/mol). The larger energetic penalty for α-sulfur substitution of APS could result from ligand-related differences in enzyme conformation, analogs to the scenario presented in the subsection above.

---

[2] In principle, APSαS could be utilized as a substrate by APS reductase. However, under saturating conditions, no evidence for formation of the S-sulfocysteine intermediate has been obtained (data not shown). At present, it is not understood why APS reductase does not effectively reduce APSαS. One possible explanation is that the α-sulfur substitution disrupts contact with residues that could be important for stabilizing charge development in the transition state, such as Arg171 and His259.

2.3.4 Affinity of Product AMP Analogs

2.3.4.1 α-Nucleotide Substitution. To probe the molecular binding determinants of APR at the α-position in greater detail, we compared the K_d value for the product, AMP to values measured for related analogs (Table 2.3). The respective effects of substitution at the α-oxygen by sulfur (AMPS) or amine (AMPN) are -0.3 and +1.8 kcal/mol, compared to AMP. The modest increase in binding energy that results from sulfur modification is similar to the effect observed with ADPαS. The reduction in binding affinity of AMPN also parallels the decrease observed for AMPPN.

In PAPS reductase, residues in the P-loop interact with the 3'-phosphate of PAP [14,42]. However, in APR the acidic residue, Asp66, interacts with amide groups of the P-loop and thus, appears to mimic the interaction of the negatively charged 3'-phosphate group. To investigate the role of the 3'-hydroxyl group in ligand discrimination (see also Section 2.4.2 below) we determined the binding affinity for 3'-AMP, which reverses the position of the 5'-phosphate and 3'-hydroxyl groups (Table 2.3). Switching the position of the phosphate moiety decreased binding by ~600-fold (3.8 kcal/mol) indicating that, while the analog binds poorly, the 3'-phosphate does not impact binding to APR, as compared to adenosine. By contrast, addition of a 3'-phosphate group to AMP, as in PAP, decreased binding affinity by 3.0 kcal/mol. The energetic penalty for 3'-phosphate in PAP, but not 3'-AMP, likely reflects additional binding interactions to the 5'-phosphate, which could decrease conformational freedom and increase unfavorable protein-ligand contacts.

2.3.4.2 Purine and Ribose Substitution. Next, we analyzed the relative energetic contributions of individual purine and ribose substitutents to the enzyme-binding interaction. Owing to the relative difficulties traditionally associated with the preparation of ADP analogs and the weak binding of adenosine, we determined affinities for a series of compounds derived from the AMP scaffold. As shown in Figure 2.6, energetic penalties for individual substitutions ranged from 0.6 to 4.7 kcal/mol. First, we probed interactions between the N6 amine and N1 of adenine and Leu85 (Figure 2.3), the first residue in the conserved LDTG motif. Loss of the N6 amine from AMP reduced the free energy of binding to APR by 1.8 kcal/mol. Replacing hydrogen atoms with methyl groups at the N6 position of adenine decreased binding affinity by 35-fold (2.1 kcal/mol) per substitution.

Figure 2.6 Free energy of binding for purine and ribose-modified analogs of product, AMP. Numbers represent the energetic effect of a given substitution in kcal/mol, relative to AMP ($\Delta\Delta G = -RT\ln(K_d^{Analog}/K_d^{AMP})$). Positive $\Delta\Delta G$'s indicate a penalty for substitution.

Inverting the hydrogen bond donor and acceptor, as in inosine 5'-monophosphate, was also disfavored (4.7 kcal/mol), presumably due to electrostatic repulsion between the O6-keto and the Leu85 carbonyl, and the N1 by the Leu85 amine. Likewise, introduction of an N1 amine markedly reduced the affinity of this analog for APR (4.7 kcal/mol). In subsequent experiments, we determined the binding potency of AMP analogs with substitutions at the 2, 7 and 8-positions of the purine ring. Methylation at N2 had a detrimental effect on binding (3.4 kcal/mol), likely due to steric clashes with the surrounding adenine-binding pocket (Figure 2.3). The structure of APR bound to APS

shows that C8-H group is directed toward the 5'-phosphosulfate moiety (Figure 2.3). Not surprisingly then, amine substitution at this position decreased the free energy of binding by 3.7 kcal/mol. No contacts are formed between N7 and APR (Figure 2.3). Consistent with this observation, replacing N7 with a carbon atom had a relatively minor effect on binding affinity (0.6 kcal/mol). Finally, we investigated the influence of modification at the 2' and 3'-hydroxyl groups of the ribose sugar. 2'-deoxy and methoxy group substitutions reduced the free energy of binding by a respective 4.0 and 3.6 kcal/mol, whereas 3'-deoxy substitution had only a modest effect on binding affinity (0.9 kcal/mol). This indicates that hydrogen bonds between the 2'-hydroxy group and Ser60 and Gly161 residues (Figure 2.3) play a vital role in substrate recognition.

2.3.5 pH Dependence of Ligand Binding. The pH dependence for ligand binding provides information about the relative affinities of the different nucleotide ionization states, and thus provides information about the active site environment. Initially, we investigated the pH dependence for APS binding. However, the substantial increase in reaction rate at higher pH precludes measurement by conventional kinetic methods (data not shown). As an alternative, we determined the affinities of APR for the substrate analog, ADP, and product, AMP, as a function of pH to investigate whether ionizations at α and β-positions are important for binding affinity (Figure 2.7). The pH dependence for ADP binding is best fit by a pK_a of 6.4 ± 0.2, which could reflect ionizations of the free enzyme and ligand (Figure 2.7a). The most likely candidate for this ionization is the ligand, as the second pK_a values of phosphate esters fall in this region [35]. If this were true, the pH profile would be expected to shift to lower pH for an ADP analog with lower pK_a values. To test this, we determined the pH dependence for ADPβS, which differs in its respective pK_a value by approximately one pH unit [32]. The pH dependence for ADPβS

binding is best fit by a pK_a of 5.8 ± 0.2 (Appendix 2.5.5a). The dependence of the pKa upon the

identity of the ligand suggests that deprotonation of the ligand is responsible for the increase in

binding at higher pH.

The pH dependence for AMP binding is best to best fit by a pK_a of 8.1 ± 0.1 (Figure 2.7b), which could reflect ionizations of the free enzyme and ligand, as described above.   The simplest model to explain the weaker binding of AMP below pH 8 is that the dianion binds more tightly than the monoanion.   However, the apparent pK_a for AMP differs from the expected pK_a of 6.8 by more than one unit. The discrepancy between the experimental data and the simplest model is most likely due to concurrent ionization of the enzyme

Figure 2.7 pH dependence for ADP (a) and AMP (b) binding. The association equilibrium constant, ($K_a = 1/K_d$) is plotted as a function of pH.   Values of K_d were determined by inhibition of APR (pH 6.0-9.5).   Buffers were as follows: MES (pH 6.0-6.5), BisTris (pH 6.5-7.5), TrisHCl (pH 7.5-9.5), CAPS (pH 9-9.5). See Experimental procedures for additional details. (a) The pH dependence for ADP binding. Nonlinear-least-squares fit of the data to a model for a single ionization gave pK_a values of 6.4 ± 0.2. (b) The pH dependence for AMP binding. The dashed line represents the best fit of a model for a single ionization and yields a pK_a of 7.9 ± 0.1.

that affects ligand binding, leading to shift in the apparent pK_a of AMP. One model that could

account for this upward deviation is that an enzymatic group with a pK_a of ~6 contributes slightly

(~5-fold) to AMP binding when protonated. The most likely residue to exert such an effect on

ligand binding is His259, which interacts with the 5'-phosphate of PAP in the structure of *S.*

cerevisiae PAPS reductase [14]. Since a stimulatory effect is not observed for ADP binding, the

C-terminal segment containing His259, and possibly the Arg-loop, may adopt different conformations depending on whether ADP or AMP is bound at the active site. To further confirm that the apparent pK_a measured for AMP depends upon the identity of the ligand, we measured the pH dependence for AMPS binding (Appendix 2.5.5b). The resulting data are best fit by a pK_a of 7.7 ± 0.1. The downward shift in apparent pK_a suggests that deprotonation of the ligand is responsible for the increase in binding at higher pH.

The observed pH dependence for ADP and AMP binding indicates that the dianion binds more tightly to APR than the monoanion. These data seemingly contradict our earlier comparison between ADP and ADPβF, whose net charges differ by one unit, but bind to APR with similar affinity (Table 2.2 and Figure 2.5). Indeed, fluorine modification is often used to determine whether binding of mono- or dianionic phosphate is favored [43]. However, hydroxyl and fluorine groups are distinguished by unique chemical properties. For example, the high electron density of fluorine gives rise to the ability to act as an acceptor in hydrogen bonds [44]. By contrast, the hydroxyl group is a strong dipole, with spatially separated partial positive and negative charges that can donate as well as accept hydrogen bonds (Figure 2.5). Hence, the weaker binding observed for the monoanion may not reflect a loss of charge-charge interactions, but rather an energetic penalty that results from unfavorable charge-dipole interactions with the hydroxyl group.

2.3.6 Effect of Mg^{2+} on Ligand Affinity. In the absence of metal ions, APS binds ~20-times tighter to APR, compared to ADP and AMP. However, the cellular concentrations of these nucleotides are higher than APS [45] and thus, raise an important question: How does APS compete against binding of ADP or AMP to the active site of APR in the cell? For the majority of

biochemical reactions using ATP and, related nucleotides, the active species is the Mg^{2+} complex rather than the free nucleotide [46]. To gain insight into ligand discrimination by

APR *in vivo*, we measured the K_d values for APS, ADP and AMP in the presence of Mg^{2+}. These studies show that the K_d value of APS was independent of Mg^{2+} concentration (data not shown). This observation is consistent with weak formation constants of APS with Mg^{2+} [47] and the general observation that other sulfonucleotide binding enzymes, such sulfokinases and sulfotransferases also do not require Mg^{2+} as a cofactor [11]. However, Mg•ADP and Mg•AMP complexes bind approximately 5-6 times weaker to APR, as compared to the free nucleotide (Appendix 2.5.2). The observed reduction in binding energy is most likely due to repelling interactions with multiple positively charged amino acids in the enzyme active site, such as Lys144, Arg242 and Arg245 (Figure 2.3). Together, these findings indicate that APR discriminates against noncognate adenosine nucleotides through favourable interactions with the sulfate moiety of APS and by disfavouring the binding of Mg^{2+}-nucleotide complexes.

2.3.7 Implications for Rational Inhibitor Design.

Given that APR is essential for mycobacterial survival during persistent infection [9], small-molecule inhibitors of APR might be a source for new drugs to treat latent tuberculosis infection. The increasing number of antibiotic-resistant strains suggests that the availability of such compounds could play an important role in treating the disease and minimizing the negative impact on human health. By defining chemical groups that are essential for molecular recognition, the work described here sets the stage for the development of such drugs. Figure 2.8 summarizes the network of interactions predicted to occur between APR active site residues and substrate, APS. The structural model was constructed by homology to *S. cerevisiae* PAPS

reductase [14] and systematically tested in the present study, from the perspective of the ligand. The total binding energy of APS resulting from these collective interactions is 9.3 kcal/mol and our data indicate several features that are essential for optimized substrate and inhibitor binding. The hydrophobic adenine-binding pocket, pyrimidine ring, 2'-hydroxyl and the α-position are the main determinants for strong target affinity (Figure 2.9). The significant losses of binding affinity that are found to result from apparently minor structural modifications of ligands at these key positions have encouraging implications for inhibitor design and suggests that, in some cases, the potency of a weak inhibitor might be greatly enhanced by one or two simple modifications. Our studies also suggest that small-molecules that target dynamic elements within the
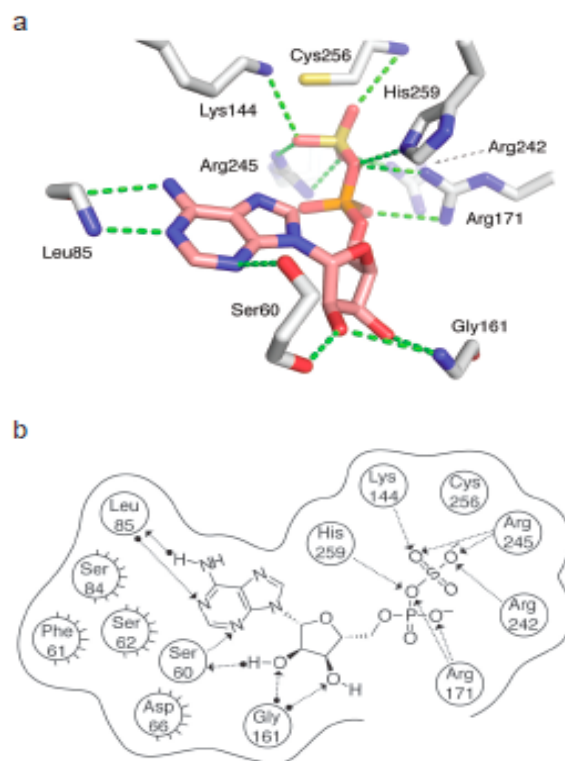
Figure 2.8 APR interactions with substrate, APS inferred from *P. aeruginosa* APR (PDB deposition 2GOY) and *S. cerevisiae* PAPS reductase (PDB deposition 2OQ2) structures and functional data obtained in the present study. (a) Summary of proposed active site contacts to APS. (b) Summary of proposed active site contacts to APS, plotted in two dimensions. A total of nine protein residues are shown in proximity around the ligand, with hydrogen bonding interactions shown where detected. Hydrogen bonds are draw as dotted lines with arrows denoting the direction of the bond. Interactions from substrate or the residue backbones of the enzyme are distinguished from the interactions with residue side chains by a solid dot at the end of the interaction line. Active site residues between *P. aeruginosa* and *M. tuberculosis* APS reductase are largely conserved, with the exception of residues implicated in hydrophobic interactions (Ser65 to Met67, Ser84 to Phe87, Phe61 to Ala44). The corresponding numbers for residues conserved between *M. tuberculosis* and *P. aeruginosa* APS reductase are: Ser65 (Ser60), Leu88 (Leu85), Lys145 (Lys144), Gly162 (Gly161), Arg171 (Arg171), Arg237 (Arg242), Arg240 (Arg245) Cys249 (Cys256), and His252 (His259). See also Appendix 2.5.3.

active site – particularly Arg171, Cys256 and His259 – may lead to inhibitors with improved binding affinity. Alternatively, molecules that trap an inactive, 'open' conformational state of APR may also represent new opportunities for inhibitor design [16].
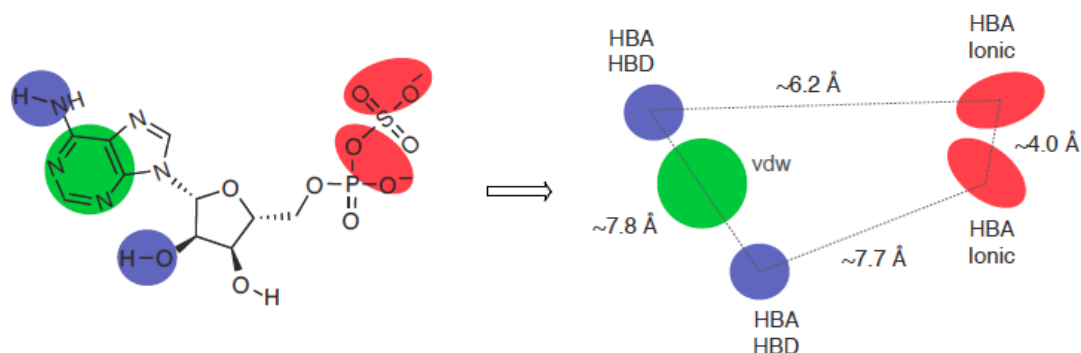
Figure 2.9 Pharmacophore model of substrate, APS. Chemical structure of APS highlighting key hydrogen bond accepting (HBA) and donating (HBD) interactions, ionic interactions, and van der Waals interaction. based on functional data obtained in the present study.

2.4 Experimental Procedures

2.4.1 Materials. Adenosine, 2-aminoadenosine, 3'-deoxyadenosine, 2'-deoxyadenosine, 1-methyladenosine and inosine-5'-O-monophosphate, were purchased from Sigma. 5'-Phosphoribose, 3'-phosphoadenosine, 3'5'-diphosphoadenosine, adenine and ribose were also purchased from Sigma. 7-Deazaadenosine-5'-O-monophosphate and purine riboside-5'-O-monophosphate were from Biology Life Science Institute. Purchased nucleosides and other analogs were of the highest purity available (≥ 95%) and were used without further purification. Additional reagents and solvents were purchased from Sigma or other commercial sources and were used without further purification.

2.4.2 General Synthetic Methods. Reactions that were moisture sensitive or using anhydrous solvents were performed under a nitrogen or argon atmosphere. Analytical thin layer

chromatography (TLC) was performed on pre-coated silica plates obtained from Analtech. Visualization was accomplished with UV light or by staining with ethanolic H2SO4 or ceric ammonium molybdate. Nucleosides were purified by flash chromatography using Merck silica gel (60-200 mesh).

2.4.3 Preparation of Nucleoside and Nucleotide Analogs. N6, N6-Dimethyl-5'-adenosine was prepared from inosine by the procedure described by Veliz and Beal [48] and purified by flash chromatography developed in 60:40 ethyl acetate:hexanes. N6-Methyl-5'-adenosine was prepared via reaction of 6-bromoinosine with methylamine as previously described [49]. 8-Aminoadenosine was prepared by selective bromination of adenosine at the C8 position, exchange of bromine for azide, followed by reductive hydrogenation to afford the amine, as previously described [50]. 2'-Methoxyadenosine was prepared from adenosine, by reaction with methyl iodide under alkaline conditions as previously described [51]. Adenosine 5'-O-a,b,-imidodiphosphate (AMPNP) was synthesized by reaction of 5'-tosyladenosine [52] with imidodiphosphate salt [52,53]. Adenosine 5'-O-a,b-difluoromethylenediphosphate (ADPβF) was prepared by coupling 5'-tosyladenosine to difluoro substituted methylenediphosphonic acid, as previously reported [52,54]. Adenosine 5'-O-thiophosphosulfate (APSaS) was synthesized by reacting pyridine-N-sulfonic acid with adenosine 5'-O-thiopshophate (AMPS), as previously described [55]. Structures and purity ($\geq$ 95%) were confirmed by 1H, 31P NMR and HPLC analysis (data not shown).

2.4.4 Nucleoside Phosphorylation. Nucleotide analogs (2'-deoxy-5'-phosphoadenosine, 2'-methoxy-5'phosphoadenosine, N6, N6-dimethyl-5'-phosphoadenosine, N6-methyl-5'-phosphoadenosine, 8-amino-5'-phosphoadenosine, 1-methyl-5'-phosphoadenosine, and 2-

amino-5'-phosphoadenosine) were synthesized by chemical phosphorylation of the corresponding adenosine analog, followed by purification via reversed phase HPLC. Nucleosides were phosphorylated by reaction of nucleoside with $POCl_3$ as described [56]. The nucleoside (0.15 mmole) was suspended in triethylphosphate at 0 °C (0.65 ml). Water (1 equiv) was added to the reaction. Subsequently, $POCl_3$ (3-5 equivalents, 42 ml-70 ml) was added over a period of 30 min with constant stirring. The suspension was kept stirring for an additional 1.5 h, when the white suspension became a clear solution. Water (1 mL) was added to hydrolyze the phosphoryl chloride and terminate the reaction. The pH was neutralized to ~7 by dropwise addition of 1 M NH4OH. The reaction was passed over a 2 g C18 SPE column (Fisher) that was conditioned in acetonitrile (6 ml) followed by H_2O (6 ml). The nucleotide was eluted from the C18 SPE column with H_2O. Nucleotides were purified by reversed phase HPLC employing isocratic separation in 20 mM ammonium acetate, pH 7 on a semi-preparative (10 x 25 cm) C18 column and the solvent was removed from the solution by repeated lyophilization. The physical and spectral data for these analogs (confirmed by ^{1}H, ^{13}C and ^{31}P NMR and mass spectrometry) were consistent with those previously reported for these compounds [56-58]. The purity (≥ 95%) was confirmed by HPLC analysis using the conditions described above. The retention time of each nucleotide analog (N6, N6-Dimethyl-5'-phosphoadenosine, N6-Methyl-5'-phosphoadenosine, 2'-methoxy-5'phosphoadenosine, 2'-deoxy-5'-phosphoadenosine, 8-amino-5'-phosphoadenosine, 1-methyl-5'-phosphoadenosine, and 2-amino-5'-phosphoadenosine) was 19.7 min, 19.6 min, 8.5 min, 6.1 min, 4.4 min, 4 min, 3.5 min, respectively. The concentrations of nucleotide analogs was determined by absorbance at 260 nm, assuming ε_{260} = 15,400 M^{-1} cm^{-1} [23].

2.4.5 Enzyme purification. Purification of APR was carried out as described in Chapter 3.

2.4.6 General Kinetic Methods. ^{35}S-labeled APS was synthesized and purified as previously described with the inclusion of an additional anion exchange purification step on a 5-ml FFQ column (GE Healthcare) eluting with a linear gradient of ammonium bicarbonate, pH 8.0. The reduction of APS to sulfite and AMP was measured in a 35S-based assay as previously described [59]. Reactions were quenched by the addition of charcoal solution (2% w/v) containing Na_2SO_3 (20 mM). The suspension was vortexed, clarified by centrifugation and an aliquot of the supernatant containing the radiolabeled sulfite product was counted in scintillation fluid. APR activity was measured in single turnover reactions, with trace amounts of ^{35}S-APS (~1 nM) and excess protein. These reactions can typically be followed to ≥90% completion (Appendix 2.5.6a), and the reaction time courses fit well to eq. 1, in which Frac P is the fraction product, k is the observed rate constant, and t is time:

$$Frac\ P = 1 - \exp^{-k_{obs}t}$$ (1)

Unless otherwise specified, the standard reactions conditions were 30 °C with 100 mM bis-tris propane at pH 7.5, DTT (5 mM), and thioredoxin (10 μM). Kinetic data were measured in at least two independent experiments and the standard error was typically less than 15%.

The affinity of APR (E) for APS was determined from the dependence of the observed rate constant for S-sulfocysteine formation on protein concentration according to eq. 2:

$$K_{obs} = K_{max} \times \left(\frac{[E]}{K_{1/2} + [E]}\right)$$ (2)

In this equation, k_{obs} is the observed rate constant at a particular protein concentration, k_{max} is the maximal rate constant with saturating protein, and $K_{1/2}$ is the protein concentration that provides half the maximal rate. To ensure that the chemical step was rate-determining, reactions were performed in NaMes (10 mM) at pH 5.5 and control experiments demonstrate

that the enzyme is stable under these assay conditions (data not shown). Because the chemical step is rate-determining for S-sulfocysteine formation (k_{st} < k_{max} is equal to the rate constant for the reaction of the E•APS complex, and $K_{1/2}$ is equal to the dissociation constant (K_d) of APS for APR. The concentration of active protein was determined by direct titration with a high concentration of APS (i.e. [APS] >> K_d). In theory, the binding affinity of APS could increase at physiological pH. However, several lines of evidence argue against this possibility. First, the pK_a of the β-sulfate moiety is less than 2 and thus, at pH 5.5, the sulfonucleotide is completely ionized. Second, the pH dependence of ADP binding (see below) reflects the pK_a of this nucleotide in solution. Finally, the K_d measured at pH 5.5 is in line with the apparent K_m value measured at pH 8.0 [22].

The affinity of various ligands for APR was determined by inhibition methods. The observed rate constant of the reaction: E + ^{35}S-APS → products (k_{obs}) was determined at varying inhibitor (I) concentrations (Appendix 2.5.6b), and the [I]-dependence was fit to a simple model for competitive inhibition (eq. 3). In eq. 3, k_o is the rate of the reaction in the absence of analog, and K_i is the inhibition constant of the analog. With subsaturating APR, K_i is equal to the equilibrium dissociation constant (K_d) of the ligand.

$$k_{obs} = k_o \times \left(\frac{K_i}{[I] + K_i} \right)$$

(3)

2.4.7 pH Dependence of Inhibitor Binding. Values of K_i were determined by inhibition of APS reduction (pH 6-9.5) with [^{35}S-APS] << $K_{1/2}$, such that K_i is expected to be the K_d. The following buffers were used for the indicated pH ranges: NaMES (6.0-7.0), Bis-Tris (6.5-7.5), Tris (7.5-9.0) and CAPS (9.0-9.5). Reactions were typically carried out with 100 mM buffer and the standard assays and conditions described above were used to monitor k_{cat}/K_m for reduction of 35S-APS in

the presence and absence of inhibitor. The rate constants at each pH value for multiple

reactions were averaged, and the standard deviations were ≤15% of the average. pK_a values

were determined using eq. 4, derived from a model where the binding of the ligand depends on

a single ionizable group.

$$K_{d,app} = K_d^{HA} \times \frac{K_a}{K_a + [H^+]} + K_d^{A-} \times \frac{[H^+]}{K_a + [H^+]}$$

(4)
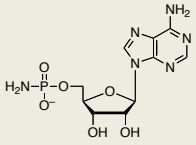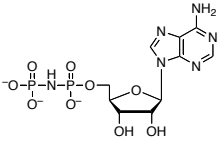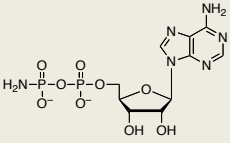
2.4.8 Energetic Contribution of Ligand Substituents to Binding. The energetic contributions of

individual ligand substituents to APR binding were expressed as $\Delta\Delta G = -RT\ln(K_d1/K_d2)$ in which R

is the gas constant, T is the temperature (303 K), and K_d is the equilibrium dissociation constant.

A negative value of $\Delta\Delta G$ indicates that a given substituent contributes to ligand binding by APR.

2.4.9 Electrostatic Surface Potentials. The electrostatic surface potential was calculated using

PM3 semi-empirical molecular orbital calculations implemented in SPARTAN software

(Wavefunction, Inc) for the fully optimized structure.

2.5 Appendix

2.5.1 Table of ligand dissociation constants for nitrogen-containing ligands at pH 7.5 and pH 9.0 with APR.[a]

Ligand	Structure	K_d pH 7.5 [μM]	K_d pH 9.0 [μM]	ΔΔG [kcal/mol][b]	pKa
5'-AMPN		100	82	-0.16	3.0 (O), 8.15 (N)[c]
AMPNP		257	110	-0.53	7.7 (O), 8.25 (N)[37]
AMPPN		410	56.8	-1.2	3.0 (O), 8.15 (N)[c]

[a] For ligands in this table values of K_i were determined at pH 7.5 or 9.0 under single turnover conditions from the dependence of the observed rate constant at a given inhibitor concentration under conditions of subsaturating APS, such that K_i is equal to the K_d. Each value reflects the average of at least two independent experiments, and the standard deviation was less than 15% of the value of the mean. Kinetic data were nonlinear-least squares fit to a model of competitive inhibition. [b] Energetic difference in affinity of ligand at pH 9.0 relative to pH 7.5, ΔΔG = -RTln($K_d^{9.0}$/$K_d^{7.5}$). [c] pKa estimate approximated from value for phosphoramidic acid (Chanley, 1963).

2.5.2 Table of ligand dissociation constants for AMP and ADP with APR in the presence and absence of MgCl$_2$.[a]

Ligand	MgCl$_2$ [mM]	K_d [μM]	ΔΔG [kcal/mol][b]
AMP	0	5.4	N/A
	0.5	21	0.82
	2.0	31	1.0
ADP	0	4.3	N/A
	0.5	7.3	0.32
	2.0	20	0.93

[a] For ligands in this table values of K_i were determined at pH 7.5 and the concentration of MgCl$_2$ indicated under single turnover conditions from the dependence of the observed rate constant at a given inhibitor concentration under conditions of subsaturating APS, such that K_i is equal to the K_d. Each value reflects the average of at least two independent experiments, and the standard deviation was less than 15% of the value of the mean. Kinetic data were nonlinear-least squares fit to a model of competitive inhibition. [b] Energetic difference in affinity for ligand with magnesium relative to without metal ion, ΔΔG = $-RT\ln(K_d^{+MgCl2}/K_d^{-MgCl2})$.

Appendix 2.5.3. Structure based sequence alignment of APRs from *Pseudomonas aeruginosa, Mycobacterium tuberculosis* and *Saccharomyces cerevisiae*.
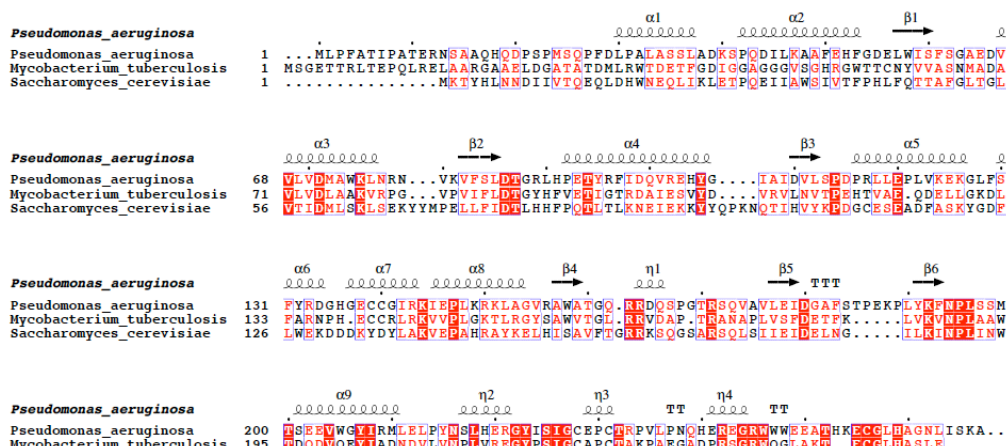
Appendix 2.5.3 Structure based sequence alignment of APS reductases from *Pseudomonas aeruginosa, Mycobacterium tuberculosis* and *Saccharomyces cerevisiae*. The ClustalW Multiple Sequence Alignment program was used. Strictly conserved residues are outlined in red, red letters indicate conserved residues and conserved regions are boxed in blue. Alignment picture was rendered with the server ESPript 2.2 (http://espript.ibcp.fr).

Appendix 2.5.4 The apparent affinity, $K_{1/2}$, of APR in single turnover experiment.
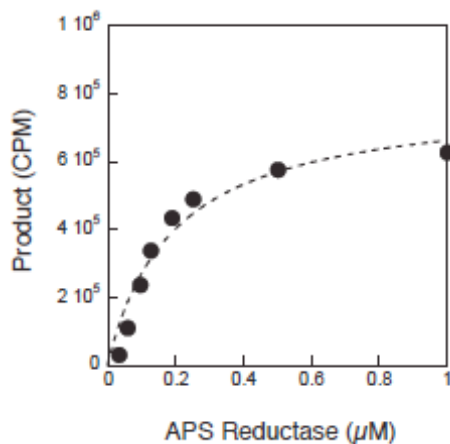
Appendix 2.5.4 The apparent affinity, $K_{1/2}$, of APR in single turnover experiment. The affinity of APS reductase (E) for APS was determined from the dependence of the observed rate constant for *S*-sulfocysteine formation on protein concentration according to: $K_{obs} = K_{max} \times \left(\dfrac{[E]}{K_{1/2} + [E]} \right)$. In this equation, k_{obs} is the observed rate constant at a particular protein concentration, k_{max} is the maximal rate constant with saturating protein, and $K_{1/2}$ is the protein concentration that provides half the maximal rate. Because the chemical step is rate-determining for *S*-sulfocysteine formation, k_{max} is equal to the rate constant for the reaction of the E•APS complex, and $K_{1/2}$ is equal to the dissociation constant (K_d) of APS for APS reductase. The concentration of active protein was determined by direct titration with a high concentration of APS (*i.e.* [APS] >> K_d).

Appendix 2.5.5 pH dependence for ADPβS and AMPS binding.
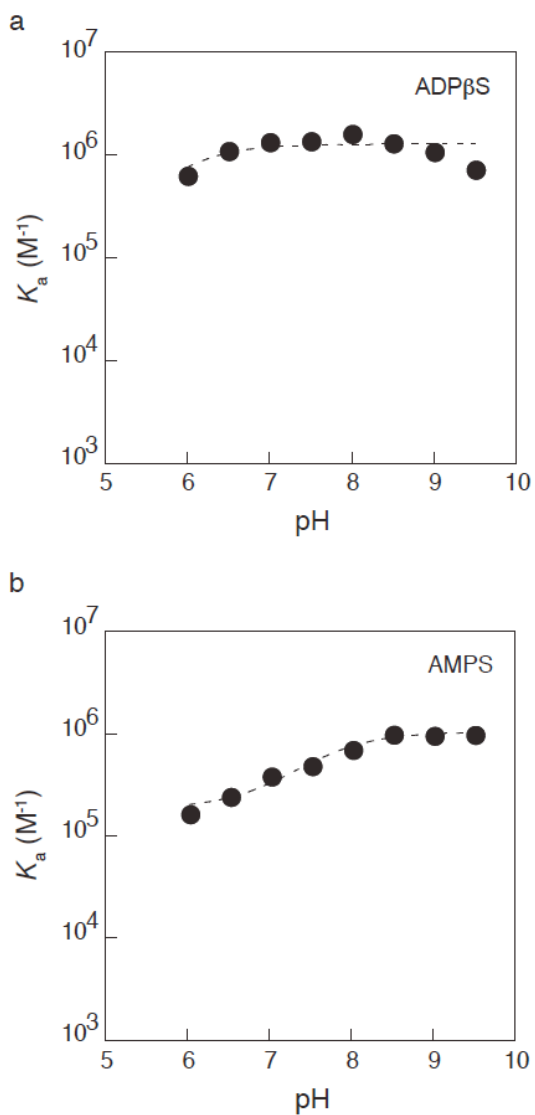
Appendix 2.5.5 pH dependence for ADPβS (a) and AMPS (b) binding. The association equilibrium constant, (K_a = 1/K_d) is plotted as a function of pH. Values of K_d were determined by inhibition of APS reduction (pH 6.0-9.5). See methods for details. (a) The pH dependence for ADPβS binding. Nonlinear-least-squares fit of the data to a model for a single ionization gave pK_a values of 5.8 ± 0.15. The pK_a of ADPβS in solution is 5.2 (Jaffe, 1978). (b) The pH dependence for AMPS binding. The dashed line represents the best fit of a model for a single ionization and yields a pK_a of 7.7 ± 0.15. The pKa of AMPS in solution is 5.3 (Jaffe, 1978).

Appendix 2.5.6 The radioactive assay for APR.

a
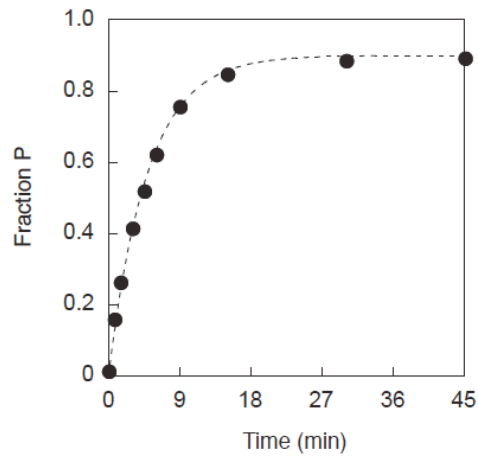
b
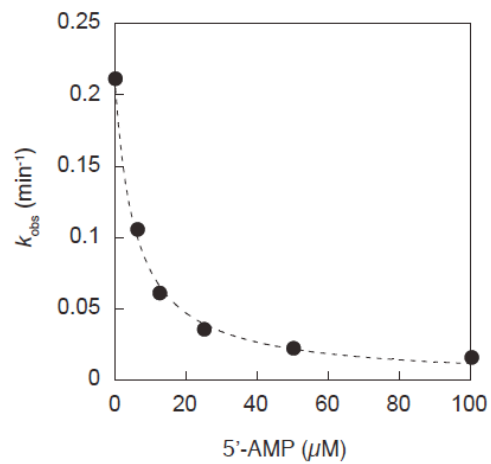
Appendix 2.5.6 The radioactive assay for APR. (a) The reaction progress curve for APR. Under the subsaturating concentration of substrate, the reaction is described by the apparent second-order rate constant, k_{cat}/K_m, which under the conditions of this assay is ~2 × 10^6 M^{-1}s^{-1}. (b) AMP inhibits APR activity. Nonlinear least squares fit to a model of competitive inhibition gives a K_d value of 5.4 μM.

2.6 References

1. Schelle MW, Bertozzi CR: **Sulfate metabolism in mycobacteria**. *Chembiochem* 2006, **7**:1516-1524.
2. Mitchell S: **Biology of sulfur**. In *Biological Interactions of Sulfur Compounds*. Edited by Mitchell S: CRC Press; 1996:20-41. vol 1.]
3. Kredich NM: **Biosynthesis of cysteine**. In *In Escherichia coli and Salmonella: Cellular and Molecular Biology*, edn 2. Edited by Niedhardt FC, Curtiss R: ASM press; 1996:514-527. vol 1.]
4. Giles NM, Watts AB, Giles GI, Fry FH, Littlechild JA, Jacob C: **Metal and redox modulation of cysteine protein function**. *Chemistry & biology* 2003, **10**:677-693.
5. Williams SJ, Senaratne RH, Mougous JD, Riley LW, Bertozzi CR: **5'-Adenosinephosphosulfate lies at a metabolic branch point in mycobacteria**. *J. Biol. Chem.* 2002, **277**:32606-32615.
6. Kopriva S, Buchert T, Fritz G, Suter M, Benda R, Schunemann V, Koprivova A, Schurmann P, Trautwein AX, Kroneck PM, et al.: **The presence of an iron-sulfur cluster in adenosine 5'-phosphosulfate reductase separates organisms utilizing adenosine 5'-phosphosulfate and phosphoadenosine 5'-phosphosulfate for sulfate assimilation**. *J. Biol. Chem.* 2002, **277**:21786-21791.
7. Bhave DP, Muse WB, 3rd, Carroll KS: **Drug targets in mycobacterial sulfur metabolism**. *Infect Disord Drug Targets* 2007, **7**:140-158.
8. Mdluli K, Spigelman M: **Novel targets for tuberculosis drug discovery**. *Current Opinion in Pharmacology* 2006, **6**:459-467.
9. Senaratne RH, De Silva AD, Williams SJ, Mougous JD, Reader JR, Zhang T, Chan S, Sidders B, Lee DH, Chan J, et al.: **5'-Adenosinephosphosulphate reductase (CysH) protects *Mycobacterium tuberculosis* against free radicals during chronic infection phase in mice**. *Mol. Microbiol.* 2006, **59**:1744-1753.
10. Carroll KS, Gao H, Chen H, Stout CD, Leary JA, Bertozzi CR: **A conserved mechanism for sulfonucleotide reduction**. *PLoS Biol.* 2005, **3**:e250.
11. Carroll KS, Gao H, Chen H, Leary JA, Bertozzi CR: **Investigation of the iron-sulfur cluster in Mycobacterium tuberculosis APS reductase: implications for substrate binding and catalysis**. *Biochemistry* 2005, **44**:14647-14657.
12. Chartron J, Carroll KS, Shiau C, Gao H, Leary JA, Bertozzi CR, Stout CD: **Substrate recognition, protein dynamics, and iron-sulfur cluster in Pseudomonas aeruginosa adenosine 5'-phosphosulfate reductase**. *J Mol Biol* 2006, **364**:152-169.
13. Chapman E, Best MD, Hanson SR, Wong CH: **Sulfotransferases: structure, mechanism, biological activity, inhibition, and synthetic utility**. *Angew Chem Int Ed Engl* 2004, **43**:3526-3548.
14. Yu Z, Lemongello D, Segel IH, Fisher AJ: **Crystal structure of Saccharomyces cerevisiae 3'-phosphoadenosine-5'-phosphosulfate reductase complexed with adenosine 3',5'-bisphosphate**. *Biochemistry* 2008, **47**:12777-12786.
15. Young DB, Gideon HP, Wilkinson RJ: **Eliminating latent tuberculosis**. *Trends Microbiol* 2009, **17**:183-188.
16. Lee GM, Craik CS: **Trapping moving targets with small molecules**. *Science* 2009, **324**:213-215.
17. Liu Y, Gray NS: **Rational design of inhibitors that bind to inactive kinase conformations**. *Nat Chem Biol* 2006, **2**:358-364.

18. Hugonnet JE, Tremblay LW, Boshoff HI, Barry CE, 3rd, Blanchard JS: **Meropenem-clavulanate is effective against extensively drug-resistant *Mycobacterium tuberculosis***. *Science* 2009, **323**:1215-1218.

19. Palomino JC, Ramos DF, da Silva PA: **New anti-tuberculosis drugs: strategies, sources and new molecules**. *Curr Med Chem* 2009, **16**:1898-1904.

20. Nguyen L, Pieters J: **Mycobacterial Subversion of Chemotherapeutic Reagents and Host Defense Tactics: Challenges in Tuberculosis Drug Development**. *Annual Review of Pharmacology and Toxicology* 2009, **49**:427-453.

21. Cosconati S, Hong JA, Novellino E, Carroll KS, Goodsell DS, Olson AJ: **Structure-based virtual screening and biological evaluation of *Mycobacterium tuberculosis* adenosine 5'-phosphosulfate reductase inhibitors**. *J Med Chem* 2008, **51**:6627-6630.

22. Sun M, Leyh TS: **Channeling in sulfate activating complexes**. *Biochemistry* 2006, **45**:11304-11311.

23. Dawson RMC, Elliott DC, Elliott WH, Jones KM: *Data for Biochemical Research* edn 3. Oxford: Oxford University Press; 1989.

24. Chargaff E, Davidson JN: *The Nucleic Acids I*. New York: Academic Press 1955.

25. Kumler WD, Eiler JJ: **The acid strength of mono and diesters of phosphoric acid. The n-alkyl esters from methyl to butyl, the esters of biological importance, and the natural guanidine phosphoric acids**. *Journal of the American Chemical Society* 1943, **65**:2355-2361.

26. Isbell HS: *Carbohydrate in Solution*. Wachington, DC: American Chemical Society; 1973.

27. Chang R: **Acids and bases**. In *General Chemistry*, edn 8. Edited by: McGraw-Hill.Inc; 2005.

28. Dzingeleski GD, Wolfenden R: **Hypersensitivity of an enzyme reaction to solvent water**. *Biochemistry* 1993, **32**:9143-9147.

29. Carlow D, Wolfenden R: **Substrate connectivity effects in the transition state for cytidine deaminase**. *Biochemistry* 1998, **37**:11873-11878.

30. Nikolic-Hughes I, Rees DC, Herschlag D: **Do electrostatic interactions with positively charged active site groups tighten the transition state for enzymatic phosphoryl transfer?** *Journal of the American Chemical Society* 2004, **126**:11814-11819.

31. *CRC Handbook of Chemistry and Physics*: edn 75. Edited by Lide DR. Boca Raton, FL: CRC Press; 1994-1995.

32. Jaffe EK, Cohn M: **[31]P nuclear magnetic resonance spectra of the thiophosphate analogues of adenine nucleotides; effects of pH and Mg^{2+} binding**. *Biochemistry* 1978, **17**:652-657.

33. Frey PA, Sammons RD: **Bond order and charge localization in nucleoside phosphorothioates**. *Science* 1985, **228**:541-545.

34. Satishchandran C, Myers CB, Markham GD: **Adenosine-5'-O-(2-fluorodiphosphate) (ADP-b-F), an analog of adenosine-5'-phosphosulfate**. *Bioorganic Chemistry* 1992, **20**:107-114.

35. Cullis PM, Maxwell A, Weiner DP: **Energy coupling in DNA gyrase: a thermodynamic limit to the extent of DNA supercoiling**. *Biochemistry* 1992, **31**:9642-9646.

36. Vogel HJ, Bridger WA: **Phosphorus-31 nuclear magnetic resonance studies of the methylene and fluoro analogues of adenine nucleotides. Effects of pH and magnesium ion binding**. *Biochemistry* 1982, **21**:394-401.

37. Reynolds MA, Gerlt JA, Demou PC, Oppenheimer NJ, Kenyon GL: **N-15 and O-17 NMR-studies of the proton binding-sites in imidodiphosphate, tetraethyl imidodiphosphate, and adenylyl imidodiphosphate**. *Journal of the American Chemical Society* 1983, **105**:6475-6481.

38. Gregoret LM, Rader SD, Fletterick RJ, Cohen FE: **Hydrogen bonds involving sulfur atoms in proteins**. *Proteins* 1991, **9**:99-107.

39. Singer B: **Nucleosides, nucleotides, and nucleic acids**. In *Practical Handbook of Biochemistry and Molecular Biology*, edn 2. Edited by Fasman GD: CRC Press; 1989:392-393. vol 1.]

40. Yount RG, Babcock D, Ballantyne W, Ojala D: **Adenylyl imidodiphosphate, an adenosine triphosphate analog containing a P--N--P linkage**. *Biochemistry* 1971, **10**:2484-2489.

41. Larsen M, Willett R, Yount RG: **Imidodiphosphate and pyrophosphate: possible biological significance of similar structures**. *Science* 1969, **166**:1510-1511.

42. Savage H, Montoya G, Svensson C, Schwenn JD, Sinning I: **Crystal structure of phosphoadenylyl sulphate (PAPS) reductase: a new family of adenine nucleotide alpha hydrolases**. *Structure* 1997, **5**:895-906.

43. Rye CS, Baell JB: **Phosphate isosteres in medicinal chemistry**. *Curr Med Chem* 2005, **12**:3127-3141.

44. O'Hagan D: **Understanding organofluorine chemistry. An introduction to the C-F bond**. *Chemical Society reviews* 2008, **37**:308-319.

45. Harris DA: **Cell chemistry and physiology: part II**. In *Principles of Medical Biology*. Edited by Bittar EE, Bittar N: Elsevier; 1996:27. vol 4.]

46. Storer AC, Cornish-Bowden A: **Concentration of MgATP^{2-} and other ions in solution. Calculation of the true concentrations of species present in mixtures of associating ions**. *Biochem J* 1976, **159**:1-5.

47. Yount RG, Simchuck S, Yu I, Kottke M: **Adenosine-5'-sulfatopyrophosphate, an analogue of adenosine triphosphate. I. Preparation, properties, and mode of cleavage by snake venoms**. *Archives of Biochemistry and Biophysics* 1966, **113**:288-295.

48. Veliz EA, Beal PA: **C6 substitution of inosine using hexamethylphosphorous triamide in conjunction with carbon tetrahalide or *N*-halosuccinimide**. *Tet. Lett.* 2000, **41**:1695-1697.

49. Veliz EA, Beal PA: **6-bromopurine nucleosides as reagents for nucleoside analogue synthesis**. *J. Org. Chem.* 2001, **66**:8592-8598.

50. Townsend LB, Tipson RS: *Nucleic Acid Chemistry:Improved and New Synthetic Procedures, Methods, and Techniques*, vol II. Edited by Townsend LB, Tipson RS. New York: Wiley; 1978.

51. Yano J, Kan LS, Ts'o POP: **A simple method for the preparation of adenosine with methyl iodide in anhydrous alkaline medium**. *Biochim. Biophys. Acta.* 1980, **629**:178-183.

52. Davisson VJ, Davis DR, Dixit VM, Poulter CD: **Synthesis of nucleotide 5'-diphosphates from 5'-O-tosyl nucleosides**. *Journal of Organic Chemistry* 1987, **52**:1794-1801.

53. Ma Q, Babbitt PC, Kenyon GL: **Adenosine 5'-[a,b-imido]triphosphate, a substrate for T7 RNA-polymerase and rabbit muscle creatine-kinase**. *Journal of the American Chemical Society* 1988, **110**:4060-4061.

54. Mohamady S, Jakeman DL: **An improved method for the synthesis of nucleoside triphosphate analogues**. *J. Org. Chem.* 2005, **70**:10588-10591.

55. Zhang HP, Leyh TS: **alpha-Thio-APS: A stereomechanistic probe of activated sulfate synthesis**. *Journal of the American Chemical Society* 1999, **121**:8692-8697.

56. Yoshikawa M, Kato T, Takenishi T: **A novel method for phosphorylation of nucleosides to 5'-nucleotides**. *Tet. Lett.* 1967, **50**:5065-5068.

57. Burgess K, Cook D: **Syntheses of nucleoside triphosphates**. *Chemical Reviews* 2000, **100**:2047-2059.

58. Freist W, Cramer F: **Synthesis of AMP and ATP analogues.** In *In Nucleic Acid Chemistry, Part 2*. Edited by Townsend LW, Tipson RS: John Wiley & Sons; 1978:827-841.

59. Gao H, Leary J, Carroll KS, Bertozzi CR, Chen HY: **Noncovalent complexes of APS reductase from M-tuberculosis: Delineating a mechanistic model using ESI-FTICR MS**. *Journal of the American Society for Mass Spectrometry* 2007, **18**:167-178.

60. Hirota K, Inoue Y, Chujo R: **Effect of the base stacking association on the phosphate ionization of 2'-deoxyguanosine 5'-monophosphate**. *Bulletin of the Chemical Society of Japan* 1984, **57**:247-250.

61. Falany CN: **Enzymology of human cytosolic sulfotransferases**. *Faseb J* 1997, **11**:206-216.

62. Chanley JD, Feageson E: **A study of hydrolysis of phosphoramides .2. Solvolysis of phosphoramidic acid and comparison with phosphate esters**. *Journal of the American Chemical Society* 1963, **85**:1181-1190.

Chapter 3

Spectroscopic Studies on the [4Fe-4S] Cluster in Adenosine-5'-

phosphosulfate Reductase from *Mycobacterium tuberculosis*

This work has been published in part as "Spectroscopic Studies on the [4Fe-4S] Cluster in Adenosine-5'-phosphosulfate Reductase from *Mycobacterium tuberculosis* " **2011** Journal of Biological Chemistry *286*; 1216-1226. I performed all biochemical, kinetic and EPR experiments, and prepared samples for Mössbauer analyses.

3.1 Abstract

Mycobacterium tuberculosis adenosine 5′-phosphosulfate (APS) reductase (MtAPR) is an iron-sulfur protein and a validated target to develop new antitubercular agents, particularly for the treatment of latent infection. The enzyme harbors a $[4Fe\text{-}4S]^{2+}$ cluster that is coordinated by four cysteinyl ligands, two of which are adjacent in the amino acid sequence. The iron-sulfur cluster is essential for catalysis; however, the precise role of the [4Fe-4S] cluster in APR remains unknown. Progress in this area has been hampered by the failure to generate a paramagnetic state of the [4Fe-4S] cluster that can be studied by electron paramagnetic resonance spectroscopy. Herein, we overcome this limitation and report the EPR spectra of MtAPR in the $[4Fe\text{-}4S]^{+}$ state. The EPR signal is rhombic and consists of two overlapping $S = ½$ species. Substrate binding to MtAPR led to a marked increase in intensity and resolution of the EPR

signal, and to minor shifts in principle *g* values that were not observed among a panel of substrate analogs, including adenosine 5′-diphosphate. Using site-directed mutagenesis, in conjunction with kinetic and EPR studies, we have also identified an essential role for the active site residue, Lys144 whose side chain interacts with both the iron-sulfur cluster and the sulfate group of APS. The implications of these findings are discussed with respect to the role of the iron-sulfur cluster in the catalytic mechanism of APR.

3.2 Introduction

In bacteria and plants, activation of inorganic sulfur is required for *de novo* biosynthesis of cysteine. To this end, the metabolic assimilation of sulfate from the environment proceeds via adenosine 5′-phosphosulfate (APS) or 3′-phosphoadenosine-5′-phosphosulfate (PAPS) [1]. These intermediates are produced by the action of ATP sulfurylase (EC 2.7.7.4), which condenses sulfate and ATP to form APS [2,3], and by APS kinase (EC 2.7.1.25), which produces PAPS from ATP and APS [4].

APS and PAPS are reduced by enzymes in the reductive branch of the sulfate assimilation pathway, producing sulfite and adenosine 5′-monophosphate (AMP) or adenosine 3′,5′-diphosphate (PAP) (see Scheme 3.1). These enzymes
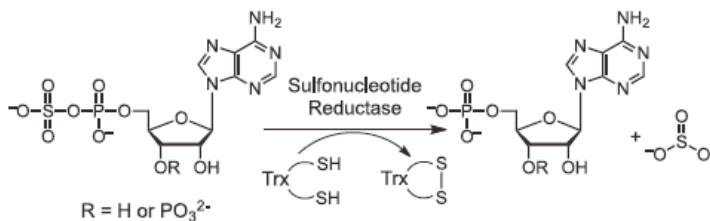
Scheme 3.1 Reaction catalyzed by sulfonucleotide reductases.
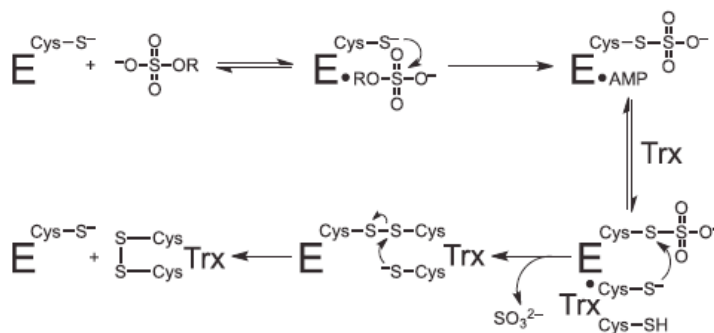
Figure 3.1 Proposed mechanism of sulfonucleotide reduction.

can be subdivided into two groups according to their substrate preference, the APS reductases (APR) and the PAPS reductases (PAPR) (EC 1.8.99.4). Functional and structural studies have been used to investigate the chemical reaction mechanism of APR and PAPR enzymes [1,5-8]. The mechanism involves nucleophilic attack by the active site cysteine on the sulfur atom of APS or PAPS to form an enzyme S-sulfocysteine intermediate (E-Cys-Sγ-SO$_3^-$), which is cleaved by thiol-disulfide exchange with thioredoxin or glutaredoxin (Figure 3.1). The sulfite product is then reduced to sulfide by sulfite reductase (EC 1.8.7.1) and utilized to synthesize cysteine and other essential sulfur-containing biomolecules [9]. In the human pathogen *Mycobacterium tuberculosis*, APR is a validated target against the latent phase of infection [10].

Only a 3′-phosphate group distinguishes PAPS from APS. Accordingly, APR and PAPR have nearly identical three-dimensional structures (1.6–Å rms deviation of backbone atoms) and share ~20% sequence identity, including the active site motif, ECG and the sulfonucleotide binding pocket [5,11,12]. However, a key difference between the two enzymes is that APR contains two conserved cysteine motifs, CXXC and CC. These four additional cysteine residues coordinate a [4Fe-4S] cluster, which is essential for catalytic activity [1,5,13]. The only known exception is *Physcomitrella patens* sulfonucleotide reductase, PpAPR-B that lacks the cysteine pairs required to bind the cofactor, but can utilize both APS and PAPS as substrates [14]. However, PpAPR-B has to pay a significant penalty for the absence of the [4Fe-4S] cluster as evidenced by second-order rate constants (k_{cat}/K_m) of 3,520 and 37 M^{-1}s^{-1} with APS and PAPS, respectively.

The 2.7 Å crystal structure of *Pseudomonas aeruginosa* APR (PaAPR) bound to substrate provides valuable insights into the arrangement of active site residues that are conserved among APRs[3] [5]. The iron-sulfur cluster is coordinated by Cys228 and Cys231, positioned at the tip of a β-loop, along with the tandem pair, Cys139 and Cys140, within an α-helix (Figure 3.2a). Coordination by sequential cysteines is highly unusual for [4Fe-4S] clusters and has been characterized in only one other crystal structure – the NuoB subunit of respiratory complex I [15]. There are four charged and/or polar NH⋯S or OH⋯S hydrogen bonds involving side-chains of absolutely conserved residues (Figure 3.2b and c). In particular, the CysCys motif
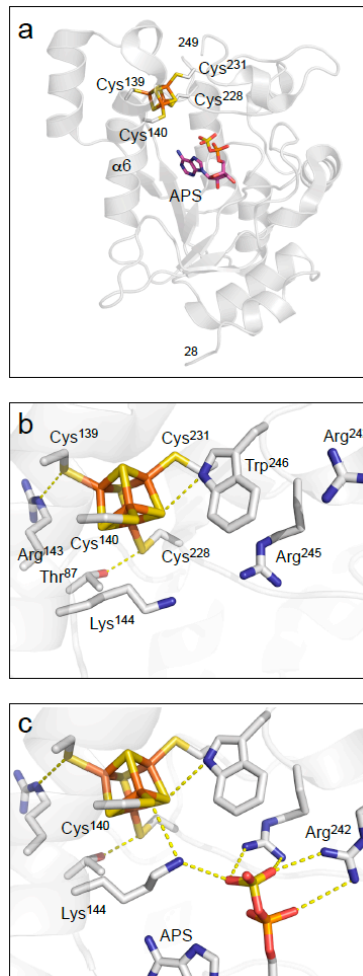
Figure 3.2 The environment of the [4Fe-4S] cluster in PaAPR. a. The structure of PaAPR bound to substrate APS. The [4Fe-4S] cluster is ligated by four cysteine residues at positions 139, 140, 228 and 231. PDB code: 2GOY. b. Four conserved residues participate in charged or polar NH…S or OH…S hydrogen bonds to inorganic S or cysteine Sγ atoms; Thr87, Arg143, Lys144 and Trp246 (yellow dashes). PDB code: 2GOY, chain A. c. Conserved basic residues Lys144, Arg242 and Arg245 in the active site interact with the phosphate and sulfate groups of APS (yellow dashes). Residues that also interact with APS, but are not depicted in this figure are Arg171 and His259; these residues interact with the α-phosphate group. The shortest distance between a sulfate oxygen atom and a cysteine sulfur atom coordinated to the [4Fe-4S] cluster is 6.0 Å. PDB code: 2GOY, chain B.

---

[3] Residue numbers in the text correspond to the PaAPR amino acid sequence. The corresponding residue numbers in MtAPR can be identified from the sequence alignment depicted in Appendix 3.6.1.

interacts with a pair of basic residues, Arg143 and Lys144. Other interactions with the iron-sulfur cluster involve Thr87 and Trp246. In the active site the phosphosulfate group of APS is positioned opposite the [4Fe-4S] cluster and, while no atoms intervene, the sulfate moiety is not in direct contact with the [4Fe-4S] cluster.

Given the unusual CysCys dyad coordination and its requirement for catalytic activity, defining the function and properties of the iron-sulfur cluster in APR has generated considerable interest [1,5,7,16,17]. Most proteins containing [4Fe-4S] clusters are redox-active [18-21], however, the [4Fe-4S]$^{2+}$ cluster in APR does not undergo redox changes during the catalytic cycle [1]. A purely structural role also appears unlikely, in light of biophysical data obtained on the apo form of APR [6,13,16] and the fact that APR and PAPR share a common protein fold [5,11,12]. Unfortunately, progress in this area has been hampered by the failure to generate a paramagnetic state of the [4Fe-4S] cluster that can be studied by electron paramagnetic resonance (EPR) spectroscopy and related methods [16,17,22].

Herein, we report the EPR spectra of MtAPR in the [4Fe-4S]$^{+}$ state. The EPR spectrum of MtAPR displays a rhombic signal, but is complex and consists of at least two overlapping $S = ½$ species. Mössbauer studies of the native and reduced forms confirm the presence of a [4Fe-4S]$^{2+/1+}$ cluster. APS binding to MtAPR is accompanied by marked sharpening of the EPR signal and an increase in intensity, which is not observed among a panel of substrate analogs, including adenosine 5′-diphosphate (ADP). In addition, kinetic and EPR investigation of the Lys144Ala variant of MtAPR demonstrate a key function for this residue in catalysis and as a link between APS and the iron-sulfur cluster. These data, together with known functional and structural information, directly implicate the iron-sulfur cluster in the catalytic mechanism of APS.

3.3 Results

3.3.1 Purification and Spectroscopic Characterization of the [4Fe-4S]$^{2+}$ Cluster in MtAPR. We have previously reported conditions for the purification of MtAPR [1]. However, yields from these preparations were low owing to the large quantity of MtAPR present in the insoluble protein fraction. In order to improve the yield and stability of purified MtAPR, we co-expressed the MtAPR gene with the gene products of the *isc* operon required for iron-sulfur cluster biosynthesis in *A. vinelandii* [23]. Under these conditions the yield of MtAPR was typically 7 mg/L of culture, which represents an improvement over ~1 mg/L obtained when MtAPR is over-expressed in the absence of the *isc* proteins. The specific activity of the purified enzyme was 5 μM min^{-1} mg protein^{-1} with thioredoxin and DTT as reductants. The UV-Vis absorbance spectrum of MtAPR showed a maximum in the visible range at 410 nm that is consistent with the presence of bound Fe (Appendix 3.6.2). Analysis of Fe content by inductively coupled plasma resonance spectrometry for MtAPR indicated that each mole of protein contained 3.5 ± 0.4 mol of Fe, which is indicative of 4 Fe atoms in the cluster. The intensity of the 410 nm peak was unaffected on addition of sodium dithionite (data not shown), but increased slightly on addition of APS (Appendix 3.6.2). These results are analogous to those found for PaAPR [6]. The minor increase in absorption at 410 nm could reflect substrate-dependent conformational changes within the C-terminal region and a concomitant alteration in cluster environment.

The 4.2-K/53-mT Mössbauer spectrum of MtAPR confirmed the presence of a [4Fe-4S]$^{2+}$ cluster (Figure 3.3). The majority of the Fe (~90%) gives rise to a quadrupole doublet with parameters typical of [4Fe-4S]$^{2+}$ clusters: isomer shift (δ) of 0.45 mm/s and quadrupole splitting parameter (ΔE_Q) of 1.09 mm/s. The appearance of a small peak at ~0.6 mm/s is indicative of a small amount of [2Fe-2S]$^{2+}$ clusters (δ = 0.25 mm/s, ΔE_Q = 0.55 mm/s, ~7% of total intensity). The

[2Fe-2S]$^{2+}$ cluster form of MtAPR has also been observed by ESI-FT-ICR MS [13] and is most likely caused by aerobic degradation, analogous to other [4Fe-4S]$^{2+}$ proteins. On addition of APS, the Mössbauer spectrum of MtAPR was nearly identical to that in the absence of substrate (Appendix 3.6.3) and can be simulated as a superposition of two quadrupole doublets representing the [4Fe-4S]$^{2+}$ clusters (δ = 0.45 mm/s, ΔE_Q = 1.12 mm/s, 90%) and [2Fe-2S]$^{2+}$ clusters (δ = 0.25 mm/s, ΔE_Q = 0.55 mm/s, 10%).
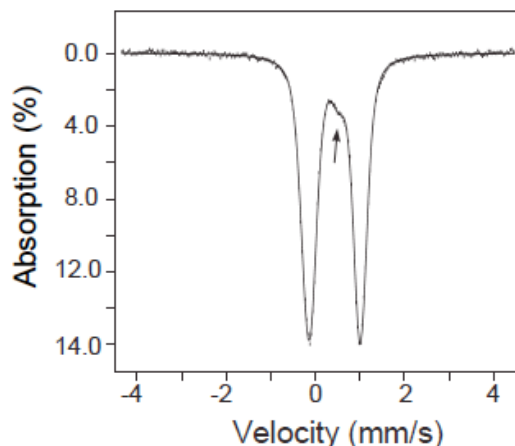
Figure 3.3 4.2-K/53-mT Mössbauer spectra of 1 mM MtAPR. Experimental spectra are shown as vertical bars. The solid line is a quadrupole doublet simulation with the parameters quoted in the text. The weak peak at ~0.6 mm/s is indicative of a small amount of [2Fe-2S]$^{2+}$ clusters (arrow).

3.3.2 Photoreduction of the [4Fe-4S]$^{2+}$ cluster in MtAPR. As-isolated APR from higher plants and *P. aeruginosa* exhibits weak isotropic signals at *g* = 2.01 attributed to a small proportion of [3Fe-4S]$^+$ cluster and at *g* = 4.3 from high-spin Fe(III) [16,17,22]. When MtAPR was prepared according to the previous method [13], similar resonances were observed (data not shown). However, such EPR signals were not present in samples of MtAPR produced via the improved co-expression system. Earlier attempts to generate new EPR signals in assimilatory APR from higher plants and bacteria by titrating the enzyme with dithionite, Ti(III)citrate or photochemical reduction with the deazaflavin/oxalate system have proven unsuccessful [16,17,22]. Similarly, our earlier studies of MtAPR found no evidence for the presence of [4Fe-4S]$^+$ after treatment with dithionite [13].

78

In the present study, we first explored reduction of the cluster in MtAPR using Ti(III)citrate. New EPR signals were observed, however, interpretation of the spectra was confounded by nonspecifically bound Ti(III)citrate that gave rise to an isotropic signal at g = 1.94 (data not shown). Next, we tested photoreduction of the $[4Fe-4S]^{2+}$ center in MtAPR in the presence of deazaflavin/oxalate. The resulting EPR spectrum is broad, but shows rhombic symmetry with apparent g-values of 2.04, 1.94 and 1.75 (Figure 3.4a). The EPR signal also gives evidence for a second component with apparent g-values at 2.13 and 1.85; however, the broad resonances precluded an accurate simulation of the two paramagnetic species. Spin quantitation of the EPR signals from g = 2.5 to 1.3 indicate 0.3 equiv of spins per mole of enzyme. On the basis of observed g-values, the resonances can be attributed to either an S = ½ $[2Fe-2Fe]^+$ or $[4Fe-4S]^+$ cluster. The temperature dependence of the EPR signal (data not shown) indicated that it was maximal between 8-10 K and was no longer visible at temperatures above 12 K, using a
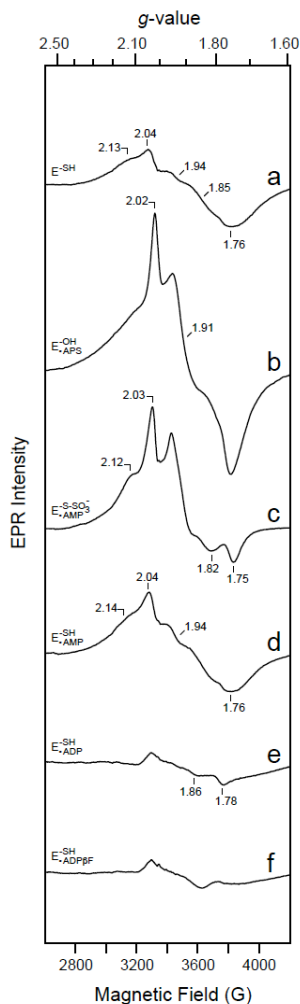
Figure 3.4 Experimental EPR spectra of photoreduced MtAPR. Anaerobic 250 μM MtAPR alone or incubated with 1 mM ligand for 10 min at 25 °C was then photoreduced as described in Experimental Procedures. Samples: *A.* MtAPR alone. *B.* Cys256Ser MtAPR bound to APS. *C.* MtAPR incubated with APS to generate the *S*-sulfocysteine intermediate bound to AMP. *D.* MtAPR bound to AMP. *E.* MtAPR bound to ADP. *F.* MtAPR bound to ADPβF. The EPR spectra were recorded at 10 K and the instrument parameters were: microwave power, 10 mW; receiver gain, 2 x 10^4; modulation amplitude, 10 G; microwave frequency, 9.43 GHz.

microwave power of 10 mW. This behavior suggests that the paramagnetic signal arises from a $[4Fe-4S]^+$ cluster. By contrast, $[2Fe-2S]^+$ clusters are slow relaxing and observable by EPR at temperatures above 70 K [24].

3.3.3 Interaction of the Photoreduced [4Fe-4S]$^+$ Cluster with Substrate and Analogs. The [4Fe-4S] cluster at the active site of APR is required for catalytic activity [1]; however, the mechanistic details are unknown and remain a central question for this family of enzymes. While the iron-sulfur cluster in APR does not undergo redox activity during the catalytic cycle [1], the 1+ state of APR can serve as a useful tool for mechanistic studies analogous to other enzymes that harbor redox-inactive iron-sulfur clusters such as aconitase [25]. Therefore, to gain insight into the functional role of the cluster we next investigated whether substrate binding would perturb the EPR spectrum of reduced MtAPR. Two types of protein-ligand complexes were prepared: (i) wild-type MtAPR treated with APS to afford the *S*-sulfocysteine intermediate form of the enzyme bound to AMP, and (ii) the catalytically inactive variant, Cys256Ser MtAPR bound to APS. Established procedures for complex formation were performed [1,13] and the resultant samples were then subjected to photoreduction.

Compared to wild-type MtAPR (Figure 3.4a), the EPR spectrum of Cys256Ser MtAPR bound to APS is markedly sharper in appearance with apparent g-values of 2.02, 1.91 and 1.76 (Figure 3.4b). The EPR signal of the enzyme *S*-sulfocysteine intermediate bound to AMP also exhibits increased resolution with apparent *g*-values of 2.03, 1.91 and 1.75 (Figure 3.4c). Additionally, both spectra (Figure 3.4b and c) indicate the presence of a second paramagnetic species. Spin quantitation of EPR signals from *g* = 2.7 to 1.6 indicate a respective 0.45 and 0.4 equiv of spin per mole for the Cys256Ser and wild-type MtAPR complexes. The heterogeneity of these

samples was essentially unaffected by the addition of 2.5 M urea, changes in sample pH between the ranges of 7.5 and 9.5, variation in temperature or microwave power levels (data not shown).

Simulation of the signal from wild-type MtAPR treated with APS suggests that it is the sum of at least two $S = ½$ components (Figure 3.5). One species has narrow lines and g-values at 2.04, 1.94, and 1.76 (component A), whereas the other has broad lines and exhibits principle g-values at 2.10 and 1.88 (component B) with an intensity ratio of 1:1.2. Although simulated and experimental spectra are in overall agreement, some discrepancies remain, particularly with respect to signal amplitudes. The addition of a third spectral component did not improve the fit quality. However, residual differences between the simulated and experimental spectra may result from weak signal intensity, minor fluctuations in temperature around 10 K, or the large number of variables required to simulate a $[4Fe-4S]^+$ cluster.

Next, we tested whether the observed APS-dependent changes in the EPR spectra of reduced MtAPR were specific to the substrate. To investigate this possibility,
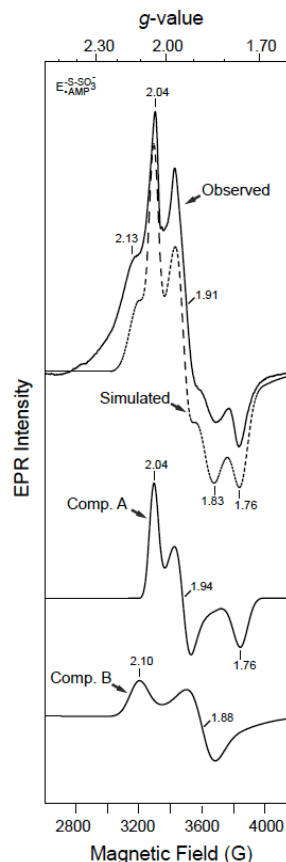
Figure 3.5 Simulated EPR spectrum of photoreduced wild-type MtAPR after addition of APS. The bottom two spectra show how two separate species might combine to give the observed signal (top spectra, solid line; see also Figure 4c). The dashed lines denote the simulated EPR spectrum, which is the sum of two components: Component A is a spectral simulation of the narrow component using g = 2.04, 1.94, 1.76, g strain (σ_g) = 0.017, 0.022, 0.020, and a Gaussian line shape. Component B is a spectral simulation of the broad component using g = 2.10, 1.88, 1.75, g strain (σ_g) = 0.038, 0.036, 0.099, and a Gaussian line shape. The ratio of Component A to Component B is 1:1.2. Simulated instrument parameters are as reported in the legend of Figure 3.4.

we analyzed the spectra of photoreduced MtAPR bound to AMP, ADP and ADPβF. The EPR signal of MtAPR bound to AMP (Figure 3.4d) was similar in shape and intensity to enzyme alone (Figure 3.4a). By contrast, the spectrum in the presence of ADP (Figure 3.4e) showed a significant reduction in signal intensity. To determine whether the observed changes in the EPR spectrum were due to the additional negative charge at a β-phosphate group (*i.e.,* ADP) relative to a β-sulfate group (*i.e.,* APS), we examined fluorine substitution of a β-nonbridging oxygen atom. Interestingly, however, the EPR spectrum of MtAPR bound to ADPβF (Figure 3.4f) was essentially the same as ADP (Figure 3.4e). Spin quantitation of MtAPR bound to ADP or ADPβF indicate less than 0.1 equiv of spins per mole of enzyme in each sample. The marked increase in signal resolution and intensity in the presence of APS, but not upon addition of substrate analogs or product reflects a unique state of the active site and cluster environment, which might be related to catalytic activity.

3.3.4 Characterization of Lys144Ala MtAPR*. The preceding EPR data support the existence of mid-range electrostatic interactions between the cluster and APS. Given that the side chain of Lys144 is positioned between coordinating Cys140 and the β-sulfate group of APS (Figure 3.2c) we reasoned that this residue might help mediate this interaction. To investigate this possibility, we generated the Lys144Ala MtAPR variant and characterized this protein through kinetic and EPR studies. An effect of 63,000-fold on k_{cat}/K_M is observed upon mutation of Lys144 to Ala (Table 3.1; see also Appendix 3.6.4). Since the chemical step (*i.e., S*-sulfocysteine formation) is rate limiting for the reaction of APS and MtAPR [26], this value represents the effect of removal of the Lys residue on the overall binding and chemical transformation. The mutation decreases the value of k_{max} by 270-fold suggesting that the Lys side chain stabilizes the transition state relative to the ground state complex.

Table 3.1 Effect of Lys144Ala Mutation on APR-Catalyzed Reduction and Binding of APS[a]

	k_{cat}/K_m (M^{-1} s^{-1})[b]	fold reduction	k_{max} (min^{-1})[c]	fold reduction	K_d (μM)	fold reduction
Wild-type	2.5 x 10^6	(1)	2.7	(1)	0.25[d]	(1)
Lys144Ala	40	6.3 x 10^4	0.01	270	≥100[e]	≥400

[a]Rate constants for single-turnover reactions were determined at 30 °C in 100 mM bis-tris propane buffer, 5 mM DTT, 10 μM Trx as described in Experimental Procedures. In all cases, the protein was in excess over substrate, with at least 2.5-fold more protein than substrate. [b]In bis-tris propane at pH 7.5. [c]In bis-tris propane at pH 6.5. [d]From (Hong, 2009). [e]The apparent K_d value was determined at 30 °C in 100 mM bis-tris propane pH 7.5 as described in Experimental Procedures.

To further explore the molecular recognition of APS, we measured the K_d value of the substrate for Lys144Ala MtAPR. Relative to wild-type MtAPR, the affinity of APS for Lys144Ala is decreased by 400-fold. The UV-Vis absorbance spectrum of Lys144Ala MtAPR showed a maximum in the visible range at 410 nm that is consistent with the presence of bound Fe (data not shown). Analysis of Fe content by inductively coupled plasma resonance spectrometry for Lys144Ala MtAPR indicated that each mole of protein contained 3.3 ± 0.4 mol of Fe, which is consistent with 4 Fe atoms in the cluster. Photoreduction of Lys144Ala MtAPR gave rise to a rhombic signal with resonances at g = 2.12, 1.99 and 1.82 (Figure 3.6a and c). However, the signal intensity was decreased relative to wild-type MtAPR and spin quantitation accounted for less than 0.05 equiv of spins per mole of enzyme. In the presence of saturating APS, the feature at g = 1.75 disappears and the remaining signal exhibits g-values at 2.12 and 1.99 (Figure 3.6b and d). A low-field isotropic Fe^{3+} signal accounting for less than 0.01 equiv of spin per mole of enzyme was also observed in the presence of APS, consistent with a small degree of cluster degradation (data not shown). Although the EPR spectra for both samples are relatively broad and weak, a modest reduction in the magnetic heterogeneity of MtAPR can be observed. Together, the kinetic and EPR data indicate a key role for Lys144 in chemistry and substrate

binding, and that this residue helps modulate APS-dependent changes in the iron-sulfur cluster environment.

3.3.5 Cryoreduction of the [4Fe-4S]$^{2+}$ Cluster in MtAPR.

Although the [4Fe-4S]$^+$ cluster serves as a useful spectroscopic tool in the study of MtAPR and variants, we recognize that it is not the native form of the active enzyme. For this reason, we attempted to probe the interaction of substrate with the [4Fe-4S]$^{2+}$ state of MtAPR through cryoreduction-EPR studies. In principle, γ-irradiation of the frozen [4Fe-4S]$^{2+}$ cluster affords the reduced state [4Fe-4S]$^+$ trapped in the geometry of the [4Fe-4S]$^{2+}$ oxidized state [27,28]. To this end, the 2+ state of MtAPR was incubated in the presence or absence of APS, frozen in liquid nitrogen and then exposed to high-energy γ-irradiation at 77 K to produce the [4Fe-4S]$^+$ cluster.

Figure 3.6. Experimental EPR spectra of photoreduced Lys144Ala MtAPR. Anaerobic 250 μM Lys144Ala MtAPR alone (a) and (c) or incubated with 1 mM APS (b) and (d) for 10 min at 25 °C was then photoreduced as described in Experimental Procedures. In (a) and (b) EPR signal intensities have been scaled to match those in Figure 3.4. In (c) and (d) the intensity of the EPR signals has been scaled 7.5-fold. The EPR spectra were recorded at 10 K and the instrument parameters were: microwave power, 10 mW; receiver gain, 2 x 10^4; modulation amplitude, 10 G; microwave frequency, 9.43 GHz.

The resulting spectrum in the absence of substrate (Appendix 3.6.5) is ill defined and relatively broad. However, the addition of substrate APS was accompanied by a marked increase in signal intensity and resolution with apparent g-values at 2.08, 2.04 and 2.02 (Appendix 3.6.5). The observation of substrate-dependent changes in the EPR spectrum is in qualitative agreement with our experimental results from photoreduction.

However, we note that the EPR spectra of cryoreduced MtAPR are distinct from those of the photochemically reduced enzyme. These findings may indicate that the substrate interacts differently with the cluster in the +2 and +1 states. An alternative possibility is that the observed EPR signals correspond to a thiyl radical formed by homolytic scission of the *S*-sulfocysteine bond. In support of this proposal, the relatively high *g*-values are consistent with literature data for a sulfur-centered species [29,30].

In addition to the aforementioned *g*-values, the cryoreduced samples contained an extremely intense signal isotropic signal at *g* = 2, which could arise from other non-specifically reduced organic radicals present in the sample (Appendix 3.6.5). 4.2-K/53-mT Mössbauer spectra of samples recorded before and after cryoreduction (Appendix 3.6.6) indicate that ~50% of the [4Fe-4S]$^{2+}$ clusters were reduced to the +1 state under these conditions. Thus, Mössbauer analysis confirms the presence of the [4Fe-4S]$^{+}$ cluster in cryoreduced samples; however, the γ-irradiation also appears to have generated extremely intense, new paramagnetic species that are distinct from a simple one-electron reduction of the +2 cluster. Lastly, no significant changes in the Mössbauer spectra from substrate-bound and substrate-free cryoreduced MtAPR were observed (Appendix 3.6.6).

3.3.6 Ferricyanide Oxidation of the [4Fe-4S]$^{2+}$ Cluster in MtAPR. The [4Fe-4S]$^{2+}$ cluster in PaAPR is partially converted to the [3Fe-4S]$^{+}$ form by treatment with the oxidant potassium ferricyanide [16]. To assess this possibility for MtAPR, a stoichiometric amount of potassium ferricyanide was added to the enzyme. The resulting EPR signal shows a well-defined EPR resonance at *g* = 2.03 and a poorly resolved high-field component at *g* = 1.99 (Appendix 3.6.7). This pattern of EPR signals is very similar to those of *S* = ½ [3Fe-4S]$^{+}$ clusters in aconitase [25]

and endonuclease III [31]. Spin quantitation of the EPR signals from g = 2.1 to 1.8 indicate less than 0.1 equiv of spins per mole of enzyme. The EPR spectrum of oxidized MtAPR also exhibited a signal accounting for less than 0.01 equiv of spins per mole of enzyme at g = 4.3 that is characteristic of high-spin Fe(III). When ferricyanide was added to MtAPR that had been pre-treated with APS, the intensity of the signal at g = 4.3 was increased by 3-fold (data not shown). Attempts to purify the [3Fe-4S]$^+$ cluster form of MtAPR were unsuccessful as the cluster rapidly decomposed upon oxidant removal. Nonetheless, these data are consistent with the existence of a labile Fe site within the [4Fe-4S]$^{2+}$ cluster of MtAPR. Given the constraints of tandem Cys coordination [5] and the proximity of Lys144, the Fe coordinated to Cys140 may correspond to the displaced atom.

3.4 Discussion

Iron-sulfur clusters are amazingly versatile cofactors with functions in electron transfer, Lewis acid-assisted enzyme catalysis, radical generation, oxidation of a wide variety of substrates under anaerobic conditions, and protein structure [32-37]. While numerous studies indicate that the iron-sulfur cluster is essential for APR activity [1,5,7,13], the specific role of the iron-sulfur cluster has been elusive. Progress on this front has been limited, in part, by the inability to generate a paramagnetic state of the [4Fe-4S] cluster that can be studied by EPR spectroscopy. The present study is the first reported case in which the [4Fe-4S]$^{2+}$ cluster of APR has been reduced to the S = ½ [4Fe-4S]$^+$ form.

Photoreduction in the presence of deazaflavin and oxalate turned out to be the most effective method to generate the paramagnetic 1+ state of MtAPR. By contrast, attempts to photochemically reduce APR from plants and bacteria such as *P. aeruginosa* and *B. subtilis* have

not been successful [13,22]. Active site residues that interact with the iron-sulfur cluster and/or the substrate (*e.g.,* Thr87, Arg143, Lys144, Arg 242, Arg245, Trp246) are highly conserved among APRs and therefore, are unlikely to account for EPR behavioral differences. On the other hand MtAPR is a monomer in solution while APR from other species exists as a homodimer or homotetramer [1,17]. Along these lines, the structure of PaAPR shows that the face of the iron-sulfur cluster opposite the active site is buried at the interface between two monomeric subunits [5]. Studies on the effect of solvent on redox potentials of model clusters indicate that water raises the reduction potential of the $[4Fe-4S]^{2+/+}$ couple [38,39]. Hence, increased solvent accessibility to the cluster of monomeric MtAPR may account for the ability to generate the 1+ state.

The EPR signal of reduced MtAPR arises from a mixture of $[4Fe-4S]^{+}$ clusters with $S = \frac{1}{2}$, possibly reflecting the existence of distinct conformational states. Multiple $S = \frac{1}{2}$ ground states have been observed for other [4Fe-4S] iron-sulfur enzymes such as the corrinoid protein from *Clostridium thermoaceticum* [40], human DNA primase [41], and the ribosomal RNA methyltransferase, RumA [42]. The apparent lack of changes in the EPR spectra between pH 6.5 and 9.5 suggests that the complexity does not result from differences in protonation state of residues near the iron-sulfur cluster. Freezing of samples after photoreduction can also led to multiple signals from the same paramagnetic center – one from aggregated protein molecules and the other from dispersed molecules [43]. To investigate this possibility, we recorded the EPR spectrum for cryoreduced MtAPR. In these experiments, the EPR signal that arises from the $[4Fe-4S]^{+}$ form of MtAPR is weak relative to other radical species generated during the γ-irradition process. Nonetheless, magnetic heterogeneity is still apparent in the spectrum (Appendix 3.6.5). Treatment with 1-2.5 M urea has also been reported to convert multiple

isomeric states of an [4Fe-4S]$^+$ cluster into a single one [40], but this was not the case with MtAPR. This observation may indicate the existence of more subtle differences between cluster forms in MtAPR such as changes in the orientation of a Cys-Sγ-Fe bond or in hydrogen bonding to a sulfur atom.

Regarding possible conformational changes, PaAPR has been fortuitously crystallized with APS bound in two of the four monomeric subunits [5]. A comparison of bound and unbound states reveals minor structural changes in residues adjacent to the iron-sulfur cluster (Figure 3.2b and c). In the absence of substrate, Lys144 is present in an extended conformation such that the distance between the side chain and the Sγ atom of Cys140 is ~5 Å. By contrast, the subunit with APS bound shows that the side chain of Lys144 adopts a bent rotamer conformation, which brings this residue within interaction range (*i.e.,* 3.5 Å) of Cys140 Sγ. In turn, the Cys140 side chain moves slightly upward (*i.e.,* 5° rotation at the β-carbon). It is possible then, that the heterogeneity observed in the EPR spectra may be related to conformational dynamics of Lys144, Cys140 and/or Cys256 within the C-terminus. In support of this hypothesis, a decrease in EPR signal complexity was observed with Lys144Ala MtAPR (Figure 3.6). Structural changes at these key residues may also account for the observation that the iron-sulfur cluster of APR is protected from oxidation on addition of APS [13] and that the resonance Raman spectra exhibit changes in Fe-Sγ stretching modes when substrate is bound [6].

Previous models for the role of the iron-sulfur cluster in APR catalysis have postulated that one or two non-bridging sulfate oxygen(s) establish a direct interaction with an Fe atom (*i.e.,* monodentate or bidentate coordination of the substrate) [44]. The interacting Fe atom could facilitate nucleophilic attack at the sulfate sulfur by acting as a Lewis acid, analogous to

aconitase [25]. Since the cluster in APR is ligated to the protein via four cysteine residues the coordination number of the interacting Fe site would increase to 5 or 6. Based on studies of direct interaction between substrate or cofactor and $[4Fe-4S]^{2+}$ clusters in aconitase [25], pyruvate formate-lyase activase [45], and biotin synthase [46] significant perturbation of the Mössbauer parameters for an interacting Fe site in MtAPR would be expected [45,47,48]. The present work, however, shows no discernable change in the Mössbauer spectrum upon addition of APS to MtAPR (Appendix 3.6.3), suggesting that the cluster and the substrate do not establish a direct interaction. This proposal is fully consistent with the crystal structure of PaAPR bound to APS, which shows that the sulfate oxygens are 7 Å from the closest Fe atom and 6 Å from the Sγ atom of Cys140 (Figure 3.2b) [5].

On the other hand, substrate binding to MtAPR led to a marked increase in intensity and resolution of the EPR signal, and to minor shifts in principle g values that were not observed with closely related substrate analogs, ADP and ADPβF (Figure 3.4). These findings correlate with observed differences in the dissociation constants (K_ds) reported for these ligands [26] and can be rationalized on the basis of differences in anionic charges: β-sulfate has a net negative charge of one distributed over three oxygen atoms (*i.e.*, -1/3 charge each; K_d = 0.25 μM), while β-phosphate has a net negative charge of two distributed over three oxygen atoms (*i.e.*, -2/3 charge each; K_d = 5 μM) and β-fluorophosphate has a net negative charge of one distributed over two oxygen atoms (*i.e.*, -1/2 charge each; K_d = 2.5 μM). By contrast, the similarity of EPR spectra obtained in the presence or absence of AMP (Figure 3.4a and d) suggests that the α-phosphate group is too distant from the cluster to exert any significant effect. Taken together, these data are indicative of mid-range electrostatic interactions between the iron-sulfur cluster

and the β-functional group of the ligand, which are finely attuned to the electrostatic properties of the sulfate in APS.

In addition to differences in formal anionic charge, the sulfur atom of sulfate is larger, more electronegative and forms shorter bonds with oxygen relative to a phosphorous atom. As a consequence, the oxygen atoms associated with a β-sulfate group are associated with less negative charge density, relative to oxygen atoms attached to phosphate [49]. As compared to APS, the increase in negative charge density associated with β-non-bridging oxygen atoms of ADP and ADPβF might strengthen their interaction with the positively charged Lys144 side chain such that this residue moves away from the Sγ atom of coordinating Cys140. Alternatively, or in addition, considering that the [4Fe-4S(Cys-Sγ)$_4$] cluster has a net charge of -2 [50], repulsive electrostatic interactions could arise when ADP or ADPβF are bound in the active site. Either scenario could account for the observed decrease in analog affinity and hamper the ability of the iron-sulfur cluster in MtAPR to accept an additional electron (*i.e.,* adopt the reduced 1+ state).

In general, spin quantitation of the EPR signals revealed less than 0.5 spin/mol MtAPR. These less than unitary values for the spin integration of the reduced spectra can be attributed to incomplete reduction of the [4Fe-4S]$^{2+}$ cluster that may result from insufficient light intensity or illumination time. However, changes in these parameters were accompanied by noticeable cluster degradation and were therefore not pursued further. Despite the modest efficiency of reduction, variations in spin quantitation between substrate-bound (or substrate analog) and substrate-free states of MtAPR were observed. These differences are likely due to ligand-dependent structural and electrostatic changes in cluster environment, as discussed above.

The positively charged side chain of Lys144 interacts with both APS and coordinating Cys140, forming a link between the substrate and the iron-sulfur cluster. Although strict conservation of Lys144 implies an important role, this study is the first to probe the precise function of this residue. Using site-directed mutagenesis, we demonstrate that Lys144 is necessary for both substrate binding and transition state stabilization (Table 3.1). Moreover, the significant decrease in EPR signal intensity for Lys144Ala MtAPR (Figure 3.6) suggests that the proximity of the positively charged side chain of this residue may be an important factor in stabilizing the reduced state of the cluster. Future measurements of midpoint reduction potentials could provide additional support for this proposal.

Comparison of the EPR spectra between wild-type, Cys256Ser (Figure 3.4) and Lys144Ala MtAPR (Figure 3.6) shows that the Lys residue plays an important role in modulating substrate-dependent changes in signal resolution and intensity. However, we note that the EPR spectrum of Lys144Ala still exhibits subtle differences in the presence or absence of APS. In particular, the APS bound state shows small changes in signal intensity at g = 2.12 and 1.99, and a decrease in the spectral feature at g = 1.82. These differences in EPR spectra may be attributable to the intrinsic electrostatic interaction between the iron-sulfur cluster and the substrate.

On the basis of the results reported herein, we propose a catalytic role for the iron-sulfur cluster in the mechanism of APS reduction, specifically in the sequence of events leading up to and through sulfuryl group transfer (Figure 3.7). Prior to APS binding, the $[4Fe-4S(Cys-S\gamma)_4]^{2-}$ cluster may serve to pre-organize the positively charged side chain of Lys144 and possibly Arg245 (Figure 3.2b and c) within the active site, so that the substrate can establish interactions with these residues. Based on the Mössbauer data and structural studies, APS binds to the $[4Fe-4S]^{2+}$

state of APR, but does not appear to come into direct contact with the cluster. Rather, EPR investigation of the $[4Fe-4S]^+$ and $[3Fe-4S]^+$ states indicate that mid-range electrostatic interactions arise between APS and the iron-sulfur cluster. The charge from and polarization within the $[4Fe-4S(Cys-S\gamma)_4]^{2-}$ cluster could serve to activate the sulfate group of APS, thereby facilitating S-OP cleavage and S-S bond formation in the reaction.
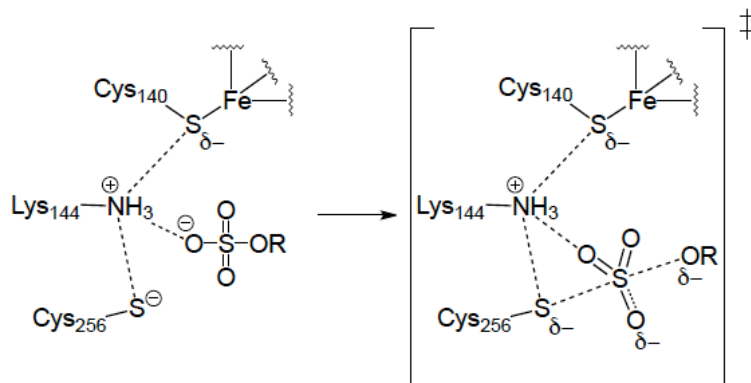
Figure 3.7 Possible reaction pathway for covalent *S*-sulfocysteine intermediate formation catalyzed by APR. The C-terminal residues 250-267, which carry the catalytically essential Cys256, are disordered in the structure of PaAPR, but can be modeled into the active site using the structure of *S. cerevisiae* PAPR (Yu, 2008). In the homology-modeled structure (Hong, 2009), Cys256 is proximal to the sulfate group of APS as well as the side-chains of Cys140 and Lys144. Electrostatic destabilization of APS may arise from the juxtaposition of the electron density and partial negative charge that resides on the sulfide and cysteinyl sulfur atoms of the iron-sulfur cluster (see ref. Torres, 2003 for theoretical treatment of charge distribution in iron-sulfur clusters). Repulsion between APS and the iron-sulfur cluster could be partially relieved in the transition state, thereby enhancing the reaction rate. The charge build-up on the bridging sulfate oxygen could be stabilized by Arg171, Arg242 and His259, which are not indicated in this figure for the sake of simplicity.

In the absence of an iron-sulfur cluster, PAPR may achieve something similar via repulsion between the extra 3'-phosphate group of PAPS and the sulfate end of the 5'-phosphosulfate. The sulfate group would then be primed for nucleophilic attack by Cys256, leading to formation of the *S*-sulfocysteine enzyme intermediate. In support of this proposal, experimental and theoretical studies of sulfuryl group transfer in sulfate esters [49,51] indicate the need for a strong polarizing agent. Regarding Lys144, our analysis demonstrates an essential role for this residue in enzyme catalysis. Although only speculative at present, it is plausible that the active site Lys144 cation may orient the incoming Cys nucleophile with respect to the sulfate moiety

and/or act as a "molecular guidewire" during sulfuryl transfer; either possibility could result in transition state stabilization. Analogous functions for Lys and Arg residues in the active site of other enzymes that catalyze sulfuryl transfer have been described [52,53].

In APR from *Bacillus subtilis*, on the basis of its short half-life ($t_{1/2}$ ~12 min) an oxygen-sensing function for has been proposed for the iron-sulfur cluster [22]. By comparison, the iron-sulfur in MtAPR is significantly more stable with a half-life of about 6 hrs [13]. Nevertheless, it is important to note that the model we have proposed above does not preclude the possibility that the cluster plays a regulatory role. Rather, the iron-sulfur cluster of APR may function both in a catalytic capacity and, in some organisms, as an oxygen-sensitive switch.

In summary, the data presented in this work are consistent with a catalytic function for the iron-sulfur cluster in APR. On the basis of these data, we have proposed that the cofactor plays a role in pre-organizing active site residues and in substrate activation. Additional experimental and theoretical tests of these proposals are currently underway and will be reported in due course. Moreover, the finding that MtAPR can be reduced to the [4Fe-4S]$^+$ state opens the door for other forms of spectroscopy such as ENDOR and ESEEM that can provide further insight into the relationship between the substrate and iron-sulfur cluster.

3.5 Experimental Procedures

3.5.1 Materials*. APS (≥95%) was obtained from Biolog Life Sciences Institute. ADP and AMP were purchased from Sigma Chemical Co. ADPβF was synthesized as previously described [54]. The structure and purity (≥98%) was confirmed by ^{1}H and ^{31}P NMR (data not shown). 10-Methyl-3-sulfopropyl-5-deazaisoalloxazine potassium salt (deazaflavin) was a generous gift from

Prof. David Ballou (University of Michigan). Titanium(III) citrate was prepared anaerobically from a 15% titanium(III) chloride solution in 1 M HCl with an equimolar amount of citrate (trisodium salt), and neutralized to pH 7.0 with saturated sodium bicarbonate.

3.5.2 Mutagenesis and Protein Expression. The construction of the expression vector encoding wild-type and Cys256Ser APR from *M. tuberculosis* cloned into the vector pET24b has been previously described [55]. The Lys144Ala variant was generated from the wild-type MtAPR template using the Quik-change site-directed mutagenesis kit (Stratagene) and the following primer sequence: 5′-GCTGCCGGTTGCGCAAGGTCGTTCCCCTGGG-3′. Plasmids encoding wild-type, Cys256Ser or Lys144Ala MtAPR pET24 and pACYC (containing genes encoding the *isc* operon of six accessory proteins required for Fe–S cluster biosynthesis in *A. vinelandii* under the control of an arabinose-inducible promoter) [23] were co-transformed into *E. coli* BL21(DE3) (Novagen) and plated on L-agar 50 μg/ml kanamycin and 100 μg/ml carbenicillin. A single colony was picked and added to 5 ml of L-broth plus antibiotics and grown overnight with shaking at 37 °C. This culture was used as a 0.5% 1 L of L-broth plus antibiotics and grown with shaking at 37 °C until absorbance at 600 nm reached approximately 0.6. Arabinose and iron citrate were added to final concentrations of 20 mM and 0.8 mM, respectively and the culture grown as above for 1 hr. At this point the flasks were removed from the incubator. IPTG was added to a final concentration of 0.3 mM and the flasks were returned to the incubator and grown overnight at 18 °C with shaking at 200 rpm. Cultures were harvested by centrifugation (4 °C, 4,300*g*). After removal of the supernatant the pellets were stored at -80 °C until required.

All purification steps were carried out at 4 °C. Cell pellets were resuspended in 30 ml Buffer A (20 mM sodium phosphate, 0.5 M NaCl, 10 mM imidazole; pH 7.4) supplemented with 0.1 mM

PMSF, 10μg/ml DNase, 5 μg/ml lysozyme and lysed by sonication. Lysates were centrifuged (20,000g, 15 min) and loaded onto a 5 ml HiTrap Chelating column (GE Healthcare, Piscataway, NJ) equilibrated in the same buffer. Unbound material was washed off with 50 ml of Buffer A and bound proteins then eluted with in Buffer B (20 mM phosphate, 0.5 M NaCl, 250 mM imidazole; pH 7.4). Fractions containing wild-type or Lys144Ala were pooled, concentrated by centrifugation (Amicon 10 kDa cutoff, Millipore, Billerica, MA) and loaded onto a 16/60 Superdex 200 size exclusion column previously equilibrated in Buffer C (50 mM Tris-HCl, 150 mM NaCl, 5 mM DTT, 10% glycerol; pH 8.5 at 4 °C). Fractions containing wild-type or Lys144Ala MtAPR were pooled, snap-frozen in liquid nitrogen, and stored at -80 °C. Protein concentrations were determined using the extinction coefficient, ε_{280}=36,815 M^{-1}cm^{-1}, obtained from quantitative amino acid analysis [1].

3.5.3 Preparation of MtAPR for EPR and Mössbauer Spectroscopy. Samples of wild-type, Cys256Ser or Lys144Ala MtAPR suitable for Mössbauer or EPR spectroscopy were prepared inside of an anaerobic chamber with O$_2$ levels ≤ 1 ppm. Purified MtAPR was exchanged into anaerobic buffer containing 50 mM Tris–HCl, 150 mM NaCl (pH 8.5 at 4 °C) and 10% glycerol. To reduce the cluster in MtAPR, reactions contained 250 μM enzyme, 25 mM sodium oxalate, 250 μM deazaflavin in a total volume of 250 μL. When included, substrate or other analogs were added to a final concentration of 1 mM and incubated with MtAPR for 10 min at 25 °C prior to photoreduction. The reaction mixtures were transferred to EPR tubes, chilled in an ice-salt bath (-6 °C) and irradiated with light from a 100 W quartz halogen lamp (Applied Photophysics, Surrey, UK) for 30 min. After illumination, samples were immediately frozen in liquid nitrogen and analyzed by low-temperature EPR. Mössbauer spectra were recorded on proteins that contained ^{57}Fe in place of natural-abundance iron. ^{57}Fe was incorporated into MtAPR via

supplementation of *E. coli* growth media, and samples contained 1 mM protein, and 2 mM APS when appropriate. After 10 min incubation with substrate, samples were transferred to Mössbauer cups and frozen in liquid nitrogen.

3.5.4 EPR Spectroscopy- X-band EPR spectra of photoreduced samples were recorded on a Bruker EMX spectrometer (Billerica, MA) equipped with an Oxford Instruments ITC4 temperature controller, a Hewlett-Packard model 5340 automatic frequency counter and Bruker gaussmeter. Figure legends contain relevant instrumental parameters. The sample buffer was used to record baselines under conditions identical to those in which the sample spectra were obtained. These baselines were subtracted from MtAPR spectra shown in the figures. Spin concentrations in MtAPR samples were determined by double integration of the EPR signal over a range of 2 kgauss and comparison with double integrals of 1 mM $Cu(ClO_4)_2$ in sample buffer. EPR spectra of cryoreduced samples were recorded on a Bruker ER-200DSRC spectrometer equipped with an Oxford Instruments ESR 910 continuous-flow cryostat. Simulations of EPR spectra were performed using Spin Count (ver 2.6.7) created by Professsor M.P. Hendrich at Carnegie Mellon University. Spin Count is available at http://www.chem.cmu.edu/groups/hendrich/.

3.5.5 Mössbauer Spectroscopy. Mössbauer spectra were recorded on a spectrometer from WEB research (Edina, MN) operating in the constant acceleration mode in transmission geometry. Spectra were recorded with the temperature of the sample maintained at 4.2 K in an externally applied magnetic field of 53 mT oriented parallel to the γ-beam. The quoted isomer shifts were relative to the centroid of the spectrum of a foil of α-Fe metal at room temperature. Data analysis was performed using the program WMOSS from WEB research.

3.5.6 Cryoreduction of MtAPR by Low-Temperature γ-Radiolysis. Samples containing 250 μM MtAPR were loaded into EPR tubes or Mössbauer cups and flash frozen in liquid nitrogen inside the glovebox. When appropriate, APS was added to a final concentration of 1 mM and incubated with protein for 10 min at 25 °C prior to freezing. Samples were γ-irradiated (^{60}Co; total dose of 4 Mrad) at the γ-irradiation facility of the Breazeale nuclear reactor at the Pennsylvania State University. During irradiation, samples were maintained at 77 K by immersion in liquid N_2.

3.5.7 MtAPR Activity Assay. Reactions were carried out at 30 °C. Unless otherwise indicated, the buffer consisted of 100 mM bis-tris propane (pH 7.5) and 100 mM NaCl supplemented with 5 mM DTT and 10 μM *E. coli* thioredoxin. Production of $^{35}SO_3^{2-}$ from ^{35}S-APS was monitored using charcoal-based separation and scintillation counting as previously reported [26]. The substrate was incubated with excess enzyme to ensure single-turnover conditions (>2.5-fold molar excess of enzyme). The reaction progress curve was plotted as the fraction of product versus time and was fit by a single exponential $F = A[1–e(–k_{obs}t)]$, where F is the fraction product, A is the fraction of substrate converted to product at completion, k_{obs} the observed rate constant, and t time. Reactions were followed for ≥5 half-lives except for very slow reactions. Under single-turnover conditions, it is expected that the concentration dependence of the enzyme will be hyperbolic (eq 1).

$$k_{obs} = \frac{k_{max}[E]}{K_{1/2} + [E]} \quad (1)$$

To determine k_{cat}/K_m, a concentration of enzyme was chosen that was at least 5-fold below the K_m value. Although we refer to the $K_{1/2}$ for maximal activity as K_m, we note that the $K_{1/2}$ for single turnover is not necessarily the same as the K_m for the multiple turnover reaction since the latter can be affected by the rate of product release. For conditions in which $[E] \ll K_m$ the second order rate constant, $k_{cat}/K_m = k_{obs}/[E]$. We note that the reported values of k_{cat}/K_m are for single-turnover conditions, but the measurement is equivalent to steady state k_{cat}/K_m. At a saturating concentration of enzyme, the observed single-turnover rate constant reaches a maximum, k_{max}. To determine k_{max}, the concentration of enzyme was varied by at least 3-fold to establish that the observed rate was independent of the concentration of enzyme, indicating that the enzyme was in excess and at a saturating concentration (*i.e.*, $k_{obs} = k_{max}$). The reported values of k_{cat}/K_m and k_{max} are the average of at least three independent determinations. Unless otherwise indicated, the standard deviation was ≤15% of the value of the mean.

3.5.8 Determination of Substrate Affinity. The apparent dissociation constant (K_d) for ^{35}S-APS from Lys144Ala MtAPR-ligand complexes was measured using an ultrafiltration binding assay reported by Hernick and Fierke [56]. Because the chemical step (*i.e.*, S-sulfocysteine formation) is rate-limiting [26] the $K_{1/2}$ is equal to K_d of APS for Lys144Ala MtAPR. In brief, the concentration of substrate was kept low (*i.e.*, below the K_d) and constant, and the concentration of the enzyme was varied (0 to 80 μM). Lys144Ala MtAPR was incubated in 100 mM bis-tris propane, pH 7.5 at 30 °C for 15 min prior to the assay to allow for ligand equilibration. Assay mixtures were then transferred into ultrafiltration devices (Microcon 30 kDa cutoff, Millipore, Billerica, MA), and the free and bound ligand separated by centrifuging the samples at 3,000 rpm for 2.5 min. Equal volumes of the filtrate and retentate were removed and quantified using

scintillation counting. The ratio of EL/L_{total} was determined as a function of $[E]_{total}$, and the K_d value was obtained by fitting eq 2 to these data.

$$\frac{EL}{L_{total}} = \frac{\left(EL/L_{total}\right)_{Endpt}}{\left(1 + \dfrac{K_d}{E_{total}}\right)} + \left(\frac{EL}{L_{total}}\right)_{Background} \qquad (2)$$

Acknowledgements

3.6 Appendix

Appendix 3.6.1 Structure based sequence alignment of 17 APS reductases from prokaryotes
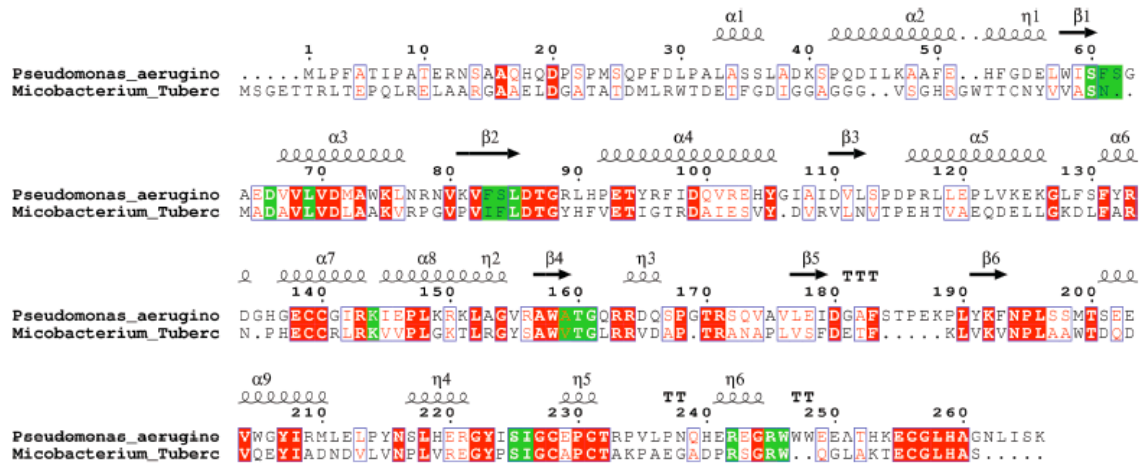
Appendix 3.6.1 Structure based sequence alignment of 17 APS reductases from prokaryotes. The ClustalW Multiple Sequence Alignment program was used. The bar graph indicates the degree of conservation per position. Strictly conserved residues are outlined in red, red letters indicate conserved residues and conserved regions are boxed in blue. Alignment pictures were rendered with the server ESPript 2.2 (http://espript.ibcp.fr).

Appendix 3.6.2 UV-vis absorption spectra of MtAPR
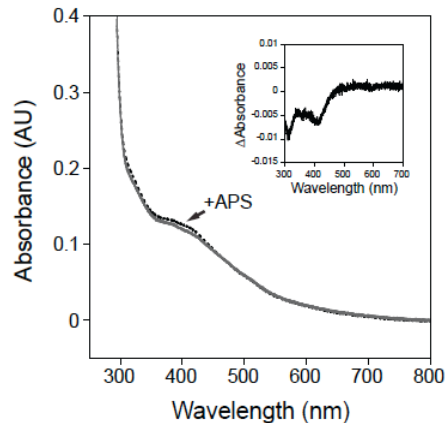
Appendix 3.6.2 UV-vis absorption spectra of MtAPR. UV-vis absorption of 10μM MtAPR in 50 mM Tris–HCl, 150 mM NaCl (pH 8.5 at 4 °C) and 10% glycerol, before (—) and after (••••) the addition of 2-fold stoichiometric excess of APS. Inset shows the corresponding difference spectrum resulting from complex formation between MtAPR and APS. The difference spectrum is the spectrum of the mixture minus spectrum of enzyme alone.

Appendix 3.6.3 Mössbauer spectra of MtAPR in the absence or presence of APS.
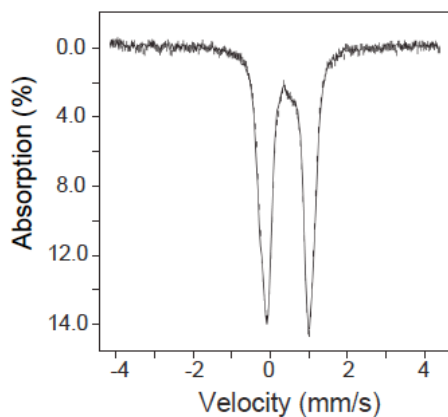
Appendix 3.6.3 4.2-K/53-mT Mössbauer spectra of 1 mM MtAPR in the absence (vertical bars) or presence of 2 mM APS (solid line).

Appendix 3.6.4 Rate and equilibrium constants for MtAPR

a

b

c
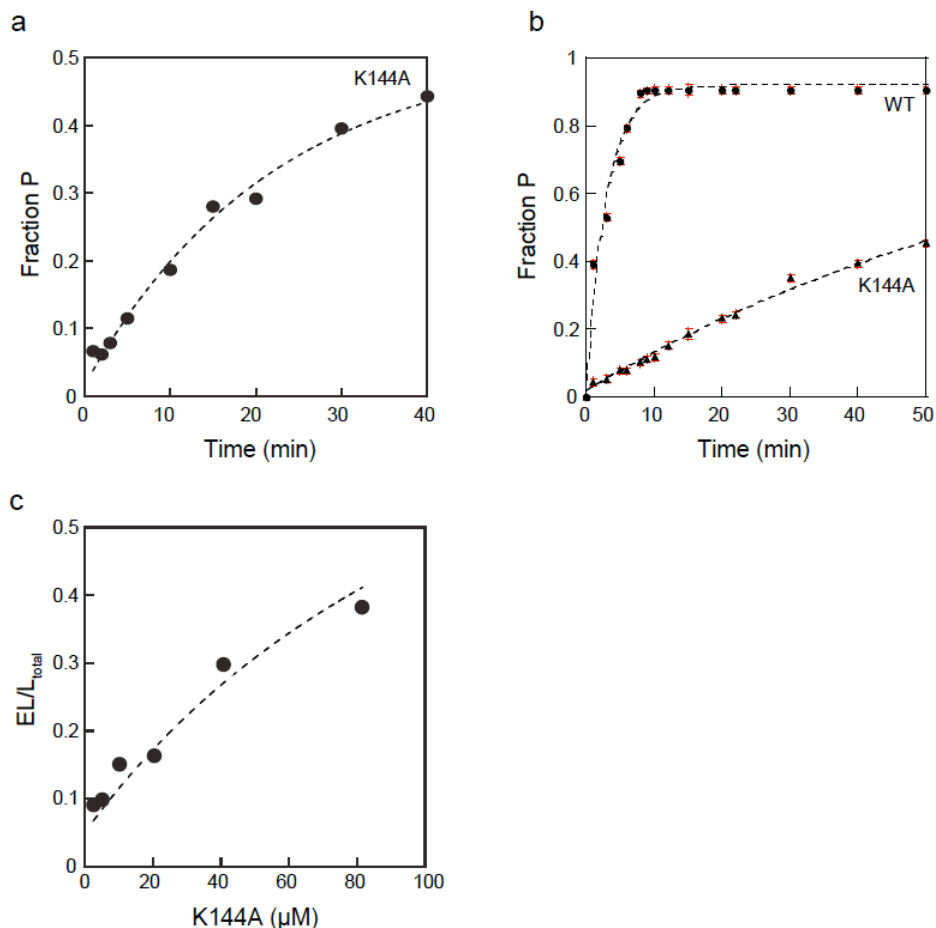
Appendix 3.6.4   Rate and equilibrium constants for MtAPR.   a. Single-turnover reduction of APS by Lys144Ala MtAPR performed under subsaturating conditions as described in Experimental Procedures. Single-turnover reaction to measure k_{cat}/K_m was performed with 5 nM wild-type MtAPR or 20 μM Lys144Ala MtAPR and 0.25 nM APS. b. Single-turnover reduction of APS by wild-type (filled circles) and Lys144Ala (filled triangles) MtAPR performed under saturating conditions as described in Experimental Procedures. Single-turnover reactions to measure k_{max} were performed with 150 μM enzyme and 50 μM APS.   c. APS binding to Lys144Ala MtAPR measured by ultrafiltration as described in Experimental Procedures.

Appendix 3.6.5 EPR spectra of radiolytically cryoreduced MtAPR.
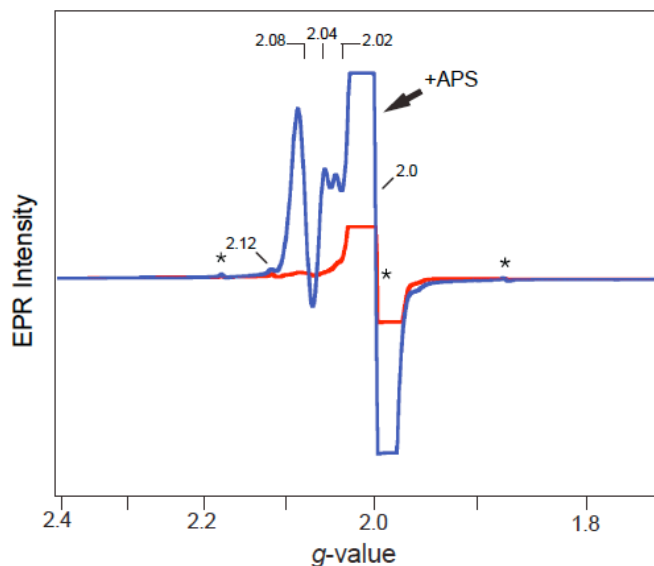
Appendix 3.6.5   EPR spectra of radiolytically cryoreduced 250 µM MtAPR in the absence (red) or pre-incubated with 1 mM APS (blue) as described in Experimental Procedures. Conditions: temperature, 77 K; microwave frequency, 9.45 GHz; microwave power, 10 mW; modulation frequency, 100 kHz; modulation amplitude, 10 G; scan time, 167 s; time constant, 167 ms. Asterisks indicate the position of the intense signal at g = 2 emanating from free radicals generated during cryoreduction and the position of the peaks of hydrogen atoms formed during cryoreduction.

Appendix 3.6.6. Mössbauer spectra of MtAPR after γ-irradiation.
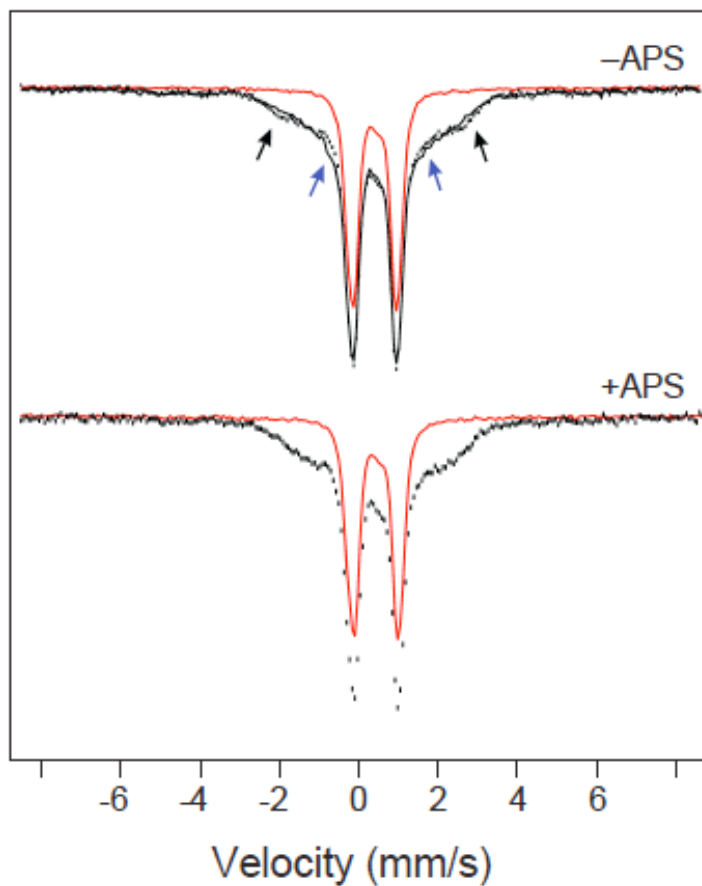
Appendix 3.6.6. 4.2-K/53-mT Mössbauer spectra of 250 µM MtAPR in the absence (top) or pre-incubated with 1 mM APS (bottom) after γ-irradiation (vertical bars) as described in Materials and Methods. In these experiments, 50% of the starting material is unchanged (red solid line). Spectral changes that result from different orientations of the externally applied 53-mT magnetic field are highlighted by the black and blue arrows.

Appendix 3.6.7 EPR spectra of oxidized wild-type MtAPR.
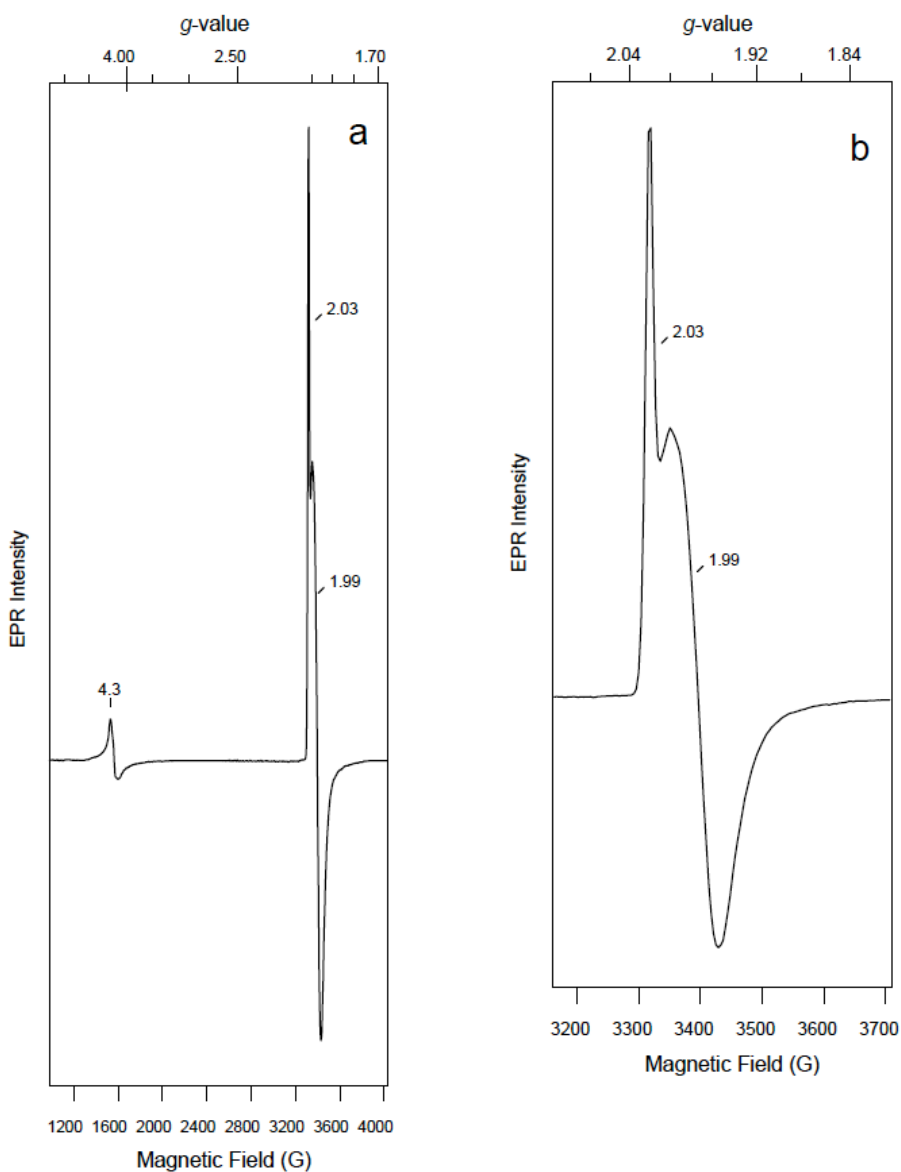
Appendix 3.6.7 EPR spectra of oxidized wild-type MtAPR. a. Spectra of 250 µM MtAPR treated with a stoichiometric amount of ferricyanide in buffer containing 50 mM Tris–HCl, 150 mM NaCl (pH 8.5 at 4 °C) and 10% glycerol. b. Expanded version of panel a around g = 2. Prior to freezing, samples with protein were incubated with ferricyanide for 5 min at rt. Unreacted potassium ferricyanide is present in the sample. However, controls reactions carried out in the absence of protein indicate that it does not contribute to features in the spectrum. Conditions: temperature, 10 K; microwave frequency, 9.38 GHz; microwave power, 10 mW.

3.7 References

1. Carroll KS, Gao H, Chen H, Stout CD, Leary JA, Bertozzi CR: **A conserved mechanism for sulfonucleotide reduction**. *PLoS Biol* 2005, **3**:e250.
2. Mougous JD, Lee DH, Hubbard SC, Schelle MW, Vocadlo DJ, Berger JM, Bertozzi CR: **Molecular basis for G protein control of the prokaryotic ATP sulfurylase**. *Mol Cell* 2006, **21**:109-122.
3. Leyh TS, Taylor JC, Markham GD: **The sulfate activation locus of Escherichia coli K12: cloning, genetic, and enzymatic characterization**. *J Biol Chem* 1988, **263**:2409-2416.
4. Renosto F, Seubert PA, Segel IH: **Adenosine 5'-phosphosulfate kinase from Penicillium chrysogenum. Purification and kinetic characterization**. *J Biol Chem* 1984, **259**:2113-2123.
5. Chartron J, Carroll KS, Shiau C, Gao H, Leary JA, Bertozzi CR, Stout CD: **Substrate recognition, protein dynamics, and iron-sulfur cluster in Pseudomonas aeruginosa adenosine 5'-phosphosulfate reductase**. *J Mol Biol* 2006, **364**:152-169.
6. Kim SK, Rahman A, Mason JT, Hirasawa M, Conover RC, Johnson MK, Miginiac-Maslow M, Keryer E, Knaff DB, Leustek T: **The interaction of 5'-adenylylsulfate reductase from Pseudomonas aeruginosa with its substrates**. *Biochim Biophys Acta* 2005, **1710**:103-112.
7. Kopriva S, Buchert T, Fritz G, Suter M, Benda R, Schunemann V, Koprivova A, Schurmann P, Trautwein AX, Kroneck PM, et al.: **The presence of an iron-sulfur cluster in adenosine 5'-phosphosulfate reductase separates organisms utilizing adenosine 5'-phosphosulfate and phosphoadenosine 5'-phosphosulfate for sulfate assimilation**. *J Biol Chem* 2002, **277**:21786-21791.
8. Chartron J, Shiau C, Stout CD, Carroll KS: **3'-Phosphoadenosine-5'-phosphosulfate reductase in complex with thioredoxin: a structural snapshot in the catalytic cycle**. *Biochemistry* 2007, **46**:3942-3951.
9. Bhave DP, Muse WB, 3rd, Carroll KS: **Drug targets in mycobacterial sulfur metabolism**. *Infect Disord Drug Targets* 2007, **7**:140-158.
10. Mdluli K, Spigelman M: **Novel targets for tuberculosis drug discovery**. *Curr Opin Pharmacol* 2006, **6**:459-467.
11. Savage H, Montoya G, Svensson C, Schwenn JD, Sinning I: **Crystal structure of phosphoadenylyl sulphate (PAPS) reductase: a new family of adenine nucleotide alpha hydrolases**. *Structure* 1997, **5**:895-906.
12. Yu Z, Lemongello D, Segel IH, Fisher AJ: **Crystal structure of Saccharomyces cerevisiae 3'-phosphoadenosine-5'-phosphosulfate reductase complexed with adenosine 3',5'-bisphosphate**. *Biochemistry* 2008, **47**:12777-12786.
13. Carroll KS, Gao H, Chen H, Leary JA, Bertozzi CR: **Investigation of the iron-sulfur cluster in Mycobacterium tuberculosis APS reductase: implications for substrate binding and catalysis**. *Biochemistry* 2005, **44**:14647-14657.
14. Kopriva S, Fritzemeier K, Wiedemann G, Reski R: **The putative moss 3'-phosphoadenosine-5'-phosphosulfate reductase is a novel form of adenosine-5'-phosphosulfate reductase without an iron-sulfur cluster**. *J Biol Chem* 2007, **282**:22930-22938.
15. Sazanov LA, Hinchliffe P: **Structure of the hydrophilic domain of respiratory complex I from Thermus thermophilus**. *Science* 2006, **311**:1430-1436.
16. Kim SK, Rahman A, Bick JA, Conover RC, Johnson MK, Mason JT, Hirasawa M, Leustek T, Knaff DB: **Properties of the cysteine residues and iron-sulfur cluster of the assimilatory 5'-**

adenylyl sulfate reductase from Pseudomonas aeruginosa. *Biochemistry* 2004, **43**:13478-13486.

17. Kopriva S, Buchert T, Fritz G, Suter M, Weber M, Benda R, Schaller J, Feller U, Schurmann P, Schunemann V, et al.: **Plant adenosine 5'-phosphosulfate reductase is a novel iron-sulfur protein**. *J Biol Chem* 2001, **276**:42881-42886.

18. Gillum WO, Mortenson LE, Chen JS, Holm RH: **Quantitative extrusions of the Fe4S4 cores of the active sites of ferredoxins and the hydrogenase of Clostridium pasteurianum**. *J Am Chem Soc* 1977, **99**:584-595.

19. Orme-Johnson WH, Holm RH: **Identification of iron--sulfur clusters in proteins**. *Method Enzymol* 1978, **53**:268-274.

20. Volbeda A, Charon MH, Piras C, Hatchikian EC, Frey M, Fontecilla-Camps JC: **Crystal structure of the nickel-iron hydrogenase from Desulfovibrio gigas**. *Nature* 1995, **373**:580-587.

21. Noodleman L, Pique M, Roberts V: **Iron-Sulfur Clusters: Properties and Functions**. *WIley Encyclopedia of Chemical Biology* 2008:1-11.

22. Berndt C, Lillig CH, Wollenberg M, Bill E, Mansilla MC, de Mendoza D, Seidler A, Schwenn JD: **Characterization and reconstitution of a 4Fe-4S adenylyl sulfate/phosphoadenylyl sulfate reductase from Bacillus subtilis**. *J Biol Chem* 2004, **279**:7850-7855.

23. Kriek M, Peters L, Takahashi Y, Roach PL: **Effect of iron-sulfur cluster assembly proteins on the expression of Escherichia coli lipoic acid synthase**. *Protein Expres Purif* 2003, **28**:241-245.

24. Hagen WR: **EPR Spectroscopy of Iron-Sulfur Proteins**. *Adv Inorg Chem* 1992, **38**:165.

25. Beinert H, Kennedy MC, Stout CD: **Aconitase as Ironminus signSulfur Protein, Enzyme, and Iron-Regulatory Protein**. *Chem Rev* 1996, **96**:2335-2374.

26. Hong JA, Bhave DP, Carroll KS: **Identification of Critical Ligand Binding Determinants in *Mycobacterium tuberculosis* Adenosine-5'-phosphosulfate Reductase**. *J Med Chem* 2009 **52**:5485-5495.

27. Walsby CJ, Hong W, Broderick WE, Cheek J, Ortillo D, Broderick JB, Hoffman BM: **Electron-nuclear double resonance spectroscopic evidence that S-adenosylmethionine binds in contact with the catalytically active [4Fe-4S](+) cluster of pyruvate formate-lyase activating enzyme**. *J Am Chem Soc* 2002, **124**:3143-3151.

28. Davydov R, Valentine AM, Komar-Panicucci S, Hoffman BM, Lippard SJ: **An EPR study of the dinuclear iron site in the soluble methane monooxygenase from Methylococcus capsulatus (Bath) reduced by one electron at 77 K: the effects of component interactions and the binding of small molecules to the diiron(III) center**. *Biochemistry* 1999, **38**:4188-4197.

29. Lawrence CC, Bennati M, Obias HV, Bar G, Griffin RG, Stubbe J: **High-field EPR detection of a disulfide radical anion in the reduction of cytidine 5'-diphosphate by the E441Q R1 mutant of Escherichia coli ribonucleotide reductase**. *Proc Natl Acad Sci U S A* 1999, **96**:8979-8984.

30. Engstrom M, Vahtras O, Agren H: **MCSCF and DFT calculation of EPR parameters of sulfur centered radicals**. *Chamical Physics Letters* 2000, **328**:483-491.

31. Cunningham RP, Asahara H, Bank JF, Scholes CP, Salerno JC, Surerus K, Munck E, McCracken J, Peisach J, Emptage MH: **Endonuclease III is an iron-sulfur protein**. *Biochemistry* 1989, **28**:4450-4455.

32. Dos Santos PC, Dean DR: **A newly discovered role for iron-sulfur clusters**. *P Natl Acad Sci USA* 2008, **105**:11589-11590.

33. Fontecave M: **Iron-sulfur clusters: ever-expanding roles**. *Nat Chem Biol* 2006, **2**:171-174.

34. Beinert H, Holm RH, Munck E: **Iron-sulfur clusters: nature's modular, multipurpose structures**. *Science* 1997, **277**:653-659.
35. Booker SJ: **Anaerobic functionalization of unactivated C-H bonds**. *Curr Opin Chem Biol* 2009, **13**:58-73.
36. Frey PA, Hegeman AD, Ruzicka FJ: **The Radical SAM Superfamily**. *Crit Rev Biochem Mol Biol* 2008, **43**:63-88.
37. Noodleman L, Lovell T, Liu T, Himo F, Torres RA: **Insights into properties and energetics of iron-sulfur proteins from simple clusters to nitrogenase**. *Curr Opin Chem Biol* 2002, **6**:259-273.
38. Langen R, Jensen GM, Jacob U, Stephens PJ, Warshel A: **Protein control of iron-sulfur cluster redox potentials**. *J Biol Chem* 1992, **267**:25625-25627.
39. Jensen GM, Warshel A, Stephens PJ: **Calculation of the redox potentials of iron-sulfur proteins: the 2-/3-couple of [Fe4S*4Cys4] clusters in Peptococcus aerogenes ferredoxin, Azotobacter vinelandii ferredoxin I, and Chromatium vinosum high-potential iron protein**. *Biochemistry* 1994, **33**:10911-10924.
40. Ragsdale SW, Lindahl PA, Munck E: **Mossbauer, EPR, and optical studies of the corrinoid/iron-sulfur protein involved in the synthesis of acetyl coenzyme A by Clostridium thermoaceticum**. *J Biol Chem* 1987, **262**:14289-14297.
41. Weiner BE, Huang H, Dattilo BM, Nilges MJ, Fanning E, Chazin WJ: **An iron-sulfur cluster in the C-terminal domain of the p58 subunit of human DNA primase**. *J Biol Chem* 2007, **282**:33444-33451.
42. Agarwalla S, Stroud RM, Gaffney BJ: **Redox reactions of the iron-sulfur cluster in a ribosomal RNA methyltransferase, RumA: optical and EPR studies**. *J Biol Chem* 2004, **279**:34123-34129.
43. Antanaitis BC, Aisen P, Lilienthal HR, Roberts RM, Bazer FW: **The novel "g' = 1.74" EPR spectrum of pink and purple uteroferrin**. *J Biol Chem* 1980, **255**:11204-11209.
44. Saunders AH, Griffiths AE, Lee KH, Cicchillo RM, Tu L, Stromberg JA, Krebs C, Booker SJ: **Characterization of quinolinate synthases from Escherichia coli, Mycobacterium tuberculosis, and Pyrococcus horikoshii indicates that [4Fe-4S] clusters are common cofactors throughout this class of enzymes**. *Biochemistry* 2008, **47**:10999-11012.
45. Krebs C, Broderick WE, Henshaw TF, Broderick JB, Huynh BH: **Coordination of adenosylmethionine to a unique iron site of the [4Fe-4S] of pyruvate formate-lyase activating enzyme: a Mossbauer spectroscopic study**. *J Am Chem Soc* 2002, **124**:912-913.
46. Cosper MM, Jameson GN, Hernandez HL, Krebs C, Huynh BH, Johnson MK: **Characterization of the cofactor composition of Escherichia coli biotin synthase**. *Biochemistry* 2004, **43**:2007-2021.
47. Emptage MH, Kent TA, Kennedy MC, Beinert H, Munck E: **Mossbauer and EPR studies of activated aconitase: development of a localized valence state at a subsite of the [4Fe-4S] cluster on binding of citrate**. *P Natl Acad Sci U S A* 1983, **80**:4674-4678.
48. Lee KH, Saleh L, Anton BP, Madinger CL, Benner JS, Iwig DF, Roberts RJ, Krebs C, Booker SJ: **Characterization of RimO, a new member of the methylthiotransferase subclass of the radical SAM superfamily**. *Biochemistry* 2009, **48**:10162-10174.
49. Catrina I, O'Brien PJ, Purcell J, Nikolic-Hughes I, Zalatan JG, Hengge AC, Herschlag D: **Probing the origin of the compromised catalysis of E. coli alkaline phosphatase in its promiscuous sulfatase reaction**. *J Am Chem Soc* 2007, **129**:5760-5765.
50. Torres RA, Lovell T, Noodleman L, Case DA: **Density functional and reduction potential calculations of Fe4S4 clusters**. *J Am Chem Soc* 2003, **125**:1923-1936.

51. Dey KR, Wong BM, Hossain MA: **Rational design of a macrocyclic-based chemosensor for anions**. *Tetrahedron Lett* 2010, **51**:1329-1332.

52. Chapman E, Bryan MC, Wong CH: **Mechanistic studies of beta-arylsulfotransferase IV**. *Proc Natl Acad Sci U S A* 2003, **100**:910-915.

53. Cleland WW, Hengge AC: **Enzymatic mechanisms of phosphate and sulfate transfer**. *Chem Rev* 2006, **106**:3252-3278.

54. Satishchandran C, Myers CB, Markham GD: **Adenosine-5'-O-(2-fluorodiphosphate) (ADPbF), an analog of adenosine-5'-phosphosulfate**. *Bioorg Chem* 1992, **20**:107-114.

55. Williams SJ, Senaratne RH, Mougous JD, Riley LW, Bertozzi CR: **5'-adenosinephosphosulfate lies at a metabolic branch point in mycobacteria**. *J Biol Chem* 2002, **277**:32606-32615.

56. Hernick M, Fierke CA: **Catalytic mechanism and molecular recognition of E. coli UDP-3-O-(R-3-hydroxymyristoyl)-N-acetylglucosamine deacetylase probed by mutagenesis**. *Biochemistry* 2006, **45**:15240-15248.

Chapter 4

A Geometric and Electrostatic Study of the [4Fe-4S] Cluster of Adenosine-5′-Phosphosulfate Reductase from Broken Symmetry Density Functional Calculations and Extended X-ray Absorption Fine Structure Spectroscopy

This work has been published in part as "Geometric and Electrostatic Study of the [4Fe-4S] Cluster in Adenosine-5'-phosphosulfate Reductase from Broken Symmetry Density Functional Calculations and Extended X-ray Absorption Fine Structure Spectroscopy" **2011** Journal Inorganic Chemistry *50*; 6610-6625. My contribution to this work included design and construction of the model clusters for calculations, preparation of the samples for EXAFS analyses, DFT and EXAFS data analyses, and preparation of the manuscript.

4.1 Abstract

Adenosine-5'-phosphosulfate reductase (APR) is an iron-sulfur protein that catalyses the reduction of adenosine-5'-phosphosulfate (APS) to sulfite. APR coordinates to a [4Fe-4S] cluster via a conserved CC-X$_{\sim 80}$-CXXC motif and the cluster is essential for catalysis. Despite extensive functional, structural and spectroscopic studies, the exact role of the iron-sulfur cluster in APS reduction remains unknown. To gain an understanding into the role of the cluster, density functional theory (DFT) analysis and extended X-ray fine structure spectroscopy (EXAFS) have

been performed to reveal insights into the coordination, geometry and electrostatics of the [4Fe-4S] cluster. XANES data confirms that the cluster is in the $[4Fe-4S]^{2+}$ state in both native and substrate-bound APR while EXAFS data recorded at ~0.1 Å resolution indicates that there is no significant change in the structure of the [4Fe-4S] cluster between the native and substrate-bound forms of the protein. On the other hand, DFT calculations provide an insight into the subtle differences between the geometry of the cluster in the native and APS-bound forms of APR. A comparison between models with and without the tandem cysteine pair coordination of the cluster suggests a role for the unique coordination in facilitating a compact geometric structure and 'fine-tuning' the electronic structure to prevent reduction of the cluster. Further, calculations using models in which residue Lys144 is mutated to Ala confirm the finding that Lys144 serves as a crucial link in the interactions involving the [4Fe-4S] cluster and APS.

4.2 Introduction

In plants and many species of bacteria such as *Mycobacterium tuberculosis* (Mt) and *Pseudomonas aeruginosa* (Pa), *de-novo* synthesis of cysteine occurs via the sulfate assimilation pathway [1]. In this pathway, inorganic sulfate is activated to form adenosine-5′-phosphosulfate (APS), which is subsequently reduced to sulfite and then sulfide, and incorporated into cysteine [2,3]. The first committed step in sulfate assimilation is carried out by the enzyme, adenosine-5′-phosphosulfate reductase (APR), which catalyzes the reduction of APS to sulfite and adenosine-5′-monophosphate (AMP) (Scheme 4.1) using reducing equivalents from thioredoxin (Trx), a protein cofactor [1,4-6]. APR has been shown to be essential for survival of bacteria in the latent phase of tuberculosis infection [7] and since there is no human homolog of APR, it represents a promising drug target for antibacterial therapy [8].
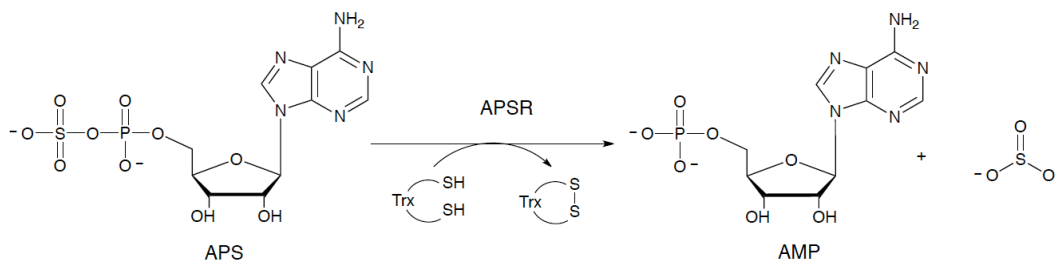
Scheme 4.1 Reaction catalyzed by APR

APRs from *M. tuberculosis* (MtAPR) and *P. aeruginosa* (PaAPR) are related by high sequence homology (27.2% of sequence identity and 41.4% of sequence similarity, Appendix 4.9.1), particularly in the residues that line the active site [9]. The mechanism of APR involves a nucleophilic attack by the catalytic Cys256 (residue numbers throughout manuscript correspond to the PaAPR sequence) in the C-terminal tail of APR on APS to form an enzyme *S*-sulfocysteine intermediate, E-Cys–S_γ–SO_3^-, which is then reduced to sulfite and AMP through intermolecular thiol–disulfide exchange with Trx (Figure 4.1) [4]. It is likely that in the initial Michaelis complex APS binds to other residues, changing their resulting mobility within the substrate-binding pocket; this could have important mechanistic implications.
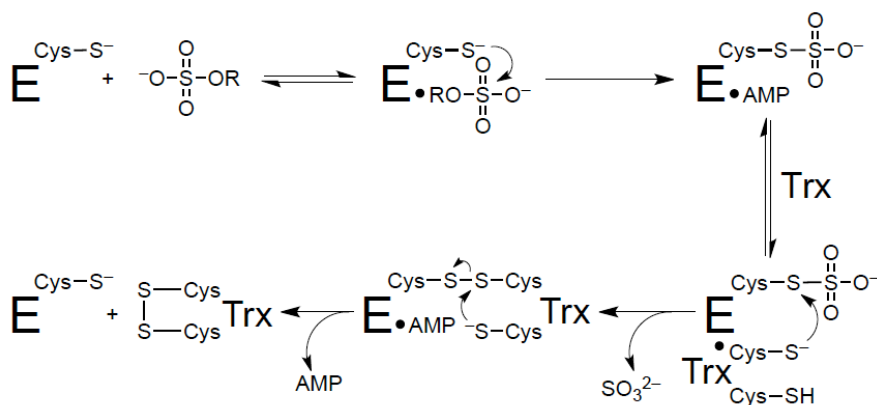
Figure 4.1. Proposed mechanism of APR. APR reduces adenosine 5'-phosphosulfate (APS) to sulfite and adenosine 5'-monosulfate (AMP) using reducing equivalents from the protein cofactor, thioredoxin (Trx).

From a structural perspective, APR is an iron-sulfur protein with a conserved CC-X$_{\sim 80}$-CXXC motif, correlated with the presence of a [4Fe-4S] cluster. The cluster has been shown to be essential for catalytic activity in both plant and bacterial APRs [3,10-12], but the exact role of the cluster in APS reduction remains unknown. Interestingly, studies by Carroll *et al.* have shown that the [4Fe-4S]$^{2+}$ cluster in APR does not undergo redox changes during the catalytic cycle [4]. The 2.7 Å crystal structure of PaAPR bound to substrate [13] shows the iron-sulfur cluster coordinated by Cys228 and Cys231, positioned at the tip of a β-loop, and a special tandem pair, Cys139 and Cys140 within a kinked helix, α$_6$ (Figure 4.2a). Helix α$_6$ is kinked where Lys144 is oriented into the active site. Amongst interactions of the cluster, there are four charged and/or polar NH···S or OH···S hydrogen bonds involving side chains of
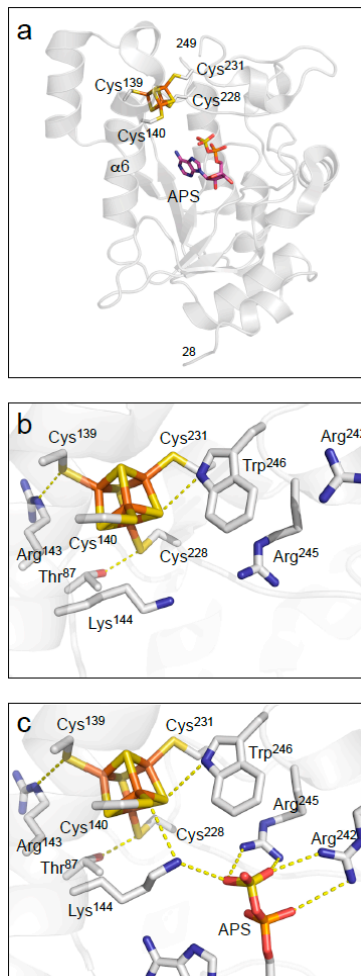
Figure 4.2 Environment of the [4Fe-4S] cluster in PaAPR (Bhave, 2011). a. The structure of PaAPR bound to substrate APS (subunit B or chain-B). The [4Fe-4S] cluster is ligated by four cysteine residues at positions 139, 140, 228 and 231. PDB code: 2GOY. b. Three conserved residues participate in charged or polar NH···S or OH···S hydrogen bonds to inorganic S or cysteine Sγ atoms; Thr87, Arg143, and Trp246 (yellow dashes). PDB code: 2GOY, chain A. c. Conserved basic residues Lys144, Arg242 and Arg245 in the active site interact with the phosphate and sulfate groups of APS (yellow dashes). In the presence of APS, Lys144 makes a NH···S hydrogen bond to the Cys140-Sγ atom. Residues that also interact with APS, but are not depicted in this figure are Arg171 and His259; these residues interact with the α-phosphate group. The shortest distance between a sulfate oxygen atom and a cysteine sulfur atom coordinated to the [4Fe-4S] cluster is 6.0 Å. PDB code: 2GOY, chain B.

absolutely conserved residues (Figure 4.2b and c). The CysCys motif interacts with a pair of

basic residues, Arg143 and Lys144. In addition, Cys140 hydrogen bonds to His136. Other

interactions with the iron-sulfur cluster involve the side chains of Thr87 and Trp246. The

phosphosulfate group of APS is positioned at a distance of approximately 7 Å to the iron site,

which coordinates to S_γ-Cys140, and as such, the sulfate moiety is not in direct contact with the

[4Fe-4S] cluster. Interestingly, however, both cluster and substrate interact with Lys144 (Figure

4.2c).

Coordination by sequential cysteines is highly unusual for [4Fe-4S] clusters and has been

characterized in only one other crystal structure – the NuoB subunit of respiratory complex I

[14]. The tandem cysteines also reside within an α-helix and the subunit of NuoB exhibits

substrate-induced conformational changes [15]. In APR, constraints imposed by the tandem

cysteine coordination do not affect the tetrahedral symmetry of the cluster, but the side chain

of Cys140 is distorted, resulting in steric clashes between the C_α proton and an inorganic sulfur

atom of the cluster [13].

In addition to the structural information available, based on differences in cysteine reactivity

and cluster stability, biochemical and mass spectrometric studies with MtAPR have suggested a

structural rearrangement in the *S*-sulfocysteine complex and AMP-bound enzyme relative to

free enzyme [16]. In fact, solution kinetics and mass spectrometric studies of MtAPR performed

with APS (at concentrations exceeding the K_d of APS and AMP), have shown that the subsequent

formation of the stable E-Cys–S_γ–SO_3^- intermediate with AMP-bound and C-terminal tail docked

in the active site, prevents cluster degradation and loss of APR activity [4,9,16]. Furthermore, a

comparison of Resonance Raman spectra of PaAPR in the native form and in the *S*-sulfocysteine

form (with AMP bound and the C-terminal tail docked in the active site of the enzyme) shows an enhancement in Fe-S$_i$(Cys) stretching modes centered near 355 and 369 cm^{-1} [17]. Recently, we demonstrated that APS binding induced an increase in intensity and resolution of the EPR signal of reduced MtAPR that was not observed among a panel of substrate analogs, including adenosine 5′-diphosphate. Additionally, through kinetic and EPR studies, Lys144 was identified as a key link between APS and the iron-sulfur cluster [18]. Mössbauer analyses of native MtAPR confirmed the presence of a [4Fe-4S]$^{2+}$ cluster, however, no change was observed in the Mössbauer spectra of MtAPR comparing samples with and without substrate-binding. Spectroscopic data taken together with known structural and functional information, implicate the iron-sulfur cluster in the catalytic mechanism of APS reduction.

The goal of this study is to determine high-resolution geometric and electronic structures of the [4Fe-4S] cluster in APR. Although the crystal structure of PaAPR is a significant advance in the characterization of this enzyme, the resolution of the structure (2.7 Å) is close to the Fe-Fe distance within a [4Fe-4S] cluster [19], placing a significant limit on the structural features that can be visualized in electron density maps calculated using the X-ray data. Given the unique coordination of the [4Fe-4S] cluster by two consecutive cysteines, it is important to obtain direct confirmation of the apparent structure. In particular, the X-ray structure shows that torsion angles of the Cys139 and Cys140 side chains are significantly strained, which could affect details of Fe-Fe and Fe-S-(S$_γ$) distances in various states of the catalytic cycle [13]. EPR studies on one-electron reduced MtAPR demonstrate mid-range electrostatic interactions involving the cluster, Lys144 and the substrate that implicate the cluster in catalysis [18]. However, changes in the geometric and electronic structure of the cluster during catalysis have not been determined by

any structure determination technique. Determining these high-resolution structures will ultimately further our understanding of the role of the iron-sulfur cluster in APS reduction.

The work described here combines Fe K-edge x-ray absorption spectroscopy investigations (both extended X-ray absorption fine structure, EXAFS, and X-ray absorption near-edge structure, XANES) with density functional theory (DFT) calculations to determine the local geometric structure, spin states, electrostatic potential charges, and ^{57}Fe Mössbauer properties of the [4Fe-4S] cluster of APR. XANES data confirms that the cluster is in the [4Fe-4S]$^{2+}$ state in native MtAPR (Figure 4.3a) and that there is no detectable change in structure when APS binds. EXAFS data recorded at ~0.1 Å resolution (k = 17 Å^{-1}) (Figure 4.3b) indicates

Figure 4.3 XAS analysis of MtAPR. a. Iron K-edge XANES spectrum. b. k^3 weighted EXAFS (inset) and Fourier transform calculated over a range of k = 2.35 ~ 17 Å^{-1}.

that there is no significant change in the average Fe-S and Fe-Fe bond lengths of the [4Fe-4S] cluster between the native and substrate-bound forms of the protein (see Appendix 4.9.2 for comparison spectra). Since the EXAFS structure reflects the average over all four irons in the cluster, it is insensitive to changes at individual sites (e.g., a decrease in one Fe-Fe distance that is compensated by an increase in a second Fe-Fe distance). To explore these changes, DFT calculations starting from the experimental X-ray structure of PaAPR [13] were used to provide

insight into the subtle changes within the geometric and electronic structure of the cluster and how they relate to the role of the [4Fe-4S] cluster in the mechanism of APS reduction.

4.3 Quantum Cluster Models for DFT Calculations

4.3.1   Wild-Type Models with and without Substrate. The initial geometries for DFT calculations of the wild type APR active site models including the [4Fe-4S] cluster were taken from the X-ray crystal structure (2GOY.pdb, 2.7 Å resolution) of PaAPR [13]. PaAPR was serendipitously crystallized such that density for APS was observed in two of the four monomeric subunits. Thus the differentially occupied subunits could be used to compare the
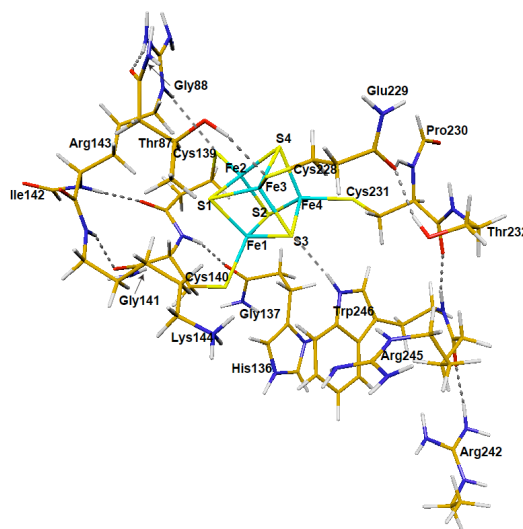
Figure 4.4 DFT optimized quantum cluster model of the [4Fe-4S] center in APR without APS. Initial geometry was taken from chain-A of the X-ray crystal structure (PDB code: 2GOY) (Chartron, 2006).

geometry and electronic structure of the [4Fe-4S] cluster in the free and substrate-bound forms of the protein. The cluster without APS was taken from subunit A (or chain-A) of the crystal structure (Figure 4.4). A closer look at the [4Fe-4S-4Cys] center is shown in Figure 4.5. The quantum cluster of the active site with APS was taken from chain-B of the crystal structure (Figure 4.6). The main or side chains of Cys139, Cys140, Cys228, Cys231, Thr87, His136, Arg143, Lys144, Arg242, Arg245, and Trp246 were also included in the quantum models. To facilitate calculations by minimizing the number of atoms in the model, some changes were made to the residues, including cleavage of certain bonds, addition of link-H atoms [20] and partial inclusion of neighboring residues to have closed valence. Explicitly, for Thr87, Cys139, His136 and Cys228,

C_α-NH was replaced with C_α-H. Since the electron density map shows δ^+ density on His136, the His136 side chain was protonated in our calculations. For Gly88, Gly137, Gly141, and Glu229, HN-C_α was included into the quantum cluster and C_α was replaced with H.
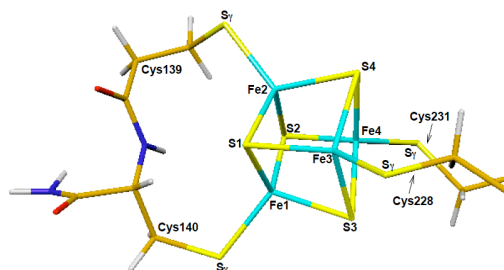
Figure 4.5 A closer look of the [4Fe-4S] center and the atom labels with the four cysteine side chains.

For Ile142 and Pro230, C_α-C=O was included in the cluster and C_α was replaced with H. For Lys144 and Thr232, C_α-C=O was replaced with C_α-H. For Arg242 and Arg245, C_γ-C_β was replaced with C_γ-H. Finally for Trp246, HN-C_α-C=O was replaced with H-C_α-H.
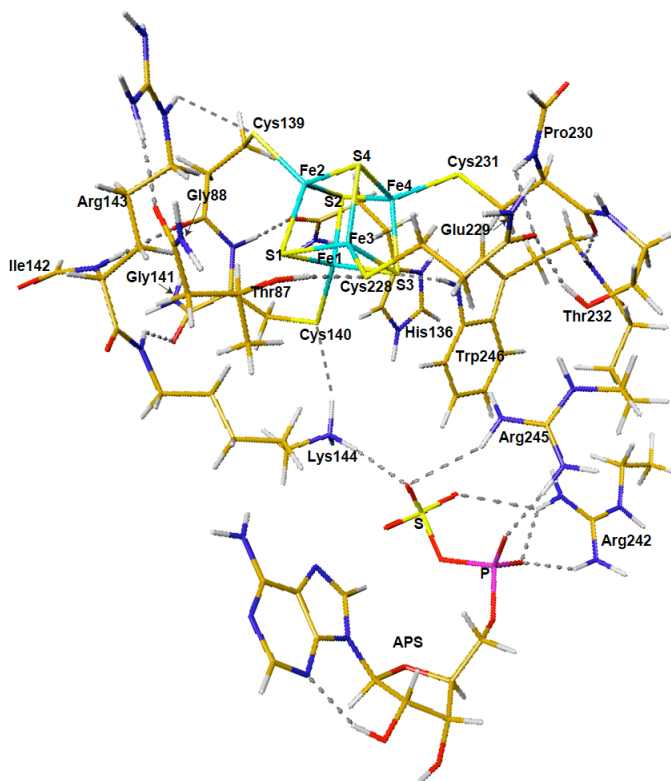
Figure 4.6 DFT optimized quantum cluster model of the [4Fe-4S] center in APR with APS. Initial geometry was taken from chain-B of the X-ray crystal structure (PDB code: 2GOY) (Chartron, 2006).

The following three H-bonds are found in the crystal structure between the inorganic S's and S_γ's of the [4Fe-4S-4Cys] cluster and the protein residues in both chain-A and chain-B: $S3\cdots HN_{\epsilon 1}$-Trp246, Cys139-$S_\gamma\cdots HN_\epsilon$-Arg143, and Cys228-$S_\gamma\cdots HO_{\gamma 1}$-Thr87. In chain-B where APS is bound, the side chain of Lys144 H-bonds with both S_γ-Cys140 and O from the sulfate group of APS. Model cluster for chain-A (Figure 4.4) has eleven H-bonds and a total of 211 atoms. By contrast, model cluster for chain-B (Figure 4.6) has eighteen H-bonds (of which, 7 involve the substrate) and a total of 250 atoms. Without APS, the Arg242 side chain H-bonds with the main chain -C=O group of Arg245 (chain-A, Figure 4.4). In the presence of APS, Arg242 rotates to form H-bonds with the phosphate and sulfate groups of APS. Arg245 also H-bonds with APS (chain-B, Figure 4.6).

4.3.2 No-Tandem Models. Since coordination by sequential cysteines in PaAPR is highly unusual for [4Fe-4S] clusters, it is valuable to determine what changes would occur in the geometric and electronic structure of the cluster if we break the linkage between Cys139 and Cys140. For this purpose, two "no-tandem" computational models were constructed by breaking the HN-CO peptide bond between Cys139 and Cys140 in both chain-A (without APS)
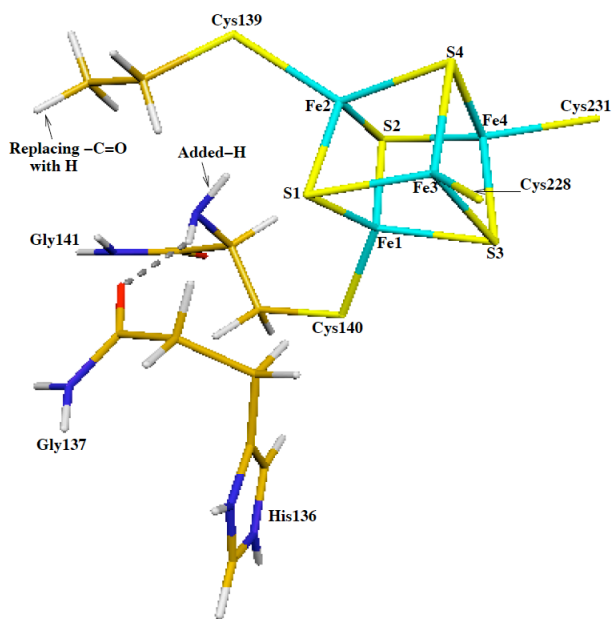
Figure 4.7 The no-tandem model cluster. The HN-CO peptide bond between Cys139 and Cys140 was cut in order to study the "no-tandem" structures in both chain-A (without substrate) and chain-B (with substrate). The -CO group of Cys139 was replaced by hydrogen, meanwhile hydrogen was added to the -NH group of Cys140 to fill the open valence.

and chain-B (with APS). The −C=O group of Cys139 was replaced by a hydrogen (Figure 4.7), meanwhile a hydrogen was added to the −NH group of Cys140 to fill the open valence. In the absence of the peptide bond, the number of atoms in each of the model clusters remained constant.

4.3.3   K144A Models.   As previously mentioned, there is biochemical and spectroscopic evidence to show that the stability and microenvironment of the cluster in APR changes upon substrate binding [4,16,21]. This indicates that APS does interact with the [4Fe-4S] cluster, not by direct contact, but via a network of electrostatic interactions. Lys144, Arg242, and Arg245 all have H-bonding interactions with APS, of which Lys144 is positioned between the [4Fe-4S] cluster and APS. Therefore we constructed the K144A models (for both chain-A and chain-B) by replacing Lys144 with Ala in order to investigate changes in the properties of the [4Fe-4S] cluster without Lys144. Explicitly, the C_{β}-C_{γ} bond of Lys144 was cut and a proton was added to C_{β} to close valence, resulting in a total of 199 and 238 atoms in the chain-A and chain-B models respectively.

4.4 Computational Methodology

All density functional spin-unrestricted calculations were performed using the Amsterdam Density Functional (ADF) package [22-24] with the OLYP functional. OLYP is the combination of Handy's optimized exchange (OPTX) [25] and LYP correlation [26]. Swart *et al.* have tested different functionals in calculating the atomization energies for the G2-set of up to 148 molecules, six reaction barriers of S_N2 reactions, geometry optimizations of 19 small molecules and 4 metallocenes, and zero-point vibrational energies for 13 small molecules [27]. Their examination shows that the OPTX containing functionals perform better than the regular general gradient approximation functionals (GGAs) like PBE [28,29], BLYP [26,30], and BP [30-32]. For organic systems, OLYP has been shown to function as well as the hybrid functional B3LYP [27,33]. Recently, Hopmann *et al.* reported that for [57]Fe Mössbauer isomer shift

calculations, the OLYP potential performs comparably well for iron nitrosyls and for iron complexes in general [34].

The resting state of the [4Fe-4S] core in APR has +2 charge, $[Fe_4S_4]^{2+}$. The core plus the four Cys side chains has a net charge of -2, $[Fe_4S_4(S_\gamma\text{-}Cys)_4]^{2-}$. Therefore each of the four equivalent iron sites has a 2.5+ oxidation state [19,35]. The antiferromagnetically (AF) coupled $S_{total} = 0$ ground state requires two mixed valence iron pairs with opposite spins. The combinations of the spin states can be: {Fe1↑Fe2↓Fe3↑Fe4↓}, {Fe1↑Fe2↓Fe3↓Fe4↑}, and {Fe1↑Fe2↓Fe3↑Fe4↓}, where "↑" and "↓" represent spin up and down, respectively. As in previous work, we perform "broken-symmetry" (BS)[42-44] calculations to represent the AF-coupled spin states. First we construct a ferromagnetically (F) spin-coupled ($S_{total} = 18/2$) determinant, where the spins on the four irons are aligned in a parallel fashion. Then we rotate the spin vector located on two of the iron sites by interchanging the α and β fit density blocks on the two sites from the output file TAPE21 created by this F-coupled calculation in ADF to get the starting spin density for the $S_{total} = 0$ state. These BS states are not pure $S_{total} = 0$ states. Instead, these states (and their energies) are weighted averages of the pure spin states, strongly weighted toward the lower S_{total} states based on the spin coupling algebra [19,35-38]. We have not included spin projection corrections in the current work since we have estimated that these will make very small differences in the DFT calculated relative energies of different states.

4.4.1 Geometry Optimization. To determine which one of the three spin states of the [4Fe-4S] cluster in APR has the lowest energy and is geometrically closest to the X-ray crystal structure, we geometry optimized the active site clusters taken from chain-A (without substrate binding) and chain-B (with substrate binding) in the {Fe1↑Fe2↓Fe3↑Fe4↓}, {Fe1↑Fe2↓Fe3↓Fe4↑}, and

{Fe1ᐟFe2ᐟFe3ᐟFe4} three BS spin states. All calculations were performed within the conductor-like screening (COSMO) [39-42] solvation model with dielectric constant ε = 20. In COSMO, the quantum cluster is embedded in a molecular shaped cavity surrounded by a continuum dielectric medium. There is no universal dielectric constant for COSMO-like solvation calculations. Although the dielectric value ε = 4 is commonly used for the protein interior, since this is the value for the dielectric constants of crystalline and polymeric amides [43] and dry protein and peptide powders [44-47], many studies show that higher effective dielectric constant values (4-30) for protein interiors are needed in reproducing the pK_a values of certain internal ionizable groups [47-54]. For the current study, since many charged groups are in the quantum cluster, a larger dielectric constant (ε = 20) was chosen for the COSMO calculations. The van der Waals radii for atoms Fe, C, S, P, O, N, and H were taken as 1.5, 1.7, 1.8, 1.8, 1.4, 1.55, and 1.2 Å, respectively [55,56]. The probe radius for the contact surface between the cluster and solvent was set to 2.0 Å. The triple-z (TZP) (for Fe and S) and double-z (DZP) (for other atoms) polarization Slater-type basis sets with frozen cores (C(1s), N(1s), O(1s), S(1s,2s,2p), P(1s,2s,2p), and Fe(1s,2s,2p) are frozen) were applied for geometry optimizations. To partially apply the strain from the protein environment, C$_\alpha$ atoms on Lys144, Thr232, Arg245, and Trp246, C$_\gamma$ of Arg242, and the link-H atoms on Thr87, Gly88, His136, Gly137, Cys139, Gly141, Ile142, Lys144, Cys228, Glu229, Pro230, Thr232, Arg242, Arg245, and Trp246, were fixed during geometry optimizations. The broken-symmetry state energies obtained after COSMO geometry optimizations were used to compare the relative energies in Section 6.

4.4.2 Mössbauer Isomer Shift and Quadrupole Splitting Calculations. For all models, we applied single-point Mössbauer isomer shift and quadruple splitting calculations at the optimized geometries using all-electron (i.e. without frozen core approximation) all TZP Slater-

type basis sets. First, a high-spin F-coupled single-point energy calculation was performed at the BS optimized geometry. Its TAPE21 file was then modified accordingly by interchanging the α and β fit density blocks on two of the iron sites. Starting from the modified TAPE21, a BS state single-point energy calculation in COSMO again with all-electron TZP Slater-type basis sets was performed to obtain the electron density ($\rho(0)$) and the electric field gradient (EFG) at the Fe nucleus.

The Mössbauer isomer shifts d were calculated based on $\rho(0)$:

$$\delta = \alpha(\rho(0) - A) + C \tag{1}$$

where $A = 11877$ is a constant. Our previous isomer shift fit based on 19 $Fe^{2.5+,3+,3.5+,4+}$ complexes (30 distinct iron sites) using OLYP/all-electron-TZP method (with INTEGRATION = 4.0) yielded: a = -0.307 and $C = 0.385$ mm s^{-1} [57]. The numerical integration accuracy parameter INTEGRATION = 4.0 is also used for the current calculations.

For calculating the Mössbauer quadrupole splittings (ΔE_Q), the EFG tensors V were diagonalized and the eigenvalues were reordered so that $|V_{zz}| \geq |V_{xx}| \geq |V_{yy}|$. The asymmetry parameter η is defined as

$$\eta = |(V_{xx} - V_{yy})/V_{zz}| \tag{2}$$

Then the ΔE_Q for ^{57}Fe of the nuclear excited state ($I = 3/2$) can be calculated as

$$\Delta E_Q = (\tfrac{1}{2})eQV_{zz}(1 + \eta^2/3)^{\frac{1}{2}} \tag{3}$$

where e is the electrical charge of a positive electron, Q is the nuclear quadrupole moment of Fe. We had used $eQ = 0.15$ electron-barn [58] in our previous publications. For the current study, we applied a slightly different $eQ = 0.158$ electron-barn taken from the careful quantum chemical calculations (non-relativistic) by Neese's group [59].

4.4.3 Fitting Atomic Charges from Electrostatic Potentials (ESP). A modified version of CHELPG code [35,60] was used to fit the atomic point charges from the molecular electrostatic potentials (ESP) obtained from the final all-electron all-TZP single-point energy calculations. The singular value decomposition (SVD) method [35] was introduced into the code to minimize the uncertainties in the fitting procedure. The total net charge and the three Cartesian dipole moment components of each cluster were used as constraint conditions for the fit. The fitted points lay on a cubic grid between the van der Waals radius and the outer atomic radius with a grid spacing of 0.2 Å. The outer atomic radius (5.0 Å here for all atoms) defines the outer boundary of the electrostatic potential that was used in the charge fitting. The same van der Waals radii were used as in COSMO calculations.

4.5 X-ray Absorption Spectroscopy (XAS) Results and Discussion

To probe the coordination and geometry of the [4Fe-4S] cluster in APR we examined MtAPR by XAS. To facilitate EXAFS analyses, monomeric MtAPR was used instead of PaAPR since PaAPR purifies as a tetramer. In order to determine the effect of APS binding on Fe-site structure, MtAPR was incubated with a 3-fold stoichiometric excess of APS, at a concentration exceeding the k_d of APS and AMP (0.2 μM and 5.4 μM respectively [9]). Therefore, the form of MtAPR in EXAFS experiments was the *S*-sulfocysteine state with AMP bound and the C-terminal docked in the active site (closed state). By contrast, for crystallization of PaAPR, ~60-fold excess of APS over enzyme was added and the stable form that crystallized was formed with the C-terminal tail out of the active site (open state) (see Figure 4.6c in ref [13])

4.5.1 Fe K-Edge XAS. The normalized Fe K-edge XANES spectrum of APR is shown in Figure 4.3. This region of the XAS spectra (1s → 3d transitions) provides valuable information about metal

ion coordination number and oxidation state [61]. The Fe pre-edge area calculated for APR (~18 × 10^{-2} eV) is consistent with a four-coordinate Fe species. This conclusion is supported by Mössbauer studies for native MtAPR which confirm the presence of a $[4Fe-4S]^{2+}$ cluster [18]. The pre-edge feature observed at ~7112 eV occurs due to an electronic dipole-forbidden quadrupole-allowed transition from the Fe 1s orbital to valence orbitals with significant Fe 3d character [61,62]. The increase in intensity of this formally forbidden transition is a result of mixing of Fe 4p-3d orbitals caused by deviation of the absorbing Fe center from centrosymmetry [63]. To investigate changes in cluster geometry and coordination during catalysis, MtAPR was incubated with APS to form the S-sulfocysteine intermediate with AMP bound in the active site and XAS was recorded for this stable conformation of the enzyme (Table 4.1, Appendix 4.9.2). No shift in position or intensity of the pre-edge energy was observed for the MtAPR S-sulfocysteine intermediate, indicating that the level of 4p mixing is identical to native MtAPR. Since the 1s → 3d transition is very sensitive to local Fe-site structure, this is a sensitive indication that not only is there no change in oxidation state or coordination number, but there is unlikely to be more than a very small change in geometry of the Fe in the [4Fe-4S] cluster between the native and S-sulfocysteine intermediate forms of MtAPR.

4.5.2 EXAFS. The EXAFS data for MtAPR, reported at high-resolution to k ~ 17 $Å^{-1}$ was shown in Figure 4.3 (inset). . The pattern in the data reflects the fact that there are at least two shells of scatterers, sulfur and iron, significantly contributing to the EXAFS spectrum. The Fourier transform (FT) of MtAPR (Figure 4.3, Table 4.1) shows an intense first-shell Fe-S interaction at 2.3 Å and a slightly less intense second-shell Fe-Fe interaction at 2.73 Å. For this k range, resolution in R space is ~0.1 Å, meaning that if the Fe-Fe or Fe-S distances differed by > 0.1 Å they should, in principle, be resolvable, and that if the distances differ by > ~0.12 Å they should

be readily resolvable into two different shells of scatterers (Two Fe-Fe distances that differed by 0.12 Å would show a "beat" in the EXAFS at $\sim k$ = 13 Å^{-1} which would be readily detectable). No improvement was seen for multiple shell fits.

Table 4.1 Extended x-ray absorption fine structure (EXAFS) curve-fitting parameters for Fe K-edge[a]

Sample	Interaction	N	R (Å)	$\sigma^2 \times 10^3$	F
MtAPR	Fe-S	4*	2.297	3.9	1.93
sample 1	Fe-Fe	3*	2.726	2.4	
	Fe-S	3.9	2.297	3.8	1.92
	Fe-Fe	2.1	2.726	2.7	
MtAPR	Fe-S	4*	2.294	3.9	1.92
sample 2	Fe-Fe	3*	2.729	2.0	
	Fe-S	3.7	2.294	3.4	1.86
	Fe-Fe	1.7	2.729	1.3	
MtAPR + APS [b]	Fe-S	4*	2.298	3.9	1.28
sample 1	Fe-Fe	3*	2.728	2.2	
	Fe-S	3.8	2.298	3.6	0.93
	Fe-Fe	2.0	2.728	2.2	
MtAPR + APS [b]	Fe-S	4*	2.297	3.8	1.48
sample 2	Fe-Fe	3*	2.730	2.5	
	Fe-S	3.6	2.297	3.4	1.44
	Fe-Fe	1.8	2.730	2.0	

[a]Coordination Number (N), Interatomic Distances (R), Mean-Square Deviations in Interatomic Distance (σ^2, Å^2), Fit-Error Function (F) is Defined as $<\{\Sigma k^6 (\chi_{calc*} - \chi_{expt})^2 / \Sigma \chi^2_{expt}\}^{1/2}>$. For MtAPR the k Range was 2.35 ~ 17 (Filtered R = 1.2 ~ 3); for MtAPR + APS the k Range was 2.15 ~ 17 (Filtered R = 1.2 ~ 3); giving resolution ~ 0.1 Å and ~17 independent degrees of freedom. Fits are shown both for fixed (marked with *) and variable N. [b]The enzyme was in the S-sulfocysteine state with AMP bound and the C-terminal docked in the active site.

It is possible, of course, that there are not two, but up to six different Fe-Fe distances (Note that if there were significant disorder, with multiple forms of the Fe/S cluster, this could increase further the number of Fe-Fe distances. This is ruled out by the absence of disorder in the Mössbauer spectra). In this case, individual Fe-Fe distances might not be resolvable. However, if this were the case, there would be an increase in the Debye-Waller factor. However, the observed Debye-Waller factors are small, indicating that there is, at most a very small (< 0.12 Å)

spread in Fe-Fe distance, consistent with the spread in Fe-Fe distances that is found in the DFT calculations (Tables 4.2 and 4.3).

If the experimental Fe-Fe σ^2 value of ~2.5×10^{-3} Å^2 is attributed solely to static disorder and if the most asymmetric possible distribution of Fe-Fe distances is assumed (i.e., 5 short and 1 long distance), the spread in Fe-Fe distances is ~$\sqrt{6}\,\sigma = 0.12$ Å.   A more reasonable estimate would recognize that the experimental σ^2 is the sum of σ^2_{vib} and σ^2_{static}. The former can be estimated from the fitted σ^2 value for *Pyrococcus furiousus* ferredoxin, 2.0×10^{-3} Å^2.   If this is attributed to vibrational motion, the apparent σ^2_{static} is 5.0×10^{-4} Å^2, suggesting a spread in Fe-Fe distances of ~0.05 Å.   While the true spread in Fe-Fe distances will depend on details of the distribution in Fe-Fe distances and the vibrational contribution to σ^2, it should be between these limits.

Coordination numbers were initially constrained to the chemically correct values (4 Fe-S and 3 Fe-Fe).   These gave excellent fits.   Modest improvement in fit quality was possible if the coordination number was allowed to vary; this improvement is consistent with that expected for a 50% increase in variable parameters.   To confirm that these data are consistent with a [4Fe-4S] cluster, we compared the EXAFS and FT of MtAPR with those previously reported data for *Pyrococcus furiosus* ferredoxin containing either an [3Fe-4S] cluster or a [4Fe-4S] clusters *(data provided by Prof. G.N. George, University of Saskatoon).* Appendix 4.9.3 unambiguously shows that the EXAFS spectrum for MtAPR is in good agreement with the spectrum for the [4Fe-4S] cluster in ferredoxin, albeit with a slightly less intense Fe-Fe peak, suggesting somewhat larger disorder in the Fe-Fe scattering in MtAPR, consistent with the fitting results.

The EXAFS spectrum and FT of the MtAPR S-sulfocysteine intermediate are identical to those of native MtAPR, and the Fe-S and Fe-Fe bond lengths remain consistent (Table 4.1, Appendix 4.9.2b and c). Although the accuracy of EXAFS bond-lengths is generally taken as ~0.02 Å, the precision is much better. We have found previously that the precision of biological EXAFS data is ~0.003 Å^2 [64]; this is reflected in the excellent reproducibility of the duplicate samples in Table 4.1. This precision, together with the invariance seen in Table 4.1, indicates that the average core structure of the [4Fe-4S] cluster in MtAPR is unaffected in the S-sulfocysteine conformation of the protein. Since XAS spectra reflect bond-lengths that are averaged over all the atoms in the cluster, it is in principle possible that small changes at one site could be compensated by equal but opposite changes at another site, such that the average distances remain the same. To probe these changes at high resolution, density functional theory calculations were undertaken.

4.6 DFT Calculation Results and Discussion

4.6.1 Calculating Results for Wild-Type [Fe$_4$S$_4$(S$_\gamma$-Cys)$_4$]$^{2-}$ Models. The main calculated properties for different spin states of the wild-type [4Fe-4S] cluster without and with the substrate are given in Tables 4.2 and 4.3, respectively. The calculated Fe-Fe and Fe-S distances and ^{57}Fe Mössbauer isomer shifts and quadrupole splittings are compared with available experimental results [18].

As previously reported [19,35], each of the optimized [Fe$_4$S$_4$(S$_\gamma$-Cys)$_4$]$^{2-}$ clusters has a compression structure with four "short" (~2.2 Å) and eight "long" (~2.3 Å) Fe-S distances. The two irons with the same spin direction are in an Fe$_2$S$_2$ rhomb distorted butterfly "plane" with four "long" Fe-S distances, and the four Fe-S bonds between the two "planes" have "short"

distances. Taking the {Fe1↓Fe2↓Fe3↑Fe4↑} state in Table 4.2 (without APS binding) as an example, Fe1 and Fe2 (spin down) are on the plane containing Fe1-S1-Fe2-S2, and Fe3 and Fe4 (spin up) are on the plane with Fe3-S3-Fe4-S4. As a result, the eight Fe-S bond lengths on the two planes are long (in average 2.32 Å), and the four Fe1-S3, Fe2-S4, Fe3-S1, and Fe4-S2 bonds between the two planes are shorter (in average 2.23 Å). Overall, the spread of the DFT calculated Fe-S (2.20-2.34 Å) and Fe-Fe (2.65-2.76 Å) distances agree with the EXAFS's results of ~2.3±0.1 Å and ~2.7 ±0.1 Å, respectively. Since the PaAPR crystal structure was solved at 2.7 Å resolution [13], the compression structure for the [4Fe-4S] cluster is not obvious in either chain-A (without APS binding) or chain-B (with APS binding). It is also not reliable to determine the spin state of the cluster based on the comparison between the calculated geometries and the crystal structure. Since the {Fe1↓Fe2↓Fe3↑Fe4↑} state yields the lowest broken-symmetry energy in both chain-A and chain-B, it is likely that the $[Fe_4S_4(S_\gamma\text{-}Cys)_4]^{2-}$ cluster of PaAPR is in the {Fe1↓Fe2↓Fe3↑Fe4↑} state before and after substrate binding.

In the presence of APS, the calculated distances of Fe1-Fe2 and Fe3-Fe4 are increased by 0.06 Å; the four "short" distances (Fe1-S3, Fe2-S4, Fe3-S1, and Fe4-S2) between the two planes "Fe1-S1-Fe2-S2" and "Fe3-S3-Fe4-S4" are shortened by 0.02 Å on average. Since the thiolate of Cys140 now has a direct H-bonding interaction with the Lys144 side chain (Figure 4.6), the Fe1-S_γ-Cys140 bond is increased by 0.06 Å, and it becomes the longest among the four Fe-S_γ-Cys bonds. The elongation of the Fe1-S_γ-Cys140 distance may explain the marked change in Fe-S_γ stretching modes observed in the Resonance Raman spectra of PaAPR upon APS binding [17].

Table 4.2 DFT results for Chain-A without APS. Fe-Fe and Fe-ligand bond lengths (Å), broken-symmetry state energies (E, eV), Fe net spin populations (NSP), and Mössbauer properties (isomer shifts δ, quadrupole splittings ΔE_Q, mm s^{-1}, and η) of the resting state [Fe$_4$S$_4$(S$_\gamma$-Cys)$_4$]$^{2-}$ cluster in wild-type PaAPR without substrate binding: comparison between calculations and experiments (Exp).

	Calculated Chain-A without APS			Exp [a]
	Fe1 Fe2 Fe3 Fe4	Fe1 Fe2 Fe3 Fe4	Fe1 Fe2 Fe3 Fe4	
Fe1-Fe2	2.685	2.700	2.651	2.7
Fe1-Fe3	2.657	2.687	2.662	2.7
Fe1-Fe4	2.707	2.742	2.724	2.7
Fe2-Fe3	2.758	2.963	2.767	2.7
Fe2-Fe4	2.684	2.711	2.750	2.8
Fe3-Fe4	2.646	2.671	2.663	2.8
Fe1-S1	2.309	2.219	2.291	2.2
Fe1-S2	2.323	2.305	2.222	2.2
Fe1-S3	2.232	2.299	2.300	2.2
Fe2-S1	2.339	2.349	2.259	2.3
Fe2-S2	2.293	2.191	2.290	2.3
Fe2-S4	2.269	2.341	2.335	2.2
Fe3-S1	2.211	2.293	2.286	2.3
Fe3-S3	2.313	2.229	2.309	2.3
Fe3-S4	2.330	2.345	2.255	2.3
Fe4-S2	2.201	2.267	2.287	2.3
Fe4-S3	2.314	2.306	2.238	2.3
Fe4-S4	2.322	2.247	2.321	2.3
Fe1-S$_\gamma$-Cys140	2.249	2.270	2.333	2.3
Fe2-S$_\gamma$-Cys139	2.311	2.312	2.267	2.3
Fe3-S$_\gamma$-Cys228	2.301	2.325	2.292	2.3
Fe4-S$_\gamma$-Cys231	2.277	2.298	2.324	2.3
E	-1193.735	-1193.369	-1193.532	
NSP(Fe1, Fe2, Fe3, Fe4)	(-3.11, -3.18, 3.16, 3.11)	(3.12, -3.17, -3.17, 3.14)	(3.10, -3.18, 3.20, -3.15)	
δ(Fe1, Fe2, Fe3, Fe4)	(0.43, 0.48, 0.45, 0.44)	(0.42, 0.46, 0.46, 0.44)	(0.39. 0.46, 0.43, 0.43)	0.45 [18]
Average δ	0.45	0.45	0.43	
ΔE_Q(Fe1, Fe2, Fe3, Fe4)	(1.17, 1.01, 0.80, -1.01)	(0.95, 1.20, 1.20, 0.78)	(0.91, 0.99, 1.04, 1.32)	1.09 [18]
Average $\lvert\Delta E_Q\rvert$	1.00	1.03	1.07	
η(Fe1, Fe2, Fe3, Fe4)	(0.48, 0.62, 0.65, 0.92)	(1.00, 0.31, 0.24, 0.77)	(0.96, 0.46, 0.55, 0.35)	

[a]The crystal structure of PaAPR was at 2.7 Å resolution, PDB code: 2GOY (Chartron, 2006). Distances are taken from chain-A without substrate binding.

Table 4.3 DFT results for Chain-B with APS. Fe-Fe and Fe-ligand bond Lengths (Å), broken-symmetry state energies (E, eV), Fe net spin populations (NSP), and Mössbauer properties (isomer shifts δ, quadrupole splittings ΔE_Q, mm s^{-1}, and η) of the resting state $[Fe_4S_4(S_r\text{-}Cys)_4]^{2-}$ cluster in wild-type PaAPR with substrate binding: comparison between calculations and experiments (Exp).

	Calculated Chain-B with APS			Exp [a]
	Fe1↑Fe2↑Fe3↓Fe4↓	Fe1↑Fe2↓Fe3↓Fe4↑	Fe1↑Fe2↓Fe3↑Fe4↓	
Fe1-Fe2	2.741	2.718	2.669	2.7
Fe1-Fe3	2.683	2.690	2.717	2.7
Fe1-Fe4	2.727	2.813	2.742	2.7
Fe2-Fe3	2.732	2.863	2.750	2.7
Fe2-Fe4	2.680	2.708	2.792	2.7
Fe3-Fe4	2.728	2.670	2.678	2.7
Fe1-S1	2.304	2.205	2.303	2.3
Fe1-S2	2.333	2.308	2.227	2.3
Fe1-S3	2.209	2.310	2.314	2.3
Fe2-S1	2.313	2.308	2.221	2.3
Fe2-S2	2.267	2.183	2.274	2.2
Fe2-S4	2.247	2.343	2.338	2.3
Fe3-S1	2.178	2.267	2.271	2.2
Fe3-S3	2.310	2.222	2.308	2.2
Fe3-S4	2.305	2.293	2.217	2.2
Fe4-S2	2.193	2.273	2.285	2.3
Fe4-S3	2.290	2.284	2.202	2.3
Fe4-S4	2.310	2.230	2.302	2.3
Fe1-S$_\gamma$-Cys140	2.304	2.329	2.326	2.3
Fe2-S$_\gamma$-Cys139	2.293	2.325	2.315	2.3
Fe3-S$_\gamma$-Cys228	2.290	2.306	2.306	2.3
Fe4-S$_\gamma$-Cys231	2.257	2.289	2.276	2.3
E	-1446.545	-1446.291	-1446.501	
NSP(Fe1, Fe2, Fe3, Fe4)	(-3.13, -3.11, 3.12, 3.07)	(3.14, -3.16, -3.12, 3.13)	(3.14, -3.14, 3.17, -3.13)	
δ(Fe1, Fe2, Fe3, Fe4)	(0.45, 0.45, 0.43, 0.42)	(0.46, 0.45, 0.43, 0.43)	(0.47, 0.46, 0.44, 0.43)	0.45 [18]
Average δ	0.44	0.44	0.45	
ΔE_Q(Fe1, Fe2, Fe3, Fe4)	(1.08, 0.95, 0.79, -1.03)	(0.87, 1.24, 1.15, 0.70)	(0.85, 1.04, 0.87, 1.23)	1.12 [18]
Average $|\Delta E_Q|$	0.96	0.99	1.00	
η(Fe1, Fe2, Fe3, Fe4)	(0.33, 0.65, 0.53, 0.88)	(0.78, 0.34, 0.29, 0.62)	(0.89, 0.64, 0.42, 0.33)	

[a.]The crystal structure was at 2.7 Å resolution, PDB code: 2GOY (Chartron, 2006). Distances are taken from chain-B with substrate binding

The net spin populations (NSP) from Mulliken population analysis are the main indication of the high-spin or intermediate-spin character of the metal sites. In the ideal ionic limit, the net unpaired spin populations are 5 and 4 for the high-spin Fe^{3+} (five d-electrons) and Fe^{2+} (six d-electrons) sites, respectively. Therefore, for the delocalized spins between the high-spin Fe^{3+} and Fe^{2+} sites, one should expect the average net spin of 4.5. However, because of the Fe-ligand covalency, our previous calculations show that the calculated net spin magnitude for a high-spin Fe^{3+}/Fe^{2+} site is normally by about 1 e^- smaller than the ionic limit [19,35,65-68]. The current calculated net spins on the four Fe sites in both chain-A and chain-B are 3.1 ~ 3.2 (Tables 4.2 and 4.3), about 1.3 ~ 1.4 e^- smaller than 4.5, indicative of the high spin $Fe^{2.5+}$ sites with substantial Fe-S covalency. The opposite signs for the spin densities indicate the AF-coupling.

Experimentally derived ^{57}Fe Mössbauer parameters were almost identical for the $[Fe_4S_4(S_\gamma-Cys)_4]^{2-}$ cluster for native APR and for the *S*-sulfocysteine intermediate form with AMP bound and C-terminal tail docked in the active site. Note that the Mössbauer analyses on MtAPR [18] were performed by incubating the enzyme with a 2-fold stoichiometric excess of APS at a concentration well above the K_d of APS or AMP, similar to the current EXAFS study. Our calculations show the subtle differences of the Mössbauer isomer shifts and quadrupole splittings for each Fe site in different spin states, with or without substrate. However the predicted isomer shifts are all around 0.45 mm s^{-1}, in excellent agreement with the experiment. The average predicted quadrupole splitting values (~1 mm s^{-1}) also agree well with the experimental values (Tables 4.2 and 4.3).

Table 4.4 ESP atomic charges. Comparison of the calculated ESP atomic charges of the $[Fe_4S_4(S_\gamma\text{-Cys})_4]^{2-}$ quantum cluster in the Fe1↑Fe2↓Fe3↑Fe4↑ spin state in different models.

	Chain-A without APS			Chain-B with APS		
	wild-type	no-tandem	K144A	wild-type	no-tandem	K144A
Fe1	0.43	0.43	0.47	0.45	0.42	0.50
Fe2	0.58	0.58	0.60	0.61	0.59	0.61
Fe3	0.62	0.63	0.63	0.61	0.65	0.61
Fe4	0.62	0.60	0.63	0.62	0.61	0.64
S1	-0.44	-0.46	-0.48	-0.44	-0.48	-0.46
S2	-0.45	-0.44	-0.44	-0.44	-0.43	-0.46
S3	-0.47	-0.46	-0.53	-0.48	-0.49	-0.54
S4	-0.70	-0.68	-0.70	-0.70	-0.67	-0.71
S_γ-Cys140	-0.41	-0.40	-0.54	-0.45	-0.39	-0.59
S_γ-Cys139	-0.63	-0.68	-0.59	-0.64	-0.67	-0.66
S_γ-Cys228	-0.61	-0.60	-0.66	-0.70	-0.70	-0.70
S_γ-Cys231	-0.65	-0.67	-0.67	-0.63	-0.66	-0.68
$\sum_{total}$	-2.11	-2.15	-2.28	-2.19	-2.22	-2.44

To understand how APS binding influences the charge distributions of the [4Fe-4S] cluster, we calculated the ESP atomic charges of the $[Fe_4S_4(S_\gamma\text{-Cys})_4]^{2-}$ clusters in chain-A and chain-B in the Fe1↑Fe2↓Fe3↑Fe4↑ spin state. The ESP charges are given in Table 4.4 under the "wild-type" columns. In chain-A without APS, Fe1 has the least positive charge (0.43), which is approximately 0.2 charge units less than Fe3 and Fe4. In addition, the Cys140 thiolate which coordinates to Fe1 has the least negative charge (-0.41), which is also by 0.2 charge units in magnitude less than the other three Cys residues. This shows the charge transfer from the Cys140 thiolate to the nearby cationic group of Lys144 side chain. In chain-B (Figure 4.6), Lys144 is in between Cys140 and APS. The distances between S_γ-Cys140 and N-Lys144, and between N-Lys144 and O-APS are 3.16 Å (3.56 Å) and 3.19 Å (3.03 Å), respectively, in the X-ray (DFT optimized) structure of chain-B. The charge transfer from Cys140 to Lys144 is decreased in the presence of APS. As a result, S_γ-Cys140 becomes more negative from -0.41 (chain-A) to -0.45 (chain-B), and the ESP charge on Fe1 is slightly increased from 0.43 (chain-A) to 0.45 (chain-B).

The repulsion between APS and Cys228 also increases the magnitude of the negative charge on S_γ-Cys228 from -0.61 (chain-A) to -0.70 (chain-B). These changes result in a subtle increase in the total negative ESP charge of the entire $[Fe_4S_4(S_\gamma\text{-Cys})_4]^{2-}$ cluster from -2.11 (Chain-A) to -2.19 (Chain-B). Even though APS does not have a direct interaction with the [4Fe-4S] cluster, the mid-range electrostatic interactions between the two species indeed influence the charge distribution and the detailed geometry within the [4Fe-4S] cluster, although the geometric changes are not large enough to be observed in EXAFS and Mössbauer experiments.

4.6.2 Calculating Results for No-Tandem $[Fe_4S_4(S_\gamma\text{-Cys})_4]^{2-}$ Models. The main Fe-Fe and Fe-S distances of the optimized no-tandem models in the {Fe1↓Fe2↓Fe3↑Fe4↑} state with and without APS are shown in Table 4.5, in the columns under "no-tandem". After breaking the peptide bond between Cys139 and Cys140 (Figure 4.7), the $[4Fe\text{-}4S]^{2+}$ core in both chain-A and chain-B expands. For chain-A without APS, the Fe1-Fe2 distance is increased by 0.08 Å compared to wild-type (Table 4.2). Fe1-Fe3, Fe1-Fe4, and Fe3-Fe4 are also increased by 0.03, 0.04 and 0.02 Å, respectively. Except for Fe2-S2, Fe2-S4, and Fe2-S_γ-Cys139, which are decreased by 0.01 Å, all other Fe-S distances are increased by 0 ~ 0.03 Å. The RMSD of the Fe-Fe and Fe-S distances between the calculated no-tandem model and the wild-type optimized cluster of chain-A is 0.022 Å. The angles ∠Fe1-S_γ-C_β-Cys140 and ∠Fe2-S_γ-C_β-Cys139 are widened from 112.6° and 109.6° to 117.3° and 112.4°, respectively. Meanwhile the distance between (S_γ-Cys140) and (S_γ-Cys139) is enlarged from 6.19 Å to 6.43 Å. From chain-A to chain-B for the no-tandem models, the Fe1-Fe2 distance is further increased by 0.06 Å, and reaches 2.82 Å, which is the longest Fe-Fe distance for the {Fe1↓Fe2↓Fe3↑Fe4↑} state of the [4Fe-4S] cluster in the current study. For chain-B with APS, the RMSD of the Fe-Fe and Fe-S distances between the no-tandem model and the optimized wild-type cluster is also 0.022 Å.

Table 4.5 DFT results for the no-tandem and K144A models. Calculated Fe-Fe and Fe-ligand Bond Lengths (Å) and Fe Net Spin Populations (NSP) for the $[Fe_4S_4(S_\gamma\text{-}Cys)_4]^{2-}$ quantum cluster in Fe1↓Fe2↓Fe3↑Fe4↑ spin state with substrate and without substrate binding in no-tandem and K144A models.

	Chain-A without APS		Chain-B with APS	
	no-tandem	K144A	no-tandem	K144A
Fe1-Fe2	2.755	2.710	2.819	2.720
Fe1-Fe3	2.683	2.661	2.700	2.676
Fe1-Fe4	2.745	2.716	2.761	2.733
Fe2-Fe3	2.742	2.754	2.735	2.731
Fe2-Fe4	2.680	2.694	2.649	2.696
Fe3-Fe4	2.662	2.689	2.705	2.727
Fe1-S1	2.317	2.311	2.306	2.303
Fe1-S2	2.340	2.323	2.326	2.317
Fe1-S3	2.238	2.224	2.218	2.208
Fe2-S1	2.349	2.340	2.311	2.317
Fe2-S2	2.284	2.298	2.272	2.276
Fe2-S4	2.253	2.262	2.242	2.251
Fe3-S1	2.218	2.203	2.210	2.175
Fe3-S3	2.325	2.340	2.308	2.317
Fe3-S4	2.333	2.340	2.298	2.302
Fe4-S2	2.208	2.203	2.199	2.201
Fe4-S3	2.326	2.335	2.296	2.296
Fe4-S4	2.332	2.341	2.310	2.318
Fe1-S_γ-Cys140	2.279	2.254	2.323	2.270
Fe2-S_γ-Cys139	2.303	2.313	2.281	2.298
Fe3-S_γ-Cys228	2.325	2.303	2.293	2.284
Fe4-S_γ-Cys231	2.288	2.284	2.257	2.276
RMSD [a]	0.022	0.014	0.022	0.012
NSP(Fe1)	-3.15	-3.12	-3.13	-3.11
NSP(Fe2)	-3.16	-3.19	-3.11	-3.13
NSP(Fe3)	3.18	3.18	3.12	3.12
NSP(Fe4)	3.14	3.14	3.07	3.10

[a]Root mean squares difference of the calculated Fe-Fe and Fe-S distances between the current modified models and the optimized wild-type models (in Fe1↓Fe2↓Fe3↑Fe4↑ state) given in Table 4.2 (for chain-A) and Table 4.3 (for chain-B).

Thus, the unique tandem pair Cys139 and Cys140 in PaAPR keeps the $[Fe_4S_4(S_\gamma\text{-Cys})_4]^{2-}$ cluster more compact, which works to prevent the cluster from being reduced. It is known that, once the $[Fe_4S_4(S_\gamma\text{-Cys})_4]^{2-}$ cluster is reduced (net charge of the cluster would be -3), the repulsion among the S···S atoms would be stronger, forcing the expansion of the overall cluster [19,35]. The tandem structure in PaAPR makes the expansion of the [4Fe-4S] energetically unfavorable, which explains why it is difficult to reduce the cluster [18]. After several attempts, we were able to reduce the $[Fe_4S_4(S_\gamma\text{-Cys})_4]^{2-}$ cluster in MtAPR but the reduction efficiency was at most 44% of the total protein [18].

The calculated ESP atomic charges for the $[Fe_4S_4(S_\gamma\text{-Cys})_4]^{2-}$ cluster in the no-tandem models in both chain-A and chain-B are given in Table 4.4 in the columns under "No-tandem". In both chain-A and chain-B, Fe1 still holds the least positive ESP charge. Overall, the calculated ESP charges of the no-tandem models are similar to the corresponding wild-type results. The total ESP charges ($\sum_{total}$) of the no-tandem models are a little more negative than those of the wild-type cluster, which increases the possibility of one-electron oxidation of the [4Fe-4S] cluster in the no-tandem form. The propensity and rate of cluster degradation after oxidation is a complex multi-step problem, and would be expected to involve both the covalent Cys linkages and H-bonding interactions with surrounding residues.

The function of the unique tandem pair Cys139 and Cys140 in PaAPR is to protect the [4Fe-4S] cluster from reduction, as will be examined by redox potential calculations in Section 6.4. Note that our current method to construct the no-tandem models is the simplest, but may not represent the best approach. An alternative possibility would be to insert one or more residues between the Cys139 and Cys140 pair. However, this would cause large conformational change

and increase the size of the clusters, which currently contain 211 (in chain-A) and 250 (in chain-B) atoms, and approach the reasonable limit of DFT/COSMO calculations. This issue could be examined in future studies, ostensibly starting with a smaller overall cluster size.

4.6.3 Calculating Results for K144A [Fe$_4$S$_4$(S$_\gamma$-Cys)$_4$]$^{2-}$ Models. The calculated Fe-Fe and Fe-S distances of the optimized K144A models in the {Fe1↓Fe2↓Fe3↑Fe4↑} spin state with and without APS binding are shown in Table 4.5, in the columns under "K144A". The calculated ESP atomic charges for the [Fe$_4$S$_4$(S$_\gamma$-Cys)$_4$]$^{2-}$ portion of the K144A models in both chain-A and chain-B have also been shown in Table 4.4 in the columns under "K144A".

There is marked anisotropy in the change of charge distribution and bond lengths when Lys144 is mutated to Ala. In particular, without charge transfer to Lys144, the negative ESP charge on S$_\gamma$-Cys140 changes significantly from -0.41 (and -0.45) in the wild type to -0.54 (and -0.59) in the K144A model of chain-A (and chain-B) (Table 4.4). This influences the charge on Fe1 such that Fe1 is more positive and in turn, the charge on S3 is more negative in both models of K144A, compared to the respective wild type model. Overall the total charge of the [Fe$_4$S$_4$(S$_\gamma$-Cys)$_4$]$^{2-}$ cluster becomes more negative from -2.11 in the wild type to -2.28 in the K144A models for chain-A, and from -2.19 to -2.44 for chain-B, respectively (Table 4.4). The increase of the negative charge of the [Fe$_4$S$_4$(S$_\gamma$-Cys)$_4$]$^{2-}$ cluster, in combination with the electrostatic interaction of the negatively charged cluster with the Lys144$^+$ *vs.* neutral Ala144, explains why the Fe-S cluster is even more difficult to reduce in K144A mutant as observed in EPR experiments [18]. The reduction potential of the K144A clusters will also be examined in Section 6.4.

In chain-B, loss of the H-bonding interaction between S_γ-Cys140 and Lys144 decreases the Fe1-S_γ-Cys140 bond length by 0.03 Å, which is greater than the other corresponding Fe-S_γ-Cys distance changes. In general, the RMSD of the calculated Fe-Fe and Fe-S distances between the K144A model and the optimized wild-type cluster is 0.014 Å for chain-A and 0.012 Å for chain-B. The cluster is more compact in the wild type protein than in the K144A model. For instance, in chain-A without APS binding, except for Fe2-Fe3, Fe1-S2, Fe1-S3, Fe2-S4, and Fe3-S1, which either remain unchanged or are decreased by less than 0.01 Å, all other Fe-Fe and Fe-S distances are increased by 0-0.04 Å from the wild-type cluster to the K144A model. Overall the cluster in K144A expands compared to the wild-type optimized cluster, which is consistent with the increasing of the electron density over the $[Fe_4S_4(S_\gamma\text{-}Cys)_4]^{2-}$ cluster, and the increasing lability of the cluster in K144A as observed in EPR experiments [18].

Additionally, a comparison between ESP charges for APS in the wild-type and K144A models shows that the overall charge on APS becomes more negative changing from -1.75 in wild type to -1.84 in the K144A model (data not shown). As indicated above, without charge transfer to Lys144$^+$, the calculated total ESP charge of the $[Fe_4S_4(S_\gamma\text{-}Cys)_4]^{2-}$ cluster also becomes more negative from -2.19 in wild-type to -2.44 in K144A (chain-B). This supports the crucial role of Lys144 such that in the absence of the positive charge, the H-bonding interactions are lost and the negative charges on both the cluster and APS are more localized making the cluster and APS more negative in the K144A model. This would result in a strong repulsion between the $[Fe_4S_4(S_\gamma\text{-}Cys)_4]^{2-}$ cluster and APS that is detrimental to substrate binding in the mutant protein. In fact, kinetic studies show that there is a 400-fold decrease in the K_d of APS for Lys144Ala MtAPR and consequently, a decrease in the catalytic efficiency of the mutant protein by almost 63,000-fold as compared to wild type MtAPR [18].

Compared to wild-type chain-B, the calculated distances of (S-APS)···(S_γ-Cys140), (S-APS)···Fe1, and (S-APS)···Fe2 increase from 6.79, 8.20, and 10.84 Å, respectively in the wild type to 7.29, 8.57, and 11.15 Å, respectively in the K144A model. Therefore, without Lys144 bridging between APS and Cys140, repulsion causes APS and the $[Fe_4S_4(S_\gamma\text{-Cys})_4]^{2-}$ cluster to move away from each other.

4.6.4 Calculated $[Fe_4S_4(S_\gamma\text{-Cys})_4]^{3-}$ Clusters and the Reduction potentials of $[Fe_4S_4(S_\gamma\text{-Cys})_4]^{2-} + e^-$ → $[Fe_4S_4(S_\gamma\text{-Cys})_4]^{3-}$ in Different Models.

If an electron is transferred to the resting state of the $[4Fe\text{-}4S]^{2+}$ core in APR, the core will change to $[4Fe\text{-}4S]^{1+}$, and the core plus the four Cys side chains will have a net charge of -3, $[Fe_4S_4(S_\gamma\text{-Cys})_4]^{3-}$. Since the $[4Fe\text{-}4S]^{2+}$ core is likely to be in the {Fe1↓Fe2↓Fe3↑Fe4↑} spin state, the added electron then either goes to the pair {Fe1,Fe2} to form the {Fe1^{2+}↓Fe2^{2+}↓Fe3$^{2.5+}$↑Fe4$^{2.5+}$↑} state, or goes to (Fe3,Fe4} to form the {Fe1$^{2.5+}$↓Fe2$^{2.5+}$↓Fe3^{2+}↑Fe4^{2+}↑} state. Our geometry optimizations show that these two states yield very similar broken-symmetry energies (less than 2 kcal mol^{-1} difference) for all the cluster models. And for most of the models (only wild-type chain-A is an exception), the {Fe1^{2+}↓Fe2^{2+}↓Fe3$^{2.5+}$↑Fe4$^{2.5+}$↑} state is slightly lower in energy than the corresponding {Fe1$^{2.5+}$↓Fe2$^{2.5+}$↓Fe3^{2+}↑Fe4^{2+}↑} state. Therefore, here we only present the geometries (Tables 4.6 and 4.7) and energies (Table 4.7) of the {Fe1^{2+}↓Fe2^{2+}↓Fe3$^{2.5+}$↑Fe4$^{2.5+}$↑} state for all the cluster models.

Table 4.6 DFT results for the $[Fe_4S_4(S_{\gamma}-Cys)_4]^{3-}$ quantum cluster in different models. Calculated Fe-Fe and Fe-ligand bond lengths (Å) and Fe net spin populations (NSP) for the $[Fe_4S_4(S_{\gamma}-Cys)_4]^{3-}$ quantum cluster in $\{Fe1^{2+}, Fe2^{2+}, Fe3^{2.5+}, Fe4^{2.5+}\}$ state with and without substrate binding in wild-type, no-tandem and K144A models.

	Chain-A without APS			Chain-B with APS		
	wild-type	no-tandem	K144A	wild-type	no-tandem	K144A
Fe1-Fe2	2.704	2.788	2.706	2.755	2.809	2.683
Fe1-Fe3	2.661	2.700	2.663	2.676	2.708	2.685
Fe1-Fe4	2.694	2.730	2.700	2.731	2.749	2.740
Fe2-Fe3	2.761	2.735	2.750	2.746	2.719	2.725
Fe2-Fe4	2.729	2.718	2.737	2.723	2.705	2.729
Fe3-Fe4	2.635	2.636	2.634	2.676	2.655	2.672
Fe1-S1	2.325	2.327	2.321	2.319	2.307	2.306
Fe1-S2	2.305	2.321	2.301	2.281	2.301	2.297
Fe1-S3	2.270	2.294	2.276	2.263	2.263	2.265
Fe2-S1	2.318	2.324	2.317	2.296	2.300	2.291
Fe2-S2	2.299	2.295	2.300	2.271	2.276	2.279
Fe2-S4	2.317	2.292	2.319	2.298	2.274	2.317
Fe3-S1	2.213	2.226	2.206	2.192	2.219	2.184
Fe3-S3	2.357	2.348	2.370	2.345	2.340	2.348
Fe3-S4	2.373	2.358	2.363	2.323	2.315	2.321
Fe4-S2	2.211	2.221	2.211	2.204	2.212	2.203
Fe4-S3	2.333	2.332	2.368	2.296	2.300	2.308
Fe4-S4	2.364	2.358	2.340	2.331	2.323	2.338
Fe1-S$_{\gamma}$-Cys140	2.296	2.336	2.296	2.329	2.387	2.313
Fe2-S$_{\gamma}$-Cys139	2.347	2.329	2.339	2.330	2.309	2.324
Fe3-S$_{\gamma}$-Cys228	2.349	2.350	2.351	2.329	2.337	2.318
Fe4-S$_{\gamma}$-Cys231	2.338	2.349	2.331	2.319	2.318	2.322
NSP(Fe1)	-2.93	-3.01	-2.92	-2.92	-2.99	-2.94
NSP(Fe2)	-3.00	-2.94	-3.01	-2.97	-2.92	-2.94
NSP(Fe3)	3.26	3.27	3.25	3.23	3.23	3.21
NSP(Fe4)	3.22	3.24	3.23	3.19	3.20	3.21

The formal net spin population of a high-spin Fe^{2+} ion is 4. Our calculated magnitudes of the net spins (2.92 ~ 3.01) of Fe1 and Fe2 in all the $\{Fe1^{2+}_{\downarrow}Fe2^{2+}_{\downarrow}Fe3^{2.5+}_{\uparrow}Fe4^{2.5+}_{\uparrow}\}$ state $[Fe_4S_4(S_\gamma\text{-Cys})_4]^{3-}$ clusters are about 1 e^- smaller than 4 (Table 4.6). The calculated net spin values for Fe3 and Fe4 in the $[Fe_4S_4(S_\gamma\text{-Cys})_4]^{3-}$ clusters (Table 4.6) are about 0.1 larger than the corresponding ones in the $[Fe_4S_4(S_\gamma\text{-Cys})_4]^{2-}$ clusters (Tables 4.2, 4.3, and 4.5). One measure of the metal-ligand covalency is the ratio of the calculated to the formal site spin population (spin population ratio), and lower percentages represent greater covalency. In wild-type chain-A, the spin population ratios of the four iron sites change from (69%, 71%, 70%, 69%) in the $\{Fe1^{2.5+}_{\downarrow}Fe2^{2.5+}_{\downarrow}Fe3^{2.5+}_{\uparrow}Fe4^{2.5+}_{\uparrow}\}$ state $[Fe_4S_4(S_\gamma\text{-Cys})_4]^{2-}$ cluster to (73%, 75%, 72%, 72%) in the $\{Fe1^{2+}_{\downarrow}Fe2^{2+}_{\downarrow}Fe3^{2.5+}_{\uparrow}Fe4^{2.5+}_{\uparrow}\}$ state $[Fe_4S_4(S_\gamma\text{-Cys})_4]^{3-}$ cluster. Very similar percentage changes are also obtained for other model clusters. Therefore, with an additional electron, the $[4Fe-4S]^{1+}$ core of the $[Fe_4S_4(S_\gamma\text{-Cys})_4]^{3-}$ cluster in general has less covalency (larger spin population ratio) than the $[4Fe-4S]^{2+}$ core of the $[Fe_4S_4(S_\gamma\text{-Cys})_4]^{2-}$ cluster. As a result, upon 1e^- reduction, the [4Fe-4S] core expands. This is seen relatively easier by comparing the average (avg) Fe-Fe and Fe-S distances (Table 4.7). Especially for the wild-type chain-A model, where upon 1e^- reduction, the (Fe-Fe)$_{avg}$ elongates from 2.690 Å to 2.697 Å, the average of the four Fe-S distances of Fe1-S3, Fe2-S4, Fe3-S1, and Fe4-S2 is increased from 2.228 Å to 2.253 Å, and the average distance of the eight Fe-S bonds on the 'Fe1-S1-Fe2-S2' and 'Fe3-S3-Fe4-S4' planes is also increased from 2.318 Å to 2.334 Å.

Based on the OLYP/COSMO calculated broken-symmetry state energies (E), we have calculated the reduction potentials (E^0) of $[Fe_4S_4(S_\gamma\text{-Cys})_4]^{2-}$ + e^- → $[Fe_4S_4(S_\gamma\text{-Cys})_4]^{3-}$ for all the cluster models according to:

$$E^0 = E\{[Fe_4S_4(S_\gamma\text{-Cys})_4]^{2-}\} - E\{[Fe_4S_4(S_\gamma\text{-Cys})_4]^{3-}\} + \Delta SHE \qquad (4)$$

where ΔSHE is the standard hydrogen electrode potential. Here we use ΔSHE = -4.34 V, obtained from Lewis *et al*'s calculations based solely on experimental data plus our electron energy threshold correction [69-71]. The calculated reduction potentials for all the model clusters are given in Table 4.7.

Table 4.7 Reduction potentials for different model clusters. Averages (avg) of the calculated Fe-Fe and Fe-ligand bond lengths (Å), broken-symmetry state energies (E, eV), and reduction potentials (E^0, V) of the $[Fe_4S_4(S_\gamma\text{-Cys})_4]^{2-}/[Fe_4S_4(S_\gamma\text{-Cys})_4]^{3-}$ (2-/3-) quantum clusters with and without substrate binding in wild-type, no-tandem and K144A models.

	Chain-A without APS					
	wild-type		no-tandem		K144A	
	2-	3-	2-	3-	2-	3-
$6(Fe\text{-}Fe)_{avg}$	2.690	2.697	2.711	2.718	2.704	2.698
$4(Fe\text{-}S)_{avg}$ [a]	2.228	2.253	2.229	2.258	2.223	2.253
$8(Fe\text{-}S)_{avg}$ [b]	2.318	2.334	2.326	2.333	2.329	2.335
$4(Fe\text{-}S_\gamma)_{avg}$	2.285	2.333	2.299	2.341	2.289	2.329
E	-1193.735	-1196.724	-1185.564	-1188.659	-1135.356	-1138.287
E^0	-1.35		-1.25		-1.41	

	Chain-B with APS					
	wild-type		no-tandem		K144A	
	2-	3-	2-	3-	2-	3-
$6(Fe\text{-}Fe)_{avg}$	2.715	2.718	2.728	2.724	2.714	2.706
$4(Fe\text{-}S)_{avg}$ [a]	2.207	2.239	2.217	2.242	2.209	2.242
$8(Fe\text{-}S)_{avg}$ [b]	2.304	2.308	2.303	2.308	2.306	2.311
$4(Fe\text{-}S_\gamma)_{avg}$	2.286	2.327	2.289	2.338	2.282	2.319
E	-1446.545	-1449.460	-1438.362	-1441.410	-1387.923	-1390.710
E^0	-1.43		-1.29		-1.55	

[a]The average of the following four Fe-S distances: Fe1-S3, Fe2-S4, Fe3-S1, and Fe4-S2 (see Figure 4.5). [b.] The average of the following eight Fe-Fe distances: Fe1-S1, Fe1-S2, Fe2-S1, Fe2-S2, Fe3-S3, Fe3-S4, Fe4-S3, and Fe4-S4.

The measured 2-/3- reduction potentials of the [4Fe-4S] clusters in ferredoxins are from -0.28 to -0.45 V [72-74]. So far, reduction of the $[Fe_4S_4(S_\gamma\text{-}Cys)_4]^{2-}$ cluster in PaAPR has not been successful. In our recent EPR experiment, we could photo reduce the $[Fe_4S_4(S_\gamma\text{-}Cys)_4]^{2-}$ cluster in MtAPR in the presence of deazaflavin/oxalate with at most 44% reduction efficiency [18]. It is likely that the 2-/3- reduction potential of the [4Fe-4S] cluster in APR is much more negative than ferredoxins, because of the tandem Cys pair and less H-bonding interactions around the [4Fe-4S] in APR. There are 10 H-bonding interactions around the [4Fe-4S] active site in ferredoxins [19]. These H-bonds are expected to stabilize the negative charges of the $[Fe_4S_4(S_\gamma\text{-}Cys)_4]^{3-}$ cluster, making the 1e$^-$ reduction easier. By contrast, there are only three H-bonding interactions with S or S_γ in the crystal structure of PaAPR (Figure 4.4).

It is still a big challenge to accurately predict the redox potentials for the Fe-S systems. The redox potentials obtained from quantum mechanical calculations within a solvation model vary with the dielectric constant of the solvent and the probe radius for the contact surface between the quantum cluster and solvent [19,35]. In general, the larger the dielectric constant and the smaller the radius, the reduced state is more stabilized, and the reduction potential is more positive (or less negative) [19,35]. Our previous calculations also show that the DFT/solvation calculations systematically predict the redox potentials of the Fe-S systems by 0 ~ 0.5 V more negative than the measured values [19,35]. Our current predicted reduction potentials for the [4Fe-4S] cluster models in PaAPR are also very negative, ranging from -1.25 to -1.55 V. Since the experimental reduction potential of PaAPR is not available, we do not have a clear picture if or how much our calculations overestimate (more negative) these reduction potentials. Therefore we will focus on the relative values of the predicted E^0's to see how the APS binding, the

breaking of the Cys tandem pair, and the K144A mutation will change the reduction potential of PaAPR.

From wild-type chain-A to wild-type chain-B, E^0 is more negative by 0.08 V (from -1.35 V to -1.43 V). With APS^{2-} nearby, the negatively charged $[Fe_4S_4(S_\gamma\text{-}Cys)_4]^{2-}$ cluster is then even more difficult to accept an electron from outside, and therefore is more difficult to reduce. From wild-type to no-tandem model, E^0 becomes more positive by 0.1 V and 0.14 V in chain-A and chain-B, respectively. Therefore, the no-tandem cluster of $[Fe_4S_4(S_\gamma\text{-}Cys)_4]^{2-}$ is easier to reduce than the wild-type. This is consistent with our conclusion in Section 6.2 that the function of the unique tandem pair Cys139/Cys140 in PaAPR is to keep the [4Fe-4S] cluster more compact and protect the cluster from reduction. In chain-A, the calculated E^0 of K144A is more negative than the wild-type by 0.06 V. In chain-B with APS, the K144A model yields the most negative E^0 (-1.55 V) among all the model clusters. Upon the Lys144 → Ala144 mutation, there is no negative charge transfer from the $[Fe_4S_4(S_\gamma\text{-}Cys)_4]^{2-}$ cluster to Lys144, the cluster is therefore more difficult to reduce, and the reduction becomes even more difficult when APS^{2-} is present, as proposed in Section 6.3.

4.7 Conclusion

In order to understand the role of [4Fe-4S] cluster in APS reduction, we have examined the coordination and geometry of the native and APS-bound forms of the enzyme by XAS. Results from the XANES and EXAFS analysis were valuable in indicating that there is no change in coordination and overall geometry of the [4Fe-4S] cluster between both forms of the enzyme. However, in terms of resolving subtle changes in the geometry and electrostatics DFT calculations were employed. Taken together, the EXAFS and DFT analyses provide a more

complete picture of the coordination, geometry and electrostatic environment of the [4Fe-4S] cluster in APR. This is the first report of the application of both of these techniques to APR and thereby contributes to the characterization of the cluster in APR with a view to gaining insight into the function of the cluster in APS reduction.

Fe K-edge EXAFS analysis confirms the presence of the [4Fe-4S] cluster and a comparison of samples of MtAPR in the native and substrate-bound forms suggests that the core of the cluster is essentially unaffected during catalysis. This is supported by biochemical evidence, which shows that the cluster in APR has no redox activity during the catalytic cycle [4] and hence we do not expect any change in the oxidation state of the cluster in MtAPR with and without APS.

DFT geometry optimizations have been performed on the [4Fe-4S] clusters of the wild-type, no-tandem, and K144A models constructed starting from the PaAPR X-ray crystal structures [13]. Both substrate-free and substrate-binding forms for each type of the models were studied. Calculations show that substrate binding influences the geometric and electronic structures of the $[Fe_4S_4(S_\gamma\text{-Cys})_4]^{2-}$ cluster, in agreement with the resonance Raman and EPR spectra experiments [11,18]. However, the geometric changes of the [4Fe-4S] core are not large enough to be observed in EXAFS and Mössbauer experiments.

Calculations with the 'no-tandem' models show that the coordinating tandem Cys139-Cys140 pair in PaAPR keeps the [4Fe-4S] cluster more compact and prevents it from reduction. The tandem pair also leads to a strain in the geometry of the cysteine side chains. Conformations of the cysteinyl ligands of an iron-sulfur cluster can result in differences in redox energies of ~100 mV that can directly influence the redox properties of the cluster [75].

Additionally, the replacement of Lys144$^+$ by Ala in our calculations has a two-fold effect: (1) Loss of the bridging charged H-bonding interactions of Lys144 with S$_\gamma$-Cys140 and the terminal sulfate moiety of APS destabilizes the Fe-S cluster as the overall charge of the cluster becomes more negative. The calculated reduction potentials of the clusters in K144A models are by 0.06 ~ 0.12 V more negative than the wild-type clusters. In fact, the lability of the cluster and difficulty in reduction have been observed in EPR experiments in which reduction of the cluster in the K144A mutant resulted in a 6-fold decrease of signal intensity and the appearance of an additional signal corresponding to free Fe^{3+} formed due to cluster degradation, compared to wild type APR [18]. (2) Loss of the bridging Lys144 cation increases the repulsion between the negatively charged APS^{2-} and the [Fe$_4$S$_4$(S$_\gamma$-Cys)$_4$]$^{2-}$ cluster. This explains why the Lys144Ala mutation is detrimental to APS-binding and catalysis [18].

The importance of Lys144 in stabilizing the sulfate moiety of APS is analogous to the role of a conserved Lys residue in sulfotransferases which acts as a catalytic acid, stabilizing the transition state of the substrate, phosphoadenosine phosphosulfate (PAPS), by interacting with the SO$_3$ moiety that is being transferred [76]. Conversely, we could glean a role for the [4Fe-4S] cluster in positioning Lys144 in the active site such that it can interact favorably with the incoming substrate. In addition to Lys144, other conserved positively charged residues such as Arg242 and Arg245, and Arg171 (present in a flexible 'Arg-loop') also play crucial roles in substrate binding [9]. Lysines and arginines are cations with long, flexible and mobile side chains. They often function as "molecular guidewires" as found in other sulfate and phosphate transfer enzymes [77-82]. The cationic side chains electrostatically screen the bound anions during group transfer, facilitating covalent bond formation.

It should also be noted that the current PaAPR crystal structure is missing the disordered C-terminal segment of residues 250-267, which carries the catalytically essential Cys256 [13]. When the missing segment was modeled into the active site of PaAPR using the structure of 3'-phosphoadenosine 5'-phosphosulfate reductase from *Saccharomyces cerevisiae*, it was observed that Cys256 is proximal to the sulfate moiety of APS, and the side chains of Cys140 and Lys144 [18]. Thus with the addition of the negatively charged, nucleophilic thiolate in the transition state, the optimum positioning of Lys144 and other cationic side chains to make key H-bonding interactions with APS, is required to maintain an energetically favorable charge balance within the active site.

In summary, our study characterizes the [4Fe-4S] cluster in APR by EXAFS spectroscopy and by findings from our DFT calculations which substantiate (1) modulation of the redox potential of the cluster brought about by the constrained tandem cysteine coordination, (2) the role of Lys144 as a critical link between the [4Fe-4S] cluster and APS, and finally, (3) a role for the Fe-S cluster in contributing to stabilization of the transition state via positioning of Lys144 and maintaining charge balance in the active site during catalysis. In order to gain further insights into the mechanism of APS reduction, efforts to determine the structure of APR with the intact C-terminal segment are currently underway.

4.8 Experimental Procedures

4.8.1 Materials *E. coli* BL21(DE3) used for expression was obtained from Novagen (Bad Soden, Germany). APS was purchased from Biolog Life Sciences Institute, ≥95% (Bremen, Germany). AMP and reagents for the buffer were obtained from Sigma-Aldrich (St. Louis, MO) and were of the highest purity available.

4.8.2 Preparation of Mt-APSR Samples for EXAFS Spectroscopy Mt-APSR was purified as detailed in Ref. 18, concentrated using 10,000 MWCO Amicon Ultra-4 centrifugal filter devices (Millipore Corporation, Billerica, MA) and used at a final concentration of 1 mM in buffer containing 50 mM Tris–HCl, 150 mM NaCl (pH 8.5 at 4 °C) and 10% (v/v) glycerol. Protein concentrations were determined using the extinction coefficient, ε_{280}=36,815 $M^{-1}cm^{-1}$, obtained by quantitative amino acid analysis. Analysis of iron content by inductively coupled plasma (ICP) mass spectrometry for Mt-APSR indicated that each mole of protein contained 3.5 ± 0.4 mol of iron, as expected for a [4Fe-4S] cluster. The iron and sulfur content of APSR is consistent with the incorporation of four irons and four inorganic sulfides per mol of protein.[4,83] The specific activity of the purified enzyme was 5.2 μM min^{-1} mg $protein^{-1}$ as determined by an assay using ^{35}S-APS described in Ref. 9 and consistent with the previously reported value.[4] For samples with ligand, 1 mM enzyme was incubated with 3 mM ligand for 15 min at room temperature, prior to loading. All samples were loaded in 1 mm Lucite cells with 37 μm Kapton windows for X-ray absorption studies, immediately frozen in liquid nitrogen, and maintained under liquid nitrogen conditions until data were collected.

4.8.3 EXAFS Measurements and Data Analysis ⸺X-ray absorption spectra were recorded at the Stanford Synchrotron Radiation Laboratory (beam line 9-3) under dedicated conditions as fluorescence excitation spectra, using a solid-state Ge detector array equipped with a Mn filter and Soller slits focused on the sample. All channels of each scan were examined for glitches, and the good channels were averaged for each sample (two independent samples for each protein composition, with or without ligand) to give the final spectrum. During data collection, samples were maintained at a temperature of approximately -263 ˚C using a liquid-helium flow cryostat. As a measure of sample integrity, XANES spectra measured for the first and last scan of each

sample were compared. No changes were observed over the course of the data collection. Data were measured with an integration time of 1 second through the edge, and between 1 and 25 seconds in the post-edge region. For each sample, between 5 and 10 35-min scans were accumulated, and each sample was measured in duplicate. The useful fluorescence count rate per channel was ~10^4 counts/second, giving a total of ~6×10^6 counts/scan at k = 17 Å^{-1}. For energy calibration, the absorption spectrum of an iron metal foil was measured simultaneously by transmittance, and the energy was calibrated with reference to the lowest-energy inflection points of the foil standard, which was assumed to be 7111.3 eV for iron. EXAFSPAK[84] was used to extract and analyze EXAFS data, using *ab initio* phase and amplitude parameters calculated using FEFF version 7.02.[85,86] with the initial threshold energy E_0 defined as 7130 eV. Non-linear least squares fits of the data used 4 variable parameters (R and s^2 for each shell) with the amplitude correction factor and DE_0 set to 0.9 and -11 eV respectively based on fits to model Fe/S clusters., XANES data were normalized to tabulated absorption coefficients[64] using MBACK.[87] The area of the 1s → 3d transition in the XANES region was calculated by fitting the pre-edge region (7107-7118 eV) using the sum of a Gaussian and an arctan function; for comparison with previously published data, the fitted Gausian area was normalized to the K-edge jump for Fe (3.556 × 10^2 cm^2/g).

Acknowledgment

4.9 Appendix

Appendix 4.9.1 Structure-based sequence alignment of APRs from *Pseudomonas aeruginosa* and *Mycobacterium tuberculosis.*
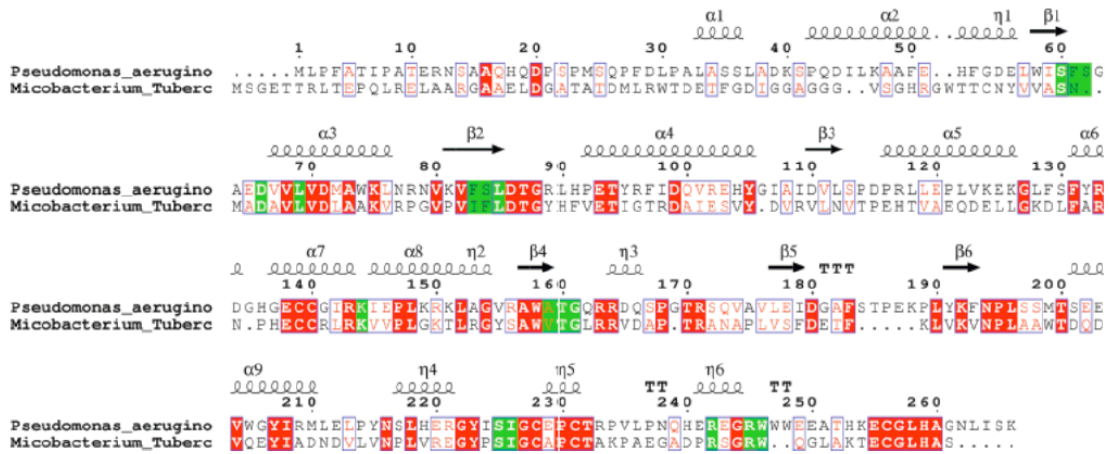
Appendix 4.9.1 Structure-based sequence alignment of APRs from *Pseudomonas aeruginosa* and *Mycobacterium tuberculosis.* The ClustalW multiple sequence alignment program was used. Strictly conserved residues are outlined in red, red letters indicate conserved residues and conserved regions are boxed in blue. Residues flanking the active site are outlined in green.

Appendix 4.9.2 Comparison of XAS spectra for MtAPR with and without substrate.
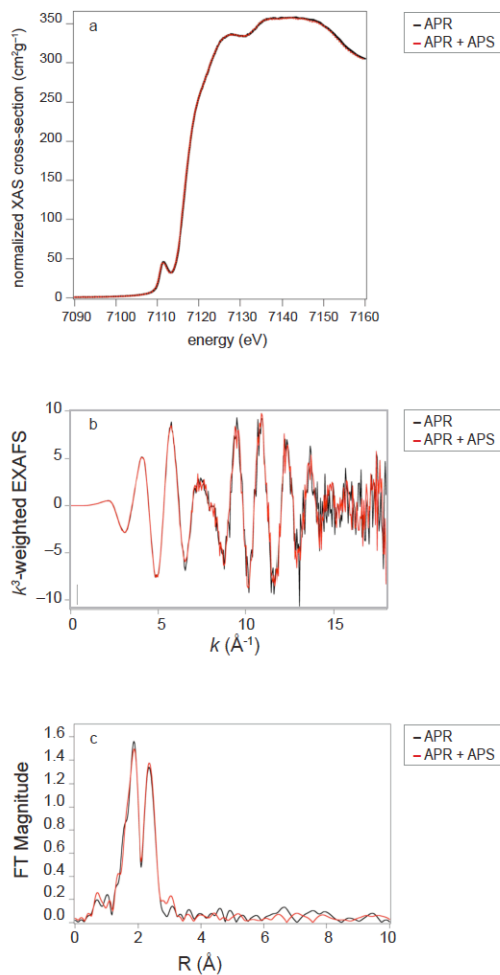
Appendix 4.9.2 Comparison of XAS spectra for MtAPR with and without APS bound. a. XANES spectra; b. k^3 weighted EXAFS; and c. Fourier transforms.

Appendix 4.9.3 Comparison of the EXAFS and Fourier transforms for MtAPR and ferredoxins
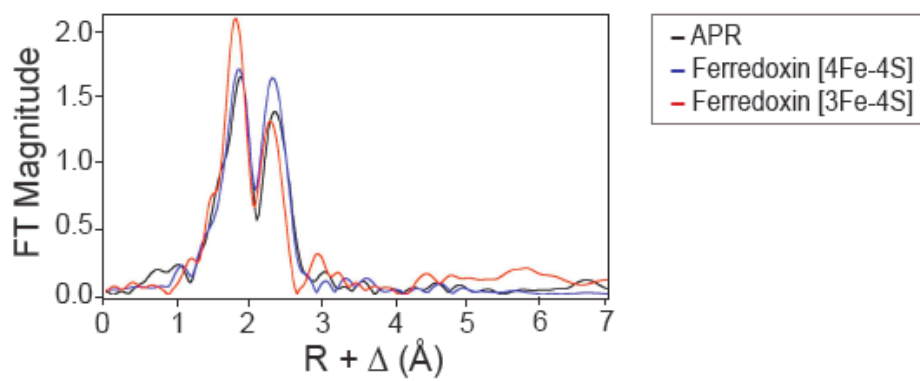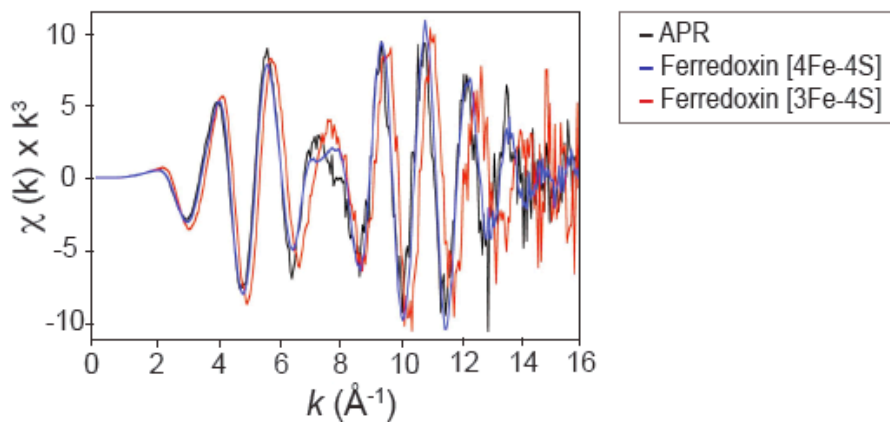
Appendix 4.9.3 Comparison of the k^3 weighted EXAFS (top) and the Fourier transforms (bottom) for MtAPR, [4Fe-4S] and [3Fe-4S] ferredoxins.

4.10 References

1. Williams SJ, Senaratne RH, Mougous JD, Riley LW, Bertozzi CR: **5'-adenosinephosphosulfate lies at a metabolic branch point in mycobacteria**. *Journal of Biological Chemistry* 2002, **277**:32606-32615.

2. Bick JA, Dennis JJ, Zylstra GJ, Nowack J, Leustek T: **Identification of a new class of 5'-adenylylsulfate (APS) reductases from sulfate-assimilating bacteria**. *J Bacteriol* 2000, **182**:135-142.

3. Kopriva S, Buchert T, Fritz G, Suter M, Weber M, Benda R, Schaller J, Feller U, Schurmann P, Schunemann V, et al.: **Plant adenosine 5'-phosphosulfate reductase is a novel iron-sulfur protein**. *J Biol Chem* 2001, **276**:42881-42886.

4. Carroll KS, Gao H, Chen H, Stout CD, Leary JA, Bertozzi CR: **A conserved mechanism for sulfonucleotide reduction**. *PLoS Biology* 2005, **3**:e250.

5. Lampreia J, Pereira AS, Moura JJG: **Adenylylsulfate reductases from sulfate-reducing bacteria.** *Methods Enzymol.* 1994, **243**:241-260.

6. Tsang ML, Schiff JA: **Assimilatory sulfate reduction in an Escherichia coli mutant lacking thioredoxin activity**. *J Bacteriol* 1978, **134**:131-138.

7. Senaratne RH, De Silva AD, Williams SJ, Mougous JD, Reader JR, Zhang T, Chan S, Sidders B, Lee DH, Chan J, et al.: **5'-Adenosinephosphosulphate reductase (CysH) protects Mycobacterium tuberculosis against free radicals during chronic infection phase in mice**. *Mol Microbiol* 2006, **59**:1744-1753.

8. Bhave DP, Muse WB, 3rd, Carroll KS: **Drug targets in mycobacterial sulfur metabolism**. *Infect Disord Drug Targets* 2007, **7**:140-158.

9. Hong JA, Bhave DP, Carroll KS: **Identification of critical ligand binding determinants in Mycobacterium tuberculosis adenosine-5'-phosphosulfate reductase**. *Journal of Medicinal Chemistry* 2009, **52**:5485-5495.

10. Kopriva S, Buchert T, Fritz G, Suter M, Benda R, Schunemann V, Koprivova A, Schurmann P, Trautwein AX, Kroneck PM, et al.: **The presence of an iron-sulfur cluster in adenosine 5'-phosphosulfate reductase separates organisms utilizing adenosine 5'-phosphosulfate and phosphoadenosine 5'-phosphosulfate for sulfate assimilation**. *J Biol Chem* 2002, **277**:21786-21791.

11. Kim SK, Rahman A, Bick JA, Conover RC, Johnson MK, Mason JT, Hirasawa M, Leustek T, Knaff DB: **Properties of the cysteine residues and iron-sulfur cluster of the assimilatory 5'-adenylyl sulfate reductase from Pseudomonas aeruginosa**. *Biochemistry* 2004, **43**:13478-13486.

12. Berndt C, Lillig CH, Wollenberg M, Bill E, Mansilla MC, de Mendoza D, Seidler A, Schwenn JD: **Characterization and reconstitution of a 4Fe-4S adenylyl sulfate/phosphoadenylyl sulfate reductase from Bacillus subtilis**. *J Biol Chem* 2004, **279**:7850-7855.

13. Chartron J, Carroll KS, Shiau C, Gao H, Leary JA, Bertozzi CR, Stout CD: **Substrate recognition, protein dynamics, and iron-sulfur cluster in Pseudomonas aeruginosa adenosine 5'-phosphosulfate reductase**. *Journal of Molecular Biology* 2006, **364**:152-169.

14. Sazanov LA, Hinchliffe P: **Structure of the hydrophilic domain of respiratory complex I from Thermus thermophilus**. *Science* 2006, **311**:1430-1436.

15. Mamedova AA, Holt PJ, Carroll J, Sazanov LA: **Substrate-induced conformational change in bacterial complex I**. *J Biol Chem* 2004, **279**:23830-23836.

16. Carroll KS, Gao H, Chen H, Leary JA, Bertozzi CR: **Investigation of the iron-sulfur cluster in Mycobacterium tuberculosis APS reductase: implications for substrate binding and catalysis**. *Biochemistry* 2005, **44**:14647-14657.

17. Kim SK, Rahman A, Mason JT, Hirasawa M, Conover RC, Johnson MK, Miginiac-Maslow M, Keryer E, Knaff DB, Leustek T: **The interaction of 5'-adenylylsulfate reductase from Pseudomonas aeruginosa with its substrates**. *Biochim Biophys Acta* 2005, **1710**:103-112.

18. Bhave DP, Hong JA, Lee M, Jang W, Krebs C, Carroll KS: **Spectroscopic studies on the [4Fe-4S] cluster in adenosine 5'-phosphosulfate reductase from mycobacterium tuberculosis**. *Journal of Biological Chemistry* 2011, **286**:1216-1226.

19. Torres RA, Lovell T, Noodleman L, Case DA: **Density functional-and reduction potential calculations of Fe4S4 clusters**. *Journal of the American Chemical Society* 2003, **125**:1923-1936.

20. Han W-G, Tajkhorshid E, Suhai S: **QM/MM study of the active site of free papain and of the NMA-papain complex**. *Journal of Biomolecular Structure & Dynamics* 1999, **16**:1019-1032.

21. Kim SK, Rahman A, Mason JT, Hirasawa M, Conover RC, Johnson MK, Miginiac-Maslow M, Keryer E, Knaff DB, Leustek T: **The interaction of 5'-adenylylsulfate reductase from Pseudomonas aeruginosa with its substrates**. *Biochimica et Biophysica Acta* 2005, **1710**:103-112.

22. ADF2008.01. Edited by: SCM, Theoretical Chemistry, Vrije Universiteit, Amsterdam, The Netherlands, http://www.scm.com.

23. te Velde G, Bickelhaupt FM, Baerends EJ, Guerra CF, Van Gisbergen SJA, Snijders JG, Ziegler T: **Chemistry with ADF**. *Journal of Computational Chemistry* 2001, **22**:931-967.

24. Guerra CF, Snijders JG, te Velde G, Baerends EJ: **Towards an order-N DFT method**. *Theoretical Chemistry Accounts* 1998, **99**:391-403.

25. Handy NC, Cohen AJ: **Left-right correlation energy**. *Molecular Physics* 2001, **99**:403-412.

26. Lee CT, Yang WT, Parr RG: **Development of the Colle-Salvetti Correlation-Energy Formula into a Functional of the Electron-Density**. *Physical Review B* 1988, **37**:785-789.

27. Swart M, Ehlers AW, Lammertsma K: **Performance of the OPBE exchange-correlation functional**. *Molecular Physics* 2004, **102**:2467-2474.

28. Perdew JP, Burke K, Ernzerhof M: **Generalized gradient approximation made simple**. *Physical Review Letters* 1996, **77**:3865-3868.

29. Perdew JP, Burke K, Ernzerhof M: **Generalized gradient approximation made simple (vol 77, pg 3865, 1996)**. *Physical Review Letters* 1997, **78**:1396-1396.

30. Becke AD: **Density-Functional Exchange-Energy Approximation with Correct Asymptotic-Behavior**. *Physical Review A* 1988, **38**:3098-3100.

31. Perdew JP: **Density-Functional Approximation for the Correlation-Energy of the Inhomogeneous Electron-Gas**. *Physical Review B* 1986, **33**:8822-8824.

32. Perdew JP: **Correction**. *Physical Review B* 1986, **34**:7406-7406.

33. Baker J, Pulay P: **Assessment of the Handy-Cohen optimized exchange density functional for organic reactions**. *Journal of Chemical Physics* 2002, **117**:1441-1449.

34. Hopmann KH, Ghosh A, Noodleman L: **Density Functional Theory Calculations on Mössbauer Parameters of Nonheme Iron Nitrosyls**. *Inorganic Chemistry* 2009, **48**:9155-9165.

35. Mouesca JM, Chen JL, Noodleman L, Bashford D, Case DA: **Density-Functional Poisson-Boltzmann Calculations of Redox Potentials for Iron-Sulfur Clusters**. *Journal of the American Chemical Society* 1994, **116**:11898-11914.

36. Noodleman L: **Valence bond description of anti-ferromagnetic coupling in transition-metal dimers**. *Journal of Chemical Physics* 1981, **74**:5737-5743.

37. Noodleman L, Case DA: **Density-functional theory of spin polarization and spin coupling in iron-sulfur clusters**. *Advances in Inorganic Chemistry* 1992, **38**:423-470.

38. Noodleman L, Lovell T, Han W-G, Liu T, Torres RA, Himo F: **Density Functional Theory**. In *Comprehensive Coordination Chemistry II, From Biology to Nanotechnology*. Edited by Lever AB: Elsevier Ltd; 2003:491-510. vol 2.]

39. Klamt A, Schüürmann G: **Cosmo - a New Approach to Dielectric Screening in Solvents with Explicit Expressions for the Screening Energy and Its Gradient**. *Journal of the Chemical Society-Perkin Transactions 2* 1993:799-805.

40. Klamt A: **Conductor-Like Screening Model for Real Solvents - a New Approach to the Quantitative Calculation of Solvation Phenomena**. *Journal of Physical Chemistry* 1995, **99**:2224-2235.

41. Klamt A, Jonas V: **Treatment of the outlying charge in continuum solvation models**. *Journal of Chemical Physics* 1996, **105**:9972-9981.

42. Pye CC, Ziegler T: **An implementation of the conductor-like screening model of solvation within the Amsterdam density functional package**. *Theoretical Chemistry Accounts* 1999, **101**:396-408.

43. Gregg EC: **Dielectric Constants of Solids**. In *Handbook of Chemistry and Physics*. Edited by: Chemical Rubber Company; 1976:E55-E60.

44. Harvey SC, Hoekstra P: **Dielectric-Relaxation Spectra of Water Adsorbed on Lysozyme**. *Journal of Physical Chemistry* 1972, **76**:2987-2994.

45. Bone S, Pethig R: **Dielectric Studies of the Binding of Water to Lysozyme**. *Journal of Molecular Biology* 1982, **157**:571-575.

46. Bone S, Pethig R: **Dielectric Studies of Protein Hydration and Hydration-Induced Flexibility**. *Journal of Molecular Biology* 1985, **181**:323-326.

47. Dwyer JJ, Gittis AG, Karp DA, Lattman EE, Spencer DS, Stites WE, Garcia-Moreno B: **High apparent dielectric constants in the interior of a protein reflect water penetration**. *Biophysical Journal* 2000, **79**:1610-1620.

48. Sham YY, Muegge I, Warshel A: **The effect of protein relaxation on charge-charge interactions and dielectric constants of proteins**. *Biophysical Journal* 1998, **74**:1744-1753.

49. Bashford D, Karplus M: **Pkas of Ionizable Groups in Proteins - Atomic Detail from a Continuum Electrostatic Model**. *Biochemistry* 1990, **29**:10219-10225.

50. Fitch CA, Karp DA, Lee KK, Stites WE, Lattman EE, Garcia-Moreno B: **Experimental pK(a) values of buried residues: Analysis with continuum methods and role of water penetration**. *Biophysical Journal* 2002, **82**:3289-3304.

51. Antosiewicz J, McCammon JA, Gilson MK: **The determinants of pK(a)s in proteins**. *Biochemistry* 1996, **35**:7819-7833.

52. Simonson T, Brooks CL: **Charge screening and the dielectric constant of proteins: Insights from molecular dynamics**. *Journal of the American Chemical Society* 1996, **118**:8452-8458.

53. Karp DA, Gittis AG, Stahley MR, Fitch CA, Stites WE, Garcia-Moreno B: **High apparent dielectric constant inside a protein reflects structural reorganization coupled to the ionization of an internal Asp**. *Biophysical Journal* 2007, **92**:2041-2053.

54. Harms MJ, Schlessman JL, Chimenti MS, Sue GR, Damjanovic A, Garcia-Moreno B: **A buried lysine that titrates with a normal pK(a): Role of conformational flexibility at the protein-water interface as a determinant of pK(a)values**. *Protein Science* 2008, **17**:833-845.

55. Bondi A: **van der Waals Volumes and Radii**. *Journal of Physical Chemistry* 1964, **68**:441-451.

56. Li J, Nelson MR, Peng CY, Bashford D, Noodleman L: **Incorporating Protein Environments in Density Functional Theory: A Self-Consistent Reaction Field Calculation of Redox Potentials of [2Fe2S] Clusters in Ferredoxin and Phthalate Dioxygenase Reductase**. *Journal of Physical Chemistry* 1998, **102**:6311-6324.

57. Han WG, Noodleman L: **Structural model studies for the high-valent intermediate Q of methane monooxygenase from broken-symmetry density functional calculations**. *Inorganica Chimica Acta* 2008, **361**:973-986.

58. Martinez-Pinedo G, Schwerdtfeger P, Caurier E, Langanke K, Nazarewicz W, Sohnel T: **Nuclear quadrupole moment of Fe-57 from microscopic nuclear and atomic calculations**. *Physical Review Letters* 2001, **87**:062701(062701-062704).

59. Sinnecker S, Slep LD, Bill E, Neese F: **Performance of nonrelativistic and quasi-relativistic hybrid DFT for the prediction of electric and magnetic hyperfine parameters in 57Fe Mossbauer spectra**. *Inorg Chem* 2005, **44**:2245-2254.

60. Breneman CM, Wiberg KB: **Determining Atom-Centered Monopoles from Molecular Electrostatic Potentials - the Need for High Sampling Density in Formamide Conformational-Analysis**. *Journal of Computational Chemistry* 1990, **11**:361-373.

61. Shulman GR, Yafet Y, Eisenberger P, Blumberg WE: **Observations and interpretation of x-ray absorption edges in iron compounds and proteins**. *Proc Natl Acad Sci U S A* 1976, **73**:1384-1388.

62. Penner-Hahn JE, Scott RA, Hodgson KO, Doniach S, Desjardina SR, Solomon EI: **Observation of an electric quadrupole transition in the X-ray absorption spectrum of a Cu(II) complex.** *Chem Phys Lett* 1982, **88**:595-598.

63. Westre TE, Kennepohl P, DeWitt JG, Hedman B, Hodgson KO, Solomon EI: **A multiplet analysis of Fe K-edge 1s --> 3d pre edge features of iron complexes.** *Journal of the American Chemical Society* 1997, **119**:6297-6314.

64. Riggs-Gelasco PJ, Mei R, Ghanotakis DF, Yocum CF, Penner-Hahn JE: **X-ray Absorption Spectroscopy of Calcium-Substituted Derivatives of the Oxygen-Evolving Complex of Photosystem II**. *Journal of the American Chemical Society* 1996, **118**:2400-2410.

65. Han W-G, Lovell T, Liu T, Noodleman L: **A density functional evaluation of an Fe(III)-Fe(IV) model dilron cluster: Comparisons with ribonucleotide reductase intermediate X**. *Inorganic Chemistry* 2003, **42**:2751-2758.

66. Han W-G, Lovell T, Liu T, Noodleman L: **Density functional study of a μ-1,1-carboxylate bridged Fe(III)-O-Fe(IV) model complex. 2. Comparison with ribonucleotide reductase intermediate X**. *Inorganic Chemistry* 2004, **43**:613-621.

67. Han WG, Liu TQ, Lovell T, Noodleman L: **Active site structure of class I ribonucleotide reductase intermediate X: A density functional theory analysis of structure, energetics, and spectroscopy**. *Journal of the American Chemical Society* 2005, **127**:15778-15790.

68. Han W-G, Giammona DA, Bashford D, Noodleman L: **Density functional theory analysis of structure, energetics, and spectroscopy for the Mn-Fe active site of Chlamydia trachomatis ribonucleotide reductase in four oxidation states**. *Inorganic Chemistry* 2010, **49**:7266-7281.

69. Lewis A, Bumpus JA, Truhlar DG, Cramer CJ: **Molecular modeling of environmentally important processes: Reduction potentials**. *Journal of Chemical Education* 2004, **81**:596-604.

70. Lewis A, Bumpus JA, Truhlar DG, Cramer CJ: **Molecular modeling of environmentally important processes: Reduction potentials (vol 81, pg 596, 2004)**. *Journal of Chemical Education* 2007, **84**:934.

71. Han W-G, Noodleman L: **DFT calculations for intermediate and active states of the diiron center with a tryptophan or tyrosine radical in** *Escherichia coli* **ribonucleotide reductase**. *Inorganic Chemistry* 2011, **50**:2302-2320.

72. Smith ET, Blamey JM, Zhou ZH, Adams MWW: **A Variable-Temperature Direct Electrochemical Study of Metalloproteins from Hyperthermophilic Microorganisms Involved in Hydrogen-Production from Pyruvate**. *Biochemistry* 1995, **34**:7161-7169.

73. Hatchikian EC, Cammack R, Patil DS, Robinson AE, Richards AJM, George S, Thomson AJ: **Spectroscopic Characterization of Ferredoxin-I and Ferredoxin-Ii from Desulfovibrio-Africanus**. *Biochimica et Biophysica Acta* 1984, **784**:40-47.

74. Mullinger RN, Cammack R, Rao KK, Hall DO, Dickson DPE, Johnson CE, Rush JD, Simopoulos A: **Physicochemical Characterization of 4-Iron-4-Sulfide Ferredoxin from Bacillus-Stearothermophilus**. *Biochemical Journal* 1975, **151**:75-83.

75. Niu S, Ichiye T: **Insight into environmental effects on bonding and redox properties of [4Fe-4S] clusters in proteins**. *Journal of the American Chemical Society* 2009, **131**:5724-5725.

76. Kakuta Y, Petrotchenko EV, Pedersen LC, Negishi M: **The sulfuryl transfer mechanism. Crystal structure of a vanadate complex of estrogen sulfotransferase and mutational analysis**. *Journal of Biological Chemistry* 1998, **273**:27325-27330.

77. Noodleman L, Lovell T, Han WG, Li J, Himo F: **Quantum chemical studies of intermediates and reaction pathways in selected enzymes and catalytic synthetic systems**. *Chem Rev* 2004, **104**:459-508.

78. Asthagiri D, Dillet V, Liu T, Noodleman L, Van Etten RL, Bashford D: **Density functional study of the mechanism of a tyrosine phosphatase: I. Intermediate formation**. *J Am Chem Soc* 2002, **124**:10225-10235.

79. Asthagiri D, Liu T, Noodleman L, Van Etten RL, Bashford D: **On the role of the conserved aspartate in the hydrolysis of the phosphocysteine intermediate of the low molecular weight tyrosine phosphatase**. *J Am Chem Soc* 2004, **126**:12677-12684.

80. Catrina I, O'Brien PJ, Purcell J, Nikolic-Hughes I, Zalatan JG, Hengge AC, Herschlag D: **Probing the origin of the compromised catalysis of E. coli alkaline phosphatase in its promiscuous sulfatase reaction**. *J Am Chem Soc* 2007, **129**:5760-5765.

81. Chapman E, Bryan MC, Wong CH: **Mechanistic studies of beta-arylsulfotransferase IV**. *Proc Natl Acad Sci U S A* 2003, **100**:910-915.

82. Cleland WW, Hengge AC: **Enzymatic mechanisms of phosphate and sulfate transfer**. *Chem Rev* 2006, **106**:3252-3278.

83. Gao H, Leary J, Carroll KS, Bertozzi CR, Chen H: **Noncovalent complexes of APS reductase from M. tuberculosis: delineating a mechanistic model using ESI-FTICR MS**. *J Am Soc Mass Spectrom* 2007, **18**:167-178.

84. George GN: *EXAFSPAK* and *EDG-FIT*. Edited by.

85. Ankudinov AL, Rehr JJ: **Relativistic calculations of spin-dependent x-ray absorption spectra**. *Physical Review B* 1997, **56**:R1712-R1716.

86. McMaster WH, Del Grande NK, Mallet JH, Hubbell JH: **Compilation of X-Ray Cross Scetions**. *University of California, Lawrence Radiation Laboratory Report No. UCRL-50174* 1969, **Sec. II, Rev. 1 (NTIS)**:350.

87. Weng TC, Waldo GS, Penner-Hahn JE: **A method for normalization of X-ray absorption spectra**. *J Synchrotron Radiat* 2005, **12**:506-510.

Chapter 5

Iron-Sulfur Cluster Engineering Provides Insight into the Evolution of

Substrate Specificity among the Family of Sulfonucleotide Reductases

This work has in part been submitted for publication as "Iron-Sulfur Cluster Engineering Provides Insight into the Evolution of Substrate Specificity among the Family of Sulfonucleotide Reductases" **2011**. Manuscript under review in ACS Chemical Biology. I performed the biochemical, metalloengineering and spectroscopic experiments, prepared samples for Mössbauer experiments and analyzed all the data.

5.1 Abstract

Assimilatory sulfate reduction supplies prototrophic organisms with reduced sulfur that is required for the biosynthesis of all sulfur-containing metabolites, including the amino acids cysteine and methionine. The reduction of sulfate requires its activation *via* an ATP-dependent activation to form adenosine-5'-phosphosulfate (APS). Depending on the organism, APS can be reduced directly to sulfite by APS reductase (APR) or undergo a second phosphorylation to yield 3'-phosphoadenosine-5'-phosphosulfate (PAPS), the substrate for PAPS reductase (PAPR). These essential enzymes have no human homolog, rendering them an attractive target for the development of novel antibacterial drugs and herbicides. APR and PAPR share sequence and structure homology as well as a common catalytic mechanism, but the enzymes are distinguished by two features, namely, the amino acid sequence of the phosphate-binding loop

(P-loop) and an iron-sulfur cofactor in APRs. Based on the crystal structures of APR and PAPR, two P-loop residues are proposed to determine substrate specificity; however, this hypothesis has not been tested experimentally. In contrast to this prevailing view, we report here that the P-loop motif has a modest effect on substrate discrimination. Instead, by means of metalloprotein engineering, spectroscopic and kinetic analyses, we demonstrate that the iron-sulfur cluster cofactor enhances APS reduction by nearly 1000-fold, thereby playing a pivotal role in substrate specificity and catalysis. These findings offer new insights into the evolution of this enzyme family, and have broader implications regarding the function of protein-bound iron-sulfur clusters.

5.2 Introduction

Assimilatory sulfate reduction supplies prototrophic organisms with reduced sulfur that is required for the biosynthesis of all sulfur-containing metabolites, including the amino acids cysteine and methionine [1,2]. The reduction of sulfate requires its activation by an ATP-dependent activation to form adenosine-5'-phosphosulfate (APS). For incorporation of sulfur into biomolecules, the sulfate in APS must be reduced to sulfite and finally into sulfide. In plants, algae, and many bacteria, APS can be reduced directly to sulfite by APS reductase (APR); alternatively, in fungi, some cyanobacteria, and γ-proteobacteria, this compound requires a second phosphorylation step to yield 3'-phosphoadenosine-5'-phosphosulfate (PAPS), the substrate for PAPS reductase (PAPR; Scheme
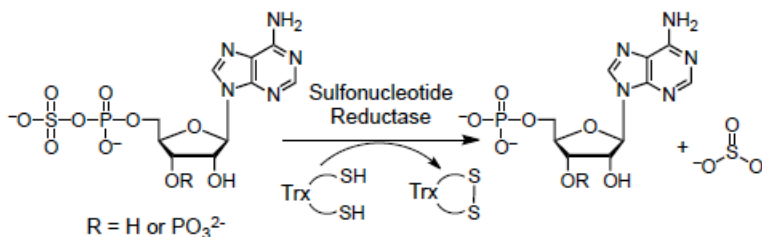
Scheme 5.1 Reaction catalyzed by sulfonucleotide reductases. The reaction is catalyzed by APR when the substrate is APS (R = H) and by PAPR when the substrate is PAPS (R = PO_3^{2-}).

160

5.1, Table 5.1 and Figure 5.1). These essential enzymes, collectively known as sulfonucleotide reductases (SRs), have no human homolog, rendering them an attractive target for the development of novel antibacterial drugs and herbicides [3-6].

The importance of SR for microbial and plant survival have motivated investigations of their catalytic and structure [6-14]. These studies support the mechanism shown in Scheme 5.2, which involves nucleophilic attack
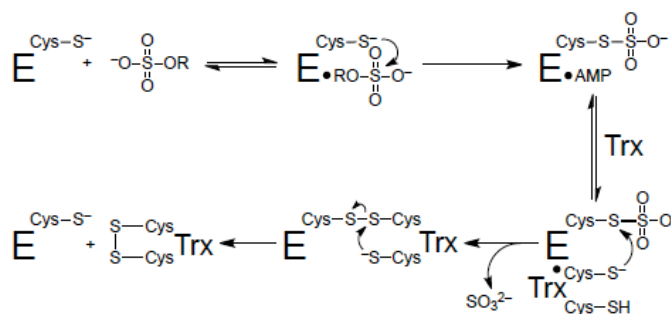
Scheme 5.2 Proposed mechanism of sulfonucleotide reduction

by a conserved C-terminal cysteine residue on the substrate leading to the formation of a covalent enzyme *S*-sulfocysteine intermediate. Sulfite is then released by thiol-disulfide exchange with free thioredoxin (Trx) in bacterial and fungal SRs or through the action of a C-terminal Trx-like domain in plants. Therefore, the general features of the thiol reaction chemistry are shared despite the differences in substrate. SRs are homologous in sequence (~25% identity; Appendix 5.6.3), particularly within active site residues that line the active site (~50% identity and 75% similarity; Appendix 5.6.4) and share a common three-dimensional structure (1.2 Å rms deviation; Figure 5.2a) [8,15]. The SR monomer adopts a Rossman-like fold and is characterized by four conserved structural elements that define the active site: the LTDG motif, phosphate-binding loop (P-loop), Arg-loop, and C-terminal ECGLH segment with the catalytic cysteine (Appendix 5.6.3).

Upon closer inspection sequence and structure alignments reveal two key differences between APR and PAPR, namely, the amino acid sequence of the P-loop and the presence of the cysteine motif, CC...CXXC, in APR. The P-loop of APR is typically comprised of an SFS–GAED motif while the corresponding sequence in PAPR is SSSFGIQA (Figure 5.1a and b). In contrast to the typical role for the P-loop in binding a 5'-phosphate group, crystal structures show that the P-loop interacts with the APS O3' hydroxyl or the PAPS 3'-phosphate (Figure 5.2b and c). The four additional cysteine residues in APR coordinate an iron-sulfur cluster, whereas the cofactor is replaced by the YN...DXXT motif in PAPR (Figure 5.1a and c and Figure 5.2d and e). Functional analysis indicates that when the [4Fe-4S] cofactor is present, it is required for catalytic activity; however, the cluster is not involved in redox chemistry and does not bind directly to
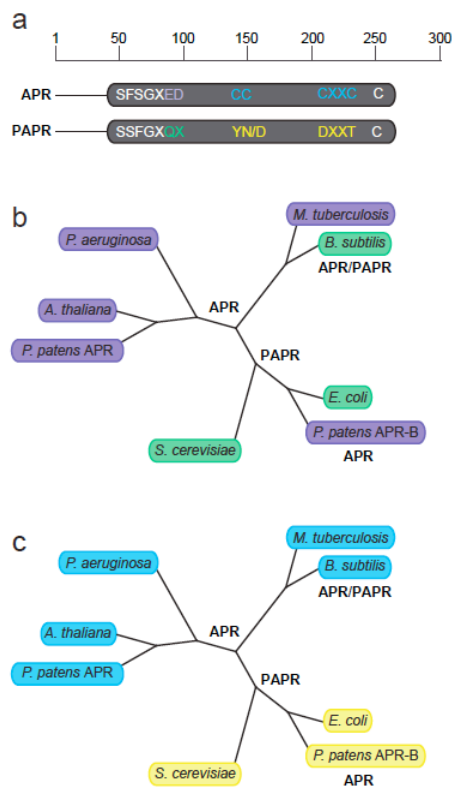
Figure 5.1 Domain organization and phylogenetic classification in the sulfonucleotide reductase family. All SRs have a catalytic cysteine at the end of the C-terminus. a) Bacterial APRs possess the cysteine motif CC...CXXC that coordinates a [4Fe-4S] cluster (blue). In PAPRs, conserved residues replace the cysteine motif (yellow). The phosphate–binding loop in APR is terminated by two negatively charged residues (purple). The 3'-phosphate moiety of PAPS can be accommodated by the P-loop motif of PAPR as it bears residues with small and neutral side chains (green). b) and c) Dendrograms illustrating the sequence homology between enzymes within the SR family. The sequence alignment was performed using ClustalW (Larkin, 2007) and the tree was constructed using the Geneious program (Drummond, 2011). Each of the three subclasses of SRs is clearly delineated: APRs from higher plants with their unique C-terminal domain (*A. thaliana, P. patens*-APR), bacterial APRs (*P. aeruginosa, M. tuberculosis, B. subtilis*) and PAPRs (*E. coli, P. patens-APR-B and S. cerevisiae*). Differentiation in the P-loop region (b) and iron-sulfur cluster coordinating residues (c) of the SRs is indicated by color: purple, APR-like; green, PAPR-like; blue, posses the [4Fe-4S] cluster; yellow, lack the [4Fe-4S] cluster. APR from *B. subtilis* is unique and can reduce both APS and PAPS.

APS [6,8,16]. Two interesting exceptions exist in *Bacillus subtilis*, which harbors the cluster, but can utilize both APS and PAPS as substrates [Bs(P)APR] [17], and the moss *Physcomitrella patens*, which lacks the cysteine pairs and associated cofactor, yet can reduce APS (PpAPR-B) [18]. Notably, these SR variants exhibit 100- to 1000-fold decreases in their second-order rate constants (k_{cat}/K_m) for substrate reduction (Table 5.1).   Based on the aforementioned observations, it has been proposed that the P-loop is the principle determinant of substrate specificity in these enzymes [7-10], and that the [4Fe-4S] cluster plays a structural and/or regulatory role [8,16,17].

Table 5.1 Apparent second-order rate constants (k_{cat}/K_m) for assimilatory SRs. Activities were measured with purified recombinant enzymes, as production of sulfite from varying concentrations of [^{35}S]-APS and [^{35}S]-PAPS, in the presence of DTT and recombinant thioredoxin from *E. coli* as the electron donor.

	Iron-sulfur cluster	Substrate	k_{cat}/K_m (M^{-1}min^{-1})	Preference[a]
P. aeruginosa APR[b]	Yes	APS	2.0×10^8	APS
		PAPS	1.6×10^4	
M. tuberculosis APR[b]	Yes	APS	2.5×10^8	APS
		PAPS	6.0×10^4	
B. subtilis APR[c]	Yes	APS	3.1×10^6	None
		PAPS	1.6×10^6	
A. thaliana APR2[d]	Yes	APS	3.8×10^8	APS
		PAPS[d]	1.3×10^4	
P. patens APR[d]	Yes	APS	3.8×10^8	APS
		PAPS[d]	3.8×10^4	
E. coli PAPR[b]	No	APS	7.2×10^2	PAPS
		PAPS	2.3×10^8	
P. patens APR-B[d]	No	APS	2.1×10^5	APS
		PAPS	2.2×10^2	

[a]Defined as difference in substrate utilization of ≥10^2. Values measured at [b]pH 8.0, [c]pH 8.0 [17], [d]pH 9.0 [18]. [e]Value estimated as the higher limit from ref. 18.

Much effort has been made to understand substrate specificity in enzymes and several attempts have been made to rationally alter the specificity of an enzyme with sequence and structural information as the blueprint for redesign [19]. One of the first successful examples was of changing the coenzyme specificity of *Escherichia coli* glutathione reductase from NADP to NAD [20]. Structurally, NADP and NAD differ by a phosphate group at the 3'-postition of the adenosine 5'-phosphate (AMP) moiety, reminiscent of APS and PAPS. In glutathione reductase, the switch in coenzyme preference was accomplished by changing amino acids within the P-loop. Similarly, protein engineering has been used successfully by Shokat and coworkers to alter the nucleotide specificity of the prototypical tyrosine kinase, Src, to accept non-native nucleotides [21]. This concept was subsequently extended to redesign kinase active sites to accept unique nucleotide inhibitors to facilitate direct identification of kinase targets [22]. Overall these studies demonstrate that enzyme redesign is a powerful tool in exploiting substrate recognition elements to elucidate the catalytic mechanism and function of an enzyme.

Although it has been proposed that SR substrate specificity is dictated by the P-loop, this hypothesis has not yet been tested and, moreover, does not address the potential role of the iron-sulfur cluster. To gain insight into the forces driving specificity and catalytic efficiency of SRs we have employed metalloprotein engineering, spectroscopic and kinetic analyses. On the basis of our findings, we propose that the iron-sulfur cluster is a major determinant of specificity in this family of enzymes, specifically by enhancing the efficacy of the chemical step of catalysis. In this way, our findings offer new perspectives on the evolution of SRs, the function of protein-bound iron-sulfur clusters, and hold value for the development of inhibitors for SRs, a validated target for antibacterial therapy, including tuberculosis [5,23,24].

5.3 Results

The P-loop residues in APRs have the SFS–GAED motif while the corresponding motif in PAPR consists of SSSFGIQA. In APR, the glutamate and aspartate residues interact with three P-loop amide groups and are positioned above the dipole of the α3 helix, as if they were mimicking the interaction of a negatively charged phosphate (Figure 5.2b and c). Conversely, the replacement of these acidic residues with Gln and Ala in PAPR would facilitate interaction of the amide groups with a 3'-phosphate and accommodate the bulkier moiety. To investigate this proposal, we generated E65Q, D66A and E65Q D66A variants of APR from *Pseudomonas aeruginosa* (PaAPR) as well as Q57E, A58D, and Q57E A58D variants of PAPR from *Escherichia coli* (EcPAPR). Of note, the enzymes from these particular species were chosen on the basis of available structural and functional information. We first tested the activity of the variants with native and non-native substrates. Interestingly, none of these substitutions increased k_{cat}/K_m for the non-native substrate (Appendix 5.6.1). In addition, the D66A and E65Q single substitutions in PaAPR
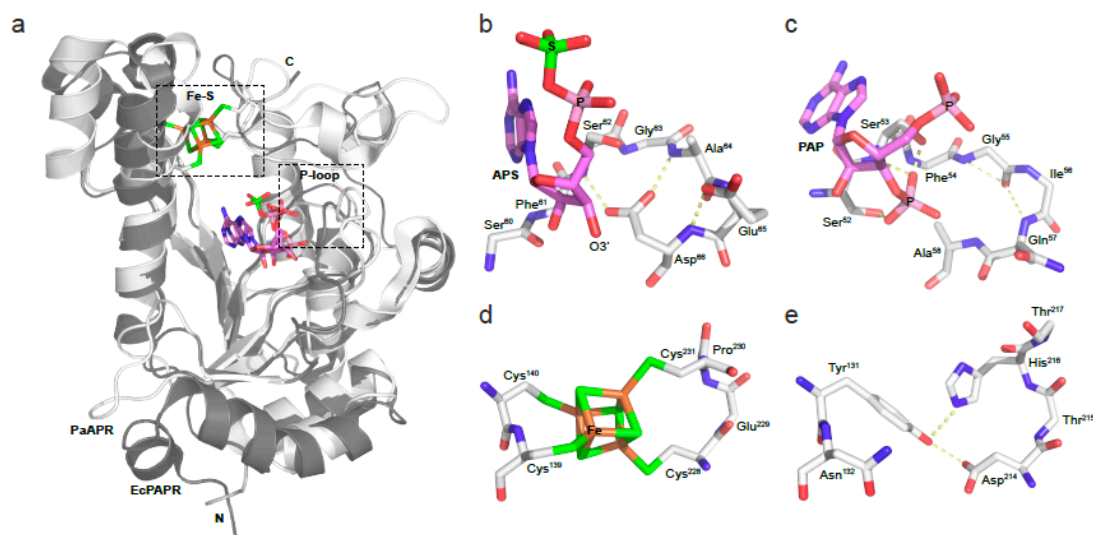
Figure 5.2 Comparison of putative substrate binding elements SRs. a. Superposition of the structures of EcPAPR in charcoal (PDB deposition 2O8V) and PaAPR in white (PDB deposition 2GOY) showing the positions of the [4Fe-4S] cluster, P-loop region, and APS or PAP ligand (modeled from PDB deposition 2OQ2). The carboxyl- and amino- termini of the proteins are indicated by C and N, respectively. Comparison between the P-loop regions of b. PaAPR bound to APS and c. EcPAPR bound to PAP. Hydrogen bonding interactions are indicated by yellow dashes. Comparison of d. the iron-sulfur cluster coordination site in PaAPR and e. the corresponding semi-conserved residues in EcPAPR.

had at most a 10-fold effect on APS reduction, whereas the Q65E and A58D replacements in EcPAPR exhibited a 1000-fold effect on the reduction of PAPS. All double mutants were significantly impaired relative to their wild-type counterparts. To complement this analysis, we measured the dissociation constants (K_d) for the reaction products AMP and 3'-phosphoadenosine-5'-phosphate
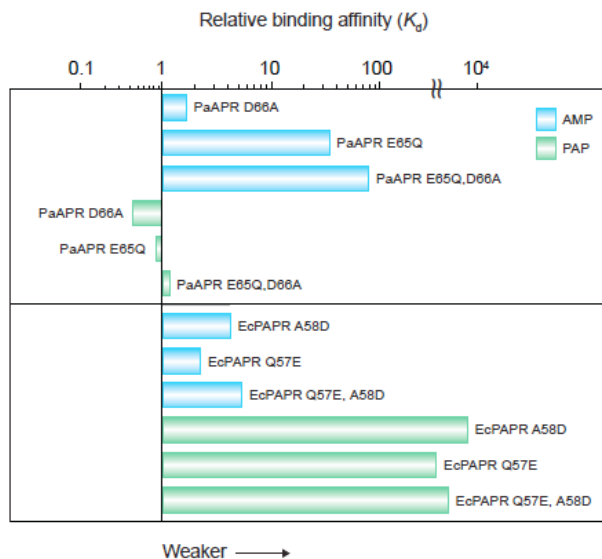
Figure 5.3 Relative change in ligand dissociation constants for wild-type APR or PAPR and P-loop variants. The ratio of K_d values is plotted relative to wild-type enzymes. Blue and green bars indicate inhibition by AMP and PAP, respectively. K_d values and other kinetic parameters for all proteins are presented in Appendix 5.6.1.

(PAP) for the P-loop variants (Figure 5.3). PaAPR variants showed at most a 2.5-fold enhancement in PAP binding, whereas no EcPAPR substitution enhanced association with AMP. Analogous to kinetic studies, the binding of P-loop variants to the native ligand was diminished, relative to the wild-type enzyme. Overall, this analysis shows that modification of the P-loop decreases binding and catalysis for the native ligand; however, the converse does not hold true as amino acid replacements do not correlate with enhancements for the non-cognate substrate or ligand.

As the P-loop substitutions did not succeed in altering substrate specificity, a possible contribution of the iron-sulfur cluster was investigated. Based on the similar three-dimensional fold of APR and PAPR, we reasoned that EcPAPR residues (Y131, N132, D214, and T218) might be replaced by cysteine, and enable coordination of an iron-sulfur cluster (Figure 5.2d and e).

Thus, site-directed mutagenesis was employed and the resulting protein was co-expressed in bacteria with the pDB1282 plasmid that harbors the *isc* operon for cluster assembly [25]. This approach afforded 10 mg of protein per liter of culture. The resulting enzyme, termed EcPAPR4cys, eluted as a dimer from the gel filtration column, analogous to wild-type EcPAPR, and the purity was estimated to be greater than 95% (Figure 5.4a, inset). The UV-Vis absorbance spectrum of EcPAPR4cys showed a maximum in the visible range at 410 nm, which is similar to the [4Fe-4S] chromophore of PaAPR (Figure 5.4a) [16]. However, ICP analysis of EcPAPR4cys showed that each mole of protein contained only 2.3 mole of iron. The amount of iron could not be increased by reconstitution or anaerobic purification (data not shown).

To identify the types and relative amounts of the Fe/S clusters in EcPAPR4cys, we employed a combination of Mössbauer and EPR spectroscopies and analytical methods. ICP analysis of a
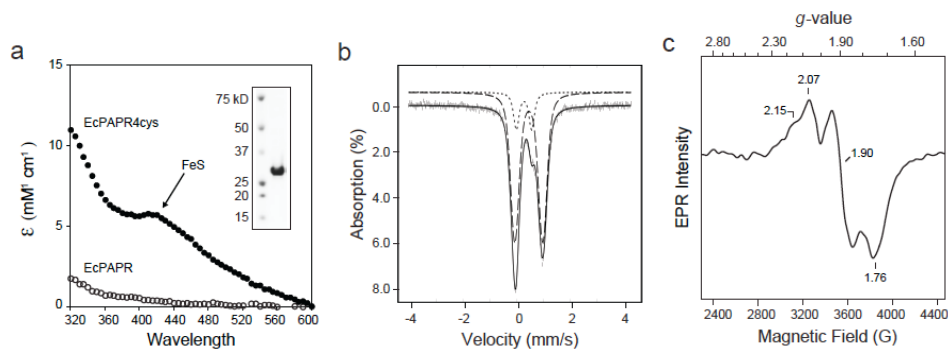
Figure 5.4 Spectroscopic characterization of EcPAPR4cys. a. UV-vis absorption spectra of EcPAPR and EcPAPR4cys. UV-Vis absorption of 10 μM EcPAPR (O) or EcPAPR4cys (●) in buffer containing 50 mM Tris–HCl, 150 mM NaCl (pH 7.4 at 25 °C) and 10% (v/v) glycerol. *Inset*, SDS-PAGE gel with Coomassie staining that shows purified EcPAPR4cys at an apparent molecular mass of ~28 kDa, corresponding to the molecular weight of the monomer. b. 4.2-K/53-mT Mössbauer spectra of 1 mM EcPAPR4cys. Experimental spectra are shown as vertical bars. The line is a quadrupole doublet simulation with the following parameters: (– –) δ_1= 0.45 mm/s, ΔE_{Q1}= 1.03 mm/s (82%) and (…) δ_2= 0.27 mm/s, $\Delta E_{Q,2}$= 0.57 mm/s (15%). The parameters for the majority species (– –) are consistent with a $[4Fe-4S]^{2+}$ cluster and the parameters for the minor species (…) are consistent with a $[2Fe-2S]^{2+}$ cluster. The remaining area of the spectrum is a broad featureless absorbing species that accounts for approximately 3% of the total area of the spectrum. c. EPR spectrum of photoreduced EcPAPR4cys. Anaerobic EcPAPR4cys (250 μM) was photoreduced as described in Experimental Procedures. The EPR spectrum was recorded at 10 K and the instrument parameters were: microwave power, 10 mW; receiver gain, 2 x 10^4; modulation amplitude, 10 G; and microwave frequency, 9.43 GHz.

sample of EcPAPR4cys enriched in [57]Fe for Mössbauer spectroscopy reveals 2.0 Fe per polypeptide. The 4.2-K/53-mT Mössbauer spectrum of this sample (Figure 5.4b) shows that the majority (82%) of the iron associated with EcPAPR gives rise to a quadrupole doublet with parameters typical of [4Fe-4S]$^{2+}$ clusters: isomer shift (δ) of 0.45 mm/s and quadrupole splitting parameter (ΔE_Q) of 1.03 mm/s. The remaining iron (15%) exhibited properties reminiscent of a [2Fe-2S]$^{2+}$ cluster (δ = 0.27 mm/s, ΔE_Q = 0.57 mm/s). The [2Fe-2S]$^{2+}$ form is also observed in plant and bacterial APRs and most likely results from partial degradation of the [4Fe-4S] cluster [16,17]. An identical EPR sample does not reveal the spectroscopic signatures of paramagnetic Fe/S clusters with S = 1/2 ground state (data not shown). Taken together, Mössbauer and ICP analyses indicate that approximately half of all EcPAPR4cys monomers coordinate a [4Fe-4S] cluster.

Although the iron-sulfur cluster in APR does not undergo redox chemistry during catalysis, the reduced form of the cluster can serve as a useful tool for characterization and mechanistic studies. Along these lines, we have recently characterized the 1+ state of the [4Fe-4S] cluster in APR from *Mycobacterium tuberculosis* (MtAPR) using electron paramagnetic resonance (EPR) spectroscopy [16]. Like MtAPR, the EPR signal of the chemically reduced EcPAPR4cys is broad, but shows rhombic symmetry with apparent *g*-values of 2.07, 1.90 and 1.76, which are characteristic of a [4Fe-4S] cluster in the 1+ state (Figure 5.4c). Spin quantitation of the EPR signals from g = 2.33 to 1.58 indicate low reduction efficiency (0.04 spins/mol compared to 0.4 spins/mol for MtAPR). A likely explanation for the lower signal intensity is that the constellation of residues surrounding the EcPAPR4cys cluster differs from MtAPR, resulting in distinct electronic environments and reduction potentials (Appendix 5.6.4). Nonetheless, the overall

similarity of Mössbauer and EPR parameters to those observed for MtAPR provides further

support for the coordination of a [4Fe-4S]$^{2+}$ cluster by EcPAPR4cys.

We next evaluated the effect of the [4Fe-4S] cluster in EcPAPR4cys on the ability of EcPAPR to use PAPS or APS as substrates. To this end, we first monitored formation of the *S*-sulfocysteine intermediate, which is stable in plant and bacterial (P)APRs in the absence of Trx [6,26]. EcPAPR4cys was incubated in the presence or absence of APS or PAPS and the mass of the intact protein was analyzed by electrospray ionization mass spectrometry (ESI-MS). The deconvoluted *m/z* values obtained from these experiments are listed in Appendix 5.6.2. In the absence of substrate, the mass spectrum of EcPAPR4cys is consistent with the molecular weight of the apoenzyme (Figure 5.5a, solid circles). Incubation of EcPAPR4cys with PAPS resulted in formation of a new series of ions with a molecular weight 80 Da higher than enzyme alone, corresponding to the *S*-sulfocysteine adduct (Figure 5.5b, asterisks). In the presence of APS two series of ions were observed

Figure 5.5 Mass-spectrometric analysis of intact EcPAPR4cys. ESI mass spectra of EcPAPR4cys (10 µM) without ligand (a), with PAPS (b) and with APS (c). Ions correspond to the enzyme (E, •) and the covalent enzyme *S*-sulfocysteine intermediate (E-SO$_3^-$, ✱). The calculated masses after deconvolution of *m/z* values are 28829.23 Da (a), 28908.55 Da (b), 28829.23 and 28909.54 Da (c). MS analysis was performed under denaturing conditions, generating the apoenzyme without the iron-sulfur cluster. See also Appendix 5.6.2.

corresponding to molecular weight of the apoenzyme (Figure 5.5c, solid circles) and to the *S*-sulfocysteine intermediate (Figure 5.5c, asterisks). Quantitative adduct formation was likely

limited by our finding that not all EcPAPR4cys monomers are associated with a [4Fe-4S] cluster. Control experiments performed with wild-type enzymes and native substrates also showed the expected mass shifts (Appendix 5.6.2). These data show that EcPAPR4cys can generate the adduct with PAPS or APS as a substrate.

As reported above, EcPAPR4cys forms an enzyme *S*-sulfocysteine intermediate with APS, which should be competent for reduction by Trx to generate sulfite. To test this possibility, we performed gel-labeling experiments with [^{35}S]-labeled PAPS or APS (Appendix 5.6.5). Incubation of [^{35}S]-PAPS or [^{35}S]-APS with EcPAPR4Cys, and analysis of the reaction by nonreducing SDS-PAGE, showed a radioactive band at the molecular weight of EcPAPR indicating transfer of the [^{35}S]-label to the enzyme. Addition of Trx to this enzyme intermediate resulted in the complete loss of radiolabeling, as expected for reduction of the thio-sulfate bond. Analogous experiments were carried out using wild-type EcPAPR, which demonstrated comparable labeling with [^{35}S]-PAPS; by contrast, only a faint band was seen in reactions that contained [^{35}S]-APS. Taken together, the MS and radiolabeling experiments demonstrate that EcPAPR4cys forms a catalytically competent *S*-sulfocysteine intermediate with PAPS or APS, and that the variant reacts with APS with an enhanced rate compared with wild-type protein.

Having established that the EcPAPR4cys iron-sulfur protein exhibits activity, we proceeded to measure kinetic parameters for this variant. Table 5.2 shows the resultant data and is presented alongside data obtained for wild-type EcPAPR and PaAPR (see also Appendix 5.6.6-5.6.11). The second-order rate constant also known as the specificity constant (k_{cat}/K_m; representing the reaction for free enzyme and substrate) demonstrates that EcPAPR4cys catalyzes APS reduction with approximately 600-fold less efficiency relative to PaAPR. Importantly, however, that the

rate of APS reduction by the variant protein is nearly 1000-fold increased compared to wild-type EcPAPR. On the other hand, the k_{cat}/K_m for reaction of EcPAPR4cys with PAPS is almost the same as the native enzyme.

Table 5.2 Single-turnover rate and equilibrium constants for PaAPR, EcPAPR and EcPAPR4cys.[a]

Enzyme	Iron content (mol Fe/mol protein)	k_{cat}/K_m $(M^{-1} min^{-1})^b$		k_{max} $(min^{-1})^c$		$K_{1/2}$ (µM)		K_d^{AMP} $(µM)^g$	K_d^{PAP} $(µM)^g$
		APS	PAPS	APS	PAPS	APS^d	$PAPS^e$		
PaAPR	3.5	2.2×10^7	1.2×10^3	3.1	$\leq 1 \times 10^{-3}$	0.1	$\geq 100^f$	35	8.1×10^3
EcPAPR	≤ 0.1	≤ 40	3.2×10^6	$\leq 1 \times 10^{-3}$	1.6	$\geq 100^f$	0.9	3.4×10^3	1.4
EcPAPR4cys	2.3	3.9×10^4	6.8×10^6	0.1	1.8	$\geq 100^f$	0.1	5.6×10^3	4.3

[a]Measurements represent the average of three or more independent determinations and the S. D. was ≤15% of the value in all cases. The concentration of protein was determined by quantitative amino acid analysis and further corrected by the amount of active enzyme present. Unless otherwise stated, reaction conditions were 100 mM Bis-Tris propane, pH 6.5, 5 mM dithiothreitol, and 10 µM thioredoxin at 30 °C (see Experimental Procedures). [b]k_{cat}/K_m values were measured as described in Experimental Procedures. [c]k_{max} measured with saturating enzyme (see Experimental Procedures). [d]10 nM or [e]1 µM thioredoxin was used to measure $K_{1/2}$ values for sulfite production, by varying the concentration of enzyme (see Experimental Procedures). [f]At high concentrations of enzyme, the reactions became too fast to measure by hand. [g]K_d measured at pH 7.5

The preceding data indicate that the iron-sulfur cluster in EcPAPR4cys contributes to catalytic efficiency by enhancing substrate affinity and/or stabilizing the catalytic transition state. To gain further insight into the role of the iron-sulfur cluster in these rate enhancements, we evaluated the saturating single-turnover rate constant (k_{max}) and the $K_{1/2}$ for EcPAPR4cys and wild-type enzymes (Table 5.2). These data reveal that EcPAPR4cys exhibits a 100-fold increase in the value of k_{max} for APS relative to EcPAPR, while the k_{max} for PAPS was the same within error. A 9-fold enhancement in the $K_{1/2}$ of PAPS was observed for EcPAPR4cys compared to wild-type, but differences in the $K_{1/2}$ of APS could not be discerned due to the limitations imparted by the maximum achievable enzyme concentration. As expected, the $K_{1/2}$ values for all enzymes with

cognate substrate were 10^2-10^3–fold greater relative to the non-cognate substrate. The binding of AMP and PAP to the aforementioned enzymes was also examined. The resulting K_d values indicate that incorporation of the iron-sulfur cluster in EcPAPR diminishes ligand binding by 1.5 to 3-fold (Table 5.2), suggesting that increased electrostatic repulsion from the negatively charged $[Fe_4S_4(Cys)_4]^{2-}$ center may hamper binding of the 5'-phosphate dianion. Collectively, these results demonstrate that the iron-sulfur cluster in EcPAPR enhances substrate binding and APS reduction.

Finally, we evaluated the time-dependent inactivation of EcPAPR and EcPAPR4cys under prolonged exposure to aerobic conditions (Figure 5.6). In the case of EcPAPR4cys, dissociation of the iron-sulfur cluster from the protein scaffold could also be monitored by loss of absorption at 410 nm. Our data show that the half-life of EcPAPR, which lacks the cluster, was ~35 hours (Figure 5.6a). However, inactivation and concomitant cluster decomposition for EcPAPR4cys occurred at an enhanced rate, with a half-life of ~10 hours (Figure 5.6b and c). A strong correlation between an intact iron-sulfur cluster and catalytic activity is consistent with previous data obtained from plant and bacterial APRs [11,17,18,27].
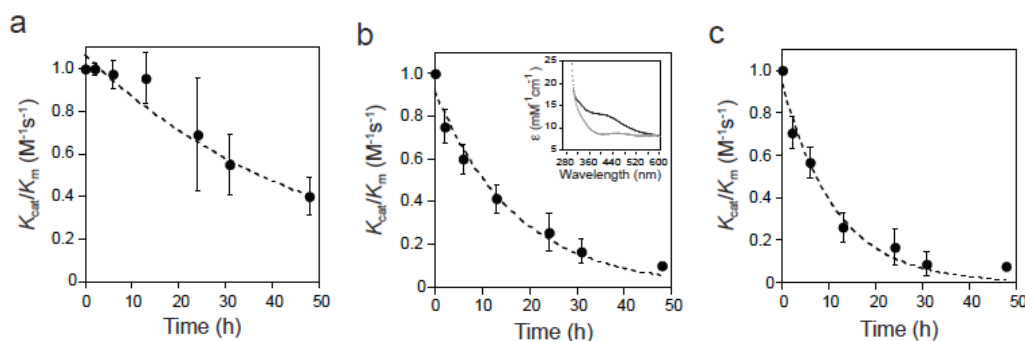
Figure 5.6 Time-dependent inactivation of SRs. Proteins (10 μM) were exposed to aerobic conditions at 4 °C over 2 days. At the indicated times, each enzyme was analyzed for its ability to catalyze the reduction of APS or PAPS. EcPAPR with PAPS (a), EcPAPR4cys with APS (b), *inset* shows the UV-vis absorption spectra of EcPAPR4cys at time 0 (black trace) and 48 h (gray trace), and EcPAPR4cys with PAPS (c).

5.4 Discussion

Assimilatory sulfonucleotide reductases – APR and PAPR – exhibit similar sequences, structure, and thiol reaction chemistry [6-9]. Analysis of the phylogenetic distribution of SRs suggests that PAPR evolved from APR through a single horizontal gene transfer event [10]. The conserved reaction mechanism serves as a template for the divergent evolution of these two subclasses, which catalyze the reduction of substrates that differ by a single 3'-phosphate group. There are over 15 such enzyme families with common reaction mechanisms despite differences in substrate utilization [28,29]. In divergent evolution, protein folds and active site structural features are frequently reused amongst different family members and adapted to new catalytic purposes [30]. Indeed, a closer look at the active sites of PaAPR and EcPAPR reveals that several strictly conserved, positively charged lysine and arginine residues interact with the sulfate moiety or α-phosphate (Figure 5.7 and Appendix 5.6.4). Moreover, the C-terminal peptide segment bearing the ECGH motif, which includes the cysteine nucleophile, is also conserved. However, two critical features distinguish APR and PAPR active sites: residues in the P-loop region and the presence/absence of an iron-sulfur cluster. These distinctions afford a unique opportunity to explore substrate recognition and identify underlying principles that govern specific features of APR that were targeted for alteration during the specialization of PAPR function.

GTP/ATP-dependent proteins contain a glycine-rich motif with the sequence, GXXGXGKT/S, known as the P-loop [7,31,32]. This structural moiety forms a large anion hole that interacts with phosphates. ATP pyrophosphatases (ATP PPases) harbor a modified P-loop, also known as the PP motif [33], with the fingerprint peptide SGGXDS/T. A highly modified version of the PP motif was discovered in EcPAPR (SXG), which is also found in enzymes with homologous protein

folds, including ATP sulfurylase and GMP synthetase [33-35]. Among ATP PPases, the P-loop

interacts with the 5'-phosphates of ATP [34,36]. Interestingly, however, structures of APR and

PAPR co-crystallized with nucleotides show that the 3'-group on the ribose interacts with

residues in the P-loop [9]. In SRs, the motif is characterized by the hydrophobic β1-strand and

α3-helix that flank the N- and C-terminal sides of the SFS–GAED and SSSFGIQA sequences in

PaAPR and EcPAPR, respectively. Differences in the P-loop motif have also been observed in

ATP synthases, wherein the sequence alterations have been suggested to imply diversity in

nucleotide recognition and/or catalytic mechanism [37]. Since SRs share a common catalytic

mechanism the change in P-loop sequences, particularly the acidic residues in APR, could be

implicated in substrate discrimination.

In this study, site-directed mutagenesis of the P-loop entailed the replacement of negatively

charged E65 and D66 PaAPR residues with corresponding neutral glutamine and alanine

residues found in EcPAPR and *visa versa*. Characterization of the resulting variants has led to

two significant observations. First, any change in P-loop residues had an adverse effect on

catalytic efficiency, underscoring the essential nature of these highly conserved motifs in the

two subclasses of catalysts. Second, variants of APR exhibited only a modest enhancement in

PAP binding. This finding indicates that while neutral P-loop residues contribute somewhat to

accommodating the 3'-phosphate group, they cannot account entirely for substrate specificity.

Moreover, P-loop variants of PAPR did not enhance binding to AMP, showing that the mere

presence of a negatively charged residue in the P-loop sequence was insufficient. Along these

lines, it is possible that additional P-loop modifications are required to enhance the binding of

PAPS. For instance, EcPAPR S52 and S53 (of the **SS**FGIQA sequence) establish hydrogen bonds

with the 3'-phosphate group of PAPS, whereas the corresponding residues in PaAPR (of the

SFSGAED sequence) do not make any contact with the APS 3'-hydroxyl group. Future experiments will be required to delineate this and other possibilities.

The second distinguishing feature among SRs is that APR contains the conserved cysteine sequence, CC…CXXC, which ligates an essential [4Fe-4S] cluster. In place of this cofactor, PAPR possesses the semi-conserved motif, YN…DXXT that links the α7-helix and C-terminal β-turn by hydrogen bond interactions. In the course of our study, we attempted to substitute the cysteine pairs in PaAPR with the YN…DT motif; however, this variant failed to express in *E. coli* (data not shown). As an alternative approach to investigate the role of this region, we engineered an iron-sulfur cluster into EcPAPR. Based on the high degree of sequence and structural homology between SRs an empirical approach was adopted to generate the new metal-binding site. This strategy has been employed to design novel metalloproteins, including the creation of a Mn(II)-binding site in cytochrome *c* peroxidase based on structural homology with manganese peroxidase [38,39]. Favorable protein folds such as the Trx scaffold have also been exploited to introduce a cofactor and alter enzyme function [40]. Assembly of a [2Fe-2S] cluster through directed evolution served to bridge two monomeric Trx subunits and enabled the resulting dimer to catalyze oxygen-dependent sulfhydryl oxidation [41,42]. In another instance, the second cysteine residue of the native CXXXCXXX motif in the catalytic subunit of dimethyl-sulfoxide reductase (DmsA) was replaced leading to the assembly of a paramagnetic [3Fe-4S] cluster [43].

In the case of EcPAPR, our goal was to introduce a [4Fe-4S] cluster in order to probe the role of the metallocenter in sulfonucleotide reduction. Spectroscopy (UV-vis, Mössbauer, EPR, mass) and single turnover kinetic analysis were employed to characterize the resulting variant, termed

EcPAPR4cys. Though we did not identify conditions that permitted quantitative cluster incorporation into each protein monomer, our spectroscopic data provides strong support for the assignment of a $[Fe_4S_4(Cys)_4]^{2-}$ center and compares favorably with studies of MtAPR [16]. Comparison of k_{cat}/K_m between EcPAPR4cys with wild-type PaAPR and EcPAPR showed that the installation of an iron-sulfur cluster dramatically improved the ability to turnover the APS (~10^3-fold). Further studies revealed a minor role in substrate binding, with the majority of the rate enhancement stemming from the improvement in k_{max}, which reports on the rate of the chemical step. Furthermore, time-dependent inactivation studies also showed that the cluster was required for catalytic activity.

Previously, we have observed mid-range electrostatic interactions between the iron-sulfur cluster and the ligand present within the APR active site [16]. These findings are also supported by computational analysis [44]. Based on these data, we proposed that the cluster cofactor plays a role in pre-organizing positively charged active site residues and in substrate activation. Specifically, that the charge from and polarization within the $[Fe_4S_4(Cys)_4]^{2-}$ cluster could serve to activate the sulfate group of APS, thereby facilitating S-OP cleavage and S-S bond formation in the reaction. In the absence of an iron-sulfur cluster, PAPR could achieve something similar *via* repulsion between the extra 3'-phosphate group of PAPS and the sulfate end of the 5'-phosphosulfate. Our observation, that insertion of an iron-sulfur cluster in PAPR enhances the rate of APS reduction, is entirely consistent with this model. In this regard, iron-sulfur clusters are extremely versatile cofactors with enzymatic functions in electron transfer, Lewis-acid assisted catalysis, radical generation, and source of sulfur during biosyntheses of cofactors [45-52]. This present study extends this list of functions to include substrate specificity.

From our study and sequence analysis, it is clear that the natural evolution of PAPR from APR involved several iterations of mutations. These factors are not easily recapitulated, and we note that none of the variants explored in this study resulted in a complete change of substrate specificity. Functional studies of EcPAPR4cys and the P-loop variants suggest that these enzymes may represent intermediates in the evolutionary pathway of SRs (Figure 5.7). This proposal is based on two interesting observations related to the catalytic efficiency and relative stability. First, is the striking similarity between (P)APR from *B. subtilis* and the P-loop variants of PaAPR. These enzymes coordinate an iron-sulfur cluster, but also contain a neutral residue in the position equivalent to residue 66 of PaAPR (or position 58 of EcPAPR). However, these
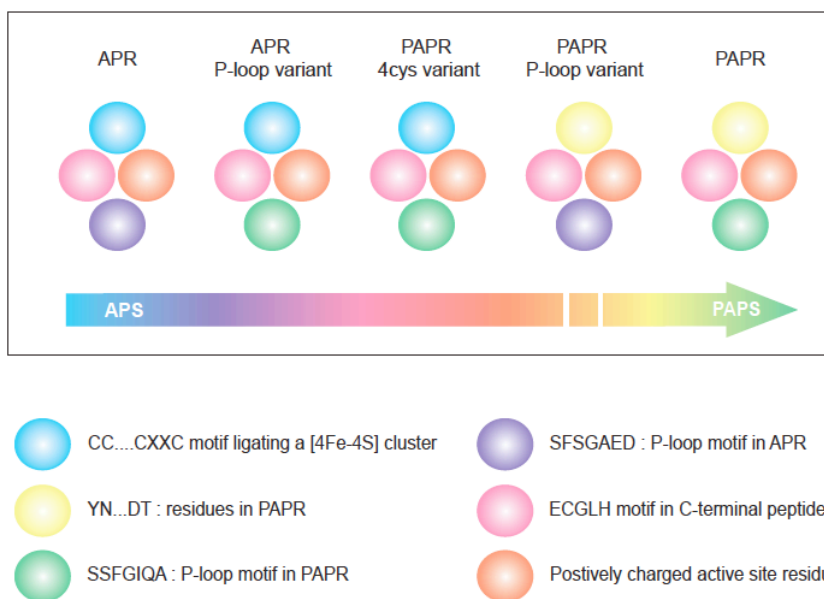
Figure 5.7 Model for divergent evolution of PAPR from APR. APR and PAPR can be considered to be at the margins of divergent evolution with optimum catalytic efficiency for APS (blue) and PAPS (green), as indicated by the color spectrum in the arrow. A comparison of their active sites reveals two consistent features, namely, strictly conserved positively charged lysine and arginine residues (orange circles) that interact with the substrate, and the C-terminal peptide bearing the ECGH motif, which includes the cysteine nucleophile, is also conserved (pink circles). The catalysts differ largely in their P-loop sequence motifs and their ability to ligate a [4Fe-4S] cluster through four cysteine residues. Based on the catalytic efficiencies for APS and PAPS, EcPAPR4cys and the P-loop variants appear to be intermediates in the evolutionary path of the functional divergence of PAPR from APR. The catalytic efficiency of the P-loop variants of EcPAPR for PAPS is comparable to the wild-type enzyme and is therefore indicated by a break in the arrow. Details regarding the kinetic parameters of all variants are presented in Table 5.2 and Appendix 5.6.1.

catalysts all exhibit a significant reduction in catalytic efficiency with APS ($\geq 10^2$), compared to wild-type PaAPR (Table 5.1). Second, like APR-B from *P. patens*, the EcPAPR P-loop variants lack the iron-sulfur cluster and also display a decrease in enzyme activity relative to wild-type PaAPR (Table 5.1). Interestingly, we note that both PpAPR-B and EcPAPR gain in stability by forfeiting the iron-sulfur cluster. EcPAPR retains enzymatic activity over 2 days in contrast to APR, which loses activity within half a day. Similarly, PpAPR-B remains active for 5 days compared to its homolog, PpAPR, which harbors a [4Fe-4S] cluster and is only active for 2 days under aerobic conditions [18]. Finally, we note that both BsAPR and PpAPR-B have markedly decreased catalytic efficiency relative to other SRs (Table 5.1), indicating that these enzymes are not as specialized for the reductase function as the latter group of catalysts. Taken together, these observations show how characteristics of our experimentally generated variants resemble those of SRs from naturally occurring species, corroborating our proposal that the variants are representative of intermediates in the path of divergent evolution of PAPR from APR (Figure 5.7).

In conclusion, the cysteine motif that coordinates the [4Fe-4S] cluster within APR can be accommodated by the PAPR scaffold and confers enhanced binding and catalytic activity for the APS substrate. This work provides valuable insight into the contribution of the iron-sulfur cluster to catalysis, and a better understanding of the mechanisms involved in the divergent evolution of PAPR from APR.

5.5 Experimental Procedures

APS (≥95%) was obtained from Biolog Life Sciences Institute (Bremen, Germany). PAPS (≥88%) was obtained from Calbiochem (La Jolla, CA). PAP, AMP, iron (III) chloride were purchased from Sigma-Aldrich (St. Louis, MO). Fe-57 metal was purchased from Isoflex USA (San Francisco, CA) and micro bio-spin P30 columns were from Bio-Rad Laboratories (Hercules, CA).

5.5.1 Cloning, Expression and Purification of SRs. Construction of the expression vectors encoding wild type PAPR from *E.coli* (EcPAPR), wild-type APR from *M. tuberculosis* (MtAPR) and wild-type APR from *P. aeruginosa* (PaAPR) cloned into the vector pET24b (Novagen) has been previously described [4,6]. The EcPAPR4cys variant was generated from the EcPAPR template using the Quik-change site-directed mutagenesis kit (Stratagene, La Jolla, CA). Successful cloning was confirmed by DNA sequencing analysis. Plasmids encoding EcPAPR4cys or PaAPR pET24 and pACYC [containing genes encoding the *isc* operon of six accessory proteins required for Fe–S cluster biosynthesis in *A. vinelandii* under the control of an arabinose-inducible promoter [53]] were co-transformed into *E. coli* BL21(DE3) (Novagen, San Diego, CA) and plated on L-agar 50 µg/ml kanamycin and 100 µg/ml carbenicillin. Plasmid encoding EcPAPR, EcPAPR A58D and EcPAPR Q57E pET24 was transformed into *E. coli* BL21(DE3) and plated on L-agar 50 µg/ml kanamycin. A single colony was picked and added to 5 ml of L-broth plus antibiotics and grown overnight with shaking at 37 °C. This culture was used as a 0.5% 1 L of L-broth plus antibiotics and grown with shaking at 37 °C until absorbance at 600 nm reached approximately 0.6. For EcPAPR4cys and PaAPR arabinose and iron citrate were added to final concentrations of 20 mM and 0.8 mM, respectively and the culture grown as above for 1 hr. At this point the flasks were removed from the incubator. IPTG was added to a final concentration of 0.3 mM and the flasks were returned to the incubator and grown overnight at 18 °C with shaking at 200 rpm. For EcPAPR, EcPAPR A58D and EcPAPR Q57E after the culture reached an absorbance of 0.6 at 600 nm, IPTG was added to a final concentration of 0.4 mM, the flasks returned to the incubator and grown for 5 hours at 30˚C. Cultures were harvested by centrifugation (4 °C, 4,300 *g*). After removal of the supernatant the pellets were stored at -80 °C until required.

All purification steps were carried out at 4 °C. Cell pellets were resuspended in 30 ml Buffer A (20 mM sodium phosphate, 0.5 M NaCl, 10 mM imidazole; pH 7.4) supplemented with 0.1 mM PMSF, 10 μg/ml DNase, 5 μg/ml lysozyme and lysed by sonication. Lysates were centrifuged ($20,000g$, 15 min) and loaded onto a 5 ml HisTrap Chelating column (GE Healthcare, Piscataway, NJ) equilibrated in the same buffer. Unbound material was washed off with 50 ml of Buffer A and bound proteins then eluted with Buffer B (20 mM phosphate, 0.5 M NaCl, 250 mM imidazole; pH 7.4). Fractions containing the desired protein were pooled, concentrated by centrifugation (Amicon 10 kDa cutoff, Millipore, Billerica, MA) and loaded onto a 16/60 Superdex 200 size exclusion column previously equilibrated in Buffer C (50 mM Tris-HCl, 150 mM NaCl, 5 mM DTT, 10% glycerol; pH 7.4 at 25 °C). Fractions containing sulfonucleotide reductase were pooled, snap-frozen in liquid nitrogen, and stored at -80 °C.

Protein concentrations were determined by quantitative amino acid analysis [Molecular Structure Facility, UC-Davis, CA and Ref. [6]] and corrected by the number of active molecules, as determined by the assay described below. Iron content of each protein preparation was determined in duplicate by inductively coupled plasma (ICP) analysis.

5.5.2 Chemical Reconstitution of EcPAPR4cys–Reconstitution experiments were performed in the glove box. EcPAPR4cys desalted into 1.5 mL Buffer C using P30 columns, was successively incubated, with gentle stirring, with 5 mM DTT (30 min), 5 M equivalents of $FeCl_3$ (added dropwise then incubated for 45 min) and $Na_2S.9H_2O$ (added dropwise then incubated for 2 h). Excess ligand was removed from the reconstitution reaction by desalting the mixture using PD10-Sepharose columns, GE Healthcare) into Buffer C.

5.5.3 Preparation of EcPAPR4cys for EPR and Mössbauer Spectroscopy. Samples of EcPAPR4cys suitable for EPR spectroscopy were prepared inside of an anaerobic chamber with O_2 levels ≤ 1 ppm. The procedure for photoreduction was carried out as previously described *[16]*. Briefly, purified EcPAPR4cys was exchanged into anaerobic buffer containing 50 mM Tris–HCl, 150 mM NaCl (pH 8.5 at 4 °C) and 10% glycerol. To reduce the cluster in EcPAPR4cys, reactions contained 250 μM enzyme, 25 mM sodium oxalate, and 250 μM deazaflavin in a total volume of 250 μL. The reaction mixtures were transferred to EPR tubes, chilled in an ice-salt bath (-6 °C) and irradiated with light from a 100 W quartz halogen lamp (Applied Photophysics, Surrey, UK) for 30 min. After illumination, samples were immediately frozen in liquid nitrogen and analyzed by low-temperature EPR. Mössbauer spectra were recorded on proteins that contained [57]Fe in place of natural-abundance iron. [57]Fe was incorporated into EcPAPR4cys by supplementation of *E. coli* growth media, and samples contained 1 mM protein, were transferred to Mössbauer cups and frozen in liquid nitrogen.

5.5.4 EPR Spectroscopy. X-band EPR spectra of photoreduced samples were recorded on a Bruker EMX spectrometer (Billerica, MA) equipped with an Oxford Instruments ITC4 temperature controller, a Hewlett-Packard model 5340 automatic frequency counter and Bruker gaussmeter. Figure legend contains relevant instrumental parameters. The sample buffer was used to record the baseline under conditions identical to those in which the sample spectra were obtained. The baseline was subtracted from the EcPAPR4cys spectrum shown in the figure. Spin concentration in EcPAPR4cys samples was determined by double integration of the EPR signal over a range of 2 kgauss and comparison with double integrals of 1 mM $Cu(ClO_4)_2$ in sample buffer. Figures were generated using Spin Count (ver 2.6.7) created by Professor M.P.

Hendrich at Carnegie Mellon University. Spin Count is available at http://www.chem.cmu.edu/groups/hendrich/.

5.5.5 Mössbauer Spectroscopy. Mössbauer spectra were recorded on a spectrometer from WEB research (Edina, MN) operating in the constant acceleration mode in transmission geometry. Spectra were recorded with the temperature of the sample maintained at 4.2 K in an externally applied magnetic field of 53 mT oriented parallel to the γ-beam. The quoted isomer shifts were relative to the centroid of the spectrum of a foil of α-Fe metal at room temperature. Data analysis was performed using the program WMOSS from WEB research.

5.5.6 Mass Spectrometry. For mass spectrometric analysis, samples were prepared by incubating 10 μM enzyme with 2 mM APS or PAPS, where appropriate, for 40 min at 30 °C to allow for formation of *S*-sulfocysteine intermediate. Subsequently, the samples were exchanged into 0.1% formic acid using Micro Bio-Spin P30 columns (Bio Rad). Intact proteins samples were analyzed on an electrospray linear ion trap mass spectrometer (LTQ-XL, Thermo Scientific) after separation on an Agilent Eclipse XDB-C8 2.1 mm x 15 mm trap with mobile phases A (0.1% formic acid in water) and B (0.1% formic acid in acetonitrile) which was used to trap, desalt and elute proteins onto a Varian 2.1 mm x 50 mm 5 μm PLRP-S C18 column with a gradient of 5% to 100% in 14 min at a flow rate of 200 μL/min.

5.5.7 Gel-labeling. In this experiment 5 μM EcPAPR or EcPAPR4cys were incubated at room temperature in 50 mM bis-tris propane (pH 7.0), 100 mM NaCl with [35S]-PAPS or [35S]-APS; or with radiolabeled substrate for 10 min followed by the addition of 10 μM Trx. Laemmeli sample buffer, without β-mercaptoethanol, was added to terminate the reaction. The reactions were

heated at 60 ˚C for 3 min and resolved by SDS-PAGE. The incorporation of radioactivity was analyzed with a Phosphorimager.

5.5.8 Kinetics Assays. Reactions were carried out at 30 °C. Unless otherwise indicated, the buffer consisted of 100 mM bis-tris propane (pH 6.5) supplemented with 5 mM DTT and 10 µM *E. coli* thioredoxin. Production of $[^{35}S]SO_3^{2-}$ from $[^{35}S]$-APS or $[^{35}S]$-PAPS was monitored using charcoal-based separation and scintillation counting as previously reported . The substrate was incubated with excess enzyme to ensure single-turnover conditions (>2.5-fold molar excess of enzyme). The reaction progress curve was plotted as the fraction of product versus time and was fit by a single exponential (eq. 1), where F is the fraction product, A is the fraction of substrate converted to product at completion, and t time. The observed rate constant (k_{obs}) is the product of the enzyme concentration and the apparent second-order rate constant k_{cat}/K_m (eq. 2). Under these conditions, the observed rate constant is linearly dependent upon enzyme concentration, and independent of substrate concentration, which demonstrated that substrate is not saturating. The reported k_{cat}/K_m values are for single-turnover conditions, but are equivalent to steady-state k_{cat}/K_m . Kinetic data were measured in at least two independent experiments and the standard error was typically less than 15%.

$$F = A[1-e(-k_{obs}t)] \qquad (1)$$

$$k_{obs} = (k_{cat}/K_m)[E] \qquad (2)$$

The maximal observed rate constant (k_{max}) was determined at a saturating concentration of enzyme ([E] >> K_d) and this was confirmed by the observation of the same rate constant at two

different concentrations of enzyme (150 μM and 300 μM). Because the observed rate constant is independent of the concentration of enzyme, this indicates that the observed rate constant is equal to the maximal single-turnover rate constant ($k_{obs} = k_{max}$) and reports on the chemical steps after substrate binding (eq. 1).

Under single-turnover conditions, it is expected that the concentration dependence of the enzyme will be hyperbolic (eq. 3). The $K_{1/2}$ value indicates the protein concentration at which half of the substrate is bound. For $K_{1/2}$ determinations, the APR concentration was varied over a wide range in the presence of Trx.

$$k_{obs} = k_{max}[E]/(K_{1/2} + [E]) \quad (3)$$

The inhibition constant (K_i) was measured for ligands, AMP and PAP by inhibiting the APR reaction under k_{cat}/K_m conditions at pH 7.5 with varying concentration of inhibitor (I). The data were fit to a simple model for competitive inhibition (eq. 4) and, with subsaturating APR, the K_i is equal to the equilibrium dissociation constant (K_d) of the inhibitor.

$$(k_{cat}/K_m)^{obs} = (k_{cat}/K_m)/(1 + [I]/K_i) \quad (4)$$

Acknowledgement

5.6 Appendix

Appendix 5.6.1 Table of single-turnover rate and dissociation constants for PaAPR, EcPAPR and the respective P-loop variants.[a]

Enzyme	k_{cat}/K_m (M^{-1}min^{-1})[b]		K_d AMP (µM)	K_d PAP (µM)
	APS	PAPS		
PaAPR	1.8×10^8	3.5×10^4	35 ± 2	8.1×10^3
PaAPR Asp66Ala	2.5×10^7	9.6×10^3	57 ± 12	3.3×10^3
PaAPR Glu65Gln	7.2×10^6	3.5×10^3	1.2×10^3	6.9×10^3
PaAPR Glu65Gln, Asp66Ala	5.0×10^5	2.5×10^3	2.8×10^3	9.7×10^3
EcPAPR	840	1.2×10^8	3.4×10^3	1.4 ± 0.6
EcPAPR Ala58Asp	720	1.3×10^5	1.4×10^4	8.0×10^3
EcPAPR Gln57Glu	420	1.7×10^5	7.6×10^3	1.0×10^3
EcPAPR Gln57Glu, Ala58Asp	420	2.6×10^4	1.8×10^4	2.4×10^3

[a]Measurements represent the average of two or more independent determinations and the S.D. was ≤25% of the value in all cases. Unless otherwise stated, reaction conditions were 100 mM Bis-Tris propane, pH 7.5, 5 mM dithiothreitol, and 10 µM thioredoxin at 30 °C (see Experimental Procedures). [b]k_{cat}/K_m values were measured as described in Experimental Procedures.

Appendix 5.6.2 Table of mass measurements of EcPAPR, EcPAPR4cys and MtAPR and associated enzyme *S*-sulfocysteine complexes.

Enzyme[a]	Measured mass (Da)[b]	Δm[c, d]
EcPAPR	28910.41 (28909.76)	N/A
EcPAPR + APS	28990.84 (28989.76)	80.43
EcPAPR + PAPS	28989.97 (28989.76)	79.56
EcPAPR4cys	28829.23 (28828.84)	N/A
EcPAPR4cys + APS	28909.54 (28908.84)	80.31
EcPAPR4cys + PAPS	28908.55 (28908.84)	79.56
MtAPR	28356.88 (28356.87)	N/A
MtAPR + APS	28437.45 (28436.87)	80.57
MtAPR + PAPS	28436.29 (28436.87)	79.41

[a]In reactions that contained APS or PAPS, the enzyme was incubated with substrate prior to mass analysis, as described in Experimental Procedures. [b]The average experimental value of the most abundant isotopic mass over the charge state distribution, calculated by deconvolution. Theoretical values are shown in parenthesis and were calculated based on the amino acid sequence. [c]The mass differences in this table have been calculated with respect to the masses of the corresponding intact protein. [d]With the exception of EcPAPR + PAPS, EcPAPR4cys + PAPS and MtAPR + APS, two series of ions were observed corresponding to the enzyme alone and the enzyme *S*-sulfocysteine adduct. Relative abundance of these species is provided in the text.

Appendix 5.6.3 Primary sequence alignment of sulfonucleotide reductases from different species.

PaAPR

```
                    1        10         20
PaAPR    1  ......MLPFATIPATERNSAAQHQDPSPMSQP.................................
MtAPR    1  MSGETTRLTEPQLRELAARGAAELDGATATD..................................
BsAPR2   1  ......MLTYDNWEEPTITFPEDDPYKGALS..................................
AtAPR2   1  ....MALAVTSSSTAISGSSFSRSGASSESKALQICS.........IRLS..DRTHLSQRRYSM..KPLNAESHSRSESWVTRASTLI
PpAPR    1  ...MALKVASLEAAVMASLAPAASTSASLSRQSIVSGLAFRGQNGFQLGGLSSAGVSSRSLALGGKKIELDIAQPRRMLPVSATAVV
EcPAPR   1  .......MSKLDLNALNELPKVDRILALAET..................................
ScPAPR   1  ........MKTYHLNNDIIVTQEQLD.......................................
PpAPR-B  1  ...MAMAMADAHLRSSTSCVPSHCPALVPALATLTSLR..........KCAFHKPSFPSLVFQSYCLGWASGRGKTAASAVPVTTSGSS
```

PaAPR α1 α2 η1 β1 α3 β2 α4

```
                30       40        50        60        70        80        90       100
PaAPR   28  ......FDLPALASSLADKSPQDILKAAFEHFGDELWISFSGAEDVVLVDMAWKL....NRNVKVFSLDTGRLHPETYRFIDQVREHYG
MtAPR   32  .......MLRWTDETFGDIGGAGGGVSGHRGWTTCNYVVASNMADAVLVDLAAKV....RPGVPVIFLDTGYHFVETIGTRDAIESVYL
BsAPR   26  ......VLKWAYGHYGDQ...............LVYACSFGIEGIVLIDLIYKV....KKDAEIVFLDTGLHFKETYETIERVKERYE
AtAPR2  73  PEVE...DFEQLAKKLEDASPLEIMDKALERFGDQIAIAFSGAEDVALIEYARLT....GKPFRVFSLDTGRLNPETYRLFDAVEKQYG
PpAPR   86  ESVQSTVDIPKLAEKLDSASPLEIMDKALSLFGDDIAIAFSGAEDVTLIEYAHLT....GRPFRVFSLETGRLNPETLKLFDDVEKRYN
EcPAPR  25  .........NAQLEKLDAEGRVAWALDNLP..GEYVLSSSFGIQAAVSLHLVNQI....RPDIPVILUDTGYLFPETYRFIDELTDKLF
ScPAPR  19  .........HWNEQLIKLETPQEIIAWSIVTFPHLFQTTAFGLTGLVTIDMLSKLS.EKYYMPELLFIDTLHHFPQTLTLKNEIEKKYY
PpAPR-B 78  DIKKCNEQARDARLQHLEAQALETLQKTVENFEKPAFPCALIAGDVVILDLLHRIGAFSDNKVKIIFIDTFHLFPETYKFLSEVEERYG
```
                                              P-loop

PaAPR β3 α5 α6 α7 α8 β4 TT β5 T...TT

```
              110      120       130       140       150       160      170       180
PaAPR   107 ...IAIDVLSPDPRLLEPLVKEKGLFSFYRDGHGECCGIRKIEPLKRKLAGVRA..WATGQRRDQSPGTRSQVAVLEIDG...AFSTPE
MtAPR   110 ...VRVLNVTPEHTVAEQDELLG..KDLFARNPHECCRLRKVVPLGKTLRGYSA..WVTGLRRVDAP.TRANAPLVSFDE...TFKLVE
BsAPR    90 ...LNIILKKPDLTLEEQAEEHG..DKLWEREPNQCCYLRKVVPLREALQDIS...LAFGLRRDQGP.SRANTNFLNKDE...KFKSVE
AtAPR2  155 ...IRIEYMFPDAVEVQALVRNKGLFSFYEDGHQECCRVRKVRPLRRALKGLKA..WITGQRKDQSPGTRSEIPIVQVDP...VFEGLI
PpAPR   171 ...IRIQYMYPDAAEVEELTRTKGLFSFYEDGHQECCRVRKVRPLRRALKGLKA..WITGQRKDQSPGTRANVPVVQVDP...AFEGLI
EcPAPR   99 ...LNLKVYRATESAAWQEARYGKLWEQGVEGIEKYNDINKVEPMNRALKELNVQTWFAGLRREQSG.SRANLPVLAIQRG..VFKVL.
ScPAPR   99 PKNQTIHVYKPDGCESEADFASKYGDFLWEKDDDKYDYLAKVEPAHRAYKELHISAVFTGRRKSQGS.ARSQLSIIEIDELNGILKIN.
PpAPR-B 167 ...FKAHVFHAADVNNKEAYDAKFGSDLFITDIEEYDRICKVEPFSRALKTLEVDAMINGRRRDHGA.ERAHLEVFEEGK...MVKVQ.
```
                                        ..

PaAPR β6 η2 α9 η3 TT TT η4 TT

```
              190      200       210       220       230       240      250       260
PaAPR   188 ..KPLYKFNPLSSMTSEEVWGYIRMLELPYNSLHERGYISIGCEPCTRPVLPN.........QHEREGRWWWEEATHKECGIHAGNLIS
MtAPR   188 .......VNPLAAWTDQDVQEYIADNDVLVNPLVREGYPSIGCAPCTAKPAEG........ADPRSGR..WQGLAKTECGIHAS.....
BsAPR   167 .......VCPHYPLTWKDIWRYTSRNELDYNPLHDQGYPSIGCAPCTSPAFTA........EDLRSGR..WNGMAKTECGIHE.....
AtAPR2  237 GVGSLVKWNPLANVEGADVWNFLRTMDVPVNALHAQGYVSIGCEPCTRPVLPG.........QHEREGRWWWEDAKAKECGIHKGNIK.
PpAPR   253 GPGSLVKWNPLSNVSGTAVWSFLRTMDVPVNALHFKGYVSIGCEPCTRAVLPG.........QHEREGRWWWEDAKAKECGIHKGNLDG
EcPAPR  181 .......PIIDWDNRTIYQYLQKHGLKYHPLWDEGYLSVGDTHTHRKWEPG.........MAEBETRH..FFGLKR.PCGLHEG.....
ScPAPR  186 ........PLINWTFEQVKQYIDANNVPYNELLDLGYRSIGDYHSHQPVKEG.........EDERAGR..WKGKAKTECGIHEASRFA
PpAPR-B 248 ........PLAYWEFRDCWDYLTKYSLPYHPLHDQGFPSIGCDVQSHIPVPREKWFEYAGERSGRFQGLTNPDGSAKTECGIHVGGRT.
```
   C-terminal peptide

Appendix 5.6.3 Primary sequence alignment of sulfonucleotide reductases from *P. aeruginosa*, *M. tuberculosis*, *B. subtilis*, *A. thaliana, P. patens* (two isoforms, APR and APR-B), *E. coli*, and *S. cerevisiae*. The ClustalW2 (v2.1) Multiple Sequence Alignment program (Larkin, 2007) was used to align all the sequences. Strictly conserved residues are outlined in red, red letters indicate conserved residues and conserved regions are boxed in blue. Residues flanking the active site are boxed in green. Positions of cysteine residues that coordinate to the [4Fe-4S] cluster are indicated below the sequence with (●). Alignment pictures were rendered with the server ESPript 2.2 (http://espript.ibcp.fr).

Appendix 5.6.4 Comparison of key active site regions in PaAPR and EcPAPR.
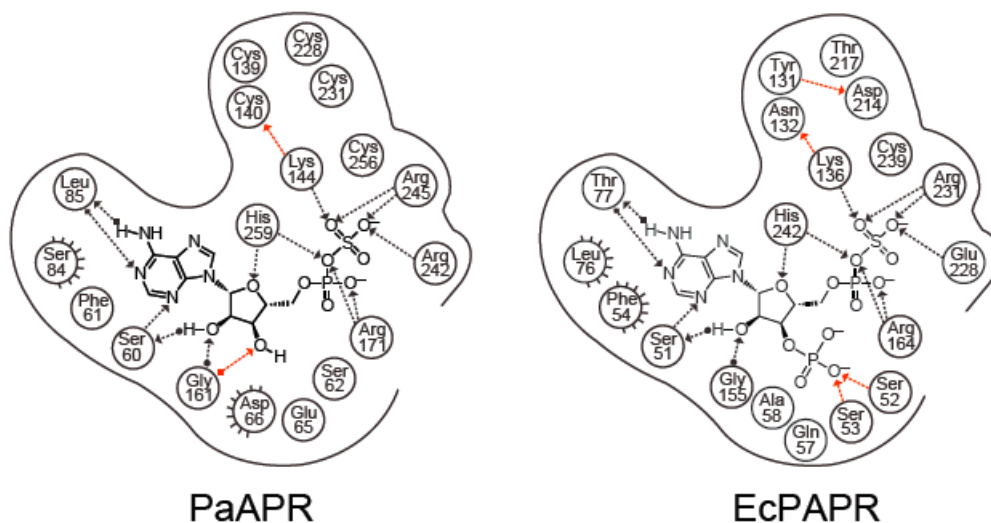
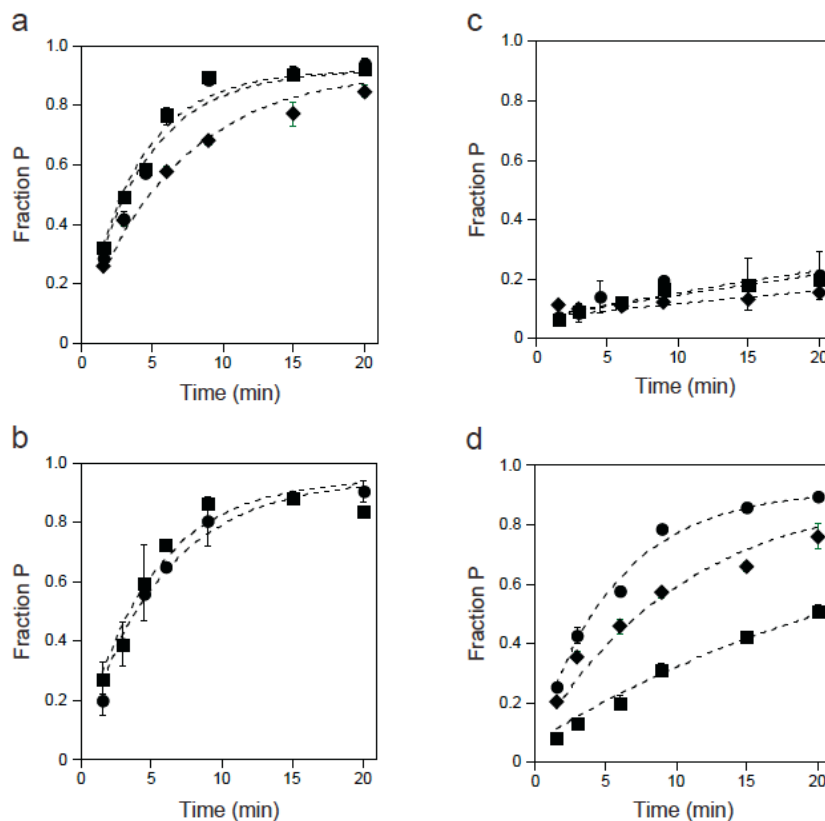PaAPR   EcPAPR

Appendix 5.6.4 Comparison of key active site regions in PaAPR and EcPAPR. Active site contacts of PaAPR and EcPAPR with APS and PAPS respectively, plotted in two dimensions. Interactions are based on PaAPR (PDB deposition 2GOY) and EcPAPR (PDB deposition 1SUR), crystal structures, prior functional studies (Hong, 2009; Chartron, 2006) and the present study. Contacts of EcPAPR with PAPS have been assumed from the coordinates of PAP (ScPAPR, PDB deposition 2OQ2) and APS (PaAPR, PDB deposition 2GOY). Protein residues in proximity of the ligand are shown, with hydrogen bonding interactions indicated as dotted lines with arrows denoting the direction of the bond. Interactions from the substrate or the residue backbones of the enzyme are distinguished from interactions with residue side chains by a solid dot at the end of the interaction line. Interactions highlighted in red are unique between the two active sites.

**Appendix 5.6.5** Gel labeling of wild type EcPAPR and EcPAPR4cys
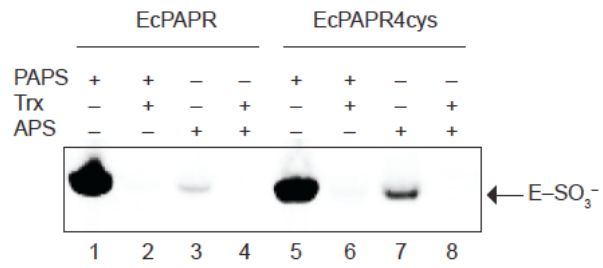
Appendix 5.6.5 Gel labeling of wild type EcPAPR and EcPAPR4cys. Gel labeling of wild type EcPAPR (lanes 1-4) and EcPAPR4cys (lanes 5-8) with either [^{35}S]-PAPS or [^{35}S]-APS, with or without Trx, was carried out as described in the Experimental Procedures.

Appendix 5.6.6 The reaction progress curve for P-loop variants of PaAPR and EcPAPR.
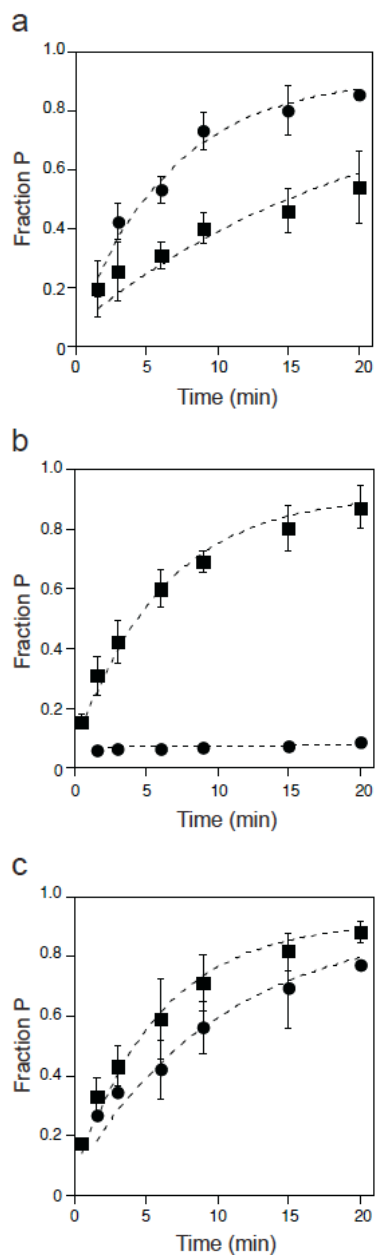

Appendix 5.6.6 The reaction progress curve for P-loop variants of PaAPR and EcPAPR. Under subsaturating concentration of substrate, the reaction is described by the apparent second order rate constant, k_{cat}/K_m. The enzyme concentration was varied as indicated due to the linear relationship between concentration and activity. a. Reduction of APS with PaAPR (2 nM, ●), D66A PaAPR (10 nM, ■) and E65Q PaAPR (20 nM, ◆). b. Reduction of APS with EcPAPR (10 μM, ●), A58D EcPAPR (10 μM, ■) and Q57E EcPAPR (10 μM, ◆). c. Reduction of PAPS with PaAPR (5 μM, ●), D66A PaAPR (10 μM, ■) and E65Q PaAPR (10μM, ◆). d. Reduction of PAPS as substrate with EcPAPR (2.5 nM, ●), A58D EcPAPR (0.5 μM, ■) and Q57E EcPAPR (0.5 μM,◆).

Appendix 5.6.7 Binding of AMP and PAP to P-loop variants of PaAPR and EcPAPR.
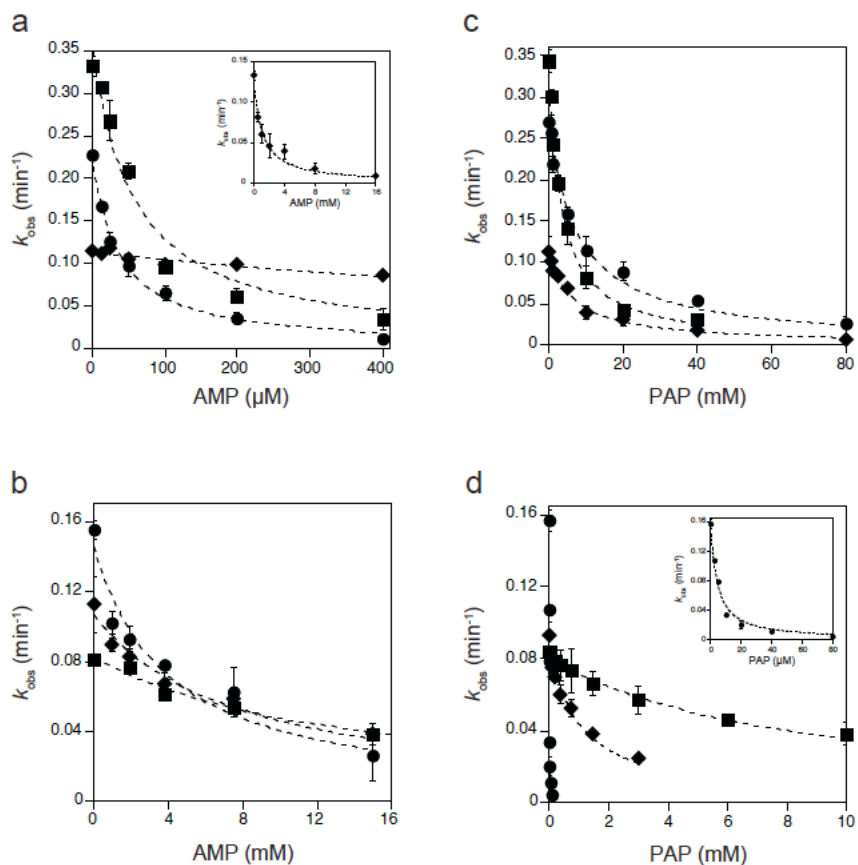
Appendix 5.6.7 Binding of AMP and PAP to P-loop variants of PaAPR and EcPAPR. Nonlinear-least-squares fit of the data to a model for simple competitive inhibition (eq. 2) gave the dissociation constant K_d. a. K_d^{AMP} of PaAPR (●), D66A PaAPR (■) and E65Q PaAPR (◆); inset, E65Q PaAPR scaled. b. K_d^{AMP} of EcPAPR (●), A58D EcPAPR (■) and Q57E EcPAPR (◆). c. K_d^{PAP} of PaAPR (●), D66A PaAPR (■) and E65Q PaAPR (◆). d. K_d^{PAP} of EcPAPR (●), A58D EcPAPR (■) and Q57E EcPAPR (◆); inset, A58D EcPAPR scaled.

Appendix 5.6.8 Reaction progress curves for PaAPR, EcPAPR and EcPAPR4cys.

Appendix 5.6.8 Reaction progress curves for PaAPR, EcPAPR and EcPAPR4cys at pH 6.5. Under subsaturating concentration of substrate, the reaction is described by the apparent second-order rate constant, k_{cat}/K_m, for PaAPR (a), EcPAPR (b) and EcPAPR4cys (c) with APS (●) and PAPS (■).

Appendix 5.6.9 Maximal rate constant, k_{max}, measured under single turnover conditions.
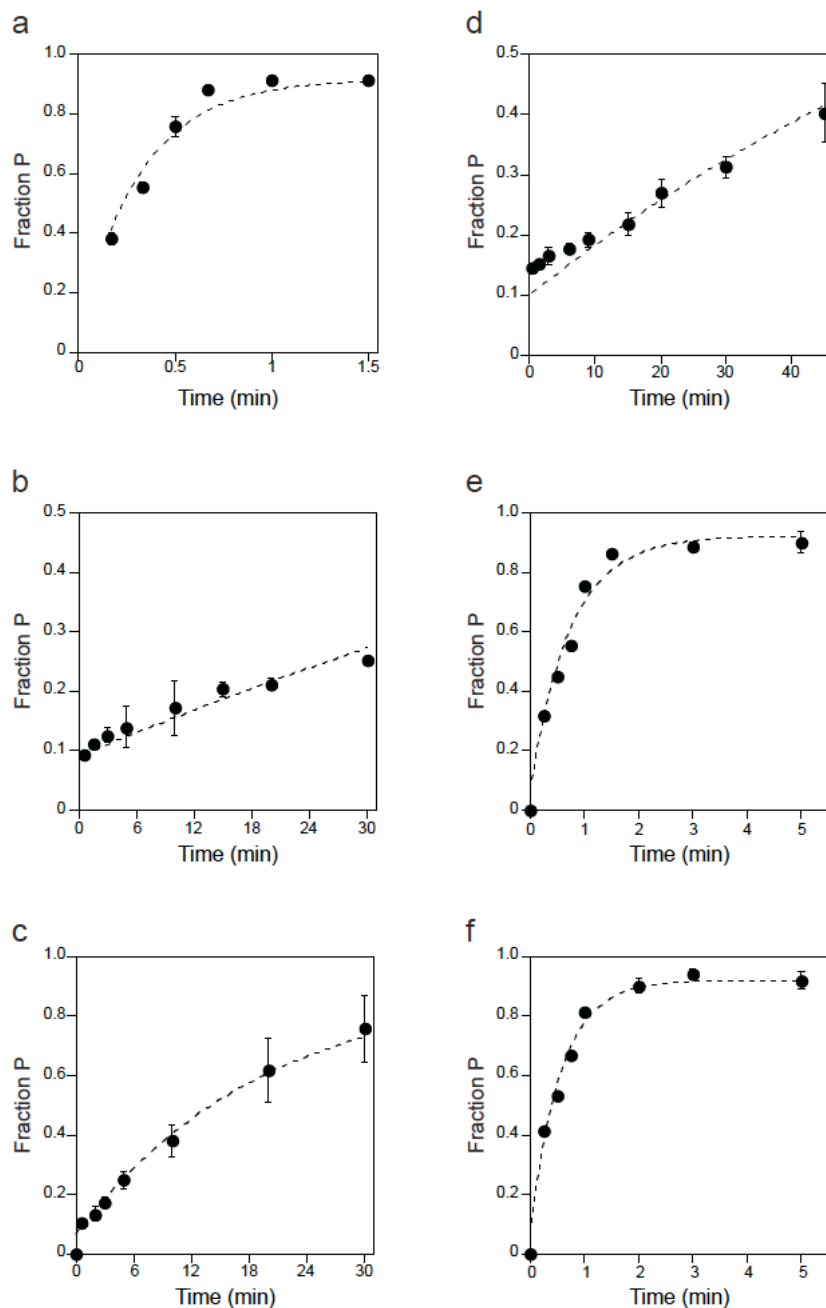
Appendix 5.6.9 Maximal rate constant, k_{max}, measured under single turnover conditions with saturating enzyme at pH 6.5 for PaAPR (a), EcPAPR (b), EcPAPR4cys (c) with APS, and for PaAPR (d), EcPAPR (e), EcPAPR4cys (f) with PAPS.

Appendix 5.6.10 The apparent affinity, $K_{1/2}$, under single turnover conditions.
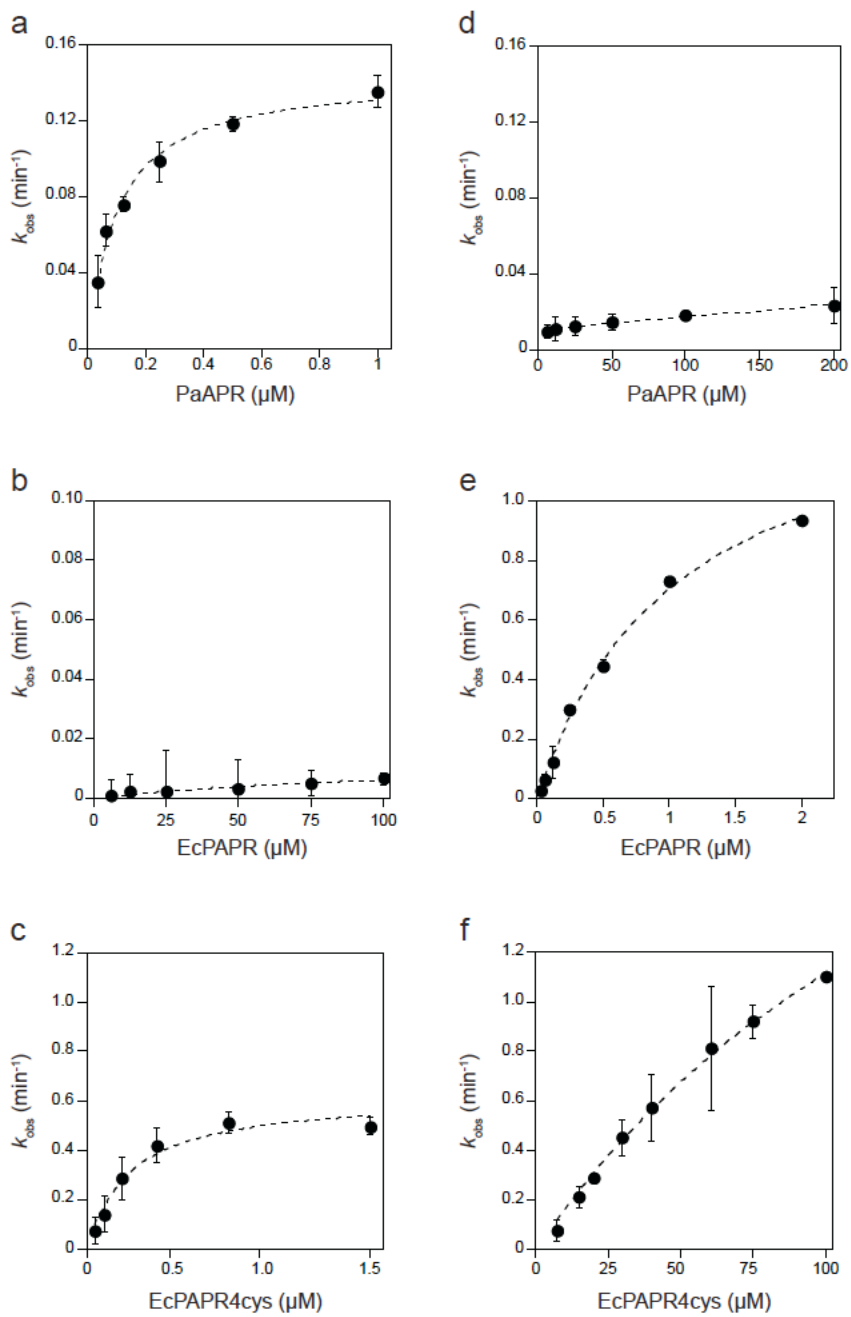
Appendix 5.6.10 The apparent affinity, $K_{1/2}$, under single turnover conditions at pH 6.5 for PaAPR (a), EcPAPR (b) and EcPAPR4cys (c) with APS, and for PaAPR (d), EcPAPR (e) and EcPAPR4cys (f) with PAPS.

Appendix 5.6.11 Binding of AMP and PAP to EcPAPR4cys.
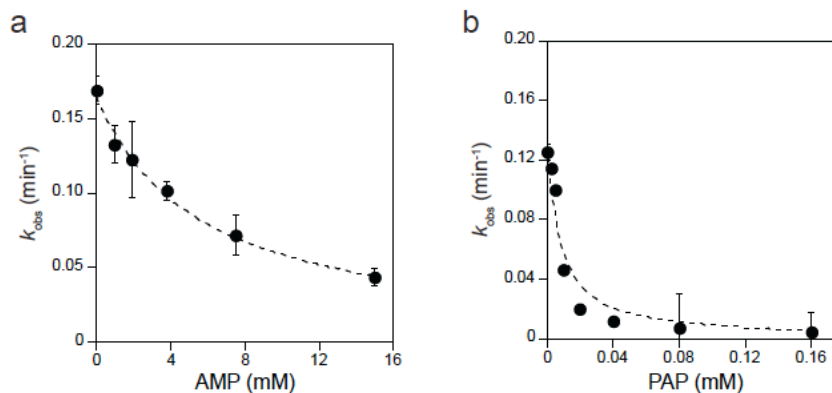
Appendix 5.6.11 Binding of AMP and PAP to EcPAPR4cys measured at pH 7.5. The average of three independent determinations is shown, and the error bars indicate the standard deviations. Nonlinear-least-squares fit of the data to a model for simple competitive inhibition (eq. 4) gave the dissociation constants K_d^{AMP} (a) and K_d^{PAP} (b) for EcPAPR4cys.

5.7 References

1. Schwenn JD: **Photosyntheitc sulfate reduction**. *Z. Naturforsch* 1994, **49c**:531-539.
2. Kredich NM: *Escherichia coli and Salmonella typhimurium: Cellular and Molecular Biology*, vol 1 edn 2nd. Edited by Niedhardt FC. Washington, D.C: ASM Press; 1996.
3. Schelle MW, Bertozzi CR: **Sulfate metabolism in mycobacteria**. *Chembiochem* 2006, **7**:1516-1524.
4. Williams SJ, Senaratne RH, Mougous JD, Riley LW, Bertozzi CR: **5'-adenosinephosphosulfate lies at a metabolic branch point in mycobacteria**. *Journal of Biological Chemistry* 2002, **277**:32606-32615.
5. Senaratne RH, De Silva AD, Williams SJ, Mougous JD, Reader JR, Zhang T, Chan S, Sidders B, Lee DH, Chan J, et al.: **5'-Adenosinephosphosulphate reductase (CysH) protects Mycobacterium tuberculosis against free radicals during chronic infection phase in mice**. *Mol Microbiol* 2006, **59**:1744-1753.
6. Carroll KS, Gao H, Chen H, Stout CD, Leary JA, Bertozzi CR: **A conserved mechanism for sulfonucleotide reduction**. *PLoS Biol* 2005, **3**:e250.
7. Savage H, Montoya G, Svensson C, Schwenn JD, Sinning I: **Crystal structure of phosphoadenylyl sulphate (PAPS) reductase: a new family of adenine nucleotide alpha hydrolases**. *Structure* 1997, **5**:895-906.
8. Chartron J, Carroll KS, Shiau C, Gao H, Leary JA, Bertozzi CR, Stout CD: **Substrate recognition, protein dynamics, and iron-sulfur cluster in Pseudomonas aeruginosa adenosine 5'-phosphosulfate reductase**. *J Mol Biol* 2006, **364**:152-169.
9. Yu Z, Lemongello D, Segel IH, Fisher AJ: **Crystal structure of Saccharomyces cerevisiae 3'-phosphoadenosine-5'-phosphosulfate reductase complexed with adenosine 3',5'-bisphosphate**. *Biochemistry* 2008, **47**:12777-12786.
10. Kopriva S, Buchert T, Fritz G, Suter M, Benda R, Schunemann V, Koprivova A, Schurmann P, Trautwein AX, Kroneck PM, et al.: **The presence of an iron-sulfur cluster in adenosine 5'-phosphosulfate reductase separates organisms utilizing adenosine 5'-phosphosulfate and phosphoadenosine 5'-phosphosulfate for sulfate assimilation**. *J Biol Chem* 2002, **277**:21786-21791.
11. Kopriva S, Buchert T, Fritz G, Suter M, Weber M, Benda R, Schaller J, Feller U, Schurmann P, Schunemann V, et al.: **Plant adenosine 5'-phosphosulfate reductase is a novel iron-sulfur protein**. *J Biol Chem* 2001, **276**:42881-42886.
12. Setya A, Murillo M, Leustek T: **Sulfate reduction in higher plants: molecular evidence for a novel 5'-adenylylsulfate reductase**. *Proc. Natl. Acad. Sci. U. S. A.* 1996, **93**:13383-13388.
13. Kim SK, Rahman A, Conover RC, Johnson MK, Mason JT, Gomes V, Hirasawa M, Moore ML, Leustek T, Knaff DB: **Properties of the cysteine residues and the iron-sulfur cluster of the assimilatory 5'-adenylyl sulfate reductase from Enteromorpha intestinalis**. *Biochemistry* 2006, **45**:5010-5018.
14. Kim SK, Gomes V, Gao Y, Chandramouli K, Johnson MK, Knaff DB, Leustek T: **The two-domain structure of 5'-adenylylsulfate (APS) reductase from Enteromorpha intestinalis is a requirement for efficient APS reductase activity**. *Biochemistry* 2007, **46**:591-601.
15. Chartron J, Shiau C, Stout CD, Carroll KS: **3'-Phosphoadenosine-5'-phosphosulfate reductase in complex with thioredoxin: a structural snapshot in the catalytic cycle**. *Biochemistry* 2007, **46**:3942-3951.
16. Bhave DP, Hong JA, Lee M, Jiang W, Krebs C, Carroll KS: **Spectroscopic studies on the [4Fe-4S] cluster in adenosine 5'-phosphosulfate reductase from Mycobacterium tuberculosis**. *J. Biol. Chem.* 2011, **286**:1216-1226.

17. Berndt C, Lillig CH, Wollenberg M, Bill E, Mansilla MC, de Mendoza D, Seidler A, Schwenn JD: **Characterization and reconstitution of a 4Fe-4S adenylyl sulfate/phosphoadenylyl sulfate reductase from Bacillus subtilis**. *J Biol Chem* 2004, **279**:7850-7855.

18. Kopriva S, Fritzemeier K, Wiedemann G, Reski R: **The putative moss 3'-phosphoadenosine-5'-phosphosulfate reductase is a novel form of adenosine-5'-phosphosulfate reductase without an iron-sulfur cluster**. *J Biol Chem* 2007, **282**:22930-22938.

19. Penning TM, Jez JM: **Enzyme redesign**. *Chem. Rev.* 2001, **101**:3027-3046.

20. Scrutton NS, Berry A, Perham RN: **Redesign of the coenzyme specificity of a dehydrogenase by protein engineering**. *Nature* 1990, **343**:38-43.

21. Shah K, Liu Y, Deirmengian C, Shokat KM: **Engineering unnatural nucleotide specificity for Rous sarcoma virus tyrosine kinase to uniquely label its direct substrates**. *Proc. Natl. Acad. Sci. U. S. A.* 1997, **94**:3565-3570.

22. Bishop AC, Ubersax JA, Petsch DT, Matheos DP, Gray NS, Blethrow J, Shimizu E, Tsien JZ, Schultz PG, Rose MD, et al.: **A chemical switch for inhibitor-sensitive alleles of any protein kinase**. *Nature* 2000, **407**:395-401.

23. Bhave DP, Muse WB, 3rd, Carroll KS: **Drug targets in mycobacterial sulfur metabolism**. *Infect Disord Drug Targets* 2007, **7**:140-158.

24. Mdluli K, Spigelman M: **Novel targets for tuberculosis drug discovery**. *Curr Opin Pharmacol* 2006, **6**:459-467.

25. Johnson DC, Unciuleac MC, Dean DR: **Controlled expression and functional analysis of iron-sulfur cluster biosynthetic components within Azotobacter vinelandii**. *J. Bacteriol.* 2006, **188**:7551-7561.

26. Weber M, Suter M, Brunold C, Kopriva S: **Sulfate assimilation in higher plants characterization of a stable intermediate in the adenosine 5'-phosphosulfate reductase reaction**. *Eur. J. Biochem.* 2000, **267**:3647-3653.

27. Carroll KS, Gao H, Chen H, Leary JA, Bertozzi CR: **Investigation of the iron-sulfur cluster in Mycobacterium tuberculosis APS reductase: implications for substrate binding and catalysis**. *Biochemistry* 2005, **44**:14647-14657.

28. Todd AE, Orengo CA, Thornton JM: **Evolution of protein function, from a structural perspective**. *Curr Opin Chem Biol* 1999, **3**:548-556.

29. Babbitt PC, Hasson MS, Wedekind JE, Palmer DR, Barrett WC, Reed GH, Rayment I, Ringe D, Kenyon GL, Gerlt JA: **The enolase superfamily: a general strategy for enzyme-catalyzed abstraction of the alpha-protons of carboxylic acids**. *Biochemistry* 1996, **35**:16489-16501.

30. Wise EL, Rayment I: **Understanding the importance of protein structure to nature's routes for divergent evolution in TIM barrel enzymes**. *Acc Chem Res* 2004, **37**:149-158.

31. Dreusicke D, Schulz GE: **The glycine-rich loop of adenylate kinase forms a giant anion hole**. *FEBS Lett.* 1986, **208**:301-304.

32. Saraste M, Sibbald PR, Wittinghofer A: **The P-loop--a common motif in ATP- and GTP-binding proteins**. *Trends Biochem. Sci.* 1990, **15**:430-434.

33. Bork P, Koonin EV: **A P-loop-like motif in a widespread ATP pyrophosphatase domain: implications for the evolution of sequence motifs and enzyme activity**. *Proteins* 1994, **20**:347-355.

34. Tesmer JJ, Klem TJ, Deras ML, Davisson VJ, Smith JL: **The crystal structure of GMP synthetase reveals a novel catalytic triad and is a structural paradigm for two enzyme families**. *Nat. Struct. Biol.* 1996, **3**:74-86.

35. Mougous JD, Lee DH, Hubbard SC, Schelle MW, Vocadlo DJ, Berger JM, Bertozzi CR: **Molecular basis for G protein control of the prokaryotic ATP sulfurylase**. *Mol Cell* 2006, **21**:109-122.

36. Smith CA, Rayment I: **Active site comparisons highlight structural similarities between myosin and other P-loop proteins**. *Biophys. J.* 1996, **70**:1590-1602.

37. Kumar A, Manimekalai MS, Balakrishna AM, Jeyakanthan J, Gruber G: **Nucleotide binding states of subunit A of the A-ATP synthase and the implication of P-loop switch in evolution**. *J Mol Biol* **396**:301-320.

38. Yeung BK, Wang X, Sigman JA, Petillo PA, Lu Y: **Construction and characterization of a manganese-binding site in cytochrome c peroxidase: towards a novel manganese peroxidase**. *Chem Biol* 1997, **4**:215-221.

39. Wilcox SK, Putnam CD, Sastry M, Blankenship J, Chazin WJ, McRee DE, Goodin DB: **Rational design of a functional metalloenzyme: introduction of a site for manganese binding and oxidation into a heme peroxidase**. *Biochemistry* 1998, **37**:16853-16862.

40. Coldren CD, Hellinga HW, Caradonna JP: **The rational design and construction of a cuboidal iron-sulfur protein**. *Proc. Natl. Acad. Sci. U. S. A.* 1997, **94**:6635-6640.

41. Masip L, Pan JL, Haldar S, Penner-Hahn JE, DeLisa MP, Georgiou G, Bardwell JC, Collet JF: **An engineered pathway for the formation of protein disulfide bonds**. *Science* 2004, **303**:1185-1189.

42. Collet JF, Peisach D, Bardwell JC, Xu Z: **The crystal structure of TrxA(CACA): Insights into the formation of a [2Fe-2S] iron-sulfur cluster in an Escherichia coli thioredoxin mutant**. *Protein. Sci.* 2005, **14**:1863-1869.

43. Trieber CA, Rothery RA, Weiner JH: **Engineering a novel iron-sulfur cluster into the catalytic subunit of Escherichia coli dimethyl-sulfoxide reductase**. *J. Biol. Chem.* 1996, **271**:4620-4626.

44. Bhave DP, Han WG, Pazicni S, Penner-Hahn JE, Carroll KS, Noodleman L: **Geometric and Electrostatic Study of the [4Fe-4S] Cluster of Adenosine-5'-Phosphosulfate Reductase from Broken Symmetry Density Functional Calculations and Extended X-ray Absorption Fine Structure Spectroscopy**. *Inorg. Chem.* 2011, **50**:6610-6625.

45. Beinert H, Holm RH, Munck E: **Iron-sulfur clusters: nature's modular, multipurpose structures**. *Science* 1997, **277**:653-659.

46. Booker SJ, Cicchillo RM, Grove TL: **Self-sacrifice in radical S-adenosylmethionine proteins**. *Curr. Opin. Chem. Biol.* 2007, **11**:543-552.

47. Beinert H, Kennedy MC, Stout CD: **Aconitase as Iron-Sulfur Protein, Enzyme, and Iron-Regulatory Protein**. *Chem Rev* 1996, **96**:2335-2374.

48. Booker SJ: **Anaerobic functionalization of unactivated C-H bonds**. *Curr Opin Chem Biol* 2009, **13**:58-73.

49. Dos Santos PC, Dean DR: **A newly discovered role for iron-sulfur clusters**. *P Natl Acad Sci USA* 2008, **105**:11589-11590.

50. Fontecave M: **Iron-sulfur clusters: ever-expanding roles**. *Nat Chem Biol* 2006, **2**:171-174.

51. Frey PA, Hegeman AD, Ruzicka FJ: **The Radical SAM Superfamily**. *Crit Rev Biochem Mol Biol* 2008, **43**:63-88.

52. Walsby CJ, Ortillo D, Yang J, Nnyepi MR, Broderick WE, Hoffman BM, Broderick JB: **Spectroscopic approaches to elucidating novel iron-sulfur chemistry in the "radical-Sam" protein superfamily**. *Inorg Chem* 2005, **44**:727-741.

53. Kriek M, Peters L, Takahashi Y, Roach PL: **Effect of iron-sulfur cluster assembly proteins on the expression of Escherichia coli lipoic acid synthase**. *Protein Expres Purif* 2003, **28**:241-245.

54. Larkin, M. A., Blackshields, G., Brown, N. P., Chenna, R., McGettigan, P. A., McWilliam, H., Valentin, F., Wallace, I. M., Wilm, A., Lopez, R., Thompson, J. D., Gibson, T. J., and Higgins, D. G. **Clustal W and Clustal X version 2.0**, *Bioinformatics 2007*, **23**, 2947-2948.
55. Drummond, A. J., Ashton, B., Buxton, S., Cheung, M., Cooper, A., Duran, C., Field, M., Heled, J., Kearse, M., Markowitz, S., Moir, R., Stones-Havas, S., Sturrock, S., Thierer, T., and Wilson, A. **Geneious v5.4**, 2011, *Available from http://www.geneious.com*.

Chapter 6

Conclusions and Future Directions

6.1 Abstract

With the emergence of multidrug resistant and latent tuberculosis infection, efforts are being made to identify new antibacterial drug targets. Toward this end, adenosine-5'-phosphosulfate reductase (APR), has been validated as a target against persistent phase tuberculosis. In the previous chapters we focused on elucidating mechanistic details of APR, in particular the role of its essential iron-sulfur cofactor. In chapters 3 and 4, we characterized the electronic and geometric properties of the [4Fe-4S] cluster of APR using spectroscopic techniques and density functional theory calculations. Additionally, we investigated the evolution of the switch in substrate specificity between APRs and PAPRs in chapter 5. In this chapter we recapitulate the key findings and significance of this work and discuss the future directions to further our understanding of the role of the iron-sulfur cluster and mechanism of catalysis of APR.

6.2 Conclusions: a Role for the [4Fe-4S] Cluster in APS Reduction

In the past decade several enzymes in mycobacterial sulfur metabolic pathways have been identified and validated as promising drug targets for anti-tubercular therapy. However, as described in chapter 1, many fundamental aspects of enzymes associated with sulfur metabolism remain poorly understood. Adenosine-5'-phosphate sulfate reductase (APR) is one such enzyme that catalyzes the first committed step of sulfate assimilation. APR coordinates to a [4Fe-4S] cluster that is essential for catalysis but the precise role of the cluster has remained

largely unknown. The overall aim of this thesis was to understand the mechanistic details of APR and in particular, to elucidate the role of its metal center. Toward this end, we developed an active site model in chapter 2, illustrating the functional features required for the interaction of APR with a ligand. These studies also provide a pharmacological roadmap for the rational design of small molecules as potential inhibitors of APR.

Further we investigated the role of the [4Fe-4S] cluster of APR using spectroscopic techniques such as electron paramagnetic resonance. Chapter 3 detailed our efforts to successfully generate a paramagnetic state of the cluster as we reported the EPR spectra of MtAPR for the first time. Additionally, using spectroscopic and kinetic analyses, we identified an essential role for the active site residue, Lys144, which interacts with both the iron-sulfur cluster and the substrate, APS. Based on this study, we proposed a role for the iron-sulfur cluster in pre-organizing active site residues such as Lys144 for catalysis and in substrate activation.

In chapter 4, we characterized the geometric and electrostatic properties of the iron-sulfur cluster in APR using density functional theory analysis and extended X-ray fine structure spectroscopy. Findings from this study highlighted a unique function for the cysteine dyad coordination in modulating the redox potential of the iron- sulfur cluster and a role for the cluster in stabilizing the transition state *via* favorable positioning of Lys144 in the active site. Thus the study also confirmed the critical role of Lys144 as a link between [4Fe-4S] cluster and APS to maintain charge balance in the active site.

Finally, we explored the switch in substrate specificity between APR and its divergent relative, PAPR focusing on the influence of the residues P-loop role and the presence of the [4Fe-4S]

cluster on substrate recognition. The results presented in the study underscore the essential role of the cluster in APR, in particular its contribution to the chemical steps in the catalytic mechanism of APS reduction.

6.3 Future Directions

6.3.1 Exploring the proximity of the iron-sulfur cluster to the substrate and active site residues during the catalytic cycle.

In chapter 3 we reported the conditions to reduce the $[4Fe-4S]^{2+}$ cluster in MtAPR to the $[4Fe-4S]^+$ state which could then be as used as a tool for mechanistic studies analogous to other iron-sulfur enzymes such as aconitase [1]. Substrate binding to MtAPR led to a marked sharpening of the EPR signal and an increase in intensity, which was not observed for a panel of substrate analogs, including ADP. Although structural and Mössbauer data show that the iron-sulfur cluster does not come into direct contact with the substrate, EPR studies indicate that there are mid-range electrostatic interactions between APS and the iron-sulfur cluster [2]. Based on our findings we have proposed a possible mechanism for the formation of the *S*-sulfocysteine intermediate of APR with APS (Figure 6.1). According to our model, the iron-sulfur cluster may serve to pre-organize the positively side chain of Lys-144 within the active site, such that the substrate can establish interactions with the residue. Through this network of interactions, the
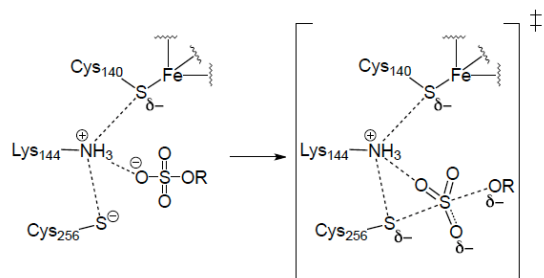

Figure 6.1 Proposed reaction pathway for covalent *S*-sulfocysteine intermediate formation catalyzed by APR. Based on the structure of *Saccharomyces cerevisiae* PAPR (Yu, 2008) , the homology model of PaAPR shows Cys256 within hydrogen-bonding distance of the sulfate group of APS as well as the side chain of Lys-144. Lys-144, in turn, is proximal to Cys-140, which coordinates to the [4Fe-4S] cluster. Through the network of interactions, the [4Fe-4S] cluster may serve to position Lys-144 and activate the substrate.

charge from and polarization within the iron-sulfur cluster may serve to activate the sulfate group of APS for catalytic reduction. A logical extension of the observations from this study would be to study the enzyme – substrate interactions by electron nuclear double-resonance (ENDOR) spectroscopy. ENDOR spectroscopy combines the principles of EPR and NMR spectroscopies and is especially useful for yielding information about nuclei that have weak interactions with the paramagnetic site. By using suitably labeled substrate (^{33}S-APS or ^{17}O-APS) or substrate analogs (ADP or ADPβF) and generating the paramagnetic [4Fe-4S]$^{+}$ state of the cluster, ENDOR spectroscopy could be applied to MtAPR to determine the proximity of the iron-sulfur center with ligand in the active site during the catalytic cycle. These analyses would thus further our understanding of the role of the iron-sulfur cluster in catalytic cycle of APR.

6.3.2 Investigating the electronic properties of the iron-sulfur cluster during the catalytic cycle.

As discussed in Chapter 3, APS reduction proceeds *via* nucleophilic attack by the catalytic Cys256 of PaAPR on APS to form a *S*-sulfocysteine intermediate (E-Cys−Sγ−SO$_3^-$). In the structure of PaAPR, crystallization was performed in the presence of an excess (60-fold over enzyme concentration) of APS [3]. Under these conditions the flexible C-terminal peptide bearing the Cys−Sγ−SO$_3^-$ moiety was likely positioned out of the active site and hence disordered in the protein crystals. This hampered investigation of finer details of the catalytic mechanism, in particular the interactions of residues in the C-terminal peptide with the active site. However, the position of Cys256 in the active site of PaAPR can be determined *via* homology modeling of PaAPR with the crystal structure of the yeast PAPR [3-5] (Figure 6.2). In the homology model, Cys256 is proximal to the sulfate group of APS (3.3 Å from the sulfur atom). Although Cys256 is about 6 Å away from the closest Fe atom in the iron-sulfur cluster, it could influence the electrostatic properties of the cluster via the Lys144 side chain (3.9 Å from Cys256), which in

turn is within hydrogen-
bonding distance of the
cluster coordinating Cys140
residue. The influence of the
C-terminal peptide on the
electrostatics of the active
site during the formation of
the *S*-sulfocysteine
intermediate can be studied
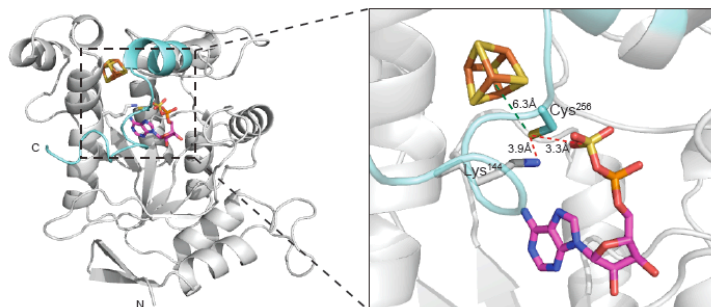by applying DFT calculations

Figure 6.2 Homology-modeled structure of PaAPR (in gray) showing the position of the C-terminal peptide (in blue) over the active site. Left, homology-model of PaAPR based on ScPAPR (Yu, 2008), coordinates of the [4Fe-4S] cluster and APS are from the structure of PaAPR (PDB entry 2GOY). The amino and carboxyl termini are indicated by N- and C- respectively. Right, closer look at the interactions of Cys256 with the sulfate moiety of APS and the side-chain of Lys144 (red dashes). Cys256 would be ~6 Å from the closest Fe atom in the [4Fe-4S] cluster (green dashes).

to a molecular cluster based on the homology model of PaAPR with the C-terminal residues 250-267 in the active site. Following the methodology outlined in chapter 4 we could determine the optimized geometry and electrostatic potential of all the components of the active site including the $[4Fe-4S]^{2+}$ cluster, Cys256, APS, and key residues in the active site. The study would help examine previously unsolved questions such as what components of the active site direct the formation and successive reduction of the *S*-sulfocysteine intermediate, the position and function of the iron-sulfur cluster and cationic residues (Lys144, Arg242, and Arg245) during the formation of the *S*-sulfocysteine intermediate and how the formation of this intermediate state protects the $[4Fe-4S]^{2+}$ cluster against oxidative degradation. Further, similar calculations could be done replacing ADP for APS to determine factors influencing substrate selectivity.

6.3.3 Examining the PAPR-Trx protein-protein interface

In chapter 5, we explored the evolution of substrate selectivity between APR and PAPR, which share sequence and structural homology and a conserved reaction mechanism. Both the

sulfonucleotide reductases (SR) require thioredoxin (Trx) to supply the electrons for reduction of the S-sulfocysteine intermediate formed with the sulfonucleotides (APS or PAPS) in the first step of the reaction [6]. Although Trx is a ubiquitous reductant that maintains cellular redox homeostasis by interacting with several redox enzymes, its association with SRs is unique in that it only interacts with the S-sulfocysteine intermediate form of the enzymes. The co-crystal structure of PAPR with Trx has revealed protein-protein interaction sites, as highlighted in figure 6.3a [7]. The first, more obvious, interaction is between Trx and the strictly conserved glutathione sequence, $Glu^{238}Cys^{239}Gly^{240}Leu^{241}His^{242}$ on PAPR (Figure 6.3b) while the second site of PAPR-Trx interaction is observed near the PAPR active site and adjacent to the C-terminal peptide of PAPR (Figure 6.3c).

The motivation for investigating the general mechanism of catalysis of SRs is that these enzymes represent potential targets for therapeutic intervention, as they are essential, but absent in humans. In chapter 1 we discussed how APR is required for the survival of persistent phase *M. tuberculosis.* Additionally, PAPR plays a role in the sulfate-dependent pathways in pathogens such *E. coli*, *Salmonella typhimurium* and *Yersinia pestis.* A closer look at the unique protein-protein interfaces between SRs and Trx would advance our understanding of the rationale for interaction of these proteins as well as facilitate the design of inhibitors that could potentially disrupt the interface. Due to the absence of an oxygen sensitive iron-sulfur cluster, PAPR could serve as a model to study the specific features of the PAPR-Trx interface that dictate protein-protein interactions. From the co-crystal structure residues on PAPR that are involved in hydrogen bonds or salt bridges with residues on Trx could be identified [7]. For instance, Trp205 in EcPAPR hydrogen bonds with the carbonyl of Glu30 of EcTrx, and EcPAPR Asp206 is involved in the salt bridge between Lys36 and Glu30 in EcTrx. The contribution of the identified residues

towards the PAPR-Trx interaction could be measured by alanine scanning followed by binding and kinetic assays with Trx.
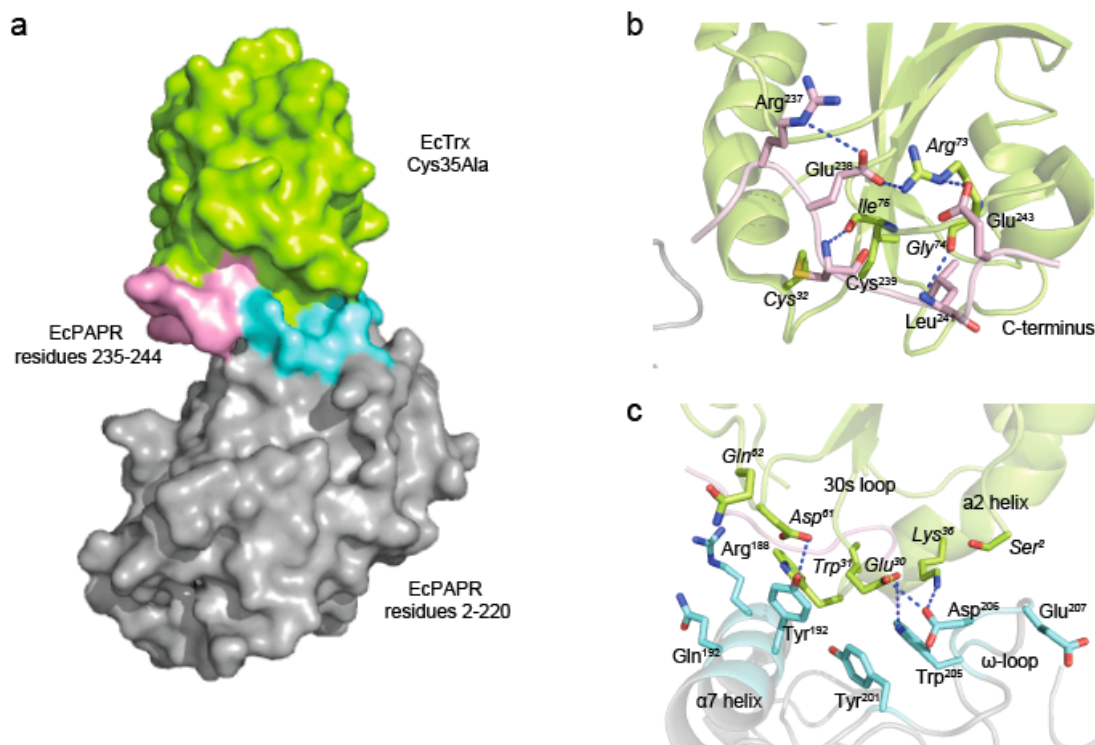

Figure 6.3 Co-crystal structure of PAPR-Trx complex, PDB entry 2O8V (Chartron, 2007). a. Solvent accessible surface depiction of PAPR-Trx complex. EcPAPR residues 2-220 are colored gray, C-terminal peptide residues 235-244 are colored pink, interface between ω-loop of PAPR and the 30s loop of Trx is colored blue, and EcTrx Cys35Ala is colored green. b. Specific recognition at the interface between the C-terminal peptide of PAPR and Trx involves hydrogen bonds, hydrophobic contacts and a network of salt bridges. c. Specific recognition at the interface between ω-loop of PAPR and the 30s loop of Trx involves hydrogen bonds, aromatic stacking and hydrophobic interactions. Trx residues are in italics.

Furthermore, observations from the structure of the PAPR-Trx complex suggest that large-scale conformational arrangements in PAPR are essential for sulfonucleotide reduction to occur [7]. For SRs, these conformational rearrangements include allosteric transitions in the quarternary structure of the protein as evidenced by biochemical studies as well as the movement of the C-terminal peptide domain carrying the catalytic Cys residue over and out of the active site signifying closed and open conformations of the enzyme [3,6]. To evaluate these conformational changes driving sulfonucleotide reduction, a truncated version of PAPR could be generated that

lacks C-terminal peptide (*i.e.*, last 10 residues). The C-terminal peptide could be synthesized following established peptide synthesis strategies. Finally, by measuring the binding affinity of both the truncated PAPR and the C-terminal peptide in the absence or presence of substrate, the contribution of each of these components toward the interaction with Trx could be determined. Overall, these studies would yield insights into the mechanism of sulfonucleotide reduction and facilitate the design of molecules that disrupt the interactions of SRs with Trx.

6.4 Concluding remarks

Ever since its discovery a decade ago, the precise role of the $[4Fe-4S]^{2+}$ in mechanism of APS reduction has remained elusive. In this thesis, we presented for the first time the generation of a paramagnetic $[4Fe-4S]^{+}$ state of the cluster which served as a useful tool for mechanistic studies using EPR spectroscopy, as demonstrated, and opened the door for other forms of spectroscopies such as ENDOR and electron spin echo envelope modulation. The application of these techniques to APR would yield valuable information about the relationship between the iron-sulfur cluster, active site residues and the substrate. Based on observations from our study, we were able to directly implicate the iron-sulfur cluster in the catalytic mechanism of APR. We provide evidence for a role of the cluster in pre-organizing active site residues, and contributing to activation of substrate and events leading to the formation of the *S*-sulfocysteine intermediate. Apart from the functional relevance of our findings, the knowledge gained from this study have important implications the design of cluster-targeted APR inhibitors that would ultimately lead to improved anti-tubercular therapies. Our study also provided insights into substrate specificity among divergent evolved groups of sulfonucleotide reductases. Collectively, this work contributes towards a better understanding of the catalytic mechanism of this unique class of enzymes and the significance of iron-sulfur cofactors in associated proteins.

6.5 References

1. Beinert H, Kennedy MC, Stout CD: **Aconitase as Iron-Sulfur Protein, Enzyme, and Iron-Regulatory Protein**. *Chem Rev* 1996, **96**:2335-2374.
2. Bhave DP, Hong JA, Lee M, Jiang W, Krebs C, Carroll KS: **Spectroscopic studies on the [4Fe-4S] cluster in adenosine 5'-phosphosulfate reductase from Mycobacterium tuberculosis**. *J Biol Chem* **286**:1216-1226.
3. Chartron J, Carroll KS, Shiau C, Gao H, Leary JA, Bertozzi CR, Stout CD: **Substrate recognition, protein dynamics, and iron-sulfur cluster in Pseudomonas aeruginosa adenosine 5'-phosphosulfate reductase**. *J Mol Biol* 2006, **364**:152-169.
4. Hong JA, Bhave DP, Carroll KS: **Identification of critical ligand binding determinants in Mycobacterium tuberculosis adenosine-5'-phosphosulfate reductase**. *J Med Chem* 2009, **52**:5485-5495.
5. Yu Z, Lemongello D, Segel IH, Fisher AJ: **Crystal structure of Saccharomyces cerevisiae 3'-phosphoadenosine-5'-phosphosulfate reductase complexed with adenosine 3',5'-bisphosphate**. *Biochemistry* 2008, **47**:12777-12786.
6. Carroll KS, Gao H, Chen H, Stout CD, Leary JA, Bertozzi CR: **A conserved mechanism for sulfonucleotide reduction**. *PLoS Biol* 2005, **3**:e250.
7. Chartron J, Shiau C, Stout CD, Carroll KS: **3'-Phosphoadenosine-5'-phosphosulfate reductase in complex with thioredoxin: a structural snapshot in the catalytic cycle**. *Biochemistry* 2007, **46**:3942-3951.